8-20-2013 12:00 AM

Development of Novel Contrast Agents for Magnetic Resonance Imaging

Mark Milne
The University of Western Ontario

Supervisor
Dr. Robert H. E. Hudson
The University of Western Ontario

Graduate Program in Chemistry
A thesis submitted in partial fulfillment of the requirements for the degree in Doctor of Philosophy

Recommended Citation

Milne, Mark, "Development of Novel Contrast Agents for Magnetic Resonance Imaging" (2013). *Electronic Thesis and Dissertation Repository*. 1529.
https://ir.lib.uwo.ca/etd/1529

Development of Novel Contrast Agents for Magnetic Resonance Imaging

(Thesis format: Integrated Article)

by

Mark Milne

Graduate Program in Chemistry

A thesis submitted in partial fulfillment
of the requirements for the degree of
Doctor of Philosophy

The School of Graduate and Postdoctoral Studies
The University of Western Ontario
London, Ontario, Canada

Abstract

Magnetic resonance (MR) has outstanding potential as a noninvasive imaging modality. Possessing spatial resolution at the millimeter scale, MR imaging of anatomical features is unrivalled by other imaging techniques. Although MR imaging has outstanding spatial resolution it suffers from inherently low signal intensity. With a low sensitivity, the signal to noise ratio is low; thus MRI scans may take upwards of an hour to generate an acceptable image without a contrast agent. This drawback clearly justifies the need for contrast agents and the long held interest in their development.

Our development of novel MRI contrast agents focuses on the synthesis and evaluation of cyclen based agents for magnetic resonance spectroscopy (MRS), spin-lattice relaxation (T_1), spin-spin relaxation (T_2) and paramagnetic chemical exchange saturation transfer (ParaCEST).

Chapters 2 and 3 discuss contrast agents based on tetra(propargyl) DOTAM lanthanide complexes for magnetic resonance spectroscopy (MRS), relaxation and ParaCEST. With respect to MRS, temperature sensitivity values from 1.05 ppm/°C to 1.76 ppm/°C were determined, which represents a 2–3 fold improvement over currently available lanthanide temperature-responsive contrast agents. Tetra(propargyl) DOTAM was further functionalized through Huisgen "click" chemistry reactions with a glucosyl azide. These complexes were characterized by a combination of ^{1}HNMR, single-crystal X-ray crystallography, relaxation and CEST experiments.

Chapter 4 focuses on the evaluation of a highly shifted amide suitable for ParaCEST imaging. The Tm^{3+} chelate of DOTAM [1,4,7,10-tetrakis(carbamoylmethyl)-1,4,7,10-tetraazacyclododecane] possessing sterically demanding *t*-butyl amide substitution favors TSAP geometry. This geometry shifts the amide signal to -100 ppm, which is beyond the frequency of macromolecule magnetization transfer and thus represents a prototype contrast agent for potential *in vivo* use.

Chapter 5 discusses a series of Dy^{3+} and Tm^{3+} tetra(substituted) DOTAM paraCEST agents incorporating *para*-substituted anilines. The aniline and *p*-methoxyaniline agents response to changes in pH near the physiologic range have been evaluated. Two distinct amide signals are observed in the CEST spectrum for Tm^{3+}-*p*-methoxyaniline complex, corresponding to SAP and TSAP isomers. A crystal structure of this agent indicates TSAP geometry with the absence of an inner sphere water molecule. Due to the lack of coordinated water, this agent produces minimal shortening of T_2 relaxation time constants. The benefit of a long T_2 relaxation is demonstrated in the higher signal to noise ratio for the agent that does not contain an inner sphere water compared to agents that have bound water.

Chapter 6 discusses a water soluble gold nanoparticle (AuNP) conjugated to over 50 Gd^{3+} chelators which has been prepared using an interfacial Michael addition. The agent was determined to be non-acutely toxic to mice and T_1-weighted *in vivo* images of mouse kidneys were obtained.

Keywords

Magnetic resonance imaging, MRI, Lanthanides, Paramagnetic resonance saturation transfer, ParaCEST, Chemical exchange saturation transfer, CEST, Relaxation, Contrast agent.

Acknowledgments

I would like to express my appreciation to Dr. Robert Hudson for his guidance and teachings for the past four years. I would like to thank him for not only being a supervisor who supported me on all of my ideas, but also as a friend who was there to discuss areas outside of research.

I would also like to thank my many lab mates for the past years for all their support and friendship, in particular, Dr. Mojmir Suchy, Dr. Dave Dodd, Andre St. Amant, Kirby Chicas, Melissa Lewis, Augusto Matarazzo , Rachel Wang , Christie Ettles and Pierangelo Gobbo. I would also like to thank Dr. Robert Bartha, Nevin McVicar, Alex Li and Miranda Bellyou for all the help with imaging and the animal studies.

I would also to thank Dr. Michael A. Kerr, Dr. Martin J. Stillman, Dr. Peter Caravan and Dr. Savita Dhanvantari for taking the time to read my thesis.

Finally I would like to thank my wife Tami Turner for being there for me throughout my degree. She always supported me with love and encouragement and was always there when I needed her.

Coauthors Statement

This thesis is written as an integrated article, because of this, contributions of co-authors will be included within chapters 3-6. Only articles in which I was first author or first co-author have been included for this thesis. The papers presented in chapters 3-6 include collaborations with the imaging group of Professor Bartha from the Robarts Research Institute. All syntheses and structural characterisation of new contrast agents were carried out by the chemistry group participants. All *in vivo* experiments were carried out by Mr. McVicar of Dr. Bartha`s group. Evaluation of CEST, T_1 and T_2 properties were shared between the two groups. The following is a detailed description of author contributions for each chapter.

- Chapter 2 has been published as a communication. The corresponding reference is:

  Mark Milne, Robert H.E. Hudson[†]. *"Contrast agents possessing high temperature sensitivity."* Chemical Communications, **2011**, 47, 32, 9194-9196.

  Professor Hudson conceived the initial molecular design, subsequently identification of possible uses of the agents was done by Mark Milne. All syntheses, characterization and initial manuscript writing were done by Mark Milne. The final submission was prepared by Dr. R.H.E Hudson.

- Chapter 3 has been published as a full paper. The corresponding reference is:

  Mark Milne, Kirby Chicas, Alex Li, Robert Bartha and Robert H.E. Hudson[†]. *"ParaCEST MRI contrast agents capable of derivatization via 'click' chemistry."* Organic and Biomolecular Chemistry, **2012**, 10, 287-292.

  Design of title compounds was shared between Mark Milne and Dr. Hudson. Mr. Chicas prepared the glucosyl azide which was used for the click reactions. Dr. Li acquired the CEST data and Dr. Martinez collected the NMRD profiles. All click reactions and sequential reactions and purification were done by Mark Milne. The manuscript was prepared by Mark Milne and the final submission was done by Dr. R.H.E Hudson.

- Chapter 4 has been published as a full paper. The corresponding reference is:

  Todd K. Stevens*, **Mark Milne***, Adam A. H. Elmehriki, Mojmir Suchý, Robert Bartha, Robert H. E. Hudson[†]. *"DOTAM-based ParaCEST agent favoring TSAP geometry for enhanced amide proton chemical shift dispersion and temperature sensitivity*." Contrast Media and Molecular Imaging, **2012**, 3, 289–292. *Contributed equally.

  The focus of this manuscript is the evaluation of ParaCEST agents that were prepared by Mr. Elmehriki and Dr. Suchy for an alternative paper.

  Adam A. H. Elmehriki, **Mark Milne**, Mojmir Suchý, , Robert H. E. Hudson[†], *"Complexes of selected late period lanthanide(III) cations with 1,4,7,10-tetraazacyclododecane-1,4,7,10-tetraacetic acid amide (DOTAM)-alkyl ligands — A new platform for the development of paramagnetic chemical exchange saturation transfer (PARACEST) magnetic resonance imaging (MRI) contrast agents*" Canadian Journal of Chemistry, **2013**, 91(3): 211-219.

  Identification of possible uses of agents was done by Mark Milne. Collection of data and evaluation of the agents and writing of the manuscript was shared between Mark Milne and Dr. Stevens. Modeling studies were done by Dr. Stevens and the final submission was prepared by Dr. R.H.E Hudson.

- Chapter 5 is currently in preparation to be published as a full paper:

  Mark Milne, Melissa Lewis, Nevin McVicar, Robert Bartha and Robert H. E. Hudson[†], *"Ratiometric approach for intramolecular amides for concentration independent evaluation of pH".* Submitted to RSC Advances, **2013**.

  Design of agents was done by Mark Milne. Synthetic protocols and 50% of the synthesis was done by Mark Milne. Data collection and evaluation of CEST, T_1, T_2 was done by Mark Milne. Images were acquired by Mr. McVicar. X-Ray data was collected and solved by Dr. Boyle. Writing of the manuscript was done by Mark Milne with the exception of the description of images, which was done by Mr. McVicar and the final submission was prepared by Dr. R.H.E Hudson.

- Chapter 6 has been submitted as a full paper. The corresponding reference is:

  Mark Milne , Pierangelo Gobbo, Nevin McVicar, Mark S. Workentin , Robert Bartha and Robert H. E. Hudson†, *"Water soluble gold nanoparticles functionalized with gadolinium through Michael addition for use as a MRI contrast agent"*. Submitted to Journal of Materials Chemistry B, **2013**.

  Design of the derivatized nanoparticles was shared between Mark Milne and Mr. Gobbo. Chelator design and synthesis was done by Mark Milne. Nano design and preparation was done by Mr. Gobbo. *In vivo* evaluation was done by Mr. McVicar. ICP-OES was a fee for service in the department of engineering. Writing of the manuscript was done by Mark Milne with the exception of the description of Michael addition onto the nanoparticles and evaluation of the *in vivo* images. The final submission was prepared by Dr. R.H.E Hudson.

Table of Contents

Chapter 1 Introduction

Chapter 2 Magnetic Resonance Spectroscopy Contrast Agents for Temperature Measurments

Chapter 3 Synthesis and Characterisation of ParaCEST MRI Agents via Click Chemistry

Chapter 4 Development of TSAP Based ParaCEST Agents

Chapter 5 Synthesis and Characterisation of Aniline Containing ParaCEST Agents

Chapter 6 Gold Nano Particles Functionalized with Gadolinium as T_1 Based Contrast Agents

List of Tables

List of Figures

List of Schemes

List of Supplemental Information

List of Abbreviations

μ	Magnetic moment
Å	Angstrom
Al_2SO_3	Aluminum oxide
AuNP	Gold nano particle
C	Concentration
CA	Contrast agent
CEST	Chemical exchange saturation transfer
CPMG	Carr-Purcell-Meiboom-Gill
CT	Computer tomography
Cw	Continuous wave
Cyclen	1,4,7,10-tetraazacyclododecane
d	Diameter
DMSO	Dimethyl sulfoxide
DOTA	1,4,7,10-tetraazacyclododecane
DOTAM	1,4,7,10-tetraazacyclododecane-1,4,7,10-tetraacetamide
DTPA	Diethylene triamine pentaacetic acid
ESI	Electro spray ionization
FCC	Flash column chromatography
FOV	Field of view
h	Planks's constant
HPLC	High performance liquid chromatography
I	Nuclear spin quantum number
ICP	Inductively coupled Plasmon
IV	Intravenous
K_2CO_3	Potassium Carbonate
kDa	Kilo dalton
MRI	Magnetic resonance imaging
MT	Magnetization transfer
Mz	Magnetization
Na_2SO_4	Sodium sulfate
$NaBH_4$	Sodium borohydride
$NaHCO_3$	Sodium bicarbonate
NMR	Nuclear magnetic resonance
NMRS	Nuclear magnetic resonance spectroscopy
NP	Nano particle
p	Angular momentum
p	Density
ParaCEST	Paramagnetic chemical exchange saturation transfer
PET	Positron emission tomography
q	Innersphere water
Rf	Radio frequency
Rt	Retention time

SAP	Square antiprismatic
SPIO	Super paramagnetic iron oxide
T	Tesla
T_1	Longitudinal relaxation time
T_2	Transverse relaxation time
TEM	Transmission electron microscopy
Tm	Thulium
TMS	Tetramethylsilane
TSAP	Twisted square anitprismatic
UPLC	Ultra performance liquid chromatography
γ	Gyromagnetic moment
δ	Chemical shift
ν	Larmor frequency
τ_m	Bound water lifetime

Introduction

1.1 Magnetic Resonance Imaging (MRI)

Magnetic resonance (MR) has become one of the leading imaging modalities used clinically for diagnosis of disease and imaging of structural anatomy. Over a 30 year period between the 1950s and the 1980s, MRI developed from building on previously known nuclear magnetic resonance (NMR) techniques to evaluate relaxation of ^{1}H and other nuclei *in vivo*. The current state of the art technology uses field gradients to create millimeter thick slices, which allow for the detailed acquisition of 2D and 3D images. With the fundamental technology based on NMR, MRI uses a radio frequency as the source of excitation during imaging, which has been shown to have no detrimental effects on patients. As a noninvasive imaging tool MRI has the potential to be less harmful compared to other imaging modalities that acquire similar images, such as, computer tomography (CT) which use X-Rays and positron emission tomography (PET) which uses radioactive materials. With patient safety in mind, MRI as a noninvasive imaging technique can be applied to a patient numerous times, with negligible side effects. This cannot be said for other imaging modalities that generate detrimental side effects due to the use of ionizing radiation as used in CT scans or the use of radioactive material in PET scans. To understand how MR images are acquired, one must first have a basic understanding of the theory of NMR.

With the goal of developing novel MRI contrast agents (CA) we are concerned with the observation of *in vivo* ^{1}H nuclei. Sources of ^{1}H nuclei are plentiful; however, this thesis will focus on bulk water ^{1}H nuclei, exchangeable and nonexchangeable ^{1}H nuclei of CAs. Accordingly, a brief explanation of the principals of MRI and NMR with respect to ^{1}H will be discussed.

In 1946 two research groups (F. Bloch, W.W. Hansen, M.E. Packard and E. M. Purcell, H. C. Torrey, R. V. Pound) independently discovered the phenomenon of nuclear magnetic resonance with Bloch and Purcell sharing the Nobel prize in physics (1952) for their contributions.[1] ^{1}H NMR spectroscopy is possible because of the interaction of the nucleus with a magnetic field, causing an angular momentum (***P***), which can be calculated by equation 1.1.[1]

$$eq. 1.1. \qquad P = \frac{h}{2\pi}\sqrt{I(I+1)}$$

Where h is Plank's constant and I is the nuclear spin quantum number equal to ± ½ for hydrogen atoms. Because a hydrogen atom has a nonzero value for the spin quantum number a ^{1}H nucleus will also have a magnetic momentum (**μ**) which can be calculated by equation 1.2.[1]

$$eq. 1.2. \qquad \mu = \gamma P$$

Where γ is the gyromagnetic ratio of hydrogen (26.75 10^7 rad T^{-1} s^{-1} or 42.577 MHz T^{-1}).

If hydrogen atoms are then placed into a magnetic field (B_0) the angular momentum splits into two possible orientations, either aligned with (+ ½) or against the magnetic field (-½). This can be calculated from equation 1.3.[1]

$$eq. 1.3. \qquad m = (2I + 1)$$

Where m is the magnetic quantum number, I = ½ for hydrogen atoms. In NMR spectroscopy, the z axis is conventionally chosen as the magnetic field direction. When the ^1H nuclei are subjected to a magnetic field they will begin to precess around axis of the magnetic field. The frequency in which the protons will precess around the axis (ν, Larmor frequency) is proportional to the field strength of the magnet and can be calculated in equation 1.4.[1]

$$eq. 1.4. \qquad \nu = \frac{\gamma}{2\pi} B_0$$

As an example for NMR spectroscopy, a ^1H nucleus exposed to a field strength of 9.4 T will have a Larmor frequency of 400 MHz. The distribution of the two energy states (± ½) is defined by a Boltzmann distribution, with a larger population being aligned with the magnetic field, or in a lower energy state. The difference in energy state population is defined as a vector with the macroscopic magnetization defined as M_0 along the z axis. Irradiation at the Larmor frequency using a Rf pulse (B_1) will move M_0 away from the z axis and onto either the x or y axis, where the receiver is situated to measure the energy released during relaxation (Figure 1.1).

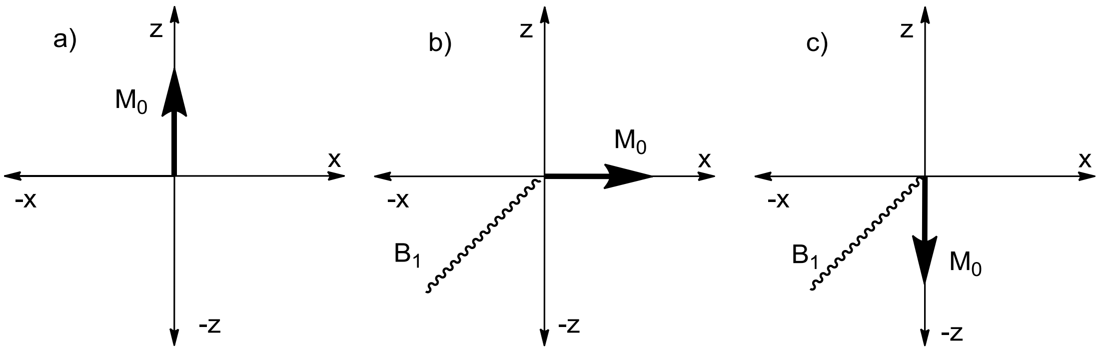

Figure 1.1. Representation of net magnetization vector (M_0) a) At equilibrium before a B_1 is applied ($M_0 = M_z$). b) After a 90° B_1 is applied ($M_0 = M_x$). c) After a 180° B_1 is applied ($M_0 = M_{-z}$).

As the ^{1}H nucleus begin to relax, their frequency of precession can be measured as the excess energy is released. The process of the data acquisition is not needed to understand the basic NMR theory in this thesis and will not be discussed further. In NMR spectroscopy the different chemical environments in which the ^{1}H nuclei are bonded will lead to different precession frequencies. As relaxation occurs, the various frequencies are measured and displayed in either Hertz (Hz) or parts per million (ppm) to identify the environment of the proton and are typically referenced to the frequency of the ^{1}H nuclei resonance of tetramethylsilane (TMS) for organic molecules. With respect to MRI, we are focused on a single chemical environment of ^{1}H nuclei (water) and therefore the majority of the ^{1}H nuclei will precess at the same frequency for a given B_0. One of the main reasons to use MR as an imaging technique is due to its excellent spatial resolution. The spatial resolution is achieved by acquiring a large number of “slices” or “planes” with resolution thicknesses as little as 100 µm. To achieve the different planes or slices it is necessary to create a gradient of magnetic field strength along the specimen being imaged. This creates a number of different micro fields all with different Larmor frequencies for protons. Using equation 1.4, its can be seen as B_0 changes so does the Larmor frequency and therefore only areas with equivalent B_0 can be imaged simultaneously as slices. Protons that do not have the same B_0 will not be affected by the Rf pulse and therefore will not be observable during the imaging. These micro variations allow for sub-millimeter precision when acquiring a MR image.

Relaxation occurs after the Rf pulse is turned off. At this point the net magnetization has been flipped onto the x or y axis now begins to relax back to the resting state. Relaxation occurs through two mechanisms. The first is spin-lattice relaxation or longitudinal relaxation (T_1). T_1 relaxation is defined as when the magnetization returns to the z axis. This is enhanced by the interaction of the excited ^{1}H nucleus with its surroundings to release energy. The surroundings in NMR can be other molecules or the NMR tube. With respect to MRI the energy can be transferred to the surrounding tissue. The second is spin-spin relaxation or transverse relaxation (T_2). After the Rf pulse has aligned the M_0 vector onto the x or y-axis the signals are bunched together in what is called phase coherence.[1] The T_2 is a measurement of how quickly the in-phase signals become out of phase. This happens spontaneously as the protons start to precess and interact with other protons. T_2 relaxation can be enhanced by magnetic field (B_0) inhomogeneity. Equation 1.4 shows that protons at a higher field should precess more quickly than those at a lower field. This difference in precession rate will dephase the signals and lead to a signal decrease.

1.2 Contrast Agents

An MRI contrast agent is any medium that aids in the acquisition of an image or enhances the information gained from an image. While MRI does not necessarily need a contrast agent, the use of CAs has shown to significantly enhance the images and due to this, roughly 50% of all MR images use some form of CA.[2] The enhancement of the signal can be accomplished in a number of ways, such as, shortening the scan time needed to acquire a similar image without agent, enhancement of regions that were not visible without an agent and measuring physiological conditions (pH, temperature). The latter does not necessarily enhance the image but rather gains information that would not be otherwise available. In MRI, the first generation of CAs were designed to increase the relaxation of the ^1H nuclei of water. The agents are typically referred to as T_1 or T_2 agents and their definition depends on which relaxation pathway is enhanced to a greater effect. T_1 agents are described as agents that increase relaxation through spin-latice and are usually incorporate a Gd^{3+} ion, while T_2 agents enhance spin-spin relaxation and typically use iron oxide nanoparticles to generate the contrast. However, new agents called T_2-exchange agents have recently been developed using lanthanides to reduce the T_2. In general, T_1 agents will increase the signal where the agent is located, while T_2 will decrease the signal, causing a darkening of the resulting image. The third design of MRI CAs that will be discussed are ParaCEST agents. These agents rely on saturation transfer between the CA and the surrounding water to decrease the overall water signal, generating contrast.

1.2.1 T_1-Based Contrast Agents

Gadolinium based T_1 agents were first developed in the 1980s with the first clinically accepted Gd^{3+} CA (Magnevist) approved in 1987. Magnevist was designed using diethylenetriaminepentaacetic acid (DTPA) as a chelating moiety around a Gd^{3+} ion (Figure 1.2). Using the eight donating sites of DTPA to coordinate the Gd^{3+} left a single site on the lanthanide open to allow for exchangeable water, as lanthanides have a nine site coordination sphere. The exchangeable water molecule (bound water) is used to transfer the efficient T_1 relaxation of the 7 unpaired electrons of Gd^{3+} to the bulk solvating water molecules. Paramagnetic molecules, especially Gd^{3+} with 7 unpaired electrons, have the ability to reduce the T_1 of ^1H nuclei substantially. This is due to the high magnetic moment of unpaired electrons (658 times stronger than a proton).[3] Since the development of Magnevist there has been research into the development of new agents that are more efficient (lower dose) and form more stable chelates, to limit toxicity of the lanthanide ions. The stability of lanthanide based contrast agents is essential, as free lanthanides are toxic. The syndrome nephrogenic systemic fibrosis has been linked to patients that have been administered gadolinium contrast agents.[4, 5] Thus, patients with impaired kidney functions, who cannot eliminate the CA quickly, will typically not be imaged using a CA. Due to the possibility of toxic side effects, macrocyclic 1,4,7,10-tetraazacyclododecane (cyclen) has been used to develop a number of clinically available CAs, as the macrocyclic chelator has been shown to be more stable *in vivo* and for this reason is our choice of chelator for our development of novel CAs.[6, 7] The simplest of the macrocyclic CAs is Gd^{3+} 1,4,7,10-tetraazacyclododecane-1,4,7,10-tetraacetic acid (Dotarem, Figure 1.2) which was accepted as a CA in the 1990s.

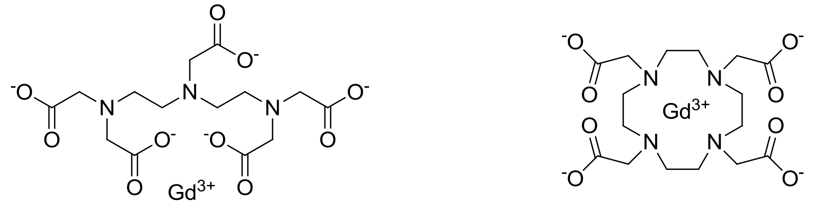

Gd^{3+} diethylenetriaminepentaacetic acid (Magnevist)

Gd^{3+} 1,4,7,10-tetraazacyclododecane-1,4,7,10-tetraacetic acid (Dotarem)

Figure 1.2. Left) Chemical structure of the first clinically available T_1 contrast agent. A Gd^{3+} ion is chelated with DTPA. Right) A Gd^{3+} contrast agent using a macrocyclic chelator.

In aid of designing more efficient Gd^{3+} CAs, mathematical models of the processes of relaxation have been developed, most notably by Bloembergen, Solomon and Morgan, and can traced to the Bloch equations. [3] The relaxivity (r_1) of a Gd^{3+} CA is described by the time for T_1 relaxation to occur at 1 mM concentration of the CA (eq. 1.5).[3]

$$eq. 1.5 \qquad \frac{1}{T_{1(Obs)}} = \frac{1}{T_{1(W)}} + r_1[Gd]$$

Where $T_{1(Obs)}$ is the bulk water T_1 measured in the presence of a paramagnetic species. $T_{1(W)}$ is the T_1 measured without any paramagnetic species. r_1 is the relaxivity of the agent ($mM^{-1}\ s^{-1}$) and [Gd] is the concentration of gadolinium present (mM). The relaxivity of an agent can further be evaluated by the inner sphere (is) coordinating water, in equation 1.6, where the exchange rate and number of coordinated water molecules are taken into account.[3]

$$eq. 1.6 \qquad \left(\frac{1}{T_1}\right)^{\text{is}} = \frac{cq}{55.5} \frac{1}{T_{1m} + \tau_m}$$

Where c is the concentration of agent, q is the number of coordinated water molecule(s), τ_m is the lifetime of the bound water and $1/T_{1m}$ is the longitudinal inner-sphere relaxation rate. From these two equations it is obvious that a higher number of coordinated water molecules and a lower bound water lifetime will give rise to a more efficient CA. The limitation on this however is the toxicity of the agent if the metal is not coordinated strongly, which can occur as the q value is increased. There are agents under development that contain more than a single bound water,[8] but these will not be discussed in this thesis. A vast number of equations have been developed and their use in fully characterizing T_1 based CAs is possible. Typically to solve these equations and extract all the parameters that affect T_1 relaxation, one would need to perform NMR field cycling experiments, electron paramagnetic resonance studies and liquid NMR of various pressures.[6, 9] In chapter 3, field cycling spectra were acquired but the relevant Bloch equations were not solved for the relaxation parameters. While it is possible to solve relaxation parameters associated with T_1 based CAs, our focus of T_1 based contrast agents was the development of new synthetic methods to conjugate cyclen to other molecules of interest. In chapter 3 there will be the discussion of "click" chemistry and in chapter 6 there will be a discussion of nanoparticles that operate as T_1 agents. Therefore a deeper understanding of the Bloch equations is not needed to appreciate the work presented in this thesis.

The acquisition of a T_1-weighted image is enhanced by Gd^{3+} agents due to the short T_1 relaxation rate of the water that interacts with the agent. A typical Gd^{3+} contrast agent on a 9.4 T MR scanner (400 MHz spectrometer) will have a relaxivity of 2-3 $mM^{-1} s^{-1}$. This means that for a sample having 1 mM CA agent the T_1 will be 333 – 500 ms for the water that interacts with the agent. While the assumption that all the water in a NMR tube would interact with the agent, the same cannot be said for *in vivo* imaging. Different tissues and different areas of a slice will not interact with an agent to the same extent. Thus relaxation times will differ for different tissues types and concentrations of agent. If a pulse sequence is designed accordingly, imaging only the quickly relaxing ^1H nuclei will be achieved, and slowly relaxing ^1H nuclei will not be observed. To put this into perspective, some T_1 relaxation rates of tissues are listed in Table 1.1.

Table 1.1 T_1 relaxation rates of ^1H_2O for brain tissues at 4T.[10]

	T_1 (s)
White Matter	1.010
Grey Matter	1.723
Blood	1.914
Cerebrospinal fluid	4.472

Taking these values as averages for *in vivo* imaging, one can see that using a CA that has an r_1 of 2-3 $mM^{-1} s^{-1}$ will change water's T_1 enough (300 – 500 ms) to generate a contrast image. This however assumes that a 1 mM concentration is achieved in the region of interest during imaging, which is not always possible. As the r_1 of the contrast agent increases the concentration needed to produce the same contrast decreases. Thus the motivation for the development of new agents possessing increased relaxivity while maintaining good stability *in vivo*. Figure 1.3 illustrates the origin of a MRI contrast enhancement in the presence of a T_1 relaxation agent. The difference in the signal with and without agent is used to generate the contrast in T_1 weighted MR images.

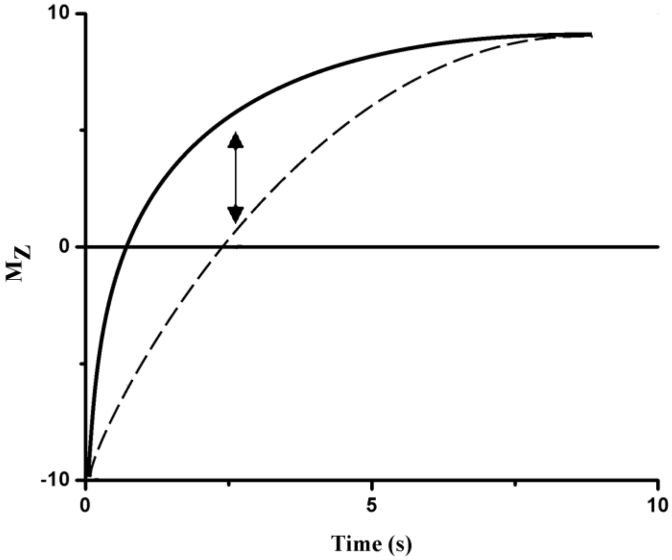

Figure 1.3. Representation of the contrast that is realized by use of a T_1 relaxation agent vs. water without a relaxation agent. The solid curve is the signal intensity of water as a function of time using an inversion recovery sequence with a relaxation agent. The dashed curve is the signal intensity of as a function of time using an inversion recovery sequence without a relaxation agent. T_1 relaxation is faster for the system where a T_1 agent is used. The difference in these two intensities allow for a contrast during T_1 weighted MR imaging.

The evaluation of T_1 agents is typically done by comparing the inverse of the T_1 values normalized to 1 mM and reported as relaxivity with units (mM^{-1} s^{-1}). The inversion recovery experiment is not a typical experiment for organic chemists and therefore will be discussed briefly for clarity. The simplest way to discuss the inversion recovery experiment is to visually represent how the magnetization (Mz) changes over time after a “flip” of the angle. Figure 1.4 has a representation of how the inversion recovery experiment is performed. Figure 1.5 has a representation of what occurs by arraying the time before the 90° pulse is applied, along with a spectral representation of the signal.

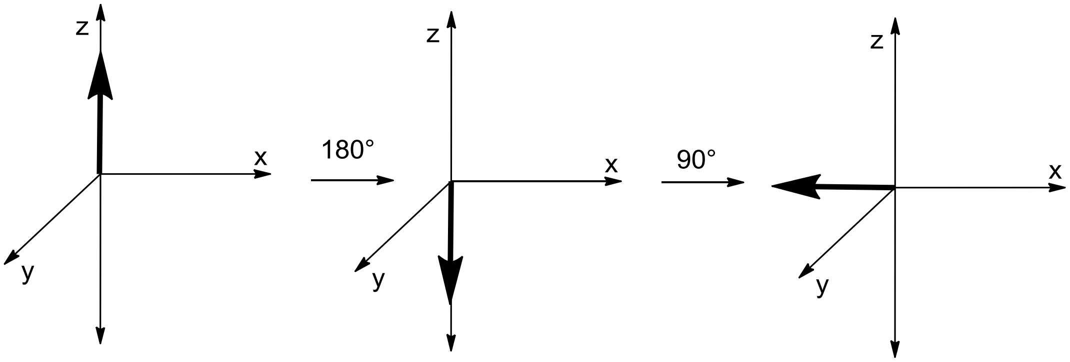

Figure 1.4. Representation of an inversion recovery experiment. Firstly a 180° pulse is applied causing the Mz to point along the –z axis. This is followed by arraying the time before a 90° pulse is applied, which flips the magnetization along the -x followed by detection.

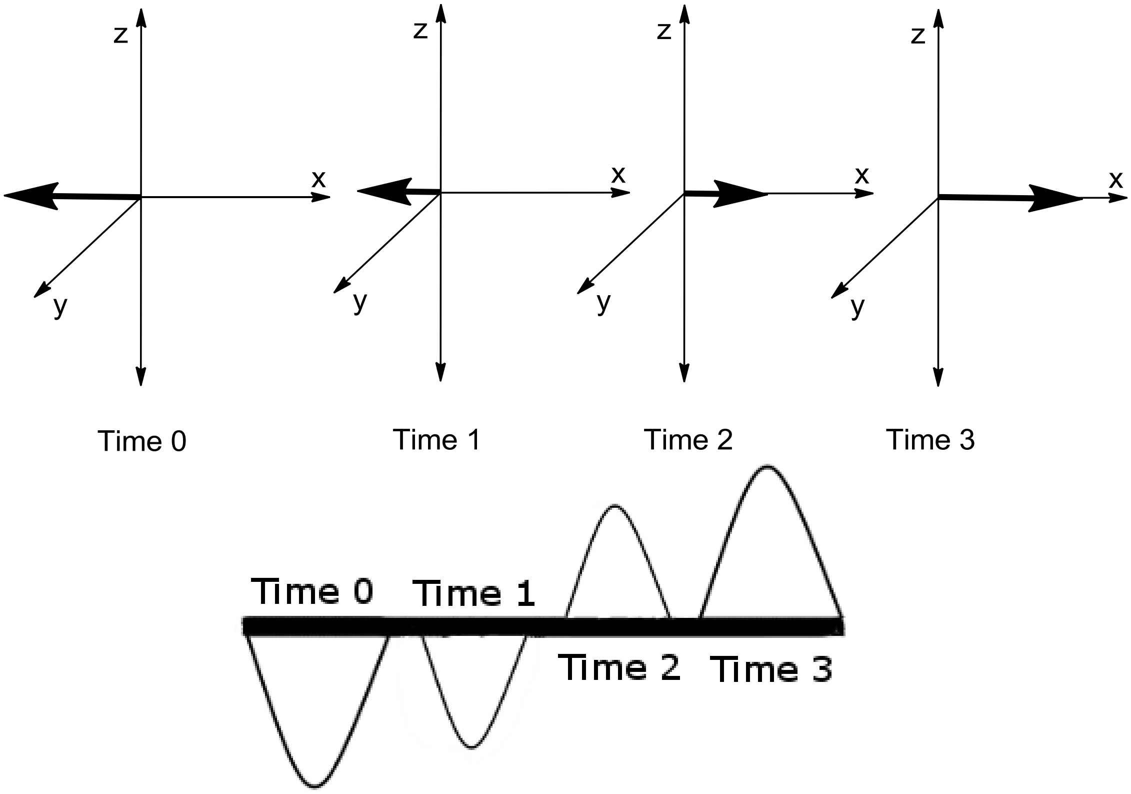

Figure 1.5. Top. Representation of the magnetization after a 90° pulse is applied at different time points. The time is arbitrary with the time 0 being the shortest and time 3 being the longest time. Bottom. Representation of the spectra after a 90° pulse is applied at varying time points.

As the time between the 180° and the 90° is delayed from time 0 to time 3 the signal changes from being negative, (or along the –x axis), to a positive signal, (or along the +x axis). When the intensities of the signal are plotted vs. time a T_1 curve is produced, such as that seen in figure 1.3. An exponential curve can then be fitted accordingly to the T_1 relaxation equation.

1.2.2 T_2-Based Contrast Agents

T_2-based contrast agents are typically designed using superparamagnetic iron oxide (SPIO) particles. The field inhomogeneity of SPIOs alters the magnetic field, which in turns creates ^1H nuclei of different frequencies and ultimately dephases the water signal (Figure 1.6). By dephasing the water being imaged, a darkening, or negative contrast, where the SPIOs are located is observed due to the signal loss of out of phase water. This is the opposite of T_1 agents that produce a brighter image (positive contrast). As no SPIOs were synthesized and tested for this thesis the focus of T_2 relaxation will be with respect to a new form of T_2 agents. Lanthanide based T_2 agents have recently been developed that rely on the field disturbance that high shifting lanthanides can produce.[11] The same macrocyclic chelator cyclen is used in these agents, but instead of gadolinium as in the T_1 agents, lanthanides that produce large hyperfine shifts are used, such as, dysprosium (Dy^{3+}), thulium (Tm^{3+}) or terbium (Tb^{3+}). As an example of the high shifting ability of lanthanides, the chemical shift of bound water on a Dy^{3+} ion has been observed above 700 ppm compared to the bulk water.[12] The difference in frequency of the bound water compared to the bulk water creates a powerful T_2 agent due to the dephasing that occurs when the bound water exchanges and interacts with the bulk system creating a decrease in the overall water signal. T_2 imaging is not a main focus of this thesis and will only be discussed to any extent in chapter 5. It is however important to remember in all MR imaging when lanthanides are present there is the possibility of increased T_2 relaxation, which could ultimately decrease the amount of signal and effect the overall efficiency of the agent.

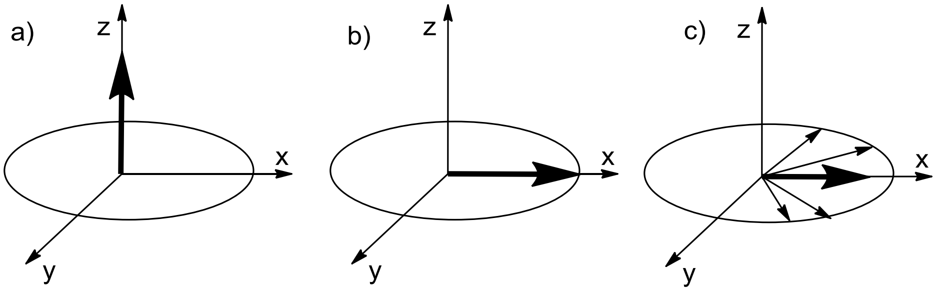

Figure 1.6. Representation of water signal loss due to T_2 relaxation. a) M_0 is aligned along z axis at equilibrium. b) After a Rf pulse flips the M_0 vector onto the x axis. c) Dephasing of the M_0 signal on the xy plane resulting in a decrease in measurable signal. Redrawn from reference 1[1]

To measure the T_2 relaxation of an agent a Carr-Purcell-Meiboom-Gill (CPMG) pulse is used. Figure 1.7 has a representation of how a CPMG sequence can be used to measure the T_2 of an agent. In brief, after a 90° pulse the magnetization resides on the xy plane (Fig 6 a). As discussed, the signal begins to dephase due to T_2 relaxation. At a time point (τ_x) (Fig 6 b), which can be arrayed, a 180° pulse is applied and the signal can be measured with loss in signal due to T_2 (Fig 6 c). After the 180° is applied the signals that were out of phase begin to move back into phase and after another period of time τ_x, the signal will be fully rephrased, but in the opposite direction on the xy plane (Fig 6 d). As the signals are still precessing at their own frequencies they begin to dephase once again (fig 6 e). At this point (τ_y) another 180° pulse can be applied and the rephasing will begin again (Fig 6 f). If an array of times (τ_n) are used and plotted vs. the amount of signal measured an exponential decay is observed, which can be fit accordingly to the T_2 equation.

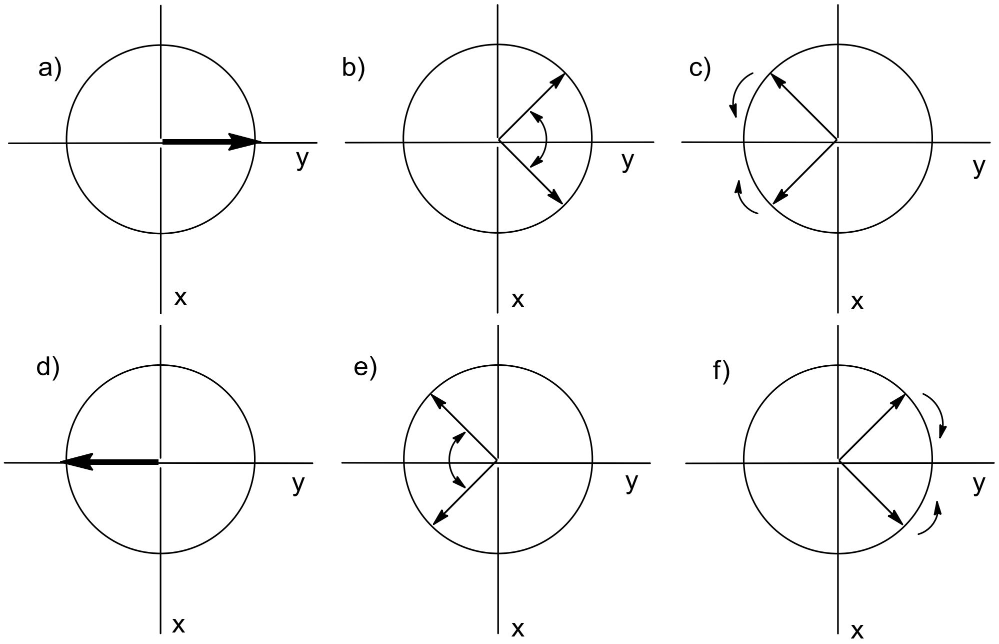

Figure 1.7. a) Magnetization on the xy plane after a 90° pulse is applied. b) Dephasing occurs due to field inhomogeneities. c) After time (τ) has elapsed a 180° pulse is applied the signals begin to rephase. d) After time τ the signals are rephased in the opposite direction. e) The signals continue to precess in the same direction and continue to dephase for another time period (τ_y). f) Rephasing of the signals occurs and will be fully rephased at time τ_y. Redrawn from reference 1.[1]

1.2.3 CEST and ParaCEST Based Contrast Agents

Chemical exchange saturation transfer (CEST) and paramagnetic chemical exchange saturation transfer (ParaCEST) are relatively new techniques for creating MRI contrast.

In this thesis no CEST agents were developed; however, the properties for ParaCEST resemble those for CEST, with the exception that ParaCEST employs a paramagnetic metal. CEST was first discussed by Balaban in 2000 as a potential technique to develop contrast in MRI[13] with ParaCEST being developed the following year.[14] The contrast for ParaCEST MR imaging is generated using exchangeable protons from amides, amine, alcohols or bound water to a paramagnetic metal of choice. In short, the contrast will be generated using the saturation of the "bound" protons, which then exchange with the "bulk" water, carrying the saturation to the bulk water, resulting in a saturation of the bulk water. For simplicity the bulk water is thought of as having a single frequency, which is usually referenced to 0 ppm and the true frequency is not important as gradients used in MRI will create new frequencies for every slice. The bound protons on a diamagnetic CEST agent can be amides, amines or alcohols and will have a chemical shift of roughly 3 - 5 ppm compared to the bulk water. In NMR terms this is the difference of water being at ~ 4.8 ppm and the exchangeable protons being ~ 7- 10 ppm. Barbituric acid was one of the first agents discussed as a possible CEST CA and is shown in figure 1.8. By applying a saturation pulse only onto the exchangeable ring protons (Δ 5 ppm compared to bulk water) the bulk water signal decreased by 32%.[13] While this result was substantial for use as an *in vitro* agent, it should be noted that there are numerous other exchangeable ^{1}H nuceli *in vivo* resonating between 3 – 5 ppm compared to bulk water. The other exchangeable ^{1}H nuclei resemble the CEST CA of interest and will complicate *in vivo* studies. Recent studies have been published where CEST is tested *in vivo* with no CAs.[15, 16]

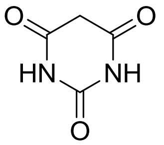

barbituric acid

Figure 1.8. Structure of barbituric acid as one of the first CAs agents tested for CEST MRI. The two symmetrical exchangeable ^{1}H nuclei on the ring are at 5 ppm compared to bulk water.[13] A CEST % of 32% was generated using a 64 mM concentration of the agent.

It has been shown that when a paramagnetic metal is placed into a magnetic field there is potential for a large chemical shift of the nearby atoms. This has previously been used in structure elucidation by NMR. Typically a europium salt (Eu^{3+}) would be added to a complex structure, such as proteins, and the shifts observed would be from protons interacting with the metal which would give information of structure and binding pockets of the protein.[17] Because of the unpaired electrons of Eu^{3+} not being symmetrically distributed it creates large chemical shifts from the typical solution state proton NMR (0 - 15 ppm) to a wide range of chemical shifts (± 50 ppm). The size and magnitude of the shift observed is dependent on distance, angle relative to the principal magnetic axis of the system as the z-axis, and the paramagnetic metal. A representation of paramagnetic properties for the lanthanides is shown in figure 1.9.

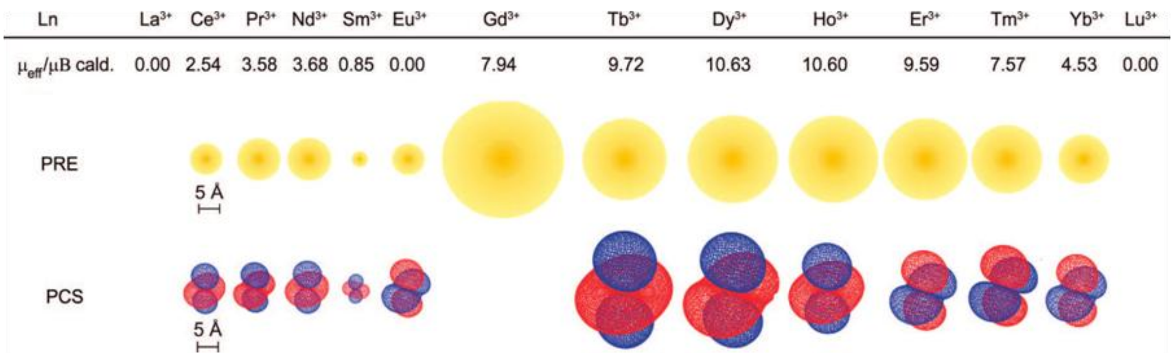

Figure 1.9. Paramagnetic properties of the lanthanides: μ_{eff} is the calculated magnetic moment based on the ground term; μ_B is the Bohr magneton PRE is the paramagnetic relaxation enhancement, and the radius of the yellow sphere indicates the distance at which ^{1}H NMR signals experience significant line broadening. PCS is the pseudocontact shift, and the isosurfaces represent the sign and magnitude of the lanthanide-induced pseudocontact shift for each ion.[18] Note that Eu^{3+} would theoretically be diamagnetic according to its $7F_0$ ground state, but its magnetic properties are also influenced by contributions from the low-lying, thermally accessible $7F_1$ and $7F_2$ levels giving rise to a magnetic moment of around 3.5 μB. Adapted for reprint with permission from reference 19. Copyright 2013 American Chemical Society.[18, 19]

Figure 1.9 illustrates the relaxation sphere around the metal as well as the pseudo contact shift of each metal. While the relaxation sphere for gadolinium is large it has no pseudocontact shift, for this reason gadolinium is used solely as a T_1 agent. The rest of the metals contain some combination of both relaxation as well as pseudo contact shift. The large shifting agents (Dy, Tb, Ho, Er) have large pseudo contact shift values as well as sizable relaxation efficiency. For this reason these agents can be used as both relaxation agents (T_1, T_2) as well as ParaCEST agents, where their chemical shifting abilities are needed. Tm, Eu, and Yb all contain sizable pseudocontact shift values while their relaxation sphere is negligible. This allows these metals to be used as ParaCEST agents without the problems of relaxation, which will be discussed in chapter 5.

The first ParaCEST agent to be discussed in the literature was a Eu^{3+} tetraglycinate by Sherry and coworkers (Figure 1.10).[14] This agent was constructed similarly to Gd^{3+} T_1 agents in the sense that a cyclen framework was employed as a chelating agent for the lanthanide with four "arms" with carbonyls to fill out four other chelating sites of the lanthanide.

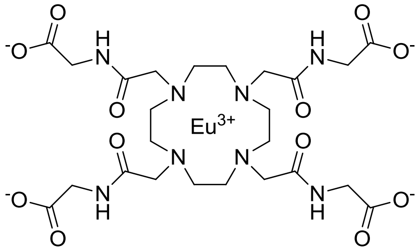

Figure 1.10. Chemical structure of Eu^{3+} tetraglycinate.

The difference in ParaCEST agents compared to T_1 agents is the use of amides in place of acids on the arms. This allows a slower exchange rate of the bound water, which is required for ParaCEST imaging. To generate contrast in the ParaCEST technique a saturation of exchangeable protons at a frequency away from the bulk system must be done. When water is bound to Eu^{3+} there is a chemical shift of 50 ppm for the bound water. With a chemical shift of 50 ppm, the bound water can be saturated without affecting the bulk water, which is referenced to 0 ppm (Figure 1.11). However, because the bound water is in exchange with the bulk water, the bound water must reside on the metal long enough to be saturated with an Rf pulse. This is the reason why the acids of the T_1 agents have been replaced with amides for ParaCEST agents. Amides are weaker electron donors compared to carboxylates. When an amide is used there is an electron deficiency on the lanthanide center creating a stronger OH_2 interaction, ultimately slowing water exchange. A second strategy for slowing water exchange is the incorporation of sterically hindering side chains. Because water exchange has been shown to be dissociative,[20] a system that is sterically hindered will have less solvent accessibility. This in turn limits the hydrogen bonding to bound water and slows water exchange.[21] With the incorporation of amides into the scaffold there is the potential for other exchangeable ^1H nuclei. If Eu^{3+} is replaced with other lanthanides (Dy^{3+}, Tm^{3+}, Tb^{3+}, Yb^{3+}) the amide proton is shifted to values that can be can be saturated without effecting bulk water ($\Delta\omega$ of amide -NH: Dy^{3+} ~ 70 ppm, Tm^{3+} ~ 50 ppm, Tb^{3+} ~ 60 ppm, Yb^{3+} ~ 16 ppm). These values are dependent on the metal chosen, as well as the distance and angle to the metal center. The values given here are average values seen in literature, but there are exceptions which will be discussed in this thesis.

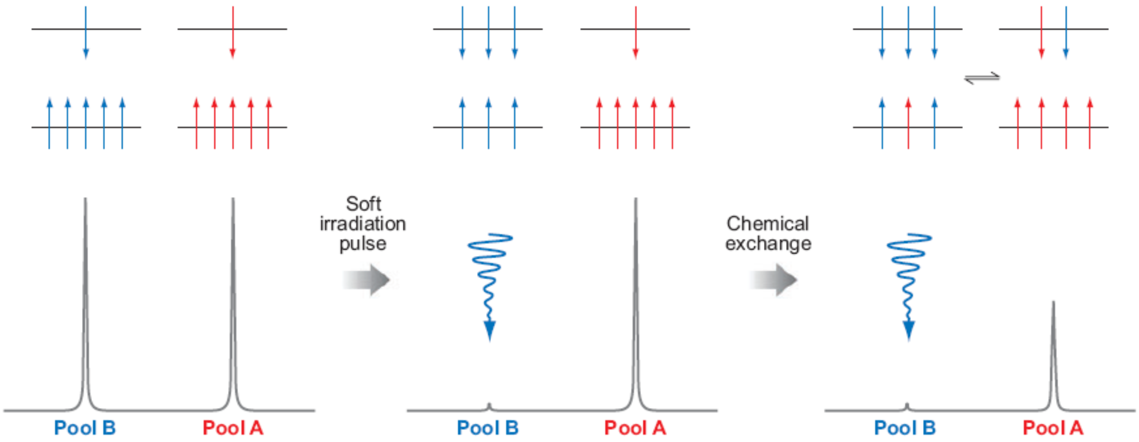

Figure 1.11. Schematic representations of the distribution of spins, aligned with and against the field (upper and lower energy levels, respectively) (*above*) and simulated NMR spectra (*below*) for two chemically distinct pools of nuclei (*left*), two spins after a saturation pulse has been applied to one pool (*middle*), and for a system undergoing chemical exchange after a saturation pulse has been applied to one pool (*right*).[22] Reproduced with permission. Copyright 2013 American Chemical Society.

The largest benefit of using ParaCEST agents over CEST agent is the large chemical shifts of exchangeable protons, on ParaCEST agents, which allow for a direct saturation at frequencies that will not interfere with bulk water. The second benefit of shifting the exchangeable signal further away from the bulk water system is removal of the signal from the magnetization transfer effect (MT). The MT effect arises because of the semisolid nature of biological tissues having a very short T_2 value (< 1 ms).[23] During the ParaCEST imaging of *in vivo* systems the biological background noise ranges from ± 100 ppm, depending on saturation power used.[23] Having an agent with an exchangeable ^{1}H nucleus that resonates outside of the MT will increase the signal to noise during *in vivo* imaging. The third benefit of having of using ParaCEST agents is the ability to either turn “on” or turn “off” the ParaCEST agent. Only when a saturation pulse is situated at the frequency of the bound water or exchangeable amides ^{1}H will there be saturation, any other frequency will not affect the signal. This gives ParaCEST imaging the potential to give unobstructed anatomical images directly before and after a ParaCEST image. This feature is unlike T_1 and T_2 imaging as those agents are always “on” and will always affect the image of nearby water. While typically lanthanides are used in ParaCEST there is also the possibility of transition metals. So far paramagnetic iron and nickel have been used and have been coined the terms FeCEST and NiCEST.[24, 25] This thesis however will focus on the lanthanide series of the 3+ states.

1.2.4 Objectives of Research

The research focus of this thesis is the development and evaluation of novel contrast agents for MR imaging. When this research began ParCEST based contrast agent development was in its infancy and thus held the opportunity to explore novel structures for their MRI CA ability. Firstly, we were interested in exploring variations on the DOTAM scaffold to investigate the ability to tune metal based water or ligand based ParaCEST properties. To this end a key intermediate, tetrapropargyl DOTAM was synthesized and expanded upon via click chemistry.

> Objective 1: Determine the utility of click chemistry on tetrapropargyl DOTAM and discover interesting "lead" compounds for further development.

Through working with variations of the amide groups the click approach was replaced by surveying structurally simple amides prepared by more traditional chemical approaches.

> Objective 2: Determine the effect of structure variations, particularly steric bulk of DOTAM amides for ParaCEST properties to discover "lead" compounds for further investigations.

Surveying of DOTAM amides with varies alkyl substitutions led to the discovery of compounds that produced unusually high chemical shifts and these were studied further.

> Objective 3: To determine the ability of the newly discovered agents to circumvent the limitation of *in vivo* use of ParaCEST agents due to MT effects.

It was also discovered that the unusually high shifting signal was due to the presence of the TSAP isomer. This led us to investigate other amides to determine if the TSAP isomer could be favoured by variation of substitution.

> Objective 4: Preparation and evaluate DOTAM analogues possessing anilides for potential steric/electronic tuning of the electronic properties.

Finally, the question of pharmacokinetic distribution and detection was investigated for nanoparticle based contrast agents.

> Objective 5: Prepare and evaluate Gd NP-Gd^{3+} conjugates for their MR imaging properties, and test their utility in biological imaging.

By focusing on the limitations of ParaCEST imaging, such as non specific biodistribution, background MT effects and loss of sensitivity due to T_2 shortening we developed general strategies to increase the sensitivity of future ParaCEST agents.

1.3 References

1. H. Friebolin, *Basic One- and Two-Dimensional NMR Spectroscopy*, 1993.
2. K. N. Raymond and V. C. Pierre, *Bioconjugate Chem.*, 2005, **16**, 3-8.
3. E. Tóth, L. Helm and A. Merbach, in *The Chemistry of Contrast Agents in Medical Magnetic Resonance Imaging*, John Wiley & Sons, Ltd, 2013, pp. 25-81.
4. E. A. Sadowski, L. K. Bennett, M. R. Chan, A. L. Wentland, A. L. Garrett, R. W. Garrett and A. Djamali, *Radiol.*, 2007, **243**, 148-157.
5. P. Marckmann, L. Skov, K. Rossen, A. Dupont, M. B. Damholt, J. G. Heaf and H. S. Thomsen, *J. Am. Soc. Nephrol.*, 2006, **17**, 2359-2362.
6. P. Caravan, J. J. Ellison, T. J. McMurry and R. B. Lauffer, *Chem. Rev.*, 1999, **99**, 2293-2352.
7. A. D. Sherry, P. Caravan and R. E. Lenkinski, *J. Magn. Reson. Imaging*, 2009, **30**, 1240-1248.
8. S. Aime, L. Calabi, C. Cavallotti, E. Gianolio, G. B. Giovenzana, P. Losi, A. Maiocchi, G. Palmisano and M. Sisti, *Inorg. Chem.*, 2004, **43**, 7588-7590.
9. P. Caravan, *Chem. Soc. Rev.*, 2006, **35**, 512-523.
10. W. D. Rooney, G. Johnson, X. Li, E. R. Cohen, S.-G. Kim, K. Ugurbil and C. S. Springer, Jr., *Magn. Reson. Med.*, 2007, **57**, 308-318.
11. T. C. Soesbe, M. E. Merritt, K. N. Green, F. A. Rojas-Quijano and A. D. Sherry, *Magn. Reson. Med.*, 2011, **66**, 1697-1703.
12. M. Milne, K. Chicas, A. Li, R. Bartha and R. H. E. Hudson, *Org. Biomol. Chem.*, 2012, **10**, 287-292.
13. K. M. Ward, A. H. Aletras and R. S. Balaban, *J. Magn. Reson.*, 2000, **143**, 79-87.
14. S. Zhang, P. Winter, K. Wu and A. D. Sherry, *J. Am. Chem. Soc.*, 2001, **123**, 1517-1518.
15. M. T. McMahon, J. Zhou, A. A. Gilad, J. W. M. Bulte and P. C. M. Van Zijl, CRC Press LLC, 2007, pp. 85-100.
16. H. Zhu, C. K. Jones, P. C. M. Van Zijl, P. B. Barker and J. Zhou, *Magn Reson Med*, 2010, **64**, 638-644.
17. J. A. Peters, J. Huskens and D. J. Raber, *Prog. Nucl. Magn. Reson. Spectrosc.*, 1996, **28**, 283-350.

18. G. Pintacuda, M. John, X.-C. Su and G. Otting, *Acc. Chem. Res.*, 2007, **40**, 206-212.

19. S. Viswanathan, Z. Kovacs, K. N. Green, S. J. Ratnakar and A. D. Sherry, *Chem. Rev.*, 2010, **110**, 2960-3018.

20. S. Aime, A. Barge, A. S. Batsanov, M. Botta, D. D. Castelli, F. Fedeli, A. Mortillaro, D. Parker and H. Puschmann, *Chem. Commun.*, 2002, **0**, 1120-1121.

21. S. R. Zhang, M. Merritt, D. E. Woessner, R. E. Lenkinski and A. D. Sherry, *Acc. Chem. Res.*, 2003, **36**, 783-790.

22. A. D. Sherry and M. Woods, *Annu. Rev. Biomed. Eng.*, 2008, **10**, 391-411.

23. A. X. Li, R. H. E. Hudson, J. W. Barrett, C. K. Jones, S. H. Pasternak and R. Bartha, *Magn. Reson. Med.*, 2008, **60**, 1197-1206.

24. S. J. Dorazio, P. B. Tsitovich, K. E. Siters, J. A. Spernyak and J. R. Morrow, *J. Am. Chem. Soc.*, 2011, **133**, 14154-14156.

25. A. O. Olatunde, S. J. Dorazio, J. A. Spernyak and J. R. Morrow, *J. Am. Chem. Soc.*, 2012, **134**, 18503-18505.

Chapter 2: Magnetic Resonance Spectroscopy Contrast Agent for Temperature Measurements

"Contrast Agents Possessing High Temperature Sensitivity" Mark Milne, Robert H. E. Hudson. *Chem. Commun.*, **2011**, 47, 32, 9194-9196.

2.1 Introduction

Noninvasive thermometric mapping has the opportunity to provide information on physiological conditions of both abnormal and normal tissues. It may also be used to gain real time information such as during thermal therapy that used in cancer treatment.[1-3] Higher than normal temperatures have been reported during imaging of cancerous tissue, a phenomenon which has been linked to an increase in the metabolism of glucose.[4, 5] Determination of such temperature abnormalities is an important step in the early detection of cancers. Currently, temperatures within a biological system may be monitored either invasively using an external probe or by noninvasive scanning techniques. For instance, fiber optic probes are capable of monitoring temperature within 0.1°C; however, these need to be implanted which poses the risk of infection and acute damage. Direct temperature sensing in this manner also relies on the probe being close to the sample area of interest to ensure accuracy. Alternatively, there are a number of noninvasive thermometry techniques such as T_1/T_2 relaxation measurements, diffusion and magnetization transfer based techniques. These methods are limited in their ability to accurately determine absolute temperature within the short time frame needed for some applications, such as thermal therapy.[1] Temperature mapping of water alone has been shown to be possible but suffers from a low sensitivity of 0.01 ppm/°C. [6] To overcome the shortcoming of a low temperature coefficient (CT), lanthanide based contrast agents have been developed with higher sensitivity to temperature and ultimately leading to shorter acquisition times. Most notable are YbDOTMA$^-$,[7] Pr[MOE-DO3A],[8-10] TmDOTMA$^-$ [11-15] and TmDOTP^{5-}, Figure 2.1.[11], [16-18]

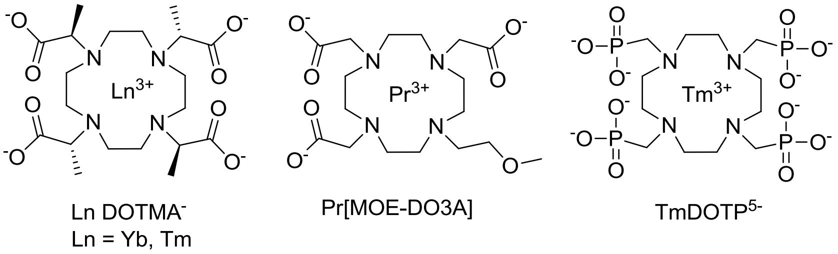

Figure 2.1: Structures of Ln^{3+} chelates used as temperature responsive agents.

YbDOTMA$^-$ was one of the first magnetic resonance spectroscopy (MRS) agents developed; however, it possesses a relatively low CT value (0.04 ppm/°C). Subsequently more sensitive agents were discovered. Pr[MOE-DO3A] possesses a CT value approximately 10 times greater than water (0.131 ppm/°C). Testing of this agent has shown that absolute temperature mapping should be possible for lanthanide DOTA like agents[9] and has led to the development of even more sensitive agents. The phosphonate methylene protons of TmDOTP^{5-} show a greater sensitivity with a CT value of 0.87 ppm/°C. To its detriment, this agent also responds to both pH and [Ca^{2+}] which interfere with the absolute temperature determination.[11, 16 17] TmDOTMA$^-$ has a CT of 0.57 ppm/°C for the 12 equivalent hydrogens and a shift of nearly -100 ppm at 35°C.

Although the CT of this chelate is nearly 60 times that of water alone, it exists as two isomers in solution; a common phenomenon for cyclen-based contrast agents. $TmDOTMA^-$ exhibits both the monocapped twisted square antiprismatic (TSAP) and monocapped square antiprismatic (SAP) in solution.[19] The TSAP conformer predominates (93%) and its methyl signal alone is used for measurements.[12]

2.2 Results and Discussion

A series of new agents for potential temperature mapping have been developed that show high sensitivity, exist as a single isomer and produce high chemical shifts. Using tetrapropargyl amide derivatized cyclen (**2.1**) as the chelating ligand,[20] a series of complexes was evaluated for their ability to report temperature by using the H_4 or H_5 protons, Figure 2.2. The chemical shifts of H_4 and H_5 are independent of either concentration, pH or $[Ca^{2+}]$[12, 13] which is important because of the uncertainty of these factors *in vivo* without pre scanning with other contrast agents.

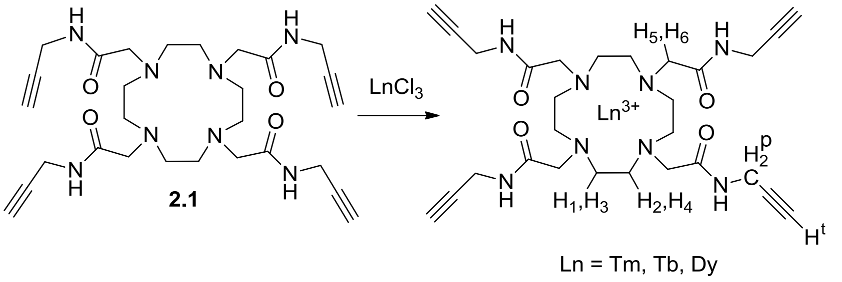

Figure 2.2. Ln chelates were prepared by treatment of ligand 1 with 1.1 eq of appropriate a 1:1 mixture of dioxane:H_2O. Protons denoted as H_1-H_6 ,CH_2 p (propargylic) and H^t for the terminal alkyne proton.

While the complexes of DOTMA show significant amounts of a minor isomer (Tm^{3+}, 7%; Tb^{3+}, 30%), conformational analysis by solution NMR along with solid state structures determined by single crystal x-ray diffraction show only the SAP isomer present in complexes of **2.1**. This is advantageous because the entire signal can be used in determining the peak position thereby improving the signal to noise ratio (SNR). The H_4 peak position of Eu^{3+} complexes of cyclen-like ligands may be used to distinguish between the TSAP and SAP conformers in solution. The chemical shift of H_4 falls between 8-10 ppm for the TSAP conformation while the signal is near 30 ppm for the SAP conformation[19, 21] Eu(**2.1**) has a peak near 25 ppm, Figure 2.3, indicative of the SAP conformation. The SAP conformation was observed in the crystal structure reported earlier for a Gd^{3+} tetrapropargyl complex,[22] as well as the crystals that we obtained for other Ln^{3+}(**2.1**) complexes.[23]

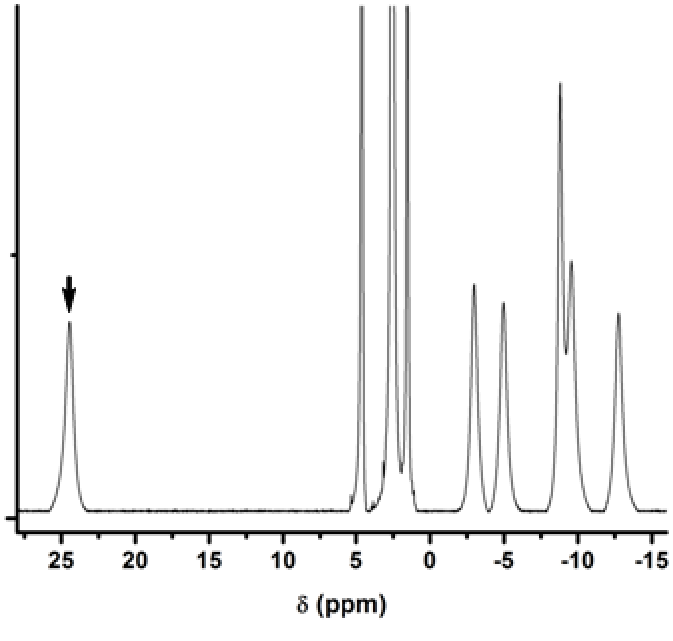

Figure 2.3. NMR spectra of Eu(**2.1**) in D_2O. The signal for H4 is observed at ~25 ppm, indicated by the arrowhead

To evaluate the ability of these contrast agents to report temperature, we selected lanthanides capable of producing large hyperfine shifts (Tm^{3+}, Tb^{3+}, Dy^{3+}). Complexes of Tm^{3+}, Tb^{3+}, and Dy^{3+} have been tested in the past for their ability to report temperature because of their high CT values (0.131 ppm/°C to 2.18 ppm/°C)[13] compared to water 0.01 ppm/°C. Plots of temperature versus peak position for Tm(**2.1**) are shown in Figures 2.4 and 2.5. Linear fit values for tested agents are (Tm(**2.1**)H_4 $R^2 = 0.983$, Tm(**2.1**)H_5 $R^2 = 0.993$, Dy(**2.1**) H_4 $R^2 = 0.997$, Tb(**2.1**)H_4 $R^2 = 0.999$).

.

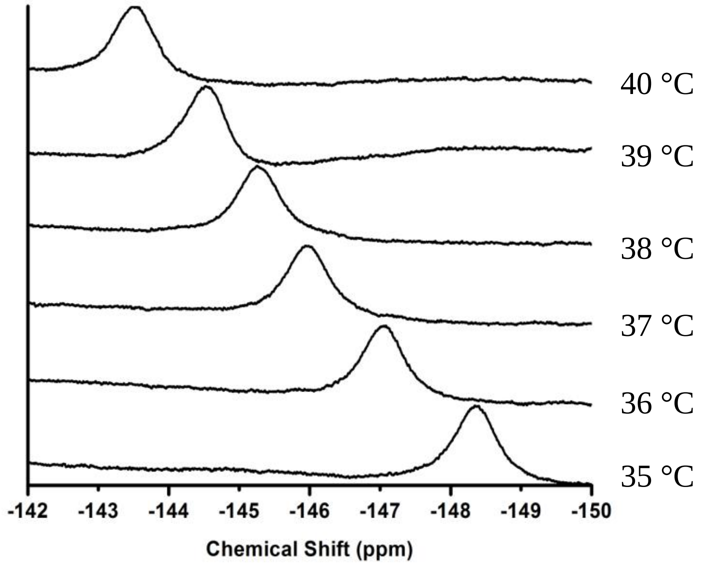

Figure 2.4. Temperature dependence of the H_5 NMR signal of Tm(**2.1**) in the range 35-40°C. See supplemental information for full listing of parameters.

A summary of the evaluation of the three most promising agents: Tm(**2.1**), Tb(**2.1**) and Dy(**2.1**), is listed in Table 2.1. The CT values range from -1.05 ppm/°C for the H_5 of Tm(**2.1**) to 1.76 ppm/°C for the H_4 of Dy(**2.1**). These values represent a substantial improvement over the state of the art compounds. The temperature sensitivity of the ligand proton signals of these compounds is ~100 more sensitive then water alone and 2-3 times greater than reported TmDOTMA and it is not sensitive to pH within the physiological range. CT values alone however are not sufficient to represent which agents will be most useful. The ratio of the line width at half maximum (FWHM) to CT ratio is a good indicator of the effectiveness of the complex as a temperature reporting agent and is a value that permits comparison to other agents. The highly-shifted signals appearing at -333 ppm (Dy(**2.1**)H_4), -287 ppm (Tb(**2.1**)H_4), 224 ppm (Tm(**2.1**)H_4) and -148 ppm (Tm(**2.1**)H_5) show the largest variation with respect to changes in temperature and were the ones exploited for the measurements reported.

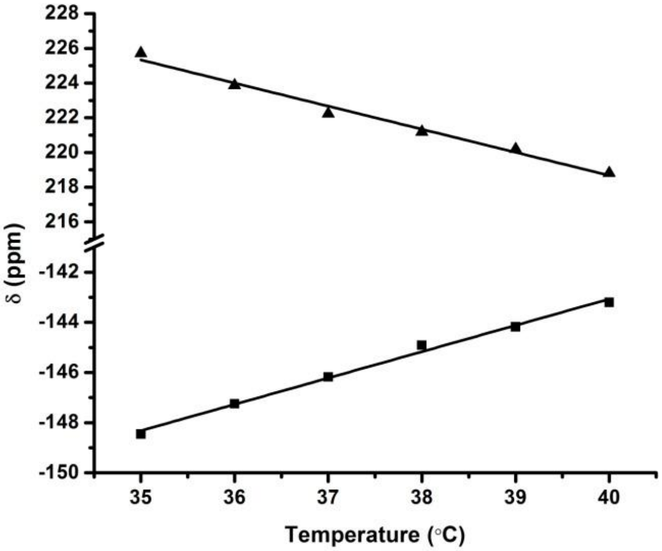

Figure 2.5. Temperature vs. chemical shift for Tm(**2.1**) H4 (▲) and H5 (■).

Table 2.1. ^{1}H Chemical shifts (ppm) at 35 °C, temperature coefficients, line widths at half max height and T_1 for Ln^{3+}(**2.1**) complexes at 20 mM

	Tb^{3+} (H_4)	Tm^{3+} (H_4)	Tm^{3+} (H_5)	Dy^{3+} (H_4)
δ (ppm)	-287.13	224.52	-148.25	-332.98
CT (ppm/°C)	1.48	-1.44	1.05	1.76
FWHM	1.25	0.80	0.64	1.41
|CT|/FWHM	1.18	1.80	1.64	1.25
T_1 (msec)	0.39	0.64	0.95	0.29

Ratios of │CT │/ FWHM between 1.0 - 2.2 have been reported; however, the highest value corresponds to a compound that is sensitive to both pH and [Ca] which is problematic for *in vivo* use where these values are variable. Dy(**2.1**) with a CT value of 1.78 ppm/°C and a line width of 1.41 ppm has a ratio of 1.25. This value is comparable to other complexes used for imaging, (1.18 for $TmDOTA^-$ and 1.36 for $TmDOTMA^-$).[11, 13, 24-26] The ratio values obtained for the other two complexes are 1.18 and 1.66 for Tb(**2.1**) and Tm(**2.1**) H_4 protons, respectively, and 1.64 for H_5 of the Tm(**2.1**) complex. The Tm^{3+} complex benefits from a narrow peak width (0.84 ppm for H_4 and 0.64 ppm for H_5) and is therefore more suitable for temperature mapping while still displaying high temperature dependence.

To further evaluate Tm(**2.1**), a 20 mM sample was prepared in a 5% w/v denatured bovine serum albumin (BSA) gel. ^{1}H NMR spectra were collected under similar conditions to the calibration samples with the exception that the scan time was reduced from 100 scans (3 min) to 16 scans (34 s), which is closer to the time for a single breath hold for imaging purposes. The CT values determined under these conditions were -1.33

(ppm/°C) for the H_4 proton and 0.90 (ppm/°C) for the H_5 proton. Using the high chemical shifting signals provides large changes with respect to temperature and also ensures they are free of signal interference from proteins (in the BSA scans) or other endogenous biomolecules. It is also expected that no exchange will occur between the protons of the cyclen backbone, therefore line broadening should not be a concern for *in vivo* use and only minimal line broadening was observed in the BSA studies. The slight increase in half line width is most likely due to the decrease in scans used in the BSA studies to demonstrate the potential of Tm(**2.1**) in a biological medium. The results indicate that we are able to perform the same temperature determination under pseudo-biological conditions with short scan times. With two proton signals for Tm^{3+} clearly outside the range of biological background signals, it should be possible to measure both H_4 and H_5 and use the shift of both peaks to yielding a sensitivity of 2.38 ppm/°C, as previously proposed.[26]

2.3 Conclusion

In summary, a series of contrast agents have been identified that are potential candidates for MR thermometry. The presence of one conformational isomer in solution enables the use of the entire signal to determine the peak position. By showing that similar results can be obtained in pseudo-biological conditions we have demonstrated the compatibility of these agents to biological applications. Cell viability tests have been performed by others indicating that at concentrations below 3 mM the contrast agent is non toxic, which will allow *in vivo* testing to be preformed.[22]

Since the publication of this paper in 2011 we were contacted by the National Institute of Standards and Technology. They believe that the Tm^{3+} agent has the potential to act as a standard for temperature controls during NMR experiments. We have prepared samples for testing and are awaiting the results of their evaluation.

2.4 Supplemental information

S2.1. **1,4,7,10-tetraazacyclododecane-1,4,7,10-tetra-*N*-(propargyl)acetamide** (**2.1**)

To a stirred solution of cyclen (38 mg, 0.22 mmol) and DIPEA (154 µL, 4 mmol) in 5 mL acetonitrile, *N*-(propargyl) chloroacetamide (**6**) (131 mg, 1 mmol) was added in one portion and then refluxed overnight. The product was precipitated with 5 mL H_2O and filtered as a white solid (66 mg, 0.11 mmol), yield 54%. ^1H NMR (400 MHz, DMSO-d6): δ 7.57 (4H, m); 3.05 (8H, m); 2.22 (10H, m); 1.79 (14H, s); 1.67 (4H, s,). ESI-m/z calc $C_{28}H_{40}N_8O_4$ $(M+H)^+$,553.3251, found 553.2574.

S2.2. **Ln^{3+}-1,4,7,10-tetraazacyclododecane-1,4,7,10-tetra-*N*-(propargyl)acetamide Chloride** (**Ln(2.1)**)

Tetrapropargyl DOTAM (**2.1**) (55 mg, 0.1 mmol) was added to a stirred solution of dioxane:H_2O (4 mL) containing one of the following lanthanides at 1.1 eq: $TbCl_3$, $DyCl_3$, $TmCl_3$. The progress of the metallation of **2.1** was monitored by UPLC/MS and upon completion the solvent was removed under reduced pressure. The solid was then taken in 1 mL H_2O and passed through a column of size exclusion gel. The fractions collected were tested against xylenol orange for the presence of free metals. Fractions identified as containing the metallated ligand were found not to contain free metal ions. ESI-m/z: $C_{28}H_{40}N_8O_4Tb$ $(M+COOH)^+$, calc 757.2481, found 757.3318; $C_{28}H_{40}N_8O_4Dy$ $(M+COOH)^+$, calc 756.2627, found 756.3125; $C_{28}H_{40}N_8O_4Tm$ $(M+COOH)^+$, calc 767.2570, found 767.3286.

S2.3. Temperature vs. δ (ppm) **Dy(2.1)** H_4

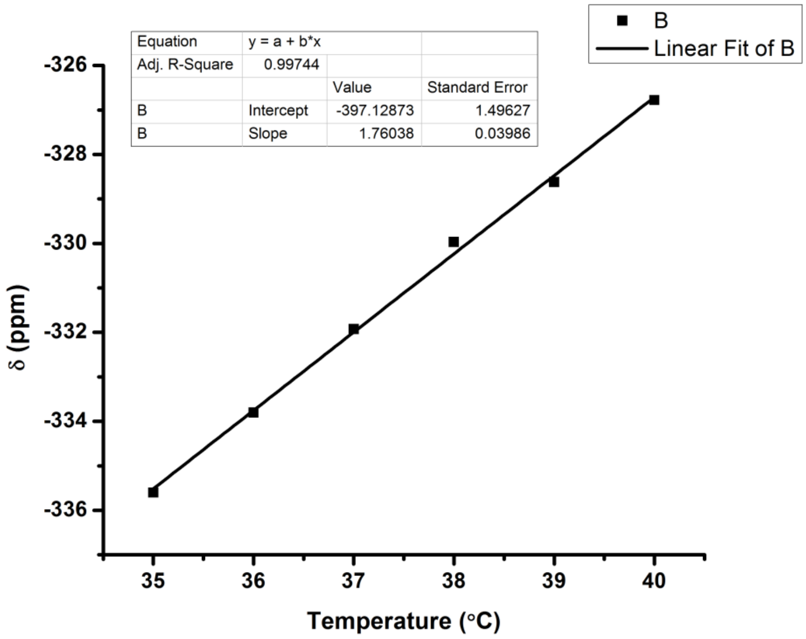

S2.4. Temperature vs. δ (ppm) **Tb(2.1)** H_4

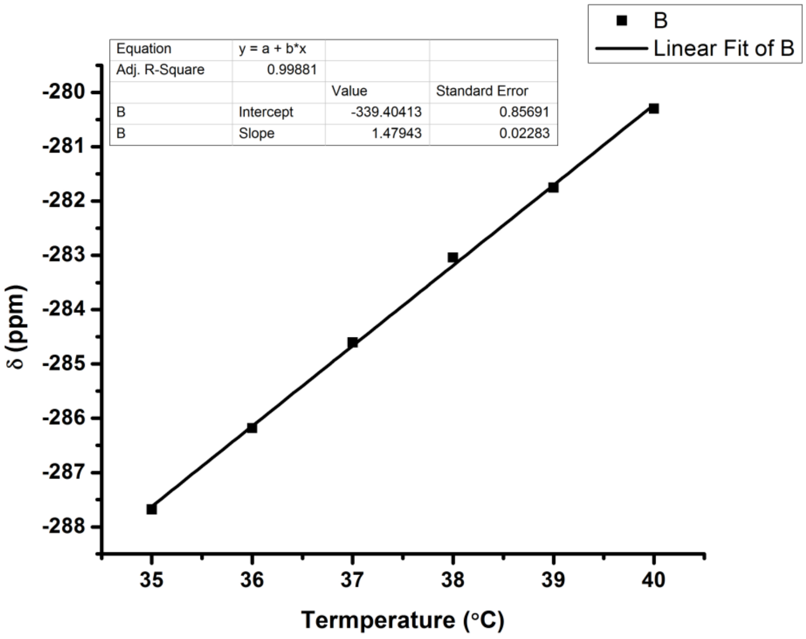

S2.5. Temperature vs. δ (ppm) **Tm(2.1)** H_4

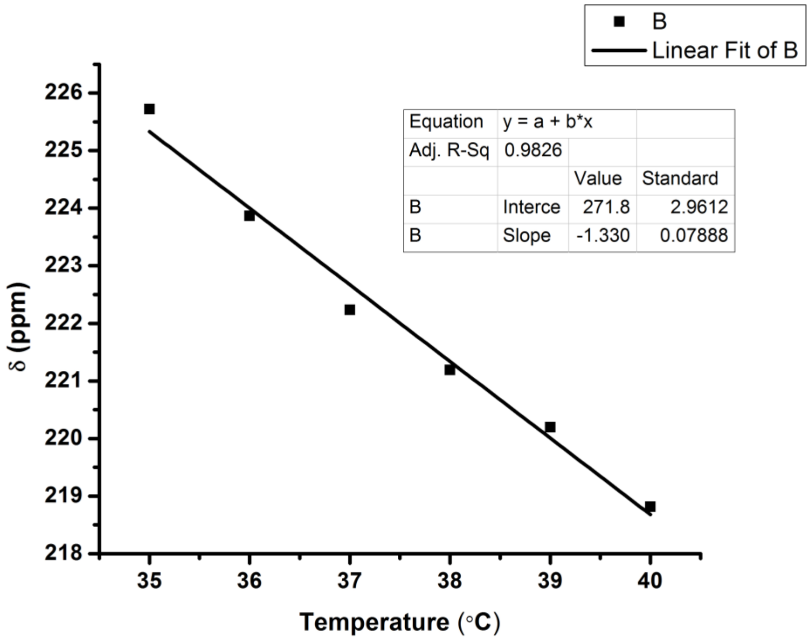

S2.6. Temperature vs. δ (ppm) **Tm(2.1)** H_5

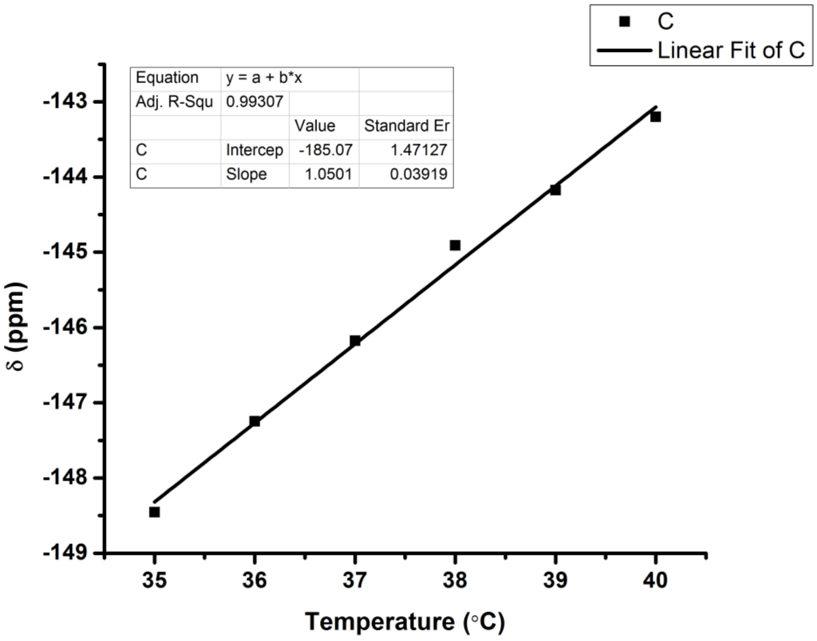

S2.7. Temperature vs. δ (ppm) **Tm(2.1)** H_4 , H_5 in 5% BSA

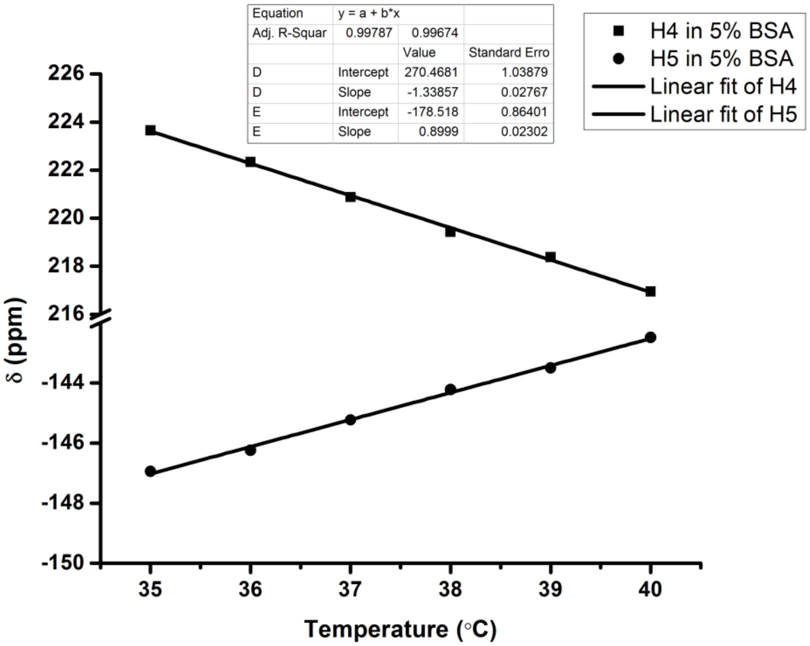

Equation	y = a + b*x		
Adj. R-Squar	0.99787	0.99674	
		Value	Standard Erro
D	Intercept	270.4681	1.03879
D	Slope	-1.33857	0.02767
E	Intercept	-178.518	0.86401
E	Slope	0.8999	0.02302

S2.8. δ ppm vs. pH of Tm(2.1)

Table. δ (ppm) vs. pH of Tm(**2.1**) H_5

pH	ppm
6.00	-144.99
6.98	-144.94
8.22	-144.92
9.22	-145.10

S2.9. NMR Parameters

The NMR experiments were preformed on a 600 MHz Varian vertical bore magnet. ^{1}H experiments of Ln^{3+} complexes were done in deuterated water. Temperature dependence studies were done in distilled water using the variable temperature (VT) control supplied, which was first calibrated using glycol. Temperature calibration experiments of Ln complexes were done at 20 mM in a range of 35˚C – 40˚C in triplicate and averaged. Parameters used, 100 scans, Tm: Relaxation delay = 0.8 sec, observed pulse = 20˚, sweep width = -170 to 250 ppm, acquisition time = 1.0 sec, overall time = 3:05. Tb: Relaxation delay = 0.8 sec, observed pulse = 20˚, sweep width = -325 to 250 ppm, acquisition time = 0.76 sec, overall time = 2:41. Dy: Relaxation delay = 0.8 sec, observed pulse = 20˚, sweep width = -250 to 150 ppm, acquisition time = 0.9 sec, overall time = 2:55.

Parameters used in 5% BSA study, 16 scans, Tm: Relaxation delay = 0.8 sec, observed pulse = 20˚, sweep width = -170 to 250 ppm, acquisition time = 1.0 sec, overall time = 34 s. FIDs were then line broadened 30 Hz, phased corrected and baseline subtracted.

2.5 References

1. V. Rieke and K. B. Pauly, *J. Magn. Reson. Imaging*, 2008, **27**, 376-390.

2. J. van der Zee, *Ann. Oncol.*, 2002, **13**, 1173-1184.

3. R. D. Issels, *Eur. J. Cancer*, 2008, **44**, 2546-2554.

4. H. Young, R. Baum, U. Cremerius, K. Herholz, O. Hoekstra, A. A. Lammertsma, J. Pruim, P. Price and C. European Org Res Treatment, *Eur. J. Cancer*, 1999, **35**, 1773-1782.

5. R. A. Gatenby and R. J. Gillies, *Nat. Rev. Cancer*, 2004, **4**, 891-899.

6. B. D. De Senneville, B. Quesson and C. T. W. Moonen, *Int. J. Hyperthermia*, 2005, **21**, 515-531.

7. S. Aime, M. Botta, M. Fasano, E. Terreno, P. Kinchesh, L. Calabi and L. Paleari, *Magn. Reson. Med.*, 1996, **35**, 648-651.

8. M. Hentschel, P. Wust, W. Wlodarczyk, T. Frenzel, B. Sander, N. Hosten and R. Felix, *Int. J. Hyperthermia*, 1998, **14**, 479-493.

9. M. Hentschel, M. Findeisen, W. Schmidt, T. Frenzel, W. Wlodarczyk, P. Wust and R. Felix, *Magma*, 2000, **10**, 52-59.

10. M. Hentschel, W. Dreher, P. Wust, S. Roll, D. Leibfritz and R. Felix, *Phys. Med. Biol.*, 1999, **44**, 2397-2408.

11. D. Coman, H. K. Trubel and F. Hyder, *NMR Biomed.*, 2010, **23**, 277-285.

12. S. K. Hekmatyar, P. Hopewell, S. K. Pakin, A. Babsky and N. Bansal, *Magn. Reson. Med.*, 2005, **53**, 294-303.

13. S. K. Hekmatyar, R. M. Kerkhoff, S. K. Pakin, P. Hopewell and N. Bansal, *Int. J. Hyperthermia*, 2005, **21**, 561-574.

14. L. Ludemann, W. Wlodarczyk, J. Nadobny, M. Weihrauch, J. Gellermann and P. Wust, *Int. J. Hyperthermia*, 2010, **26**, 273-282.

15. S. K. Pakin, S. K. Hekmatyar, P. Hopewell, A. Babsky and N. Bansal, *NMR Biomed.*, 2006, **19**, 116-124.

16. Y. Sun, M. Sugawara, R. V. Mulkern, K. Hynynen, S. Mochizuki, M. Albert and C. S. Zuo, *NMR Biomed.*, 2000, **13**, 460-466.

17. C. S. Zuo, J. L. Bowers, K. R. Metz, T. Nosaka, A. D. Sherry and M. E. Clouse, *Magn. Reson. Med.*, 1996, **36**, 955-959.

18. C. S. Zuo, K. R. Metz, Y. Sun and A. D. Sherry, *J. Magn. Reson.*, 1998, **133**, 53-60.

19. K. J. Miller, A. A. Saherwala, B. C. Webber, Y. Wu, A. D. Sherry and M. Woods, *Inorg. Chem.*, 2010, **49**, 8662-8664.

20. P. Antoni, M. Malkoch, G. Vamvounis, D. Nystrom, A. Nystrom, M. Lindgren and A. Hult, *J. Mater. Chem.*, 2008, **18**, 2545-2554.

21. F. A. Dunand, S. Aime and A. E. Merbach, *J. Am. Chem. Soc.*, 2000, **122**, 1506-1512.

22. J. Martinelli, B. Balali-Mood, R. Panizzo, M. F. Lythgoe, A. J. P. White, P. Ferretti, J. H. G. Steinke and R. Vilar, *Dalton Trans.*, 2010, **39**, 10056-10067.

23. M. Milne, K. Chicas, A. Li, R. Bartha and R. H. E. Hudson, *Org. Biomol. Chem.*, 2012, **10**, 287-292.

24. D. Cornan, H. K. Trubel, R. E. Rycyna and F. Hyder, *NMR Biomed.*, 2009, **22**, 229-239.

25. C. S. Zuo, A. Mahmood and A. D. Sherry, *J. Magn. Reson.*, 2001, **151**, 101-106.

26. S. K. Hekmatyar, H. Poptani, A. Babsky, D. B. Leeper and N. Bansal, *Int. J. Hyperthermia*, 2002, **18**, 165-179.

Chapter 3: Synthesis and Characterization of ParaCEST MRI Agents via Click Chemistry

"ParaCEST MRI Contrast Agents Capable of Derivatization via 'Click Chemistry' ". Mark Milne, Kirby Chicas, Alex Li, Robert Bartha and Robert H.E. Hudson. *Org. Biomol. Chem*., **2012**, 10, 287-292.

3.1 Introduction

Cyclen-based chelates of lanthanide ions, particularly gadolinium although other metals are being actively investigated, are widely used as contrast agents in magnetic resonance imaging (MRI). These agents rely on the exchange of water between the bulk and the coordination sphere of the lanthanide.[1-7] The exchange rate of bound water depends both on the nature of the ligand and the identity of the metal ion. The exchange rate of bound water has been described as fast in 1,4,7,10-tetrakis(carboxymethy1)-1,4,7,10-tetraazacyclododecane (DOTA) type ligands, or slow to intermediate, as in 1,4,7,10-tetraazacyclododecane-1,4,7,10-tetraacetamide (DOTAM) type ligands. Due to these two possible exchange rate regimes, two different techniques have been developed to create contrast in MRI. Fast exchange occurs when Gd^{3+} is used in combination with DOTA type ligands wherein the change in T_1 is used to produce the contrast. Alternatively, contrast agents in the slow to intermediate exchange regime, such as the combination of DOTAM type ligands and Eu^{3+}, use paramagnetic chemical exchange saturation transfer (ParaCEST) phenomenon to produce contrast. Not only does the exchange rate depend on the gross chemical features of the ligand, it is also sensitive to the geometry of the chelator about the metal centre. It has been described that cyclen-based contrast agents are found in either a twisted square antiprismatic (TSAP) form, in which exchange is fast, or in a square antiprismatic (SAP) form in which the exchange is slower.[2, 6-10] In order to maximize the ParaCEST signal, it is desirable to have ligands which exist only in the SAP geometry.

Development of targeted contrast agents using glycoconjugates have been studied recently. A number of different synthetic approaches have been investigated producing contrast agents ranging from those possessing a single saccharide up to dendrimeric structures containing twelve glucose moieties.[11-14] Most of these agents have relied on Gd^{3+} to produce contrast using the theory of relaxivity as previously discussed. The use of other lanthanides which produce large chemical shifts suitable for use in ParaCEST experiments have not been exploited to the same extent. By incorporating metal ions that are compatible with the ParaCEST approach, we are able to measure the metal-bound water of Eu^{3+} complexes, as well as the exchangeable amide protons in the other lanthanide complexes (especially Dy^{3+}, Tm^{3+} and Tb^{3+}). The latter group of lanthanides have elicited interest lately due to the sensitivity of amide proton exchange to changes in pH and the potential for *in vivo*, non-invasive pH measurement. The potential for the measurement of physiological parameters, such is pH, is one of the advantages of ParaCEST agents over conventional T_1 agents. Determination of *in vivo* pH has implications for the early detection of cancerous tissue which is known to be acidic compared to healthy tissue.[15, 16] A second benefit of using the signal from exchangeable amide protons is the increased CEST sensitivity compared to bound water due to the greater number of equivalent protons, provided that the contrast agent is symmetrical.[17]

3.2 Results and Discussion

A recent publication[18] on related compounds has prompted us to report our ongoing studies on the structure and properties of a tetraalkyne DOTAM series of lanthanide complexes toward the development of new contrast agents.[19] The synthesis of tetraalkyne DOTAM was prepared by a modification of a literature procedure (Scheme 3.1).[20]

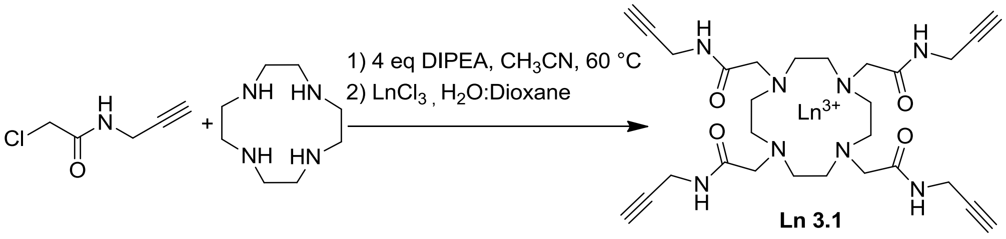

Ln = Ce, Pr, Nd, Pm, Sm,
Eu, Gd, Dy, Ho, Er, Tm, Yb

Scheme 3.1. Synthesis of **Ln 3.1**

Complexation of the lanthanide metal series was carried out by adding 1.1 eq of appropriate $LnCl_3$ (Ln^{3+} = Ce, Pr, Nd, Sm, Eu, Gd, Tb, Dy, Ho, Er, Tm, Yb) to the tetraalkyne DOTAM ligand (**3.1**) in 2 mL of a 1:1 mixture of dioxane:H_2O followed by overnight stirring. The solvent was evaporated and the solids were taken up in 1 mL H_2O

and passed through a column of size exclusion gel to remove free Ln^{3+} ions which was confirmed by the xylenol orange test. The solvent was evaporated to yield Ln^{3+} complexes. Conformational analysis was done by solution ^{1}H NMR, Figure 3.1 and Table 3.1 The signal at ~25 ppm (**Eu-3.1**) is characteristic of SAP geometry and the lack of a signal at 8-10 ppm indicates the absence of the TSAP isomer in solution. The solution phase NMR data taken together with solid state X-ray crystal structures (**Nd-3.1**, **Tb-3.1**, **Dy-3.1**, **Yb-3.1**, Figure 3.2), indicate that only the SAP isomer is present for the lanthanide series of tetraalkyne DOTAM.

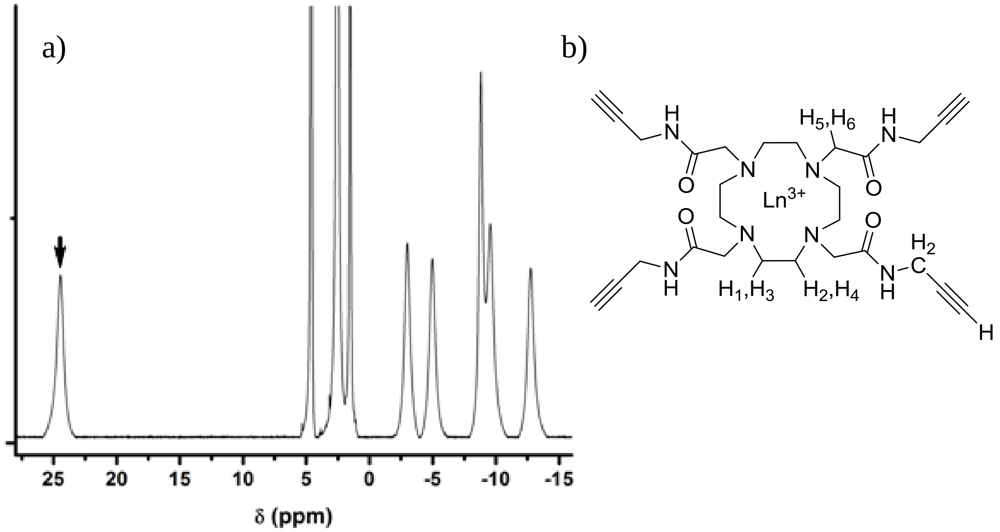

Figure 3.1. a) ^{1}H NMR spectra of **Eu-3.1**. H_4 indicated by arrowhead. b) Designation of ligand hydrogen atoms (H_1-H_6) present in the **Ln-3.1** complexes.

Table 3.1 ^{1}H NMR chemical shifts (ppm) at 25˚C for the Ln^{3+} series.

Ln	H_1	H_2	H_3	H_4	H_5	H_6	CH_2	CH
Ce^{3+}	6.71	1.66	0.75	-7.58	7.45	5.17	4.97	4.97
Pr^{3+}	14.09	3.22	0.79	-22.65	16.99	10.76	6.69	3.82
Nd^{3+}	10.61	5.62	5.02	-11.38	12.34	5.62	7.46	5.48
Sm^{3+}	4.39	1.61	1.79	-0.02	5.93	3.72	4.30	2.79
Eu^{3+}	-9.58	-2.98	-4.98	24.43	-12.76	-8.83	2.57	1.53
Tb^{3+}	104.74	-80.15	-83.30	-310.02	202.11	57.05	35.58/30.82	19.61
Dy^{3+}	123.52	-83.04	-83.04	-356.08	234.87	77.18	38.76/33.88	22.04
Ho^{3+}	65.27	-47.36	-43.19	-181.61	122.53	35.31	22.17/19.55	12.55
Er^{3+}	-34.82	2.20	11.69	106.08	-61.37	-39.64	-2.50	-2.82
Tm^{3+}	-85.88	30.33	40.30	247.40	-156.17	-74.56	-12.18/-13.22	-9.87
Yb^{3+}	-30.64	14.19	17.14	94.09	-55.40	-25.15	-2.23	-2.58

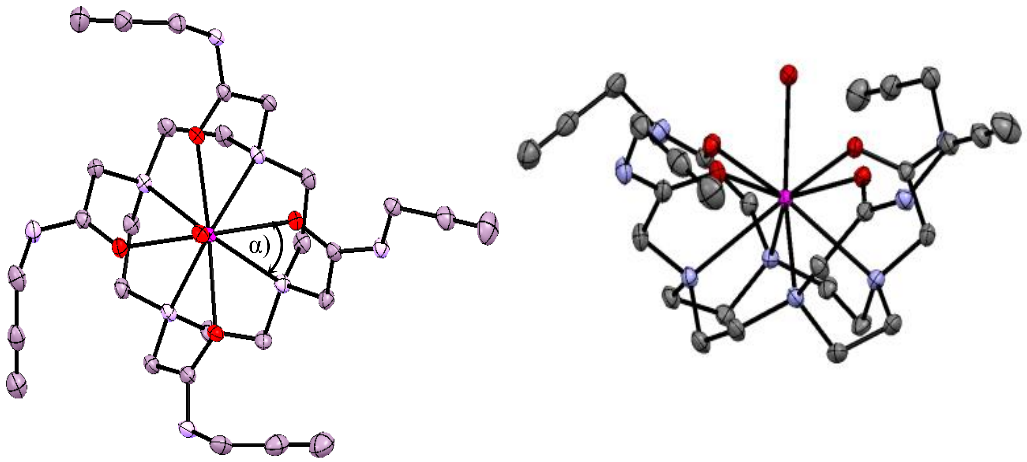

Figure 3.2. Left: Top down view of a molecular representation of the crystal structure of **Dy-3.1**. α indicates the angle between the planes created by N-Ln-N and O-Ln-O and are listed in Table 2. Right: side on view showing water coordinated to the metal centre, the positions of hydrogen atoms were not determined experimentally and are omitted for clarity.

The lanthanide tetraalkyne DOTAM complexes possess nonplanar conformations with C4 symmetry which can be identified by the presence of 8 proton signals, denoted H_1 to H_6, CH_2 (propargylic methylene) and CH (terminal proton). Those protons closer to the metal centre exhibit higher chemical shifts than in the free ligand due to the magnetic moment of the metal centres (Table 3.1).[21] Of note, the protons for the CH_2 group for Dy^{3+}, Ho^{3+}, Tb^{3+} and Tm^{3+} compounds show two separate peaks, where the rest of the metals show a single peak. This is likely due to the large shift capabilities of these four compounds resolving the diastereotopic protons. Proton analysis was not performed for the **Gd-3.1** complex due to line broadening.

These results are notable, particularly, when compared to other high chemical shift lanthanide complexes which have shown two isomers in solution.[8] The SAP isomer is desirable for two reasons: firstly, it produces greater hyperfine shifts of the ligand (cyclen) associated protons that may be useful for magnetic resonance spectroscopic applications. Secondly, the SAP isomer has the slower water exchange rate of the two isomers and this feature is important for ParaCEST-based contrast agents.

To illustrate the competence of the DOTAM alkyne to be derivatized, we have taken tetraacetylglucosyl propylazide and performed a copper-catalyzed azide-alkyne 1,3 dipolar cycloaddition (CuACC) or “click”[22] reaction to give a tetra glucose $(OAc)_4$.[23] This chemistry was performed on a series of pre-metallated ligand (**Ln-3.1,** Ln = Eu^{3+}, Dy^{3+}, Tm^{3+}, Tb^{3+}, Gd^{3+}) to avoid metal sequestration by the naked ligand and subsequent need for transmetallation.

The acetyl-protected glucose intermediates **Ln-3.2** were purified by HPLC, isolated in 60-82% yield, and their identities were confirmed by high resolution mass spectrometry. The glucose moieties were deacetylated using a catalytic amount of potassium carbonate in methanol and this reaction was subsequently quenched by stirring with Amberlite 120 resin. This treatment afforded the fully deprotected tetraglucoside (**Ln-3.3**) products in high yield (99 %), (Scheme 3.2).

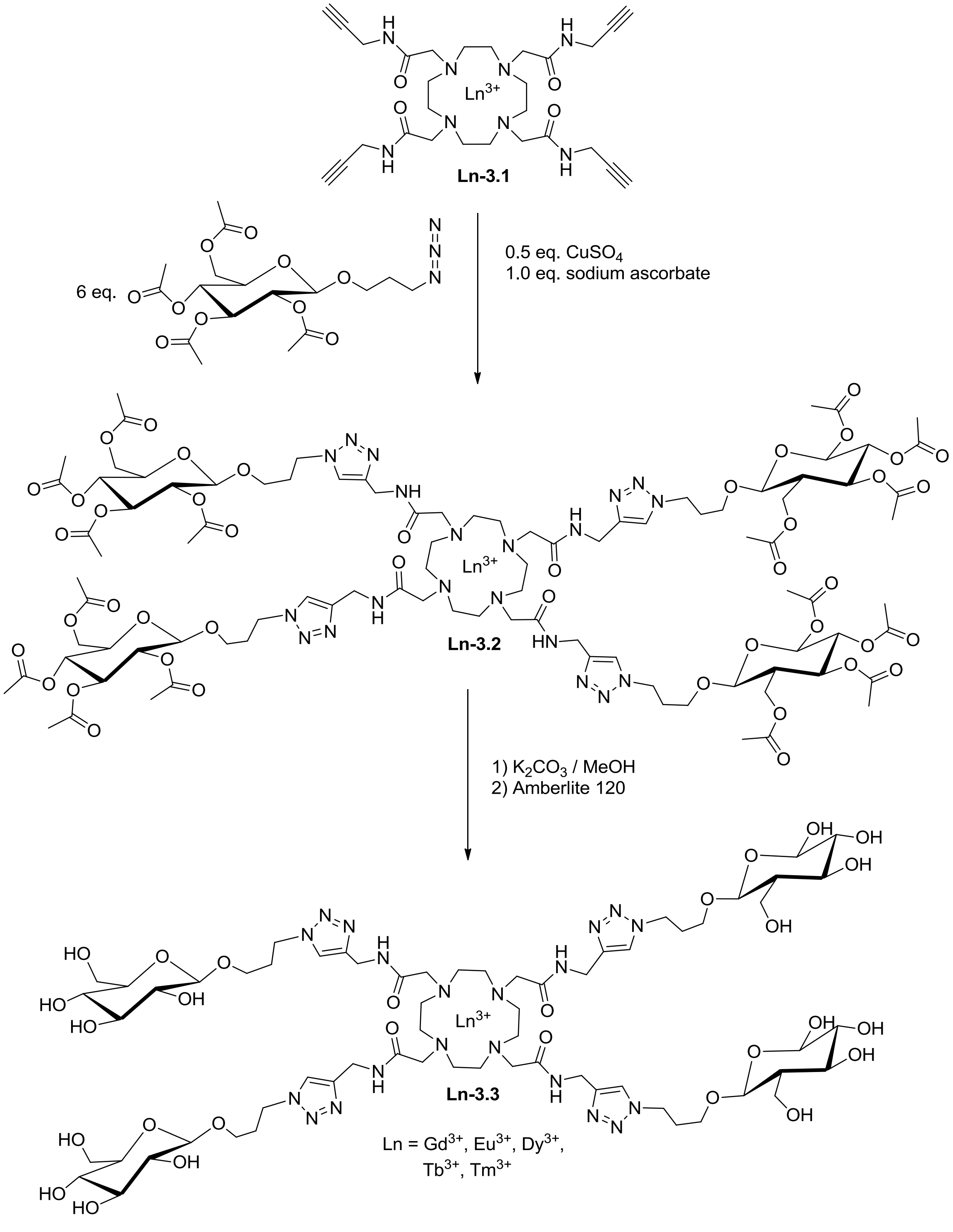

Scheme 3.2. Synthesis of a tetraglucoside functionalized DOTAM via the acetyl-protected intermediate by Huisgen copper catalyzed alkyne-azide cycloaddition (CuAAC).

A selection of lanthanides was used in the click reactions based on their potential as contrast agents. Gd^{3+} was chosen for its ability as a T_1 relaxation agent while the other lanthanides (**Eu^{3+}**, **Dy^{3+}**, **Tb^{3+}**, **Tm^{3+}**) were chosen because of their favourable characteristics as ParaCEST contrast agents.

To evaluate the series of complexes as potential contrast agents for MRI, relaxation measurements and CEST experiments were made. NMRD profiles were acquired at 25°C using a STELLAR fast field cycling NMR. CEST spectra were acquired at 25°C, at 10 mM in phosphate buffer (pH 7) and show observable signals due to bound water and amide protons.

The measured r_1 value at 20 MHz for **Gd-3.1**was 2.53 $mM^{-1}\ s^{-1}$, which is comparable to the value previously reported for Gd^{3+}-DOTAM (2.5 $mM^{-1}\ s^{-1}$).[6] The relaxivity of the products of the "click" reaction: the tetrakis(tetra-*O*acetylglycoside) **Gd-3.2** and the deprotected agent **Gd-3.3** were also evaluated. (Table 3.2) A value of 1.96 $mM^{-1}\ s^{-1}$ at 20 MHz, 25°C was obtained for **Gd-3.2** while a slightly higher value of 2.08 $mM^{-1}\ s^{-1}$ was obtained for the deacetylated compound **Gd-3.3**. The relaxivity measured at 400 MHz was similar in that **Gd-3.1** was the greatest with a value of 2.22 $mM^{-1}\ s^{-1}$ while there was a decrease for **Gd-3.2** (1.96 $mM^{-1}\ s^{-1}$) and an increase in **Gd-3.3** (2.13 $mM^{-1}\ s^{-1}$) compared to **Gd-3.2**. This pattern is somewhat surprising when considering the size difference between these three compounds. Relaxivity theory states that as the size increases so should the rotational time, ultimately giving rise to an increase in relaxivity.[24] This however is not the pattern observed for the Gd series. **Gd-3.2** is roughly 3 times larger than **Gd-3.1** but a decrease in relaxivity of 12% is measured. This unique situation is also shown in the change between **Gd-3.2** to **Gd-3.3** where relaxivity increases 8% while the size decreases by 27%. This can be explained by assuming that the rotational time is not the leading factor associated with the relaxivity but instead water exchange rate or accessibility to bulk water is more important in the slow-intermediate exchange regime of DOTAM ligands.

The dependence on water accessibility can also be seen in the CEST experiments for both the bound water of Eu series as well as the exchanging amide of the Tm series. CEST experiments were performed on complexes (**Eu-(3.1-3.3)**, **Tb-(3.1-3.3)**, **Tm-(3.1-3.3)**, **Dy-(3.1-3.3)**) to evaluate their potential to act as ParaCEST contrast agents, Figure 3.3 and Tables 3 and 4. The high shifting lanthanides show CEST signals associated with the exchangeable amide protons with results between 14 % (**Tb-3.1**, **Dy-3.1**) and 16 %, (**Tm-3.1**). Exchangeable, metal coordinated water is observed for **Dy-3.1** (4.4%), **Tb-3.1** (5.4%) and **Eu-3.1** (40%). By increasing the hydrophobic nature of the agents Eu-2 and Tm-2, the CEST responses decrease to 18% for **Eu-3.2** (H_2O) and 2% for **Tm-3.2** (amide). After deprotection of the glucose there is then an increase of 5% and 4% observed for **Eu-3.3** and **Tm-3.3** respectively. This may be explained by the accessibility of bulk water to exchange with the bound water or the amides in these systems where the acetylated glucose possesses a greater barrier of accessibility for bulk water compared to the deacetylated, which in turn is greater than the parent **Ln-3.1** complexes. Because DOTAM based contrast agents are in a slow-intermediate exchange regime the CEST response and the relaxivity are both responsive to the hydrophibicity of the agents and less responsive to the size change and rotational time. The CEST signals **Dy-(3.2,3.3)** and **Tm-(3.2,3.3)** were not observed for both amide and bound water.

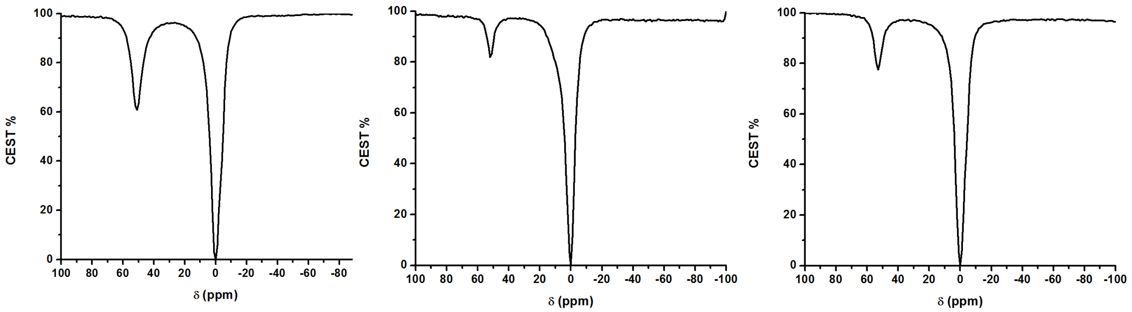

Figure 3.3. CEST spectra acquired using parameters, 10 mM, 25 ˚C, 15 μT saturation pulse for 4 seconds. a) **Eu-3.1** b) **Eu-3.2** c) **Eu-3.3**. Peak position and intensities are listed in tables 3.3 and 3.4.

Table 3.2. Relaxivities of Gd^{3+} complexes (mM^{-1} s^{-1})

Ln^{3+}	r_1(20 MHz)	r_1(400 MHz)
Gd-1	2.53	2.22
Gd-2	1.96	1.96
Gd-3	2.08	2.13

Table 3.3. Chemical shifts and CEST signals of exchangeable amides

Ln^{3+}	δ (ppm) amide	CEST (%) amide
Dy-3.1	81	14
Tb-3.1	65	14
Tm-3.1	-54	16
Tm-3.2	-49	2
Tm-3.3	-51	6

Table 3.4. Chemical shifts and CEST signals of bound water

Ln^{3+}	δ (ppm) H_2O	CEST (%) H_2O
Dy-3.1	-765	4.4
Tb-3.1	-640	5.4
Eu-3.1	51	40
Eu-3.2	52	18
Eu-3.3	53	23

Crystals suitable for X-ray diffraction were grown by slow diffusion of acetone into a concentrated aqueous solution of the complexes. All of the crystal structures displayed nine-fold coordination of the metal centre consisting of four nitrogens from cyclen, four oxygens from the pendant arms, and the last coordination site occupied by a single water molecule of varying bond length (Nd = 2.47 Å , Tb = 2.44 Å , Dy = 2.43 Å , Yb = 2.42 Å). The angle between the planes of N-Ln-N and O-Ln-O was found to be between 37-39° for all crystals, indicating a SAP geometry in the solid state. Selected bond lengths and angles are summarized in Table 3.5 and are comparable to previously reported similar DOTAM crystals.[18] N-Ln distances of ~ 2.65 Å and O-Ln distances of 2.35 Å are comparable to previously reported Gd DOTA crystals.[25] Crystallography data is summarized in Table 8**.**

Table 3.5. Summary of torsion angle of pendent arms α (˚) and key bond lengths (Å)

	Nd-3.1	**Tb-3.1**	**Dy-3.1**	**Yb-3.1**
α angle	37.48	38.94	39.04	39.51
N_2-C-C-O_1	22.8	35.1	30.0	22.9
N_3-C-C-O_2	35.8	30.1	28.3	34.0
N_5-C-C-O_3	28.3	28.4	23.3	30.1
N_7-C-C-O_4	30.7	23.2	34.6	28.3
N_2-Ln	2.70	2.65	2.64	2.60
N_3-Ln	2.70	2.65	2.60	2.62
N_5-Ln	2.72	2.61	2.63	2.61
N_7-Ln	2.66	2.64	2.64	2.57
O_1-Ln	2.43	2.36	2.35	2.30
O_2-Ln	2.48	2.36	2.41	2.30
O_3-Ln	2.41	2.36	2.35	2.36
O_4-Ln	2.45	2.42	2.35	2.36
H_2O-Ln	2.47	2.44	2.43	2.42

CEST spectra were acquired on a 9.4 T scanner with the following parameters, FOV (field of view): 25.6 x 25.6 mm^2, matrix 128 x 128, flash pulse, TR: 6ms, TE: 3 ms, flip angle: 6 degrees. The bound water paraCEST spectra for Eu^{3+}, Tb^{3+} and Dy^{3+} was acquired by applying a presaturation pulse at 15 µT for 4 seconds in steps of 5 ppm from -1000 to 1000 ppm. Amide exchange spectra (Tb^{3+}, Tm^{3+} and Dy^{3+}) were acquired by applying a presaturation pulse at 15 µT for 4 seconds in steps of 1 ppm from -100 to 100 ppm. All solvents were HPLC grade and used as such, except for dioxane and CH_2Cl_2 (dried by passing through columns of activated Al_2O_3) and water (18.2 MΩ·cm^{-1} deionized). Organic extracts were dried with Na_2SO_4 and solvents were removed under reduced pressure in a rotary evaporator. Size exclusion chromatography was carried out on BIO-GEL P2, 45-90 mesh resin (20 g, column size 15 × 2 cm per 0.1 mmol of compound). HPLC analysis was carried out using a high performance liquid chromatograph using a Microsorb-CN column (particle size 5 µm; 4.6 id×200 mm). Mobile phase: Gradient: 80:20 H_2O:CH_3CN to 35:65 H_2O:CH_3CN over 8 min 35:65 H_2O:CH_3CN for 7 min. **Ln-3.2** (R_t =7.55 min). **Ln-3.3** (R_t =1.50 min) NMR spectra were recorded on a 400 MHz spectrometer; for ^1H (400 MHz), chemical shift values (*δ* are reported relative to TMS and were referenced to the residual proton in the deuterated solvents as follows: $CDCl_3$ (7.26 ppm); DMSO-d_6 (2.49 ppm); D_2O (4.75 ppm). Mass spectra (MS) were obtained using electrospray ionization (ESI).

2-chloro-*N*-(propargyl)acetamide

Chloroacetyl chloride (5.97 ml, 75 mmol) was added dropwise to a stirred solution of propargylamine HCl. (455 mg, 50 mmol) and $NaHCO_3$ (12.75 g, 150 mmol) in 50 mL dry DCM. The solution was stirred for 3h, filtered and washed with 5% $NaHCO_3$. The organic layer was dried over $MgSO_4$ and dried under reduced pressure giving a brown solid (3.52 g, 27 mmol), yield 54%. ^1H NMR (400 MHz, $CDCl_3$): δ 6.81 (1H, br, s); 4.01 (2H, s); 4.10 (2H, m); 4.07 (2H, s); 2.28 (1H, t, J = 2.5 Hz).

1,4,7,10-tetraazacyclododecane-1,4,7,10-tetra-*N*-(propargyl)acetamide (3.1)

To a stirred solution of cyclen (267 mg, 1.5 mmol) and DIPEA (955 µl, 24.8 mmol) in 10 mL acetonitrile, *N*-(propargyl) chloroacetamide (816 mg, 6.2 mmol) was added in one portion and then refluxed overnight. The product was precipitated by the addition of 50 mL H_2O and isolated by filtration. White solid (680 mg, 1.2 mmol), yield 76%. ^1H NMR

(400 MHz, DMSO-d6): δ 7.57 (4H, m); 3.05 (8H, m); 2.22 (10H, m); 1.79 (14H, s); 1.67 (4H, s,). ESI-TOF. m/z calcd for $C_{28}H_{40}N_8O_4$ $(M+H)^+$, 553.3251, found 553.2574.

Ln^{3+}-1,4,7,10-tetraazacyclododecane-1,4,7,10-tetra-*N*-(propargyl)Acetamide chloride (Ln-3.1)

1,4,7,10-tetraazacyclododecane-1,4,7,10-tetra-*N*-(propargyl)acetamide (**3.1**) (55 mg, 0.1 mmol) was added to a stirring solution of dioxane:H_2O (4 mL) containing one of the following lanthanides at 1.1eq: $CeCl_3$, $PrCl_3$, $NdCl_3$, $TbCl_3$, $SmCl_3$, $EuCl_3$, $GdCl_3$, $DyCl_3$, $HoCl_3$, $ErCl_3$, $TmCl_3$, $YbCl_3$. Metallation was monitored by UPLC/MS and upon completion was dried under reduced pressure. ESI-TOF. m/z $C_{28}H_{40}N_8O_4Ce$ $(M+COOH)^+$, calcd for 736.2455, found 736.2704. $C_{28}H_{40}N_8O_4Pr$ $(M+COOH)^+$ calcd for 737.2147, found 737.2833. $C_{28}H_{40}N_8O_4Nd$ $(M+COOH)^+$, calcd for 742.2461, found 742.2865. $C_{28}H_{40}N_8O_4Tb$ $(M+COOH)^+$, calcd for 757.2481, found 757.3318. $C_{28}H_{40}N_8O_4Sm$ $(M+COOH)^+$, calcd for 749.2346, found 749.1833. $C_{28}H_{40}N_8O_4Eu$ $(M+COOH)^+$, calcd for 749.2426, found 749.1849. $C_{28}H_{40}N_8O_4Gd$ $(M+COOH)^+$, calcd for 752.2582, found 752.3073. $C_{28}H_{40}N_8O_4Dy$ $(M+COOH)^+$, calcd for 756.2627, found 756.3125. $C_{28}H_{40}N_8O_4Ho$ (M+COOH)+, calcd for 763.2531, found 763.3088. $C_{28}H_{40}N_8O_4Er$ (M+COOH)+, calcd for 762.2672, found 762.3002. $C_{28}H_{40}N_8O_4Tm$ (M+COOH)+, calcd for 767.2570, found 767.3286. $C_{28}H_{40}N_8O_4Yb$ (M+COOH)+, calcd for 768.2723, found 768.3187.

Ln^{3+}-(1,4,7,10-tetraazacyclododecane-1,4,7,10)tetrakis(N-((1-(3-*β*-D-tetra(-*O*-acetyl)gluco)pyranodiyl)propyl)-1H-1,2,3-triazol-4-yl)methylacetamide chloride (3.2)

General synthesis of Ln-2 (Ln = Gd^{3+}, Eu^{3+}, Dy^{3+}, Tb^{3+}, Tm^{3+}) Gd-1 (40 mg, 0.057 mol) was dissolved in 2 mL 1:1 H2O:isopropanol and tetra-Oacetylglucosyl propylazide (147 mg, 0.34 mol, 6 eq) was added in one portion. Copper sulphate (0.03 mol) and sodium ascorbate (0.06 mol) was added under an atmosphere of nitrogen and the mixture was stirred overnight. The product was isolated by HPLC to yield 113 mg (yield = 82%) of a colourless solid. ESI-TOF: m/z calcd for $C_{96}H_{140}N_{20}O_{44}Gd$ (M+H)+, 2431.8559, found 2431.8442. calcd for $C_{96}H_{140}N_{20}O_{44}Tb$ (M+H)+, 2438.8821, found 2438.6610. calcd for $C_{96}H_{140}N_{20}O_{44}Dy$ (M+H)+, 2443.8933, found 2443.7889. calcd for $C_{96}H_{140}N_{20}O_{44}Eu$ (M+H)+, 2427.8531, found 2427.6267. calcd for $C_{96}H_{140}N_{20}O_{44}Tm$ (M+H)+, 2445.8675, found 2445.6516.

Ln^{3+}-Deprotection of 2 to give (1,4,7,10-tetraazacyclododecane-1,4,7,10)tetrakis(N-((1-(3-*β*-D-gluco)pyranodiyl)propyl)-1H-1,2,3-triazol-4-yl)methylacetamide chloride (3.3)

General synthesis of Ln-3 (Ln = Gd^{3+}, Eu^{3+}, Dy^{3+}, Tb^{3+}, Tm^{3+}). Deprotection of compound **Gd-3.2** was done by addition of catalytic amount of K_2CO_3 (5 mg) to 50 mg (0.02 mmol) DOTAM glucose click in methanol. The reaction was stirred 1.5 hr and then Amberlite 120 resin was then added and mixture was stirred for an additional 30 min. The solvent was filtered and dried to yield 35 mg (yield 99 %) of deacetylated complex Gd-3. ESI-TOF: m/z calcd for $C_{64}H_{108}N_{20}O_{28}Gd$ (M+H)+, 1759.6868, found 1759.6890. calcd for $C_{64}H_{108}N_{20}O_{28}Tb$ (M+H)+, 1764.6974, found 1764.7158. calcd for $C_{64}H_{108}N_{20}O_{28}Dy$ (M+H)+, 1768.6934, found 1768.7091. calcd for $C_{64}H_{108}N_{20}O_{28}Eu$ (M+H)+, 1757.6854, found 1757.6976. calcd for $C_{64}H_{108}N_{20}O_{28}Tm$ (M+H)+, 1773.6984, found 1773.6870.

3.3 Conclusion

We have synthesised and characterised a series of lanthanide tetraalkyne DOTAM complexes. Solution phase ^1H NMR and solid state structures indicate that only SAP geometry is present in these compounds, which is useful for development of magnetic resonance spectroscopy (MRS) and is critical for paramagnetic chemical exchange saturation transfer (ParaCEST) MR imaging agents. The complexes **Tm-3.1**, **Dy-3.1** and **Tb-3.1** show strong CEST signals due to the exchangeable amide protons at 25˚C, at 10 mM, pH 7. A response of 40% is observed for **Eu-3.1** at 51ppm along with significant CEST effect (~5%) due to metal-bound water was observed for **Tb-3.1** and **Dy-3.1** at –640 and -765 ppm, respectively. Complexes producing such highly shifted signals are of interest in the development of ParaCEST contrast agents that are free of interference from background magnetization transfer effects.

We have also the used “click” chemistry to functionalize the central ligand in good yields en route to the development of targeted contrast agents. Relaxivity measurements were used to characterize the gadolinium-containing parent and derivative agents. All of these agents possess smaller r1 values than the carboxylate ligand DOTA, which is expected on the basis of slower water exchange in the DOTAM complexes. CEST experiments were performed on **Tm-(3.2,3.3)**, **Tb-(3.2,3.3)**, **Dy-(3.2,3.3)**, and **Eu-(3.2,3.3)**. **Tm-3.3** shows a significant amide CEST response for what can be considered a targeted contrast agent for glucose receptors as well as Eu-2 and Eu-3 which show promising results for bound water. Dy and Tb complexes did not have any observable CEST response for both amide and water.

Previous studies have shown that glucose conjugates can cross the blood-brain barrier,[26] and target cancerous tissues due to their high demand for glucose.[15, 16] Bearing these results in mind, we have pursued a flexible “click” chemistry synthesis of multivalent carbohydrate decorated MR contrast agents.

Table 3.6. Crystallography data for **Nd-3.1**, **Yb-3.1**, **Tb-3.1** and **Dy-3.1**

Compound reference	**Tb-3.1**	**Dy-3.1**	**Nd-3.1**	**Yb-3.1**
Chemical formula	$C_{28}H_{42}N_8O_5Tb$ $(C_3H_{15}O_5Cl_3)$	$C_{28}H_{42}N_8O_5Dy$ $(C_3H_{16}O_5Cl_3)$	$C_{28}H_{42}N_8O_5Nd$ $(C_3H_{16}O_5Cl_3)$	$C_{28}H_{42}N_8O_5Yb$ $(C_3H_{12}O_5Cl_3)$
Formula Mass	967.12	971.70	953.44	977.20
Crystal system	Triclinic	Triclinic	Triclinic	Triclinic
a/Å	10.8916(5)	10.8844(4)	11.1524(6)	10.8858(5)
b/Å	14.3620(6)	14.3626(6)	13.9136(7)	14.3185(6)
c/Å	15.4604(10)	15.4658(10)	15.2106(12)	15.4483(7)
α/°	113.338(2)	113.395(3)	110.878(3)	113.484(2)
β/°	103.205(3)	103.121(3)	103.133(3)	102.767(2)
γ/°	99.220(2)	99.252(2)	100.034(2)	99.404(2)
Unit cell volume/Å3	2075.04(19)	2074.15(18)	2061.4(2)	2067.00(16)
Temperature/K	150(2)	150(2)	150(2)	150(2)
Space group	$P\bar{1}$	$P\bar{1}$	$P\bar{1}$	$P\bar{1}$
No. of formula units per unit cell, Z	2	2	2	2
No. of reflections measured	246235	286221	220951	278130
No. of independent reflections	10723	12145	9849	10268
Rint	0.0518	0.0682	0.0831	0.1154
Final R1 values (I > 2σ(I))	0.0224	0.0237	0.0269	0.0303
Final wR(F2) values (I > 2σ(I))	0.0574	0.0593	0.0615	0.0631
Final R1 values (all data)	0.0263	0.0289	0.0347	0.0431
Final wR(F2) values (all data)	0.0598	0.0620	0.0647	0.0683

3.4 Supplemental information

S3.1. NMR Spectra of **Yb-3.1**

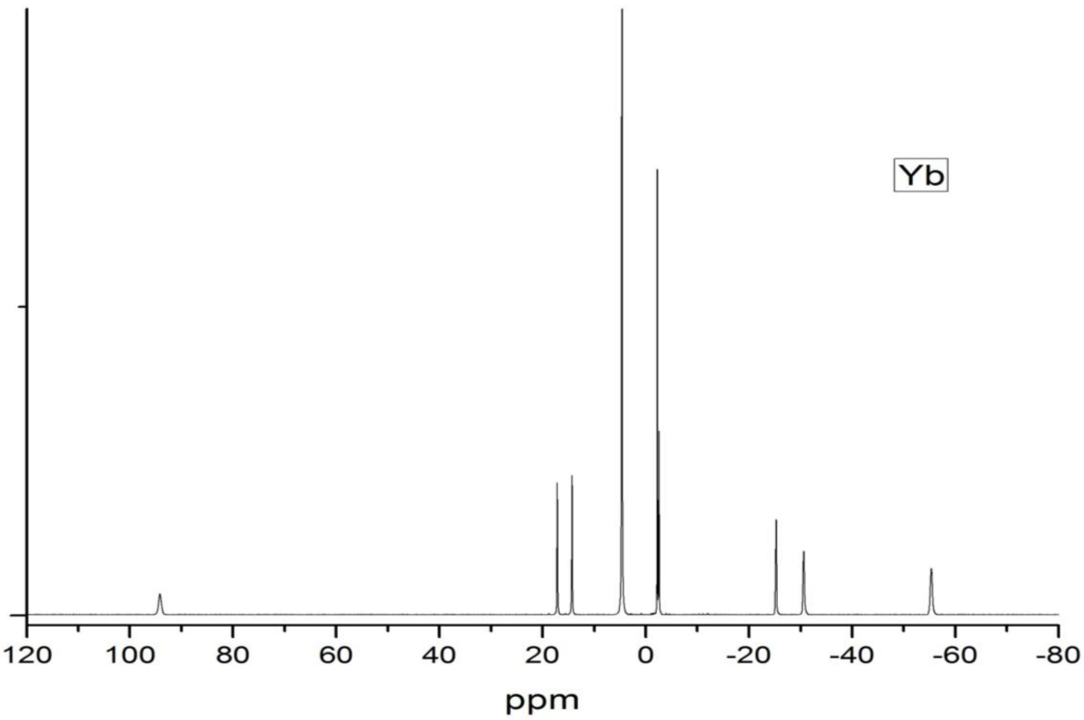

S3.2. NMR Spectra of **Ce-3.1**

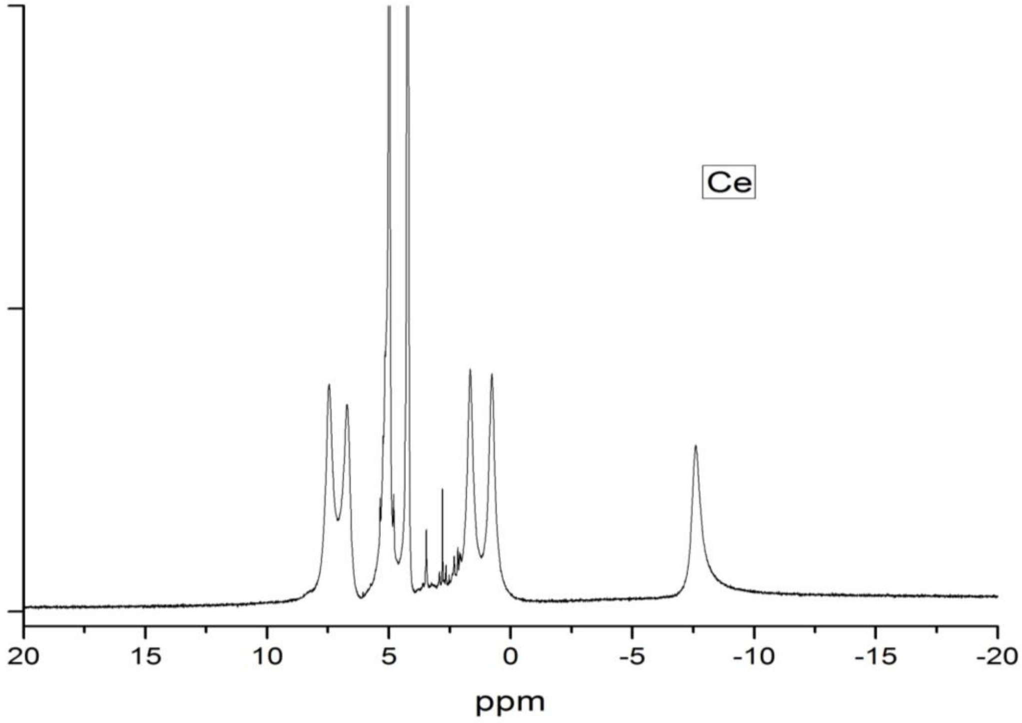

S3.3. NMR Spectra of **Eu-3.1**

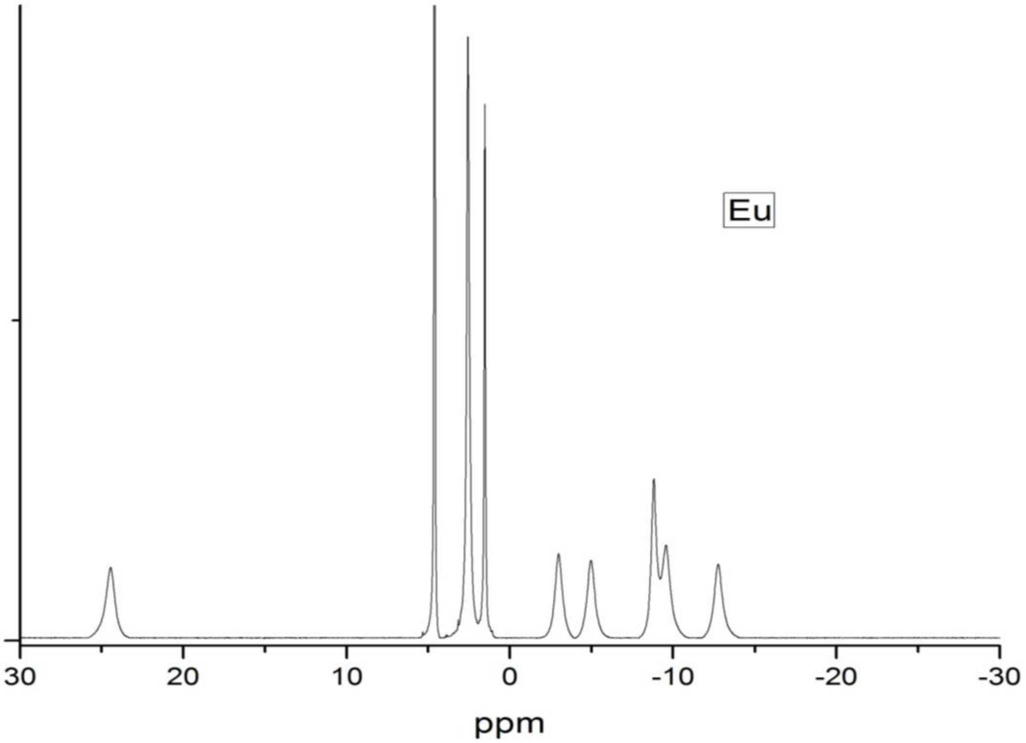

S3.4. NMR Spectra of **Tm-3.1**

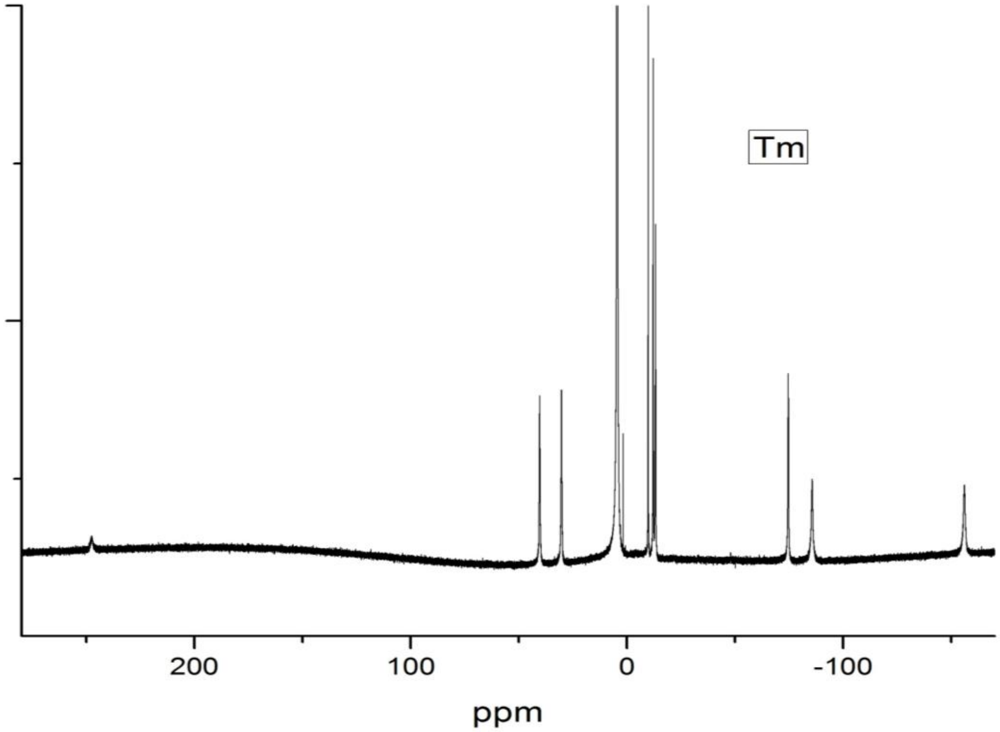

S3.5. NMR Spectra of **Tb-3.1**

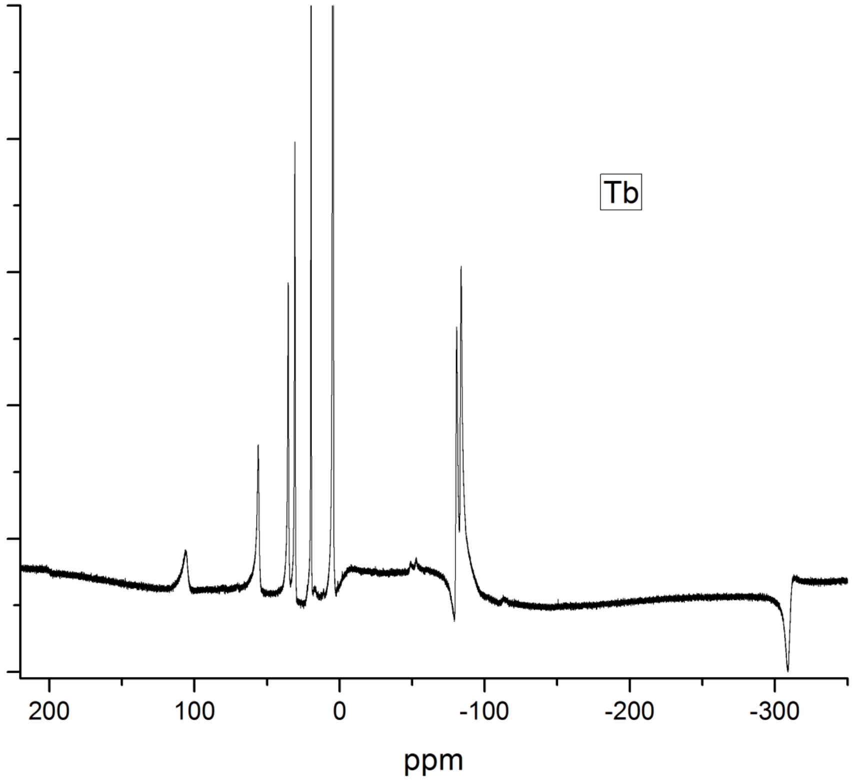

S3.6. NMR Spectra of **Er-3.1**

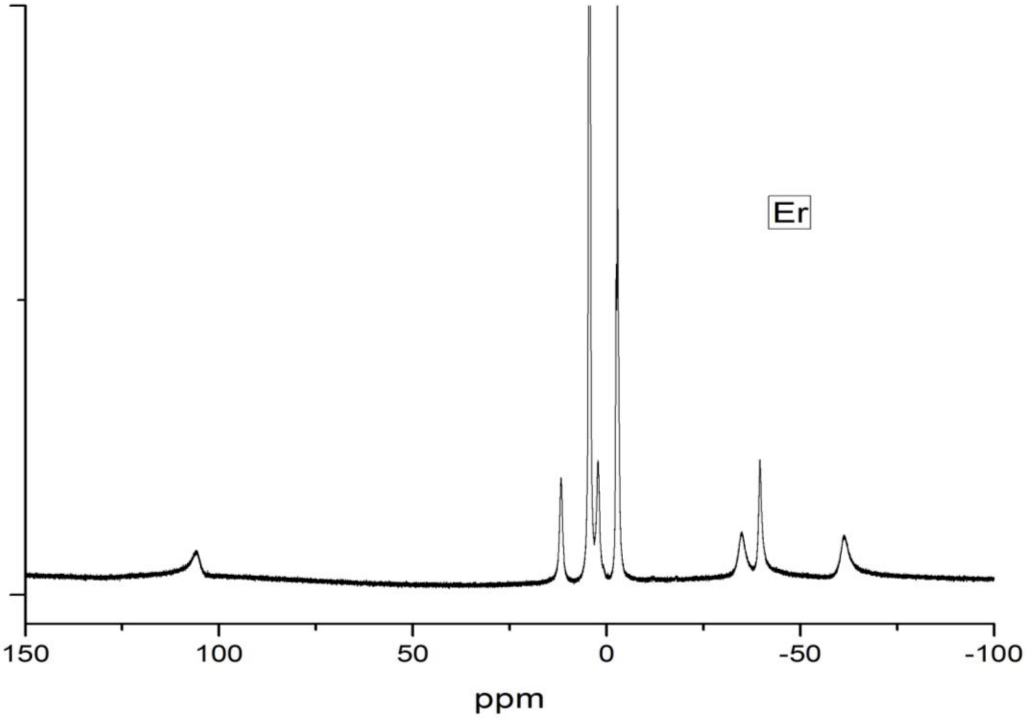

S3.7. NMR Spectra of **Gd-3.1**

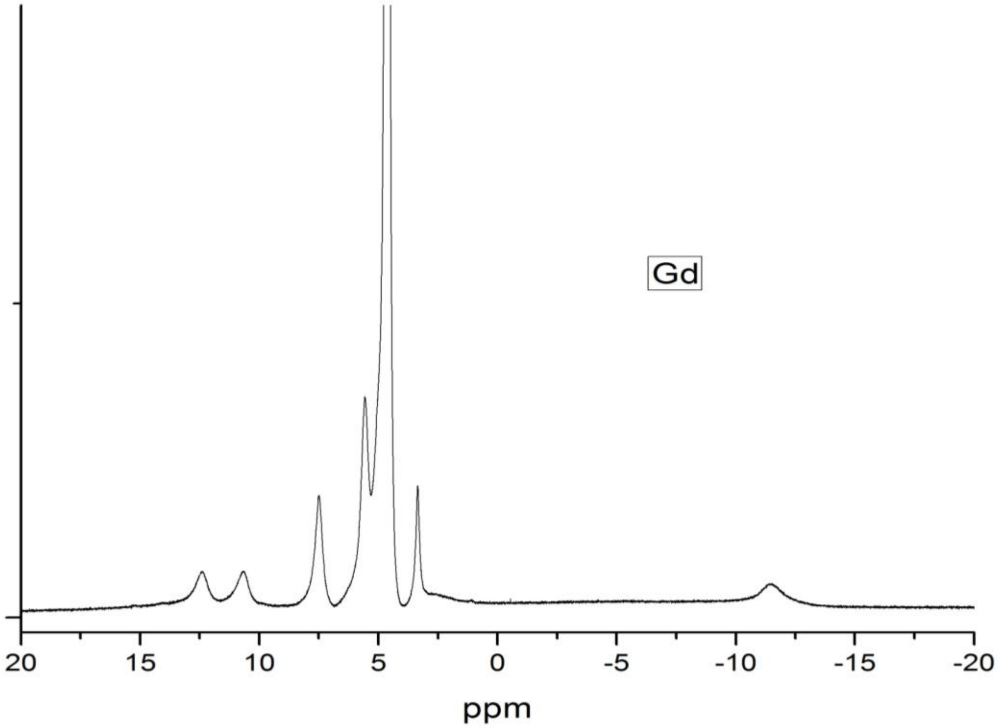

S3.8. NMR Spectra of **Ho-3.1**

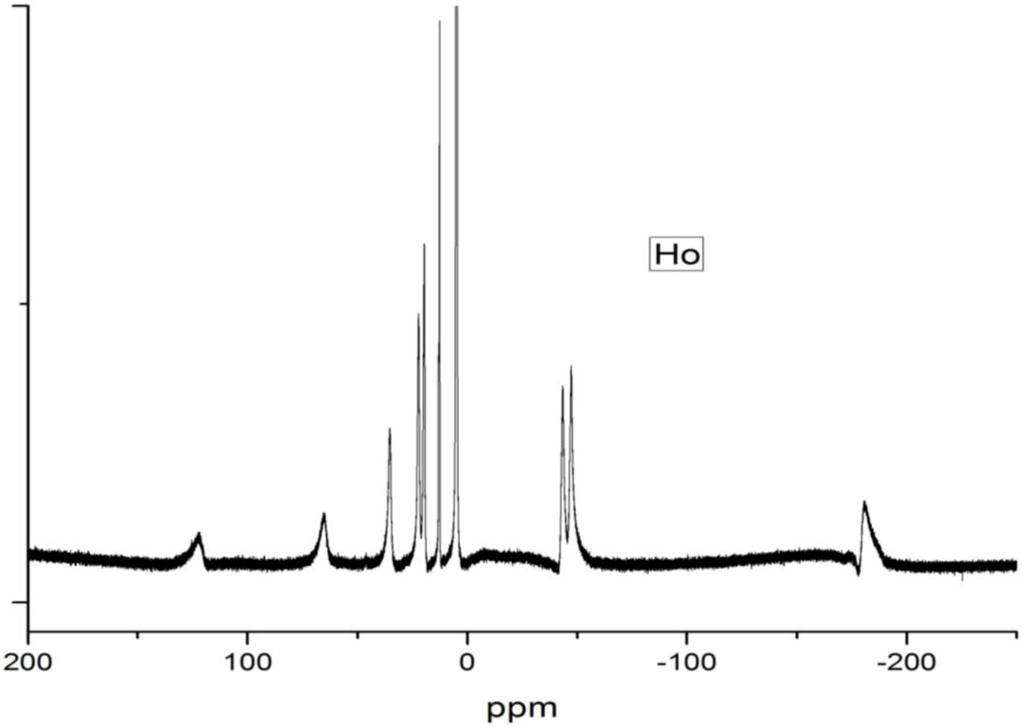

S3.9. NMR Spectra of **Dy-3.1**

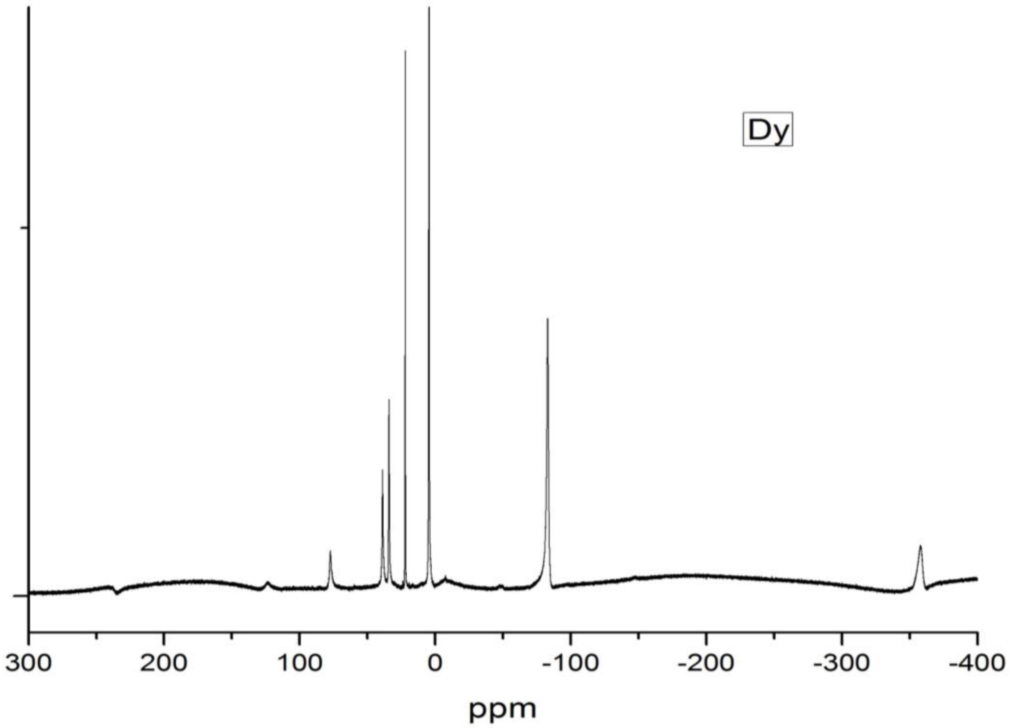

S3.10. NMR Spectra of **Sm-3.1**

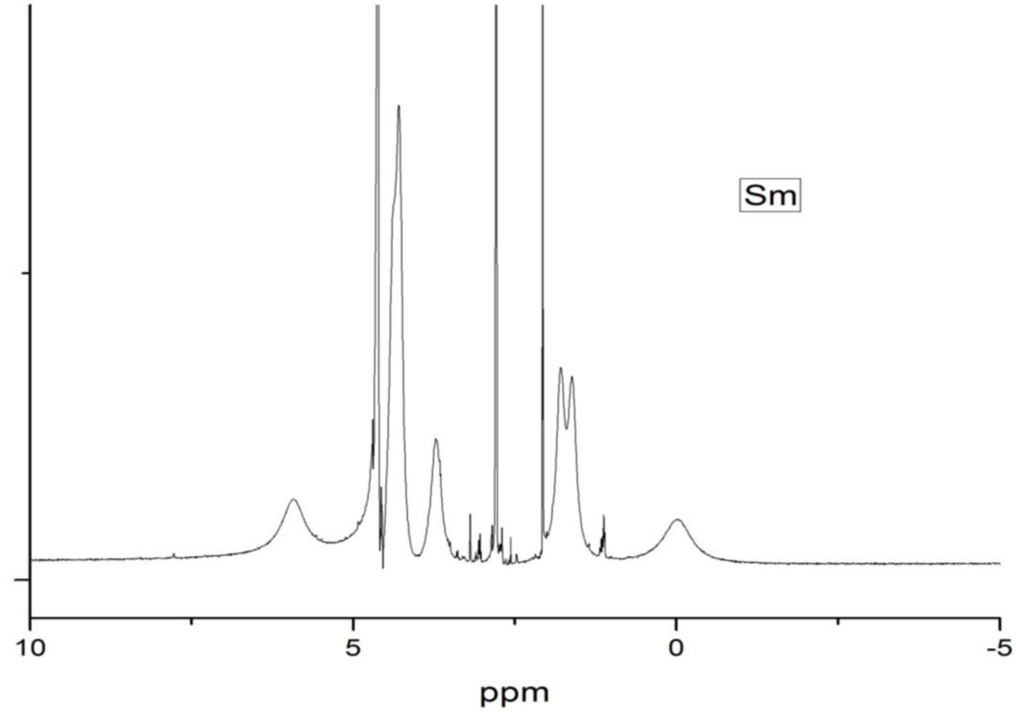

S3.11. NMR Spectra of **Nd-3.1**

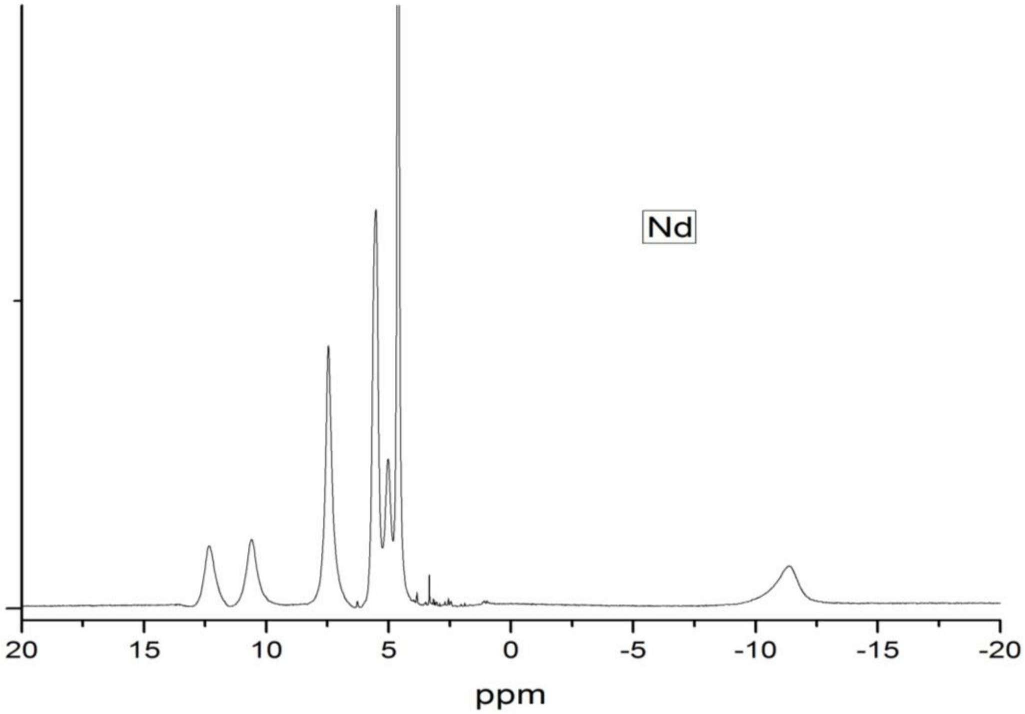

S3.12. NMR Spectra of **Pr-3.1**

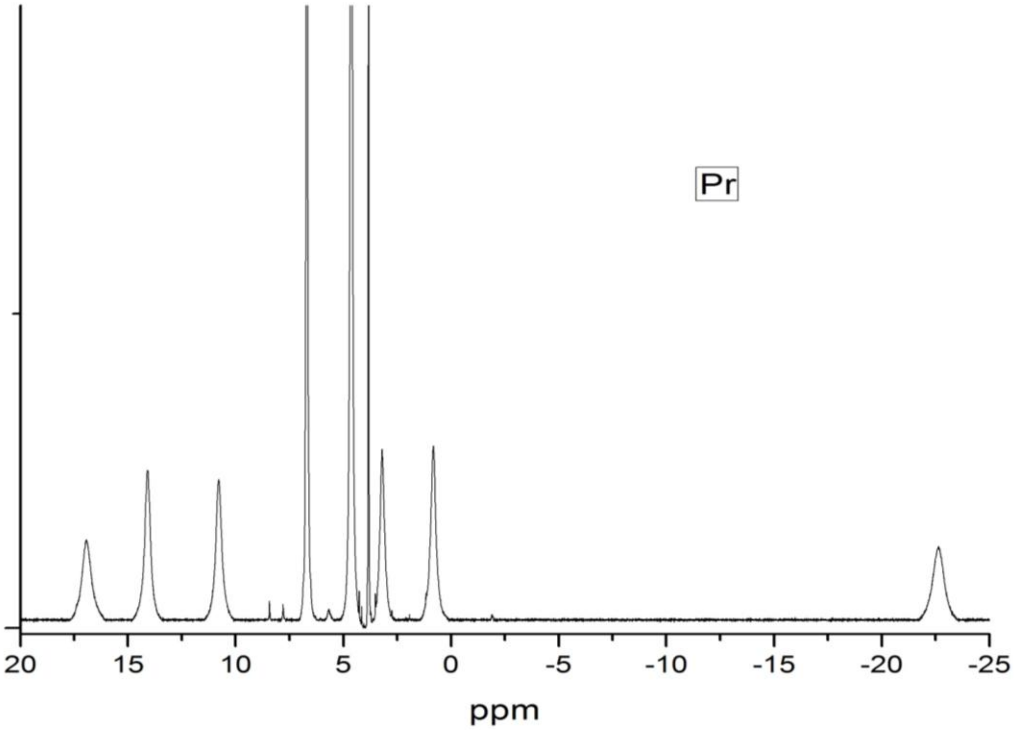

S3.13. NMRD Profile of **Gd-3.1**

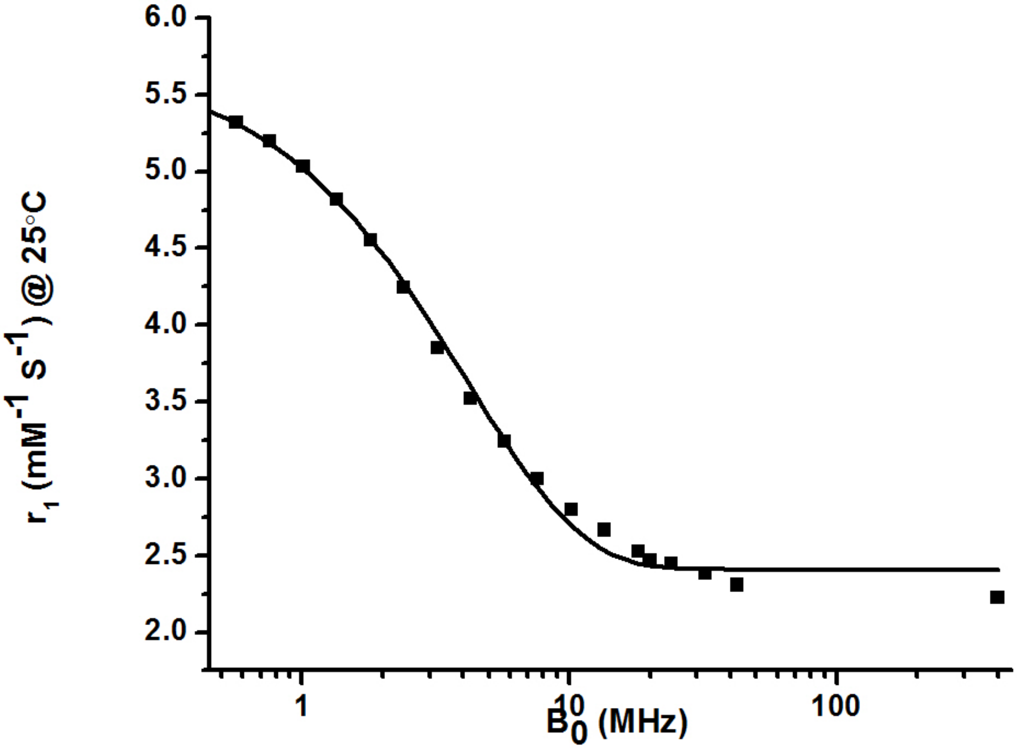

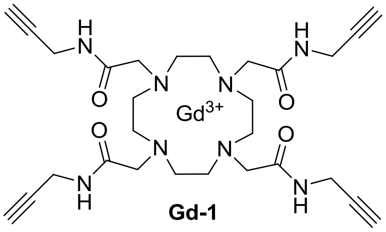

Gd-1

S3.14. NMRD Profile of **Gd-3.2**

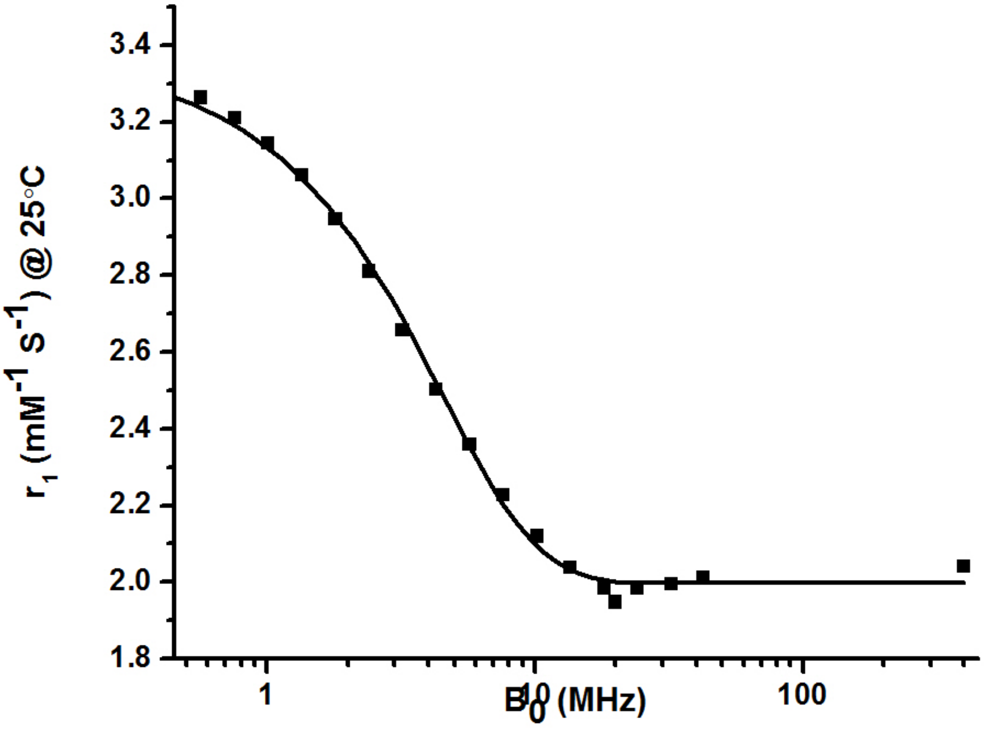

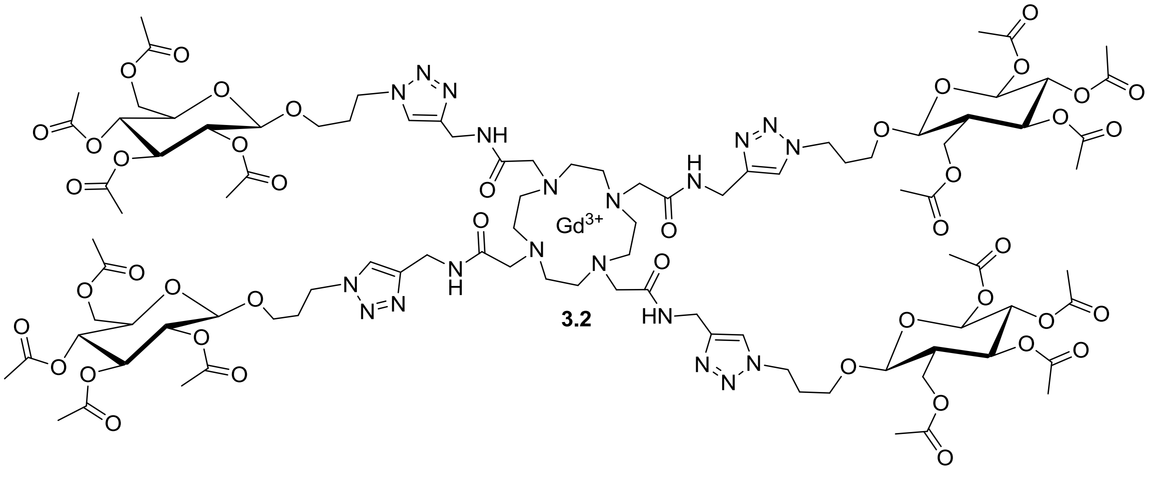

3.2

S3.15. NMRD Profile of **Gd-3.3**

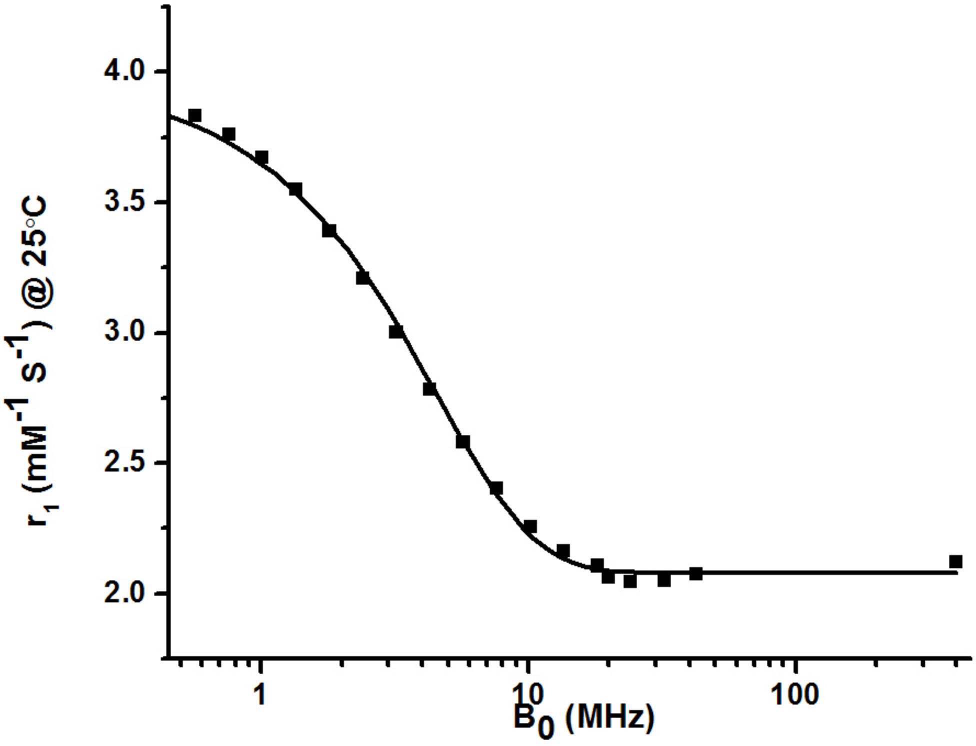

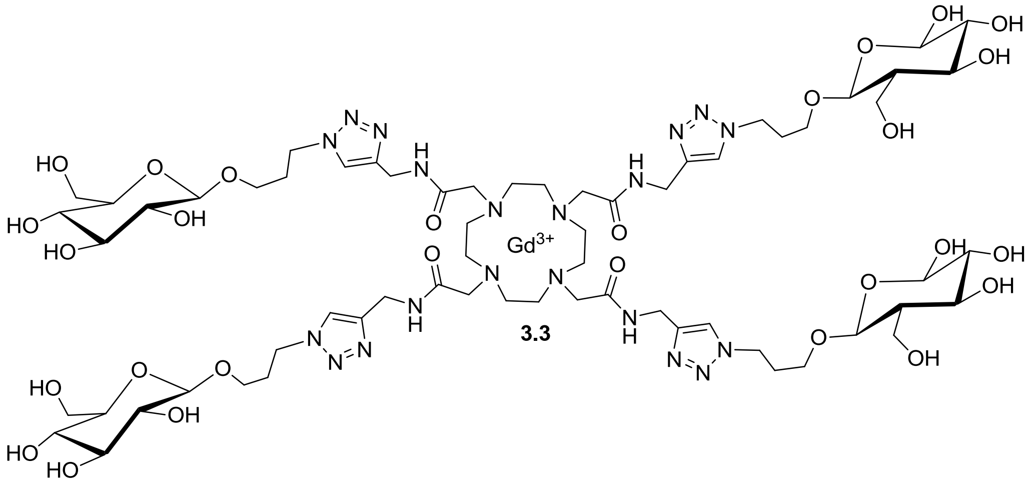

3.3

S3.16.CEST Spectra of **Dy-3.1**

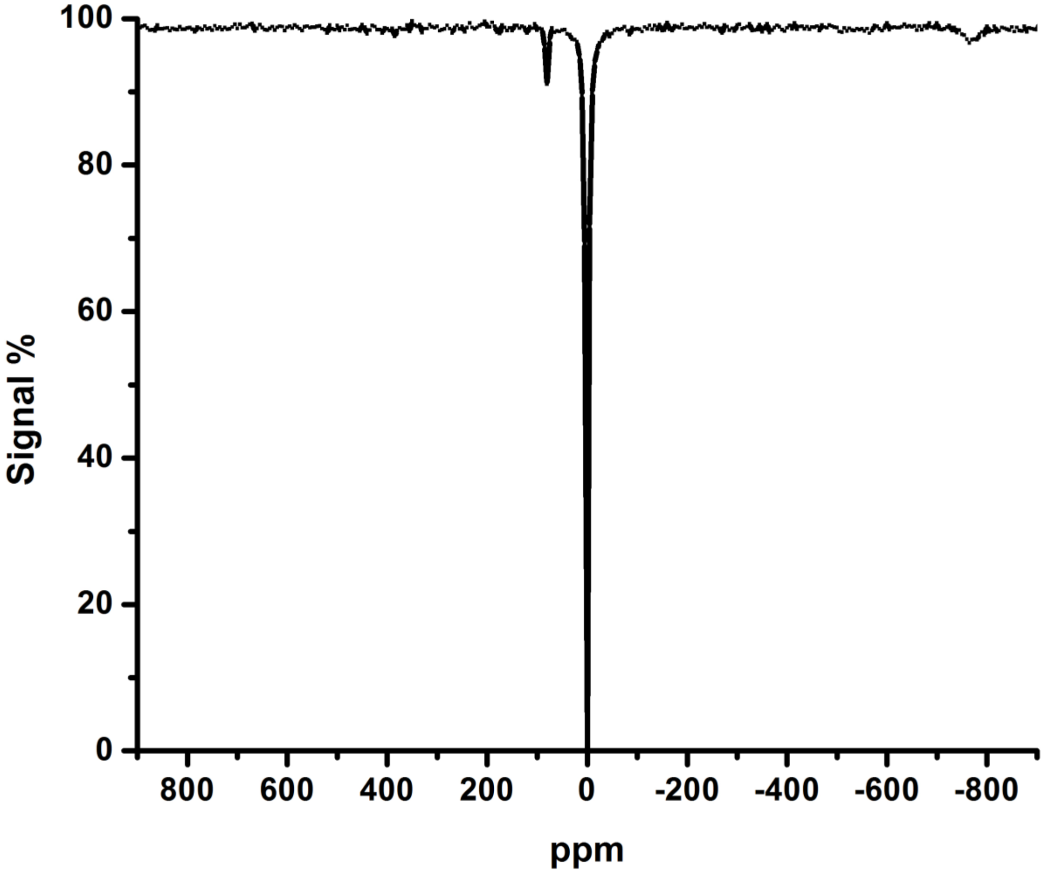

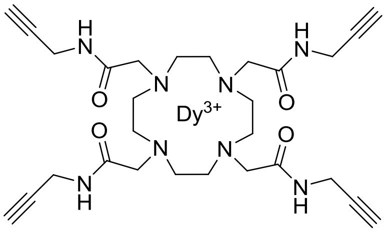

S3.17.CEST Spectra of **Dy-3.2**

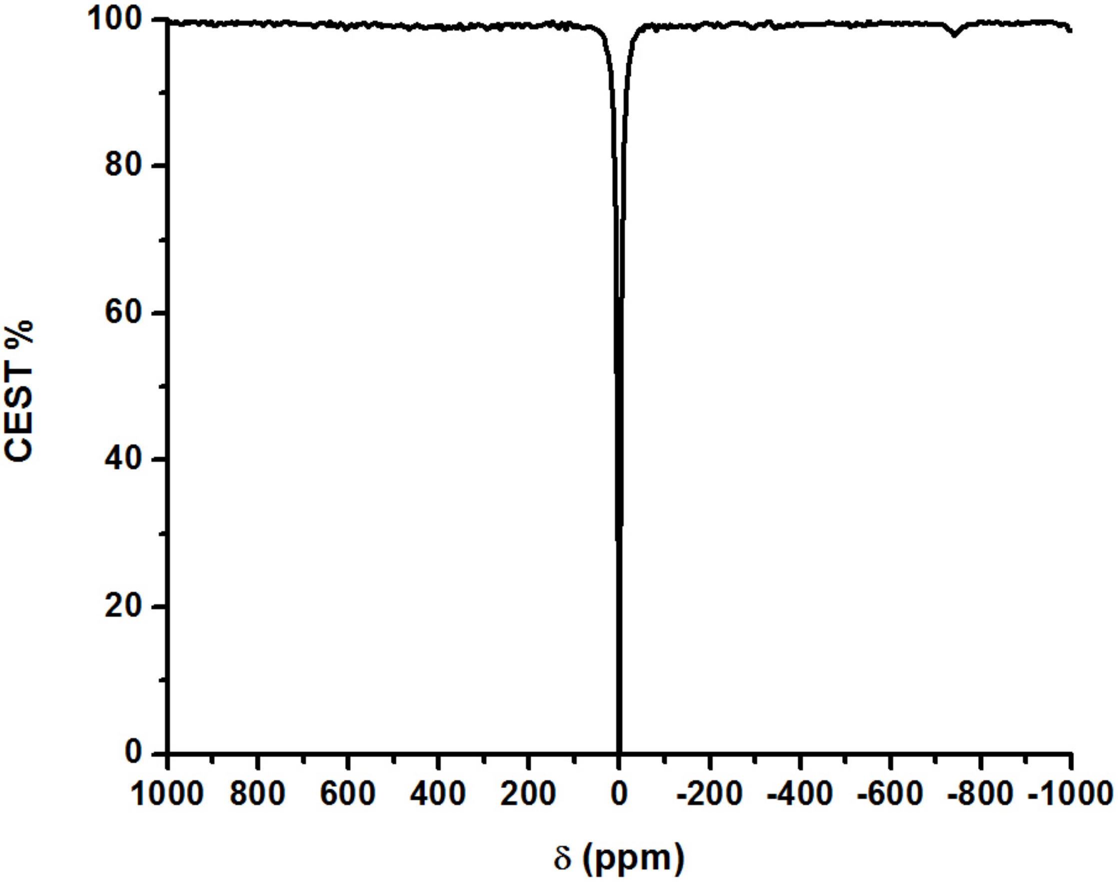

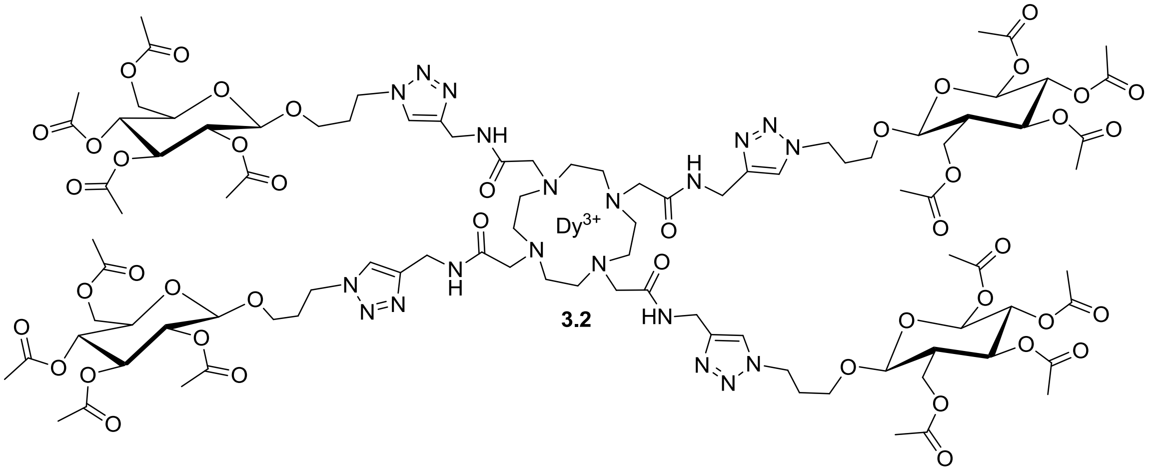

3.2

S3.18. CEST Spectra of **Dy-3.3**

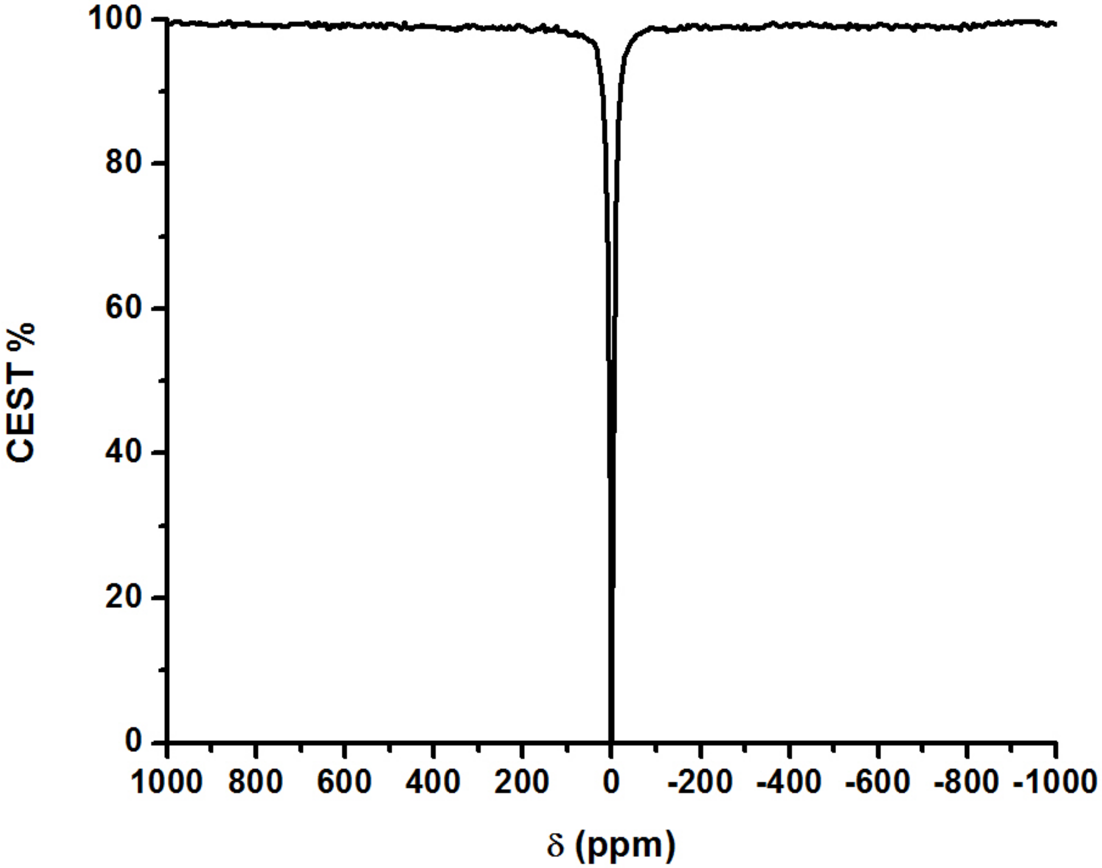

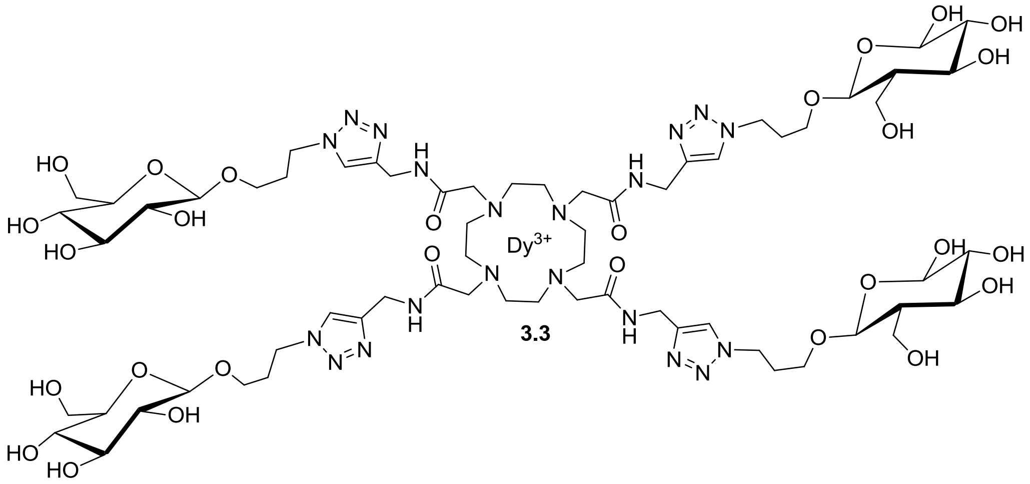

3.3

S3.19.CEST Spectra of **Eu-3.1**

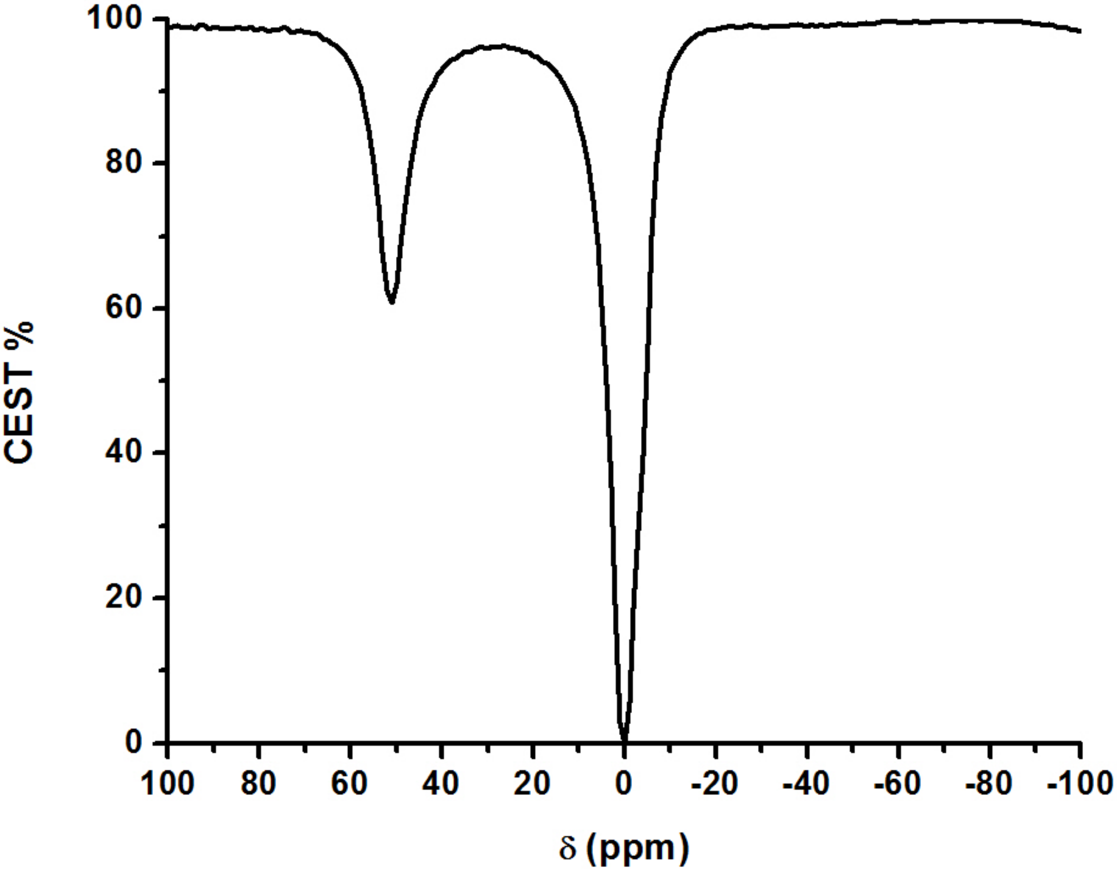

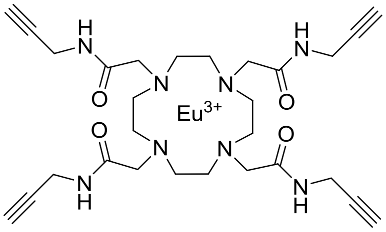

S3.20.CEST Spectra of **Eu-3.2**

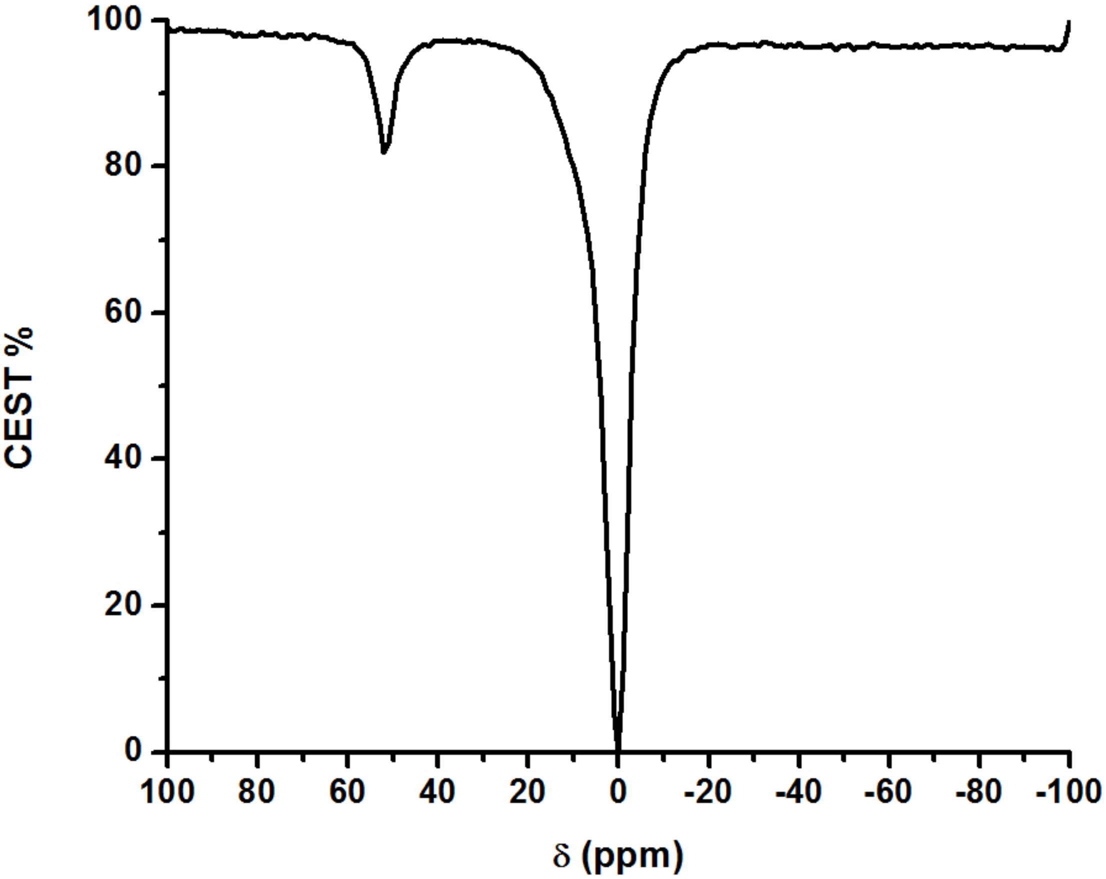

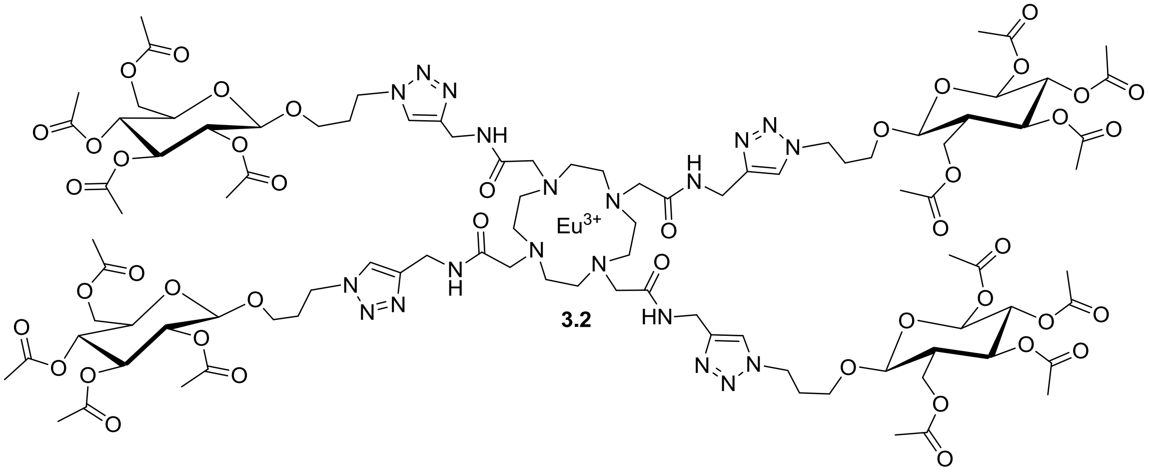

3.2

S3.21.CEST Spectra of **Eu-3.3**

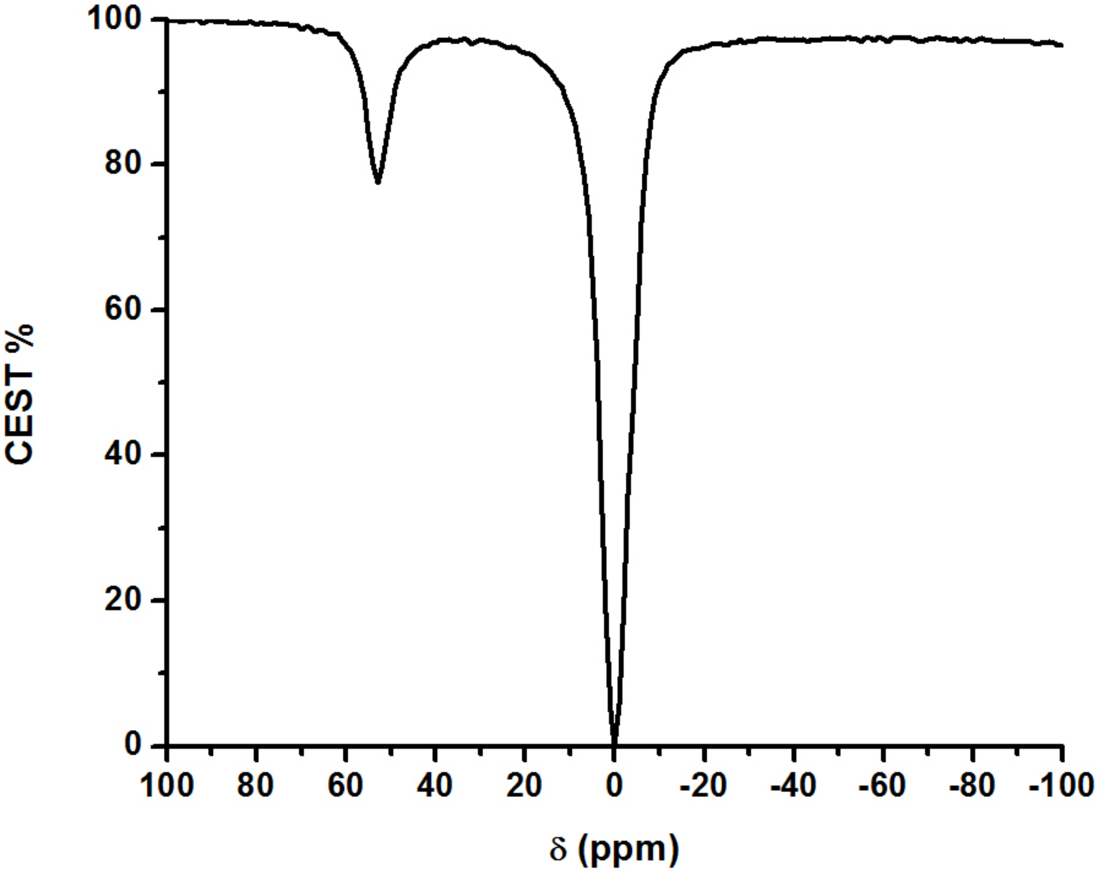

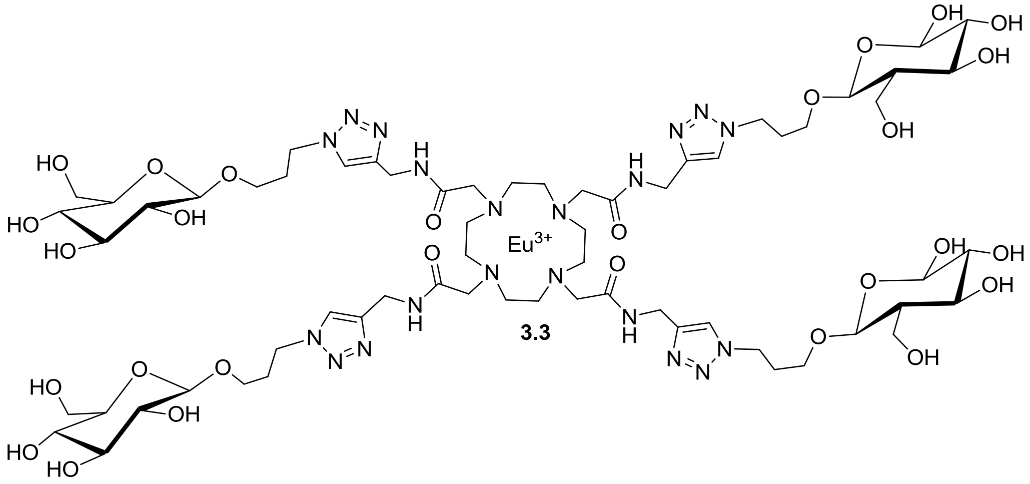

3.3

S3.22.CEST Spectra of **Tb-3.1**

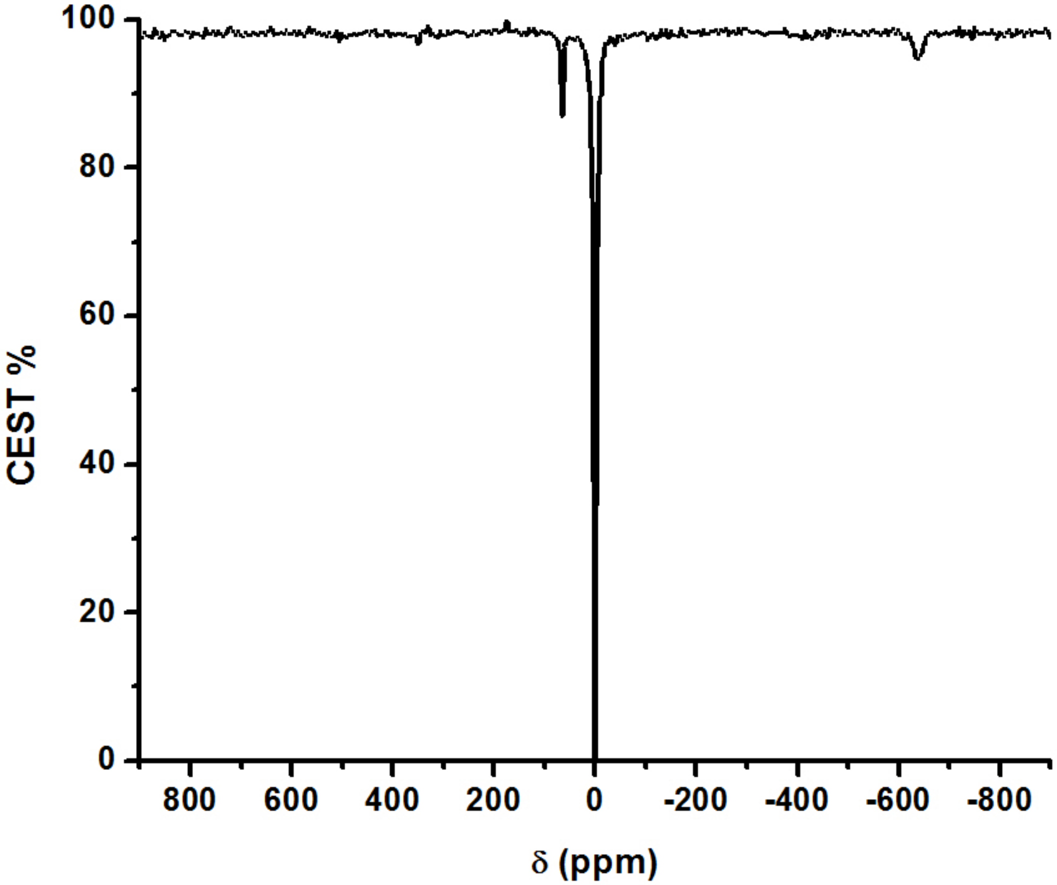

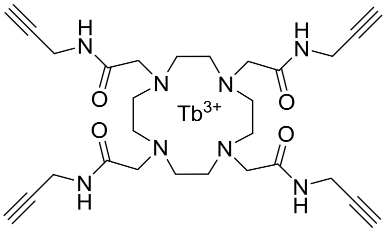

S3.23.CEST Spectra of **Tb-3.2**

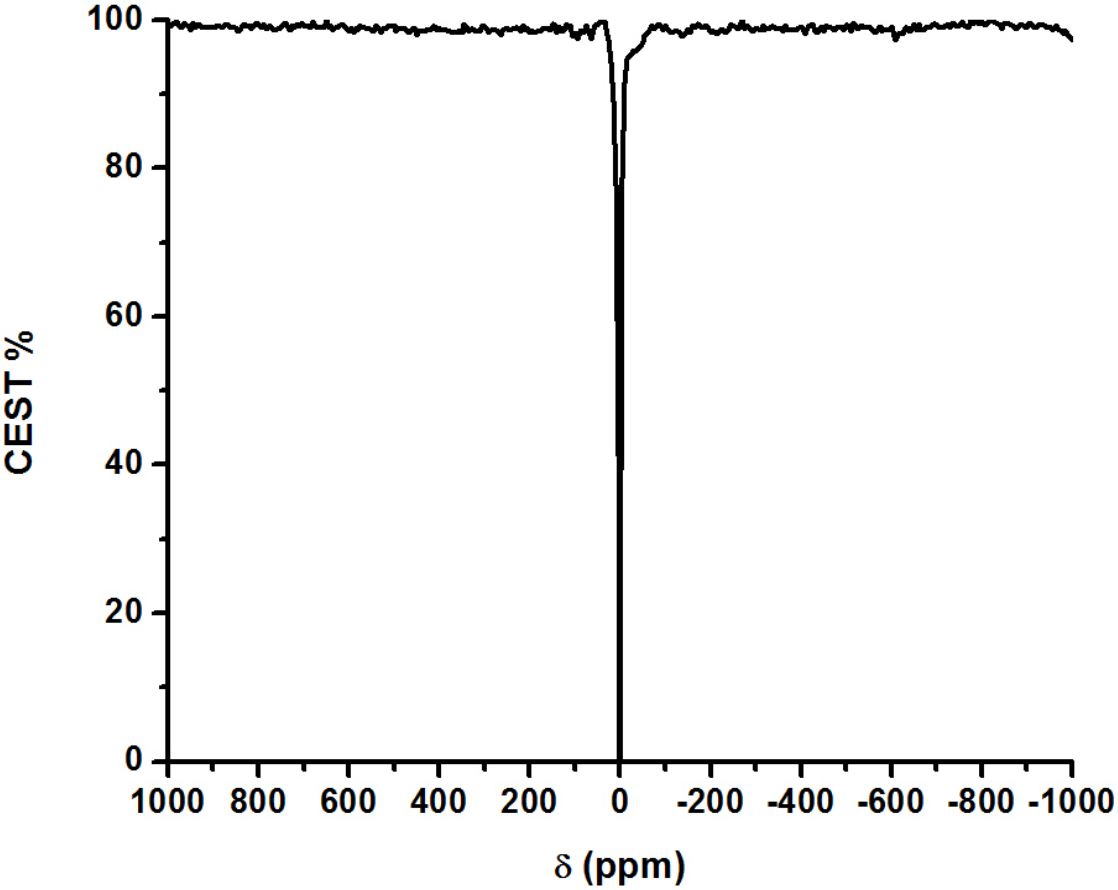

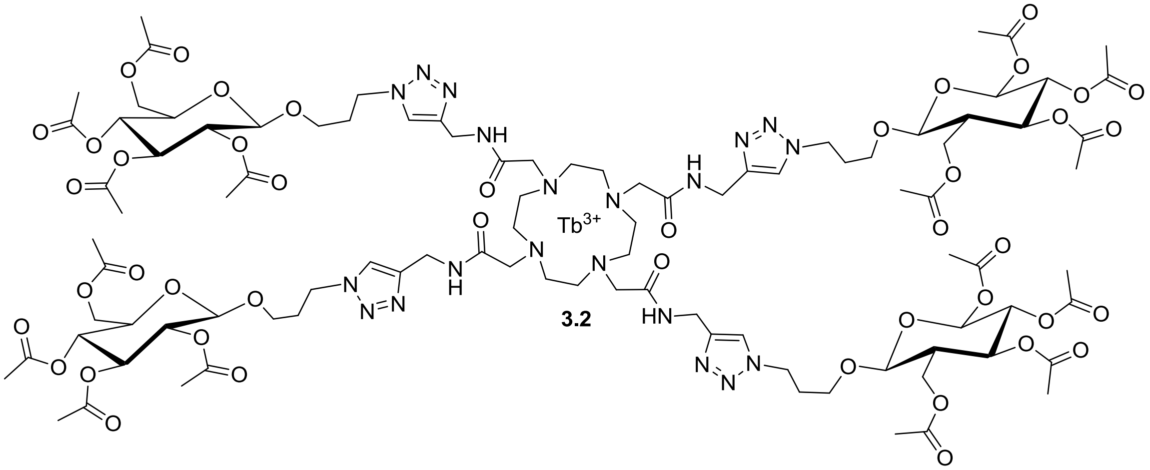

3.2

S3.24.CEST Spectra of **Tb-3.3**

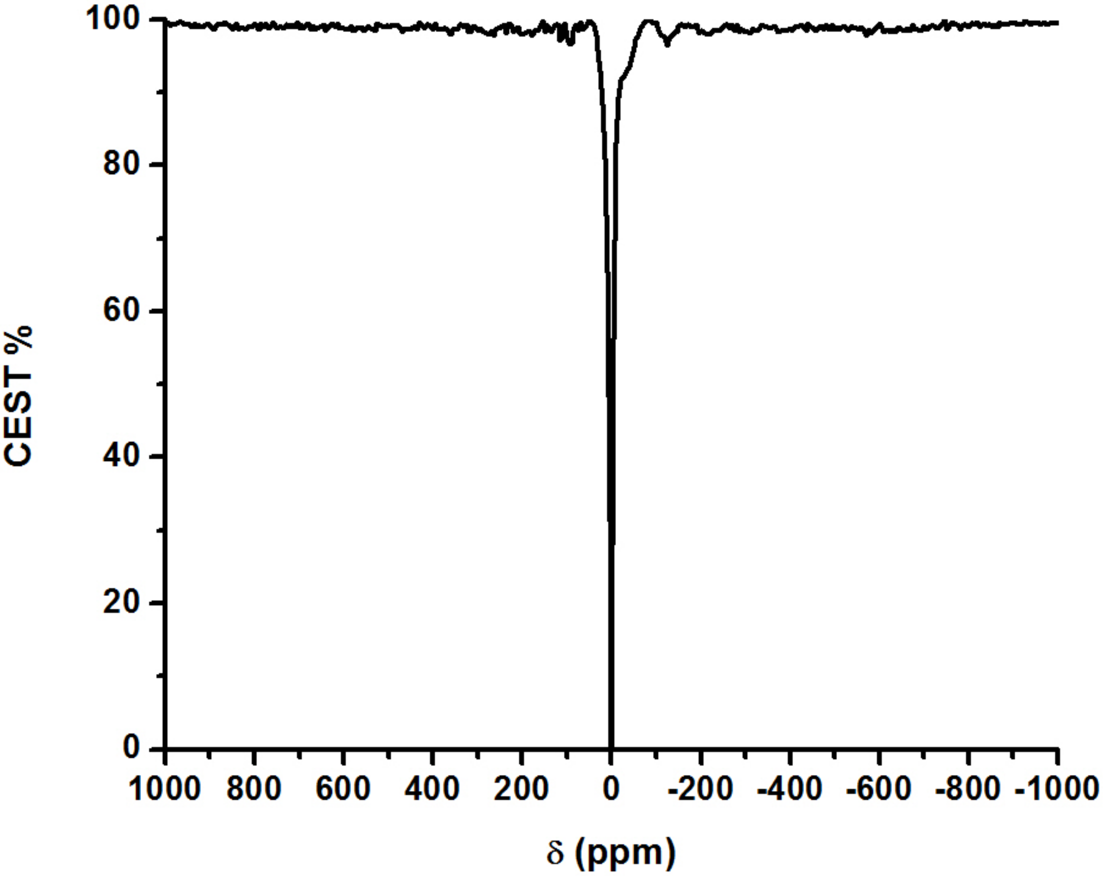

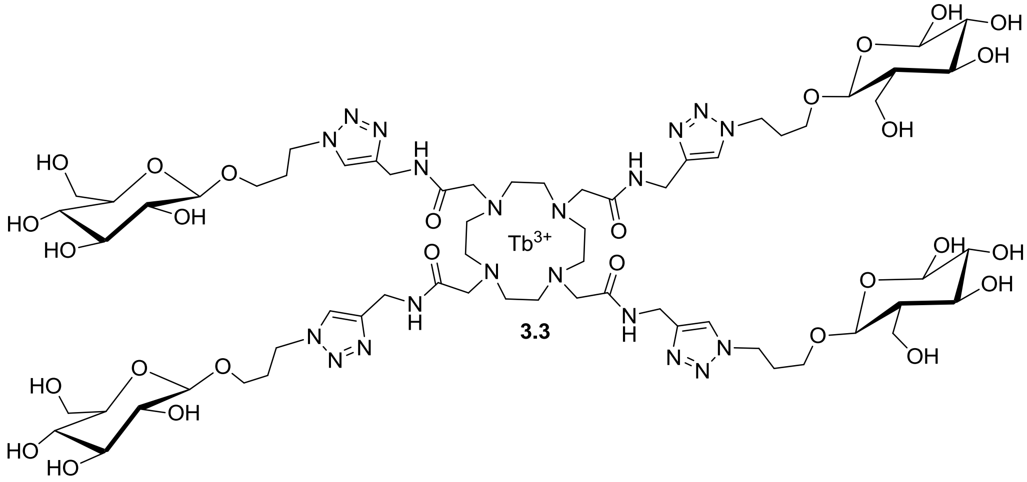

3.3

S3.25.CEST Spectra of Tm-3.1

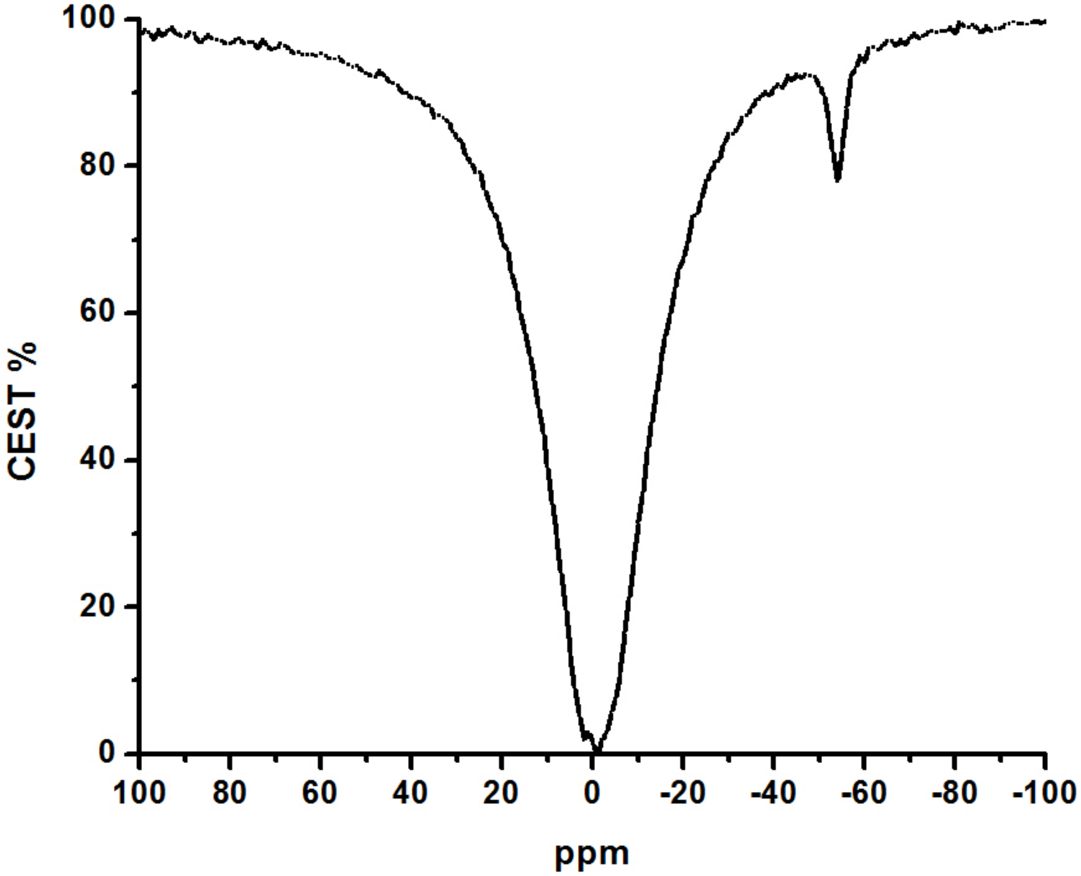

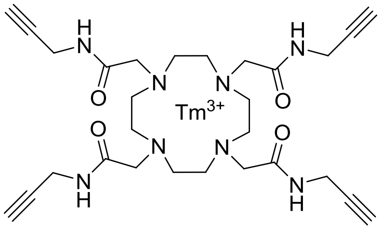

S3.26.CEST Spectra of **Tm-3.2**

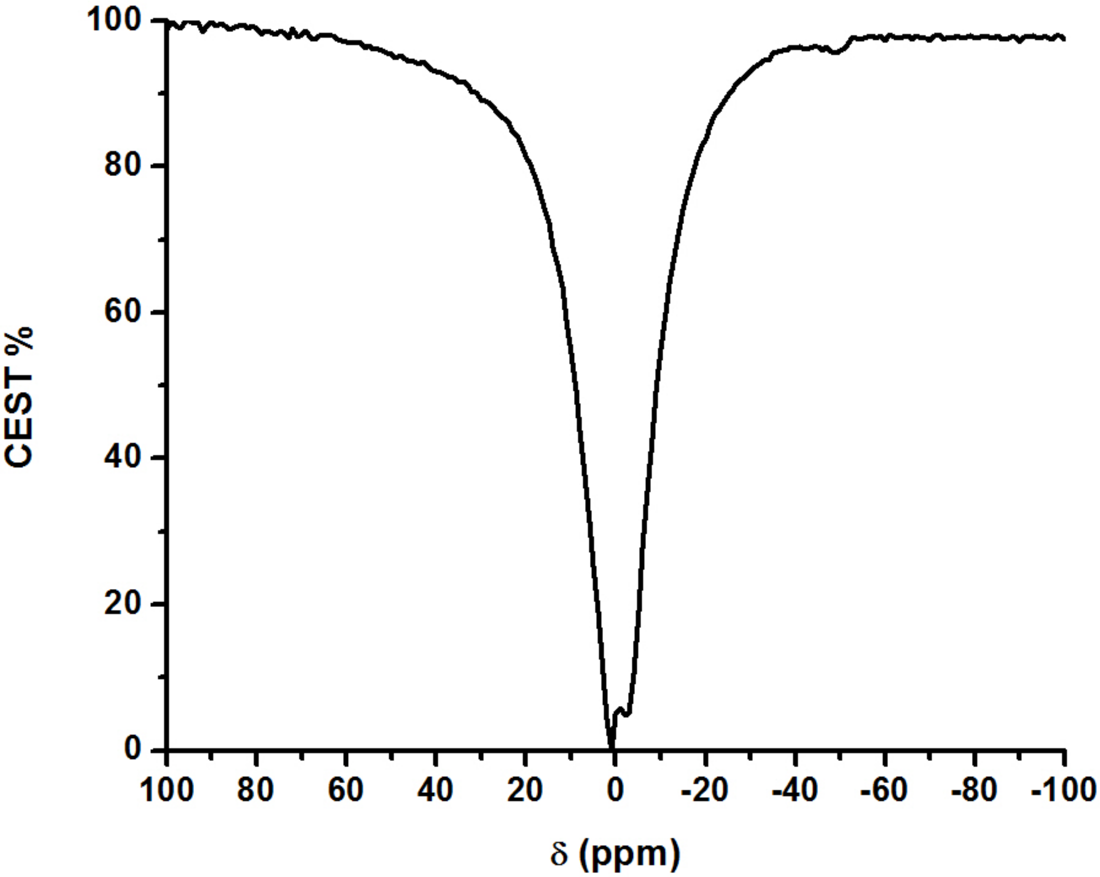

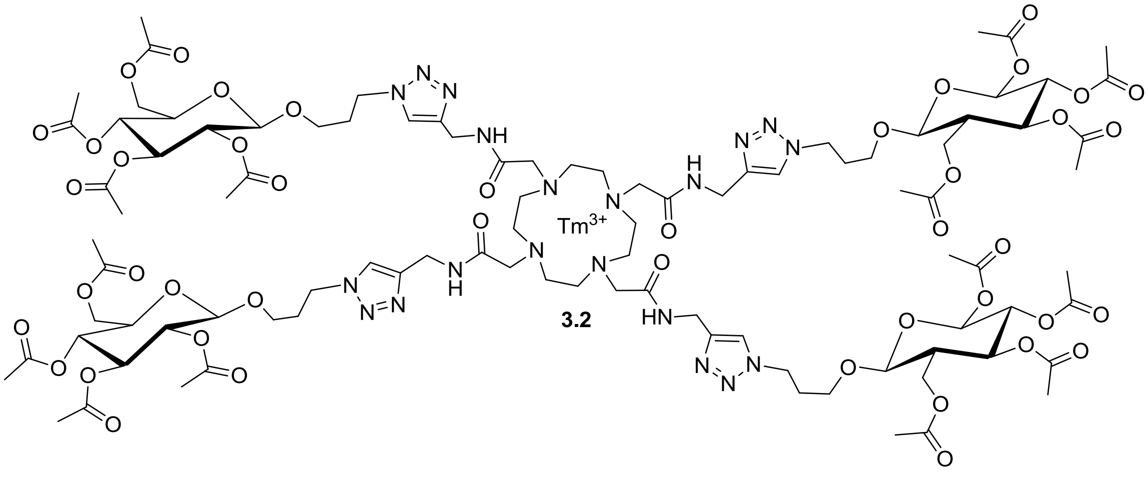

3.2

S3.27.CEST Spectra of **Tm-3.3**

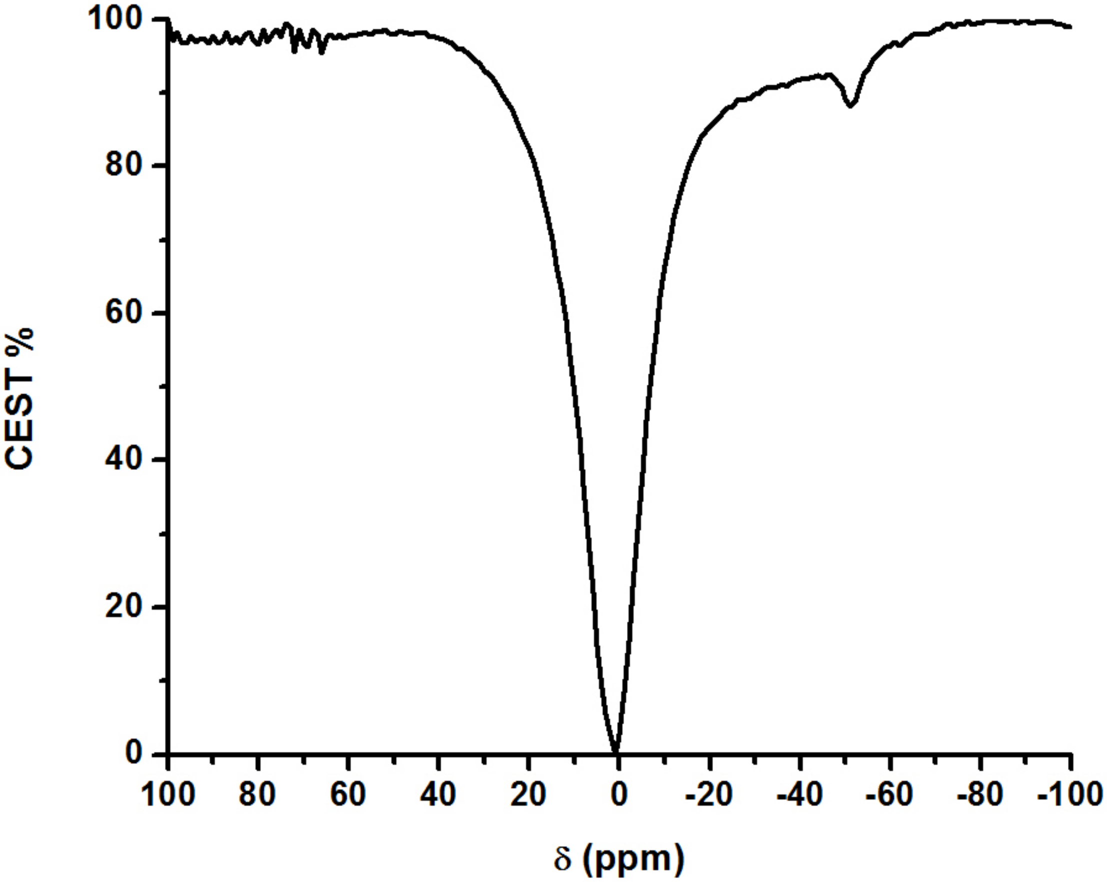

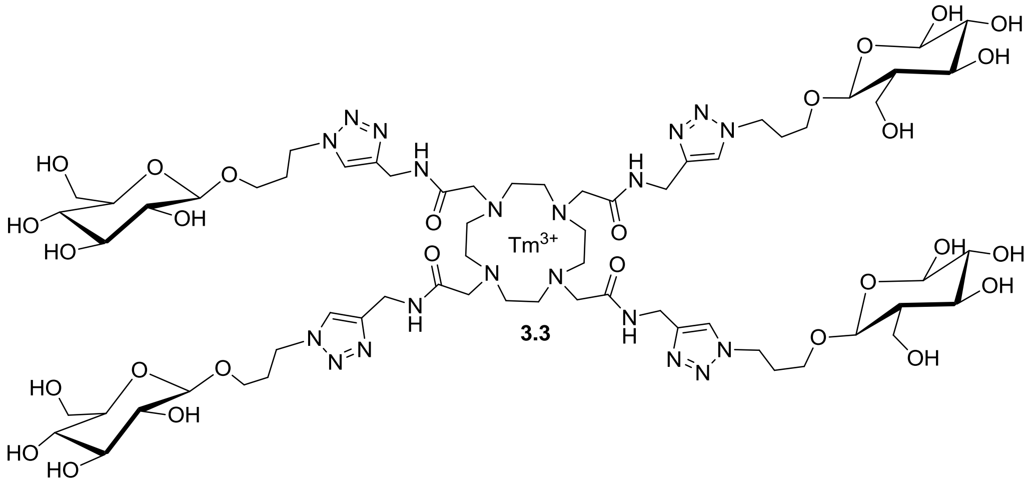

3.3

S3.28. HPLC Trace of **3.2**

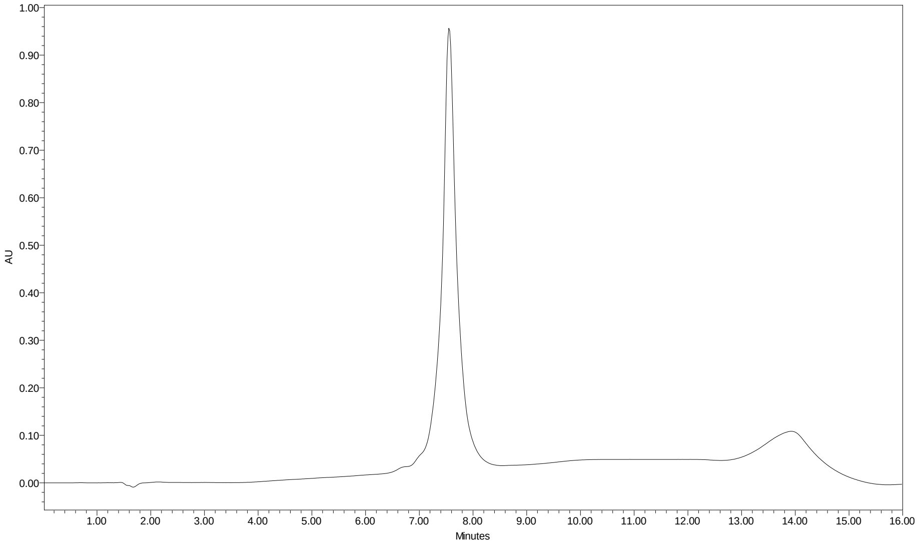

S3.29. HPLC Trace of **3.3**

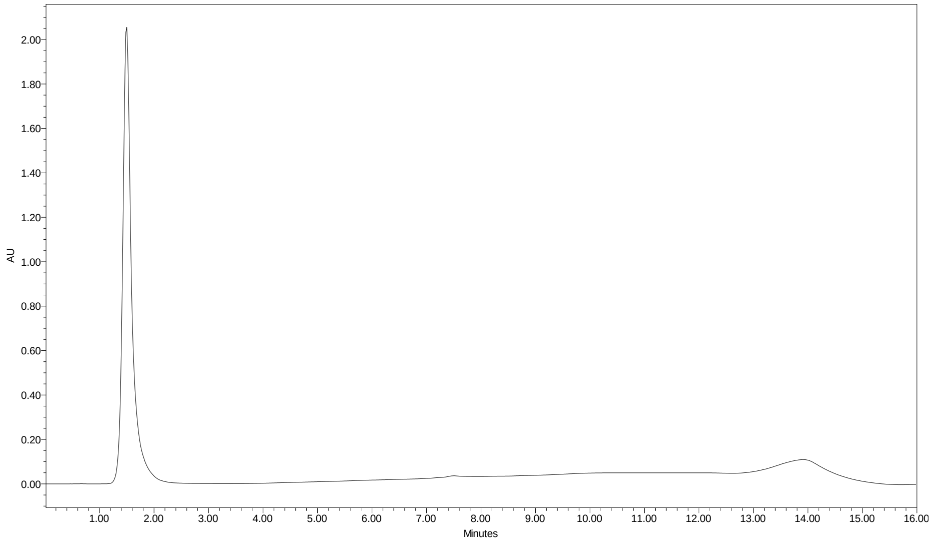

S3.30. Relaxivity comparison of Gd series at 20 MHz

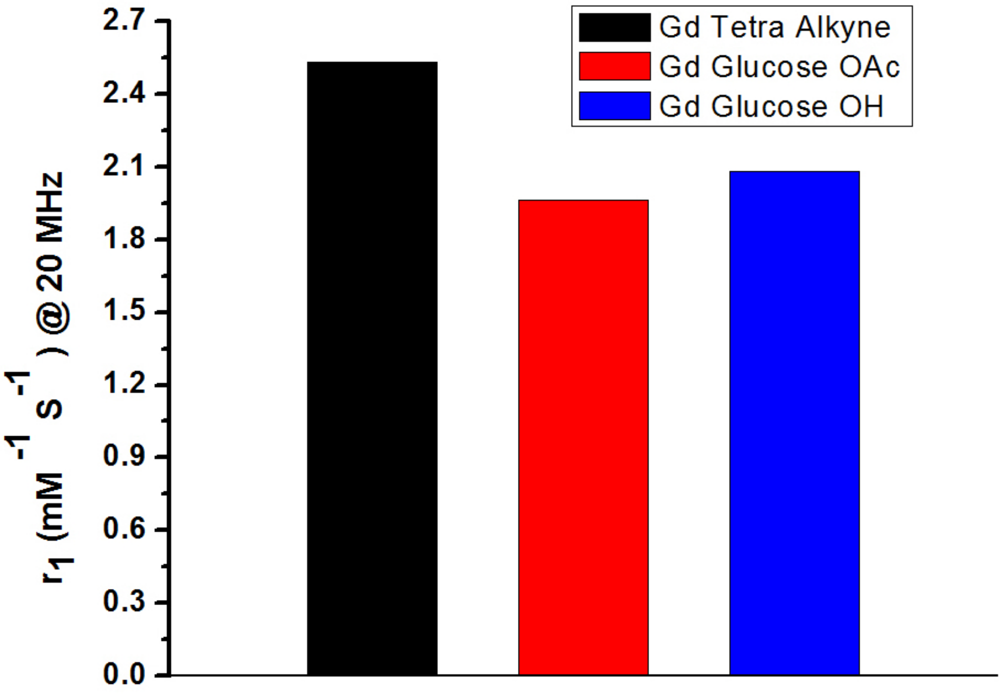

S3.31. Relaxivity comparison of Gd series at 400 MHz

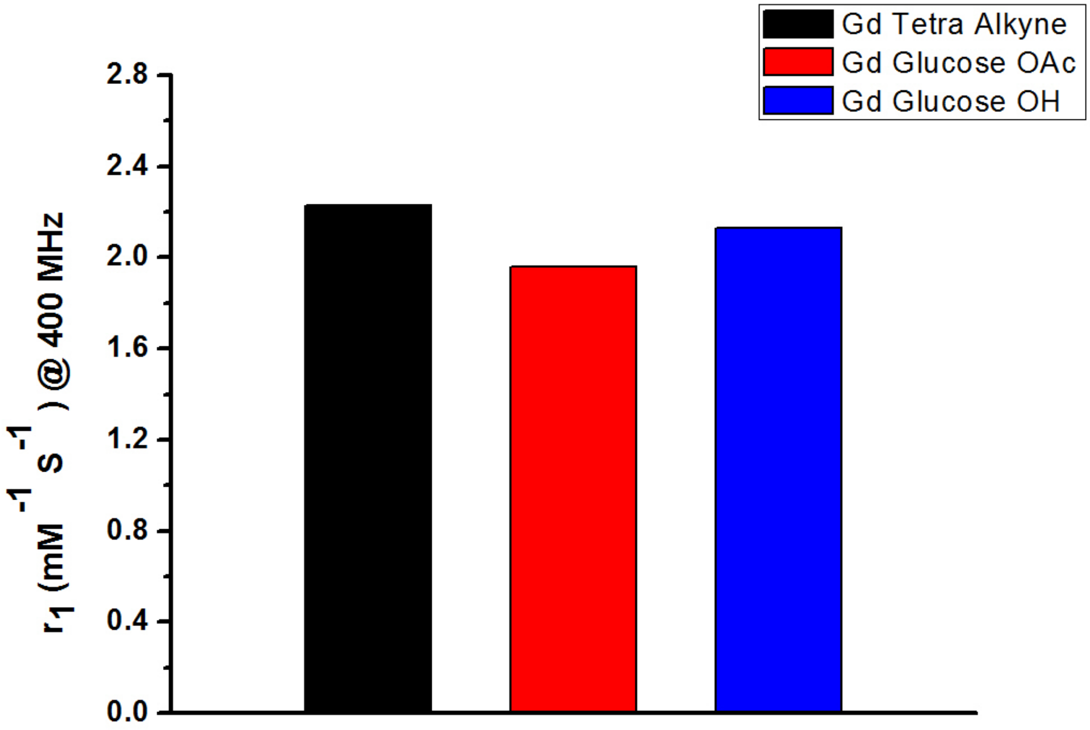

S3.32. CEST comparison of Eu series (Water)

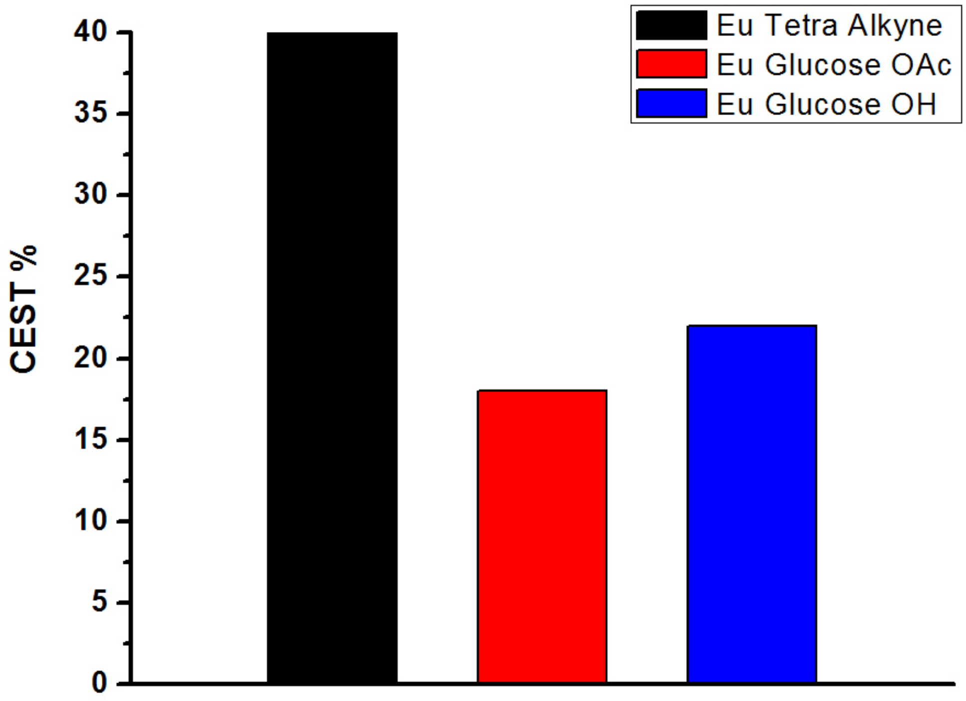

S3.32. CEST comparison of Tm series (Amide)

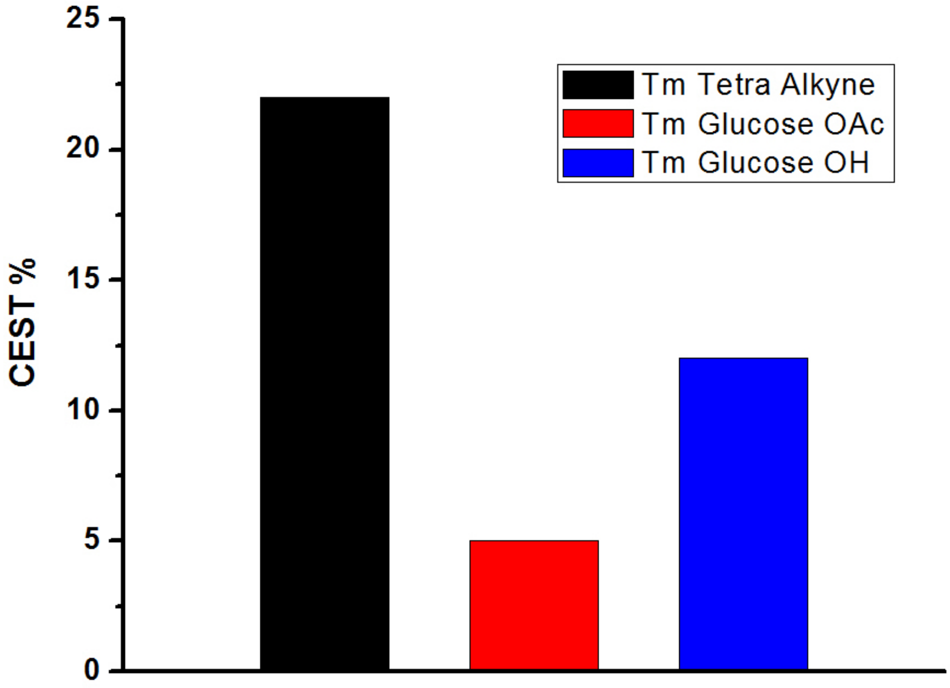

3.5 References

1. A. X. Li, R. H. E. Hudson, J. W. Barrett, C. K. Jones, S. H. Pasternak and R. Bartha, *Magn. Reson. Med.*, 2008, **60**, 1197-1206.

2. C. Geraldes and S. Laurent, *Contrast Media Mol. Imaging*, 2009, **4**, 1-23.

3. S. Aime, S. G. Crich, E. Gianolio, G. B. Giovenzana, L. Tei and E. Terreno, *Coord. Chem. Rev.*, 2006, **250**, 1562-1579.

4. M. Woods, E. W. C. Donald and A. D. Sherry, *Chem. Soc. Rev.*, 2006, **35**, 500-511.

5. K. M. Ward, A. H. Aletras and R. S. Balaban, *J. Magn. Reson.*, 2000, **143**, 79-87.

6. S. Aime, A. Barge, J. I. Bruce, M. Botta, J. A. K. Howard, J. M. Moloney, D. Parker, A. S. de Sousa and M. Woods, *J. Am. Chem. Soc.*, 1999, **121**, 5762-5771.

7. P. Caravan, J. J. Ellison, T. J. McMurry and R. B. Lauffer, *Chem. Rev.*, 1999, **99**, 2293-2352.

8. K. J. Miller, A. A. Saherwala, B. C. Webber, Y. Wu, A. D. Sherry and M. Woods, *Inorg. Chem.*, 2010, **49**, 8662-8664.

9. M. M. Ali, G. S. Liu, T. Shah, C. A. Flask and M. D. Pagel, *Acc. Chem. Res.*, 2009, **42**, 915-924.

10. S. Aime, A. Barge, M. Botta, A. S. De Sousa and D. Parker, *Angew. Chem. Int. Ed.*, 1998, **37**, 2673-2675.

11. D. A. Fulton, E. M. Elemento, S. Aime, L. Chaabane, M. Botta and D. Parker, *Chem. Commun.*, 2006, 1064-1066.

12. M. Gottschaldt and U. S. Schubert, *Chem. Eur. J.*, 2009, **15**, 1548-1557.

13. J. P. Andre, C. Geraldes, J. A. Martins, A. E. Merbach, M. I. M. Prata, A. C. Santos, J. J. P. de Lima and E. Toth, *Chem. Eur. J.*, 2004, **10**, 5804-5816.

14. C. F. G. C. Geraldes, K. Djanashvili and J. A. Peters, *Future Med. Chem.*, 2010, **2**, 409-425.

15. R. A. Gatenby and R. J. Gillies, *Nat. Rev. Cancer*, 2004, **4**, 891-899.

16. R. J. Gillies, N. Raghunand, G. S. Karczmar and Z. M. Bhujwalla, *J. Magn. Reson. Imaging*, 2002, **16**, 430-450.

17. M. Woods, A. Pasha, P. Zhao, G. Tircso, S. Chowdhury, G. Kiefer, D. E. Woessner and A. D. Sherry, *Dalton Trans.*, 2011, **40**, 6759-6764.

18. J. Martinelli, B. Balali-Mood, R. Panizzo, M. F. Lythgoe, A. J. P. White, P. Ferretti, J. H. G. Steinke and R. Vilar, *Dalton Trans.*, 2010, **39**, 10056-10067.

19. M. Milne, M. Suchy, A. X. Li, R. Bartha and R. H. E. Hudson, in *CSC*, Toronto, Ontario, Canada., 2010.

20. P. Antoni, M. Malkoch, G. Vamvounis, D. Nystrom, A. Nystrom, M. Lindgren and A. Hult, *J. Mater. Chem.*, 2008, **18**, 2545-2554.

21. M. P. M. Marques, C. Geraldes, A. D. Sherry, A. E. Merbach, H. Powell, D. Pubanz, S. Aime and M. Botta, *J. Alloy. Compd.*, 1995, **225**, 303-307.

22. H. C. Kolb, M. G. Finn and K. B. Sharpless, *Angew. Chem. Int. Ed.*, 2001, **40**, 2004-2021.

23. J. A. F. Joosten, V. Loimaranta, C. C. M. Appeldoorn, S. Haataja, F. A. El Maate, R. M. J. Liskamp, J. Finne and R. J. Pieters, *J. Med. Chem.*, 2004, **47**, 6499-6508.

24. S. Aime, M. Fasano and E. Terreno, *Chem. Soc. Rev.*, 1998, **27**, 19-29.

25. C. A. Chang, L. C. Francesconi, M. F. Malley, K. Kumar, J. Z. Gougoutas, M. F. Tweedle, D. W. Lee and L. J. Wilson, *Inorg. Chem.*, 1993, **32**, 3501-3508.

26. A. Luciani, J. C. Olivier, O. Clement, N. Siauve, P. Y. Brillet, B. Bessoud, F. Gazeau, I. F. Uchegbu, E. Kahn, G. Frija and C. A. Cuenod, *Radiol.*, 2004, **231**, 135-142.

Chapter 4: Development of TSAP Based ParaCEST Agents

"DOTAM-based ParaCEST Agent Favoring TSAP Geometry for Enhanced Amide Proton Chemical Shift Dispersion and Temperature Sensitivity". Todd K. Stevens*, Mark Milne*, Adam A. H. Elmehriki, Mojmir Suchý, Robert Bartha, Robert H. E. Hudson. *Contrast Media Mol. Imaging*. **2012**, 3, 289–292.

4.1 Introduction

The use of paramagnetic chemical exchange saturation transfer (paraCEST) contrast agents have shown promise in sensing environmental conditions within *in vivo* systems.[1, 2] However, a challenge in using paraCEST methods in–vivo, is the loss in sensitivity due to magnetization transfer (MT) from endogenous macromolecules following the application of radiofrequency (rf) saturation pulse.[3] The MT effect is a competing mechanism that saturates bulk water spins lowering the contrast efficiency of paraCEST agents within the MT frequency range. Consequently, a paraCEST agent with an exchangeable proton pool exhibiting a chemical shift beyond the MT bandwidth would be highly desirable.

Contrast agents incorporating the cyclen macrocycle such as DOTA, DOTAM, and their derivatives exist in either a square antiprismatic (SAP) geometry or a twisted SAP (TSAP) geometry, which describes the relative orientation between the planes of nitrogen and oxygen atoms in the chelate.[4, 5] To date, most paraCEST agents have been optimized for molecular water exchange, in which the slower exchange rates yielded by SAP geometry chelates are often advantageous for contrast generation.[4-7] For paraCEST chelates such as DOTAM, the amide group provides a second pool of magnetically distinct protons that are in exchange with the bulk water pool.[8-16] Unlike bound water based paraCEST, amide paraCEST signals can potentially be detected in both SAP and TSAP chelate isomers. As the amide exchange rate should be insensitive to the macrocycle geometry, the principal SAP/TSAP effect on the amide CEST signal is a change in the lanthanide–induced frequency shift arising from a variation of the amide proton to lanthanide distance or orientation or both.[17] The presence of two distinct Tm^{3+} DOTAM *t*–butyl isomers in solution is expected to give rise to two unique chemically shifted amide proton frequencies. If an isomer produces a signal at a chemical shift that is greater than the frequency associated with endogenous MT, an increase in *in vivo* detection sensitivity could be realized. Given the paucity of data on the paraCEST properties of DOTAM-based agents possessing predominently TSAP geometry, we have prepared and evaluated such an agent in order to investigate the effect of the geometry on the chemical shift dispersion of the exchangeable amide proton pool.

4.2 Results and Discussion

The paraCEST agent biased toward TSAP geometry was synthesized by incorporating the bulky *t*–butyl amide group in combination with the later lanthanide metal thulium (Tm^{3+}).[18] Full synthetic details of Tm^{3+} DOTAM *t*-butyl are listed in supplemental information . This compound has been previously synthesized in efforts to modulate the SAP/TSAP ratios for the purpose of optimizing exchange rates for bound–water paraCEST; however, amide proton paraCEST has not been reported.[19, 20] NMR signal integration of the highly shifted cyclen proton peaks of Tm^{3+} DOTAM *t*–butyl determined the population to be 66% TSAP isomer at 293 K, which is in agreement with previous work.[20] The proportion of TSAP isomer increased to 82% at 310 K, the temperature used for the NMR experimentation described herein.

As shown previously, when two similar but distinct chelators are present (i.e. stereoisomers), two unique signals can be observed, as is the case with the present agent.[21] To investigate the effect of the presence of two isomers, a z spectrum was measured which showed two signals; one signal which was anomolously highly shifted (-102 ppm). Thus, it was of interest to us to investigate the effect of increased chemical shift on CEST contrast in the presence of an MT background. The CEST contrast for Tm^{3+} DOTAM *t*–butyl was acquired and compared to that of a previously reported dipeptide agent, Tm^{3+} DOTAM Gly–Lys–OH, which exists in a SAP geometry and generates a CEST signal at –47 ppm relative to bulk water.[22] In addition to characterizing the CEST frequency response of the Tm^{3+} DOTAM *t*–butyl chelate, the temperature sensitivity of these signals was evaluated over a biologically relevant range.

Aqueous solutions (10 mM) of Tm^{3+} DOTAM *t*–butyl (**4.1**) and Tm^{3+} DOTAM Gly–Lys–OH (**4.2**) (Figure 4.1) were produced in 10% phosphate buffered saline to control pH and 90% D_2O to mitigate radiation damping effects as well as increase CEST signal amplitudes via slower T_1 relaxation, thus optimizing the evaluation of frequency information in the CEST spectra. To mimic the MT background signal found in *in vivo* z spectra, both agents were also evaluated in the presence of heat–prepared 6% (w/w) agar gel using the same solvent as above. All samples were tested at 310 K.

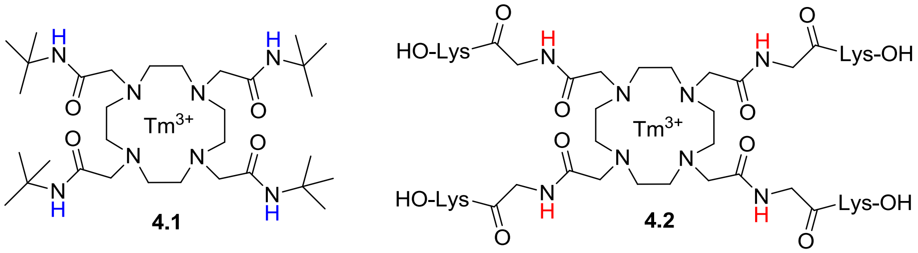

Figure 4.1. Chemical structure of Tm^{3+} DOTAM *t*–butyl (**4.1**) and Tm^{3+} DOTAM Gly–Lys-OH (**4.2**).

First, z spectra were acquired for both the Tm^{3+} DOTAM *t*–butyl and Tm^{3+} DOTAM Gly–Lys-OH agents without (Figure 4.2a) and with (Figure 4.2b) agar gel using 2 s continous wave (cw) saturation. The saturation frequency offset was varied between –150 ppm to 150 ppm (relative to the bulk water signal) in a random order to allow for retrospective correction of small baseline drifts without affecting measured CEST or MT effects. The z spectra were normalized against true baseline data that were acquired with saturation offsets of ±1000 ppm to eliminate any possible inference from CEST, MT and direct saturation effects. A 10 s repetition time delay was used to prevent T_1 weighting between successive acquisitions (T_1 time constants were determined to be between 1.1 s and 1.2 s using a saturation recovery sequence). The CEST contrast represented by the asymmetry in the longitudinal magnetization M_z about the bulk water frequency (calculated as $M_{z,off} - M_{z,on}$ where “off–resonance” describes positive saturation frequency offsets and “on–resonance” describes negative offsets) was also calculated for each z spectra (Figure 4.2, *insets*). To investigate the amide proton exchange dynamics underlying observed differences in CEST contrast due to the presence of an MT background, the z spectra for the two Tm^{3+} DOTAM *t*–butyl samples were modeled with McConnell–Bloch equations.[23] From these 3–pool (no agar) and 4–pool (agar) models,[3] effective exchange rates for the more highly shifted amide proton pool (–102 ppm) were determined and compared.

Secondly, the temperature sensitivity of the Tm^{3+} DOTAM *t*–butyl amide CEST signals was investigated. Windowed z spectra were acquired at 0.2 ppm intervals around the amide proton frequency of the two isomers (–102 ppm and –68 ppm) to determine the chemical shift changes of these CEST signals over the physiologically relevant temperature range of 308 K to 315 K (Figure 4.3a). The precise chemical shifts were determined with bi–Gaussian fitting of the windowed peaks, and the temperature responses of the peaks were fit to determine a linear rate of frequency change with temperature (Figure 4.3b).

In the absence of macromolecule MT signal loss, the difference in z spectrum water linewidths for the Tm^{3+} DOTAM *t*–butyl and Tm^{3+} DOTAM Gly–Lys–OH samples was evident (Figure 4.2a). This difference is explained by the higher molecular water exchange rate associated with the TSAP geometry of the Tm^{3+} DOTAM *t*–butyl agent (approximately 67% TSAP), which minimizes the intermediate exchange regime line broadening (due to interactions with Tm^{3+}) seen in the slower DOTAM Gly–Lys–OH agent. By matching the two Tm^{3+} DOTAM *t*–butyl CEST signal amplitudes to the isomer ratio determined by integration of the cyclen proton signals,[20] the more disperse signal at –102 ppm most likely arises from the TSAP isomer, however no direct evidence has been acquired to link the exchangeable proton to TSAP geometry. In the Tm^{3+} DOTAM *t*–butyl samples with and without agar (Figure 4.2, *blue*), the ability to identify both the assumed TSAP signal at –102 ppm and the assumed SAP signal at –68 ppm demonstrates that the interconversion between these two isomers is slow relative to the NMR timescale; specifically, the interconversion rate must be much smaller than the 20 kHz chemical shift difference between these signals.

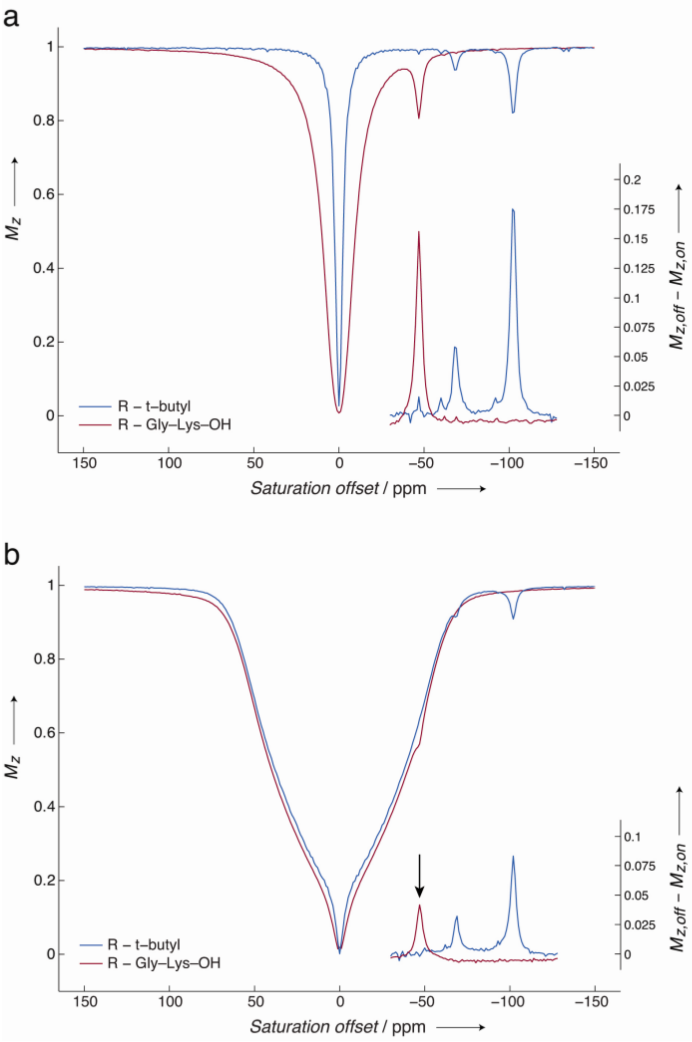

Figure 4.2. Z spectra for 10 mM aqueous solutions of Tm^{3+} DOTAM *t*–butyl (**4.1**, blue line) and Tm^{3+} Gly–Lys–OH (**4.2**, red line), both without (a) and with (b) 6% w/w agar gel (2s, 20 μT saturation, 310 K, acquired at 14 T). Shown are amide CEST signals at –102 ppm and –68 ppm assigned to the TSAP and SAP conformations of agent **4.2**, respectively. The signal at –47 ppm is due to agent **4.1** (in a SAP conformation). Asymmetry differences (i.e. CEST contrast) for these amide proton signals are shown inset. The arrow in (b) highlights a decrease in contrast from Tm^{3+} DOTAM–Gly–Lys–OH (**4.2**) relative to that of the Tm^{3+} DOTAM *t*–butyl (**4.1**) in the presence of the MT background.

For the samples without agar (Figure 4.2a), the CEST contrast produced at –102 ppm by the Tm^{3+} DOTAM *t*–butyl agent was similar to that produced at –47 ppm by the Tm^{3+} DOTAM Gly–Lys–OH agent (17.5% and 15.6%, respectively), while 5.8% contrast was observed at the –68 ppm offset for Tm^{3+} DOTAM *t*–butyl. In the presence of MT effects from agar (Figure 4.2b, *blue*), the CEST contrast associated with the Tm^{3+} DOTAM *t*–butyl sample was approximately half: 8.3% at –102 ppm and 3.2% at –68 ppm. McConnell–Bloch modeling of the z spectra *(not shown)* suggested that this loss in contrast, despite a lack of overlap with the MT background, was likely due to decreases in the effective exchange rates between the amide proton and bulk water proton pools. Specifically, the effective exchange rate for the highly shifted amide proton pool, which represents information about both the proton exchange rate at the amide site as well as the bulk diffusion rate of protons in the sample, was determined to be 0.9 kHz without agar, and 0.5 kHz with agar present. Possible mechanisms for this rate reduction may have been hydrogen bonding interaction of the paraCEST amide protons with the agar matrix or a reduction in water diffusion due to long–range restrictions imposed by the agar matrix over the 2 s saturation time. Reduced diffusion would result in slower refreshment of unsaturated protons in the water hydration layer accessible to the amide site, and thus lower CEST contrast. For the Tm^{3+} DOTAM Gly–Lys–OH agent, the CEST contrast was reduced by a factor of four down to 4.2% when agar was introduced (Figure 4.2b, *red*). Although the exchange dynamics are likely slowed by the agar matrix similar to those of the Tm^{3+} DOTAM *t*–butyl agent, the more pertinent source of contrast loss for this agent is likely the competing MT effect, which produces enough saturation at

–47 ppm to limit the efficiency of the CEST mechanism (i.e. the agent is less likely to be acting on previously unsaturated protons).

Evaluation of the temperature dependence of the amide proton chemical shifts showed a distinct difference between the assumed SAP and TSAP geometries. While both SAP and TSAP amide proton shifts varied linearly with temperature (Figure 4.3b), those associated with the highly shifted protons (-100 ppm, 0.57 ppm/K) were over three times more sensitive than the inside amides shift (-65 ppm, 0.16 ppm/K). Since these measures are based on frequency, they reflect the ability to monitor temperature in an agent concentration–independent manner. Moreover, the amplitude of the observed CEST contrast also increased with increasing temperature, from 16.3% to 24.9% for the TSAP amide proton signal and from 5.0% to 8.9% for the SAP signal over the range of 308 K to 315 K. These increases in contrast at elevated temperatures are likely due to faster amide proton exchange[24] combined with more rapid turnover of the water hydration layer.

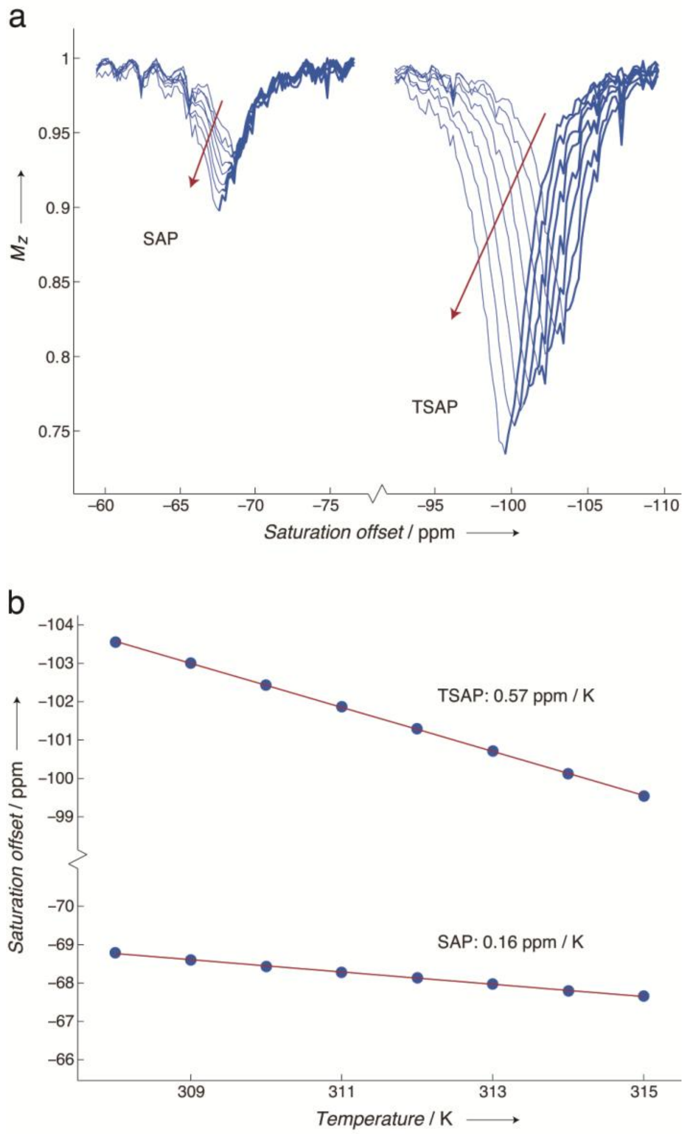

Figure 4.3. Plots showing the CEST chemical shift variation with temperature for the amide pool of Tm^{3+} DOTAM t–butyl (**4.1**) in both SAP and TSAP conformations. Experiments were performed at 14 T using a 10 mM aqueous solution (90% D_2O) of the agent and 2 s, 20 uT rf saturation. (a) Windowed z spectra showing the post–saturation Mz CEST signals at –68 ppm and –102 ppm, with the direction of variation due to increasing temperature shown in red. (b) Chemical shift values and best fits demonstrating the linear response of the SAP and TSAP shifts with temperature.

4.3 Conclusion

In conclusion, it has been shown that DOTAM–based paraCEST agents with a TSAP geometry may produce increased chemical shift dispersion of the exchangeable amide protons. The more highly shifted signals possess greater temperature sensitivity than less shifted signals. To our knowledge, these results represent the largest frequency offset of a paraCEST amide proton signal at physiological temperatures, which may facilitate paraCEST detection in the presence of MT background signals such as those characteristic of in-vivo systems.

A secondary paper to this research in which I was second author was published in Can. J. Chem in 2012.[18] In this paper we discuss the synthesis of not only the agent in this paper, Tm^{3+} t-butyl, but a series of 7 chelators that incorportated alkyl groups other then t-butyl. This series was then metallated with Dy^{3+}, Tb^{3+} or Tm^{3+} giving a total of 21 new contrast agents. After their synthesis was completed their amide ParaCEST properties were studied. Further discussion of this paper will not be found in this thesis, but I believe that the recognition of Adam Elmehriki to the synthesis of these agents is important.

4.4 Supplemental information

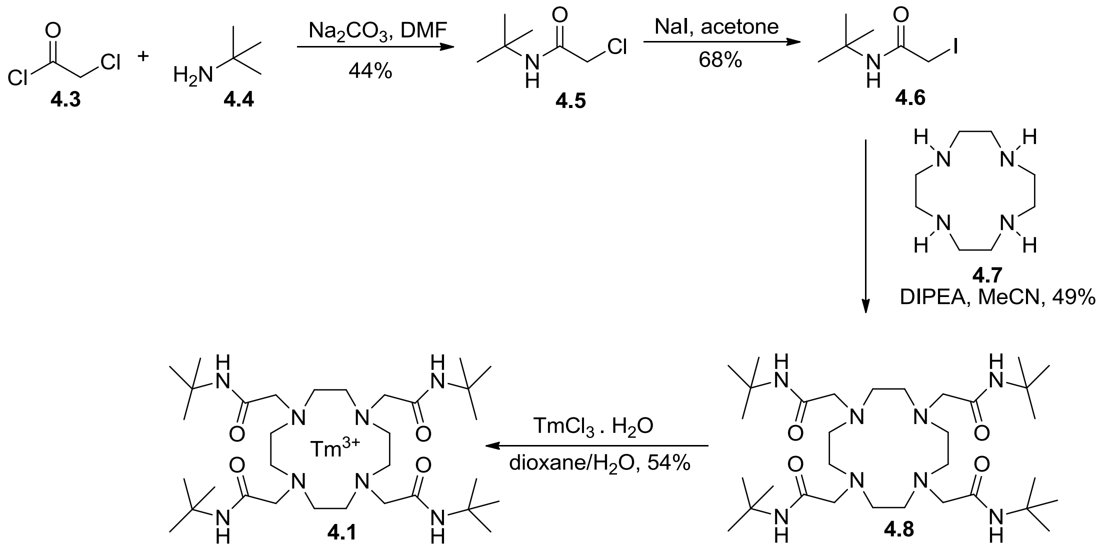

Scheme S4.1: Synthesis of Tm^{3+} DOTAM *t*-butyl

S4.2 Synthesis of agents used.

Preparation of *N*-*t*-butyl chloroacetamide (4.5): Chloroacetyl chloride (**4.3**, 1.03 ml, 13 mmol) was added dropwise (within 1 minute) to a suspension of *t*-butylamine (**4.4**, 1.05 ml, 10 mmol) and Na_2CO_3 (2.12g, 20 mmol) in dry DMF (2 ml) cooled to 0 °C. The cooling bath was removed and the mixture was stirred for 24 h at room temperature (rt). Saturated solution of $NaHCO_3$ (50 ml) was added to the mixture followed by the extraction with EtOAc (2 × 40 ml). The combined organic extract was washed with brine (2 × 40 ml), was dried and was concentrated to dryness. The residue was crystallized from CH_2Cl_2/hexanes to give *N*-*t*-butyl chloroacetamide (**4.5**) as colorless crystals (658 mg, 44%). ^1H NMR ($CDCl_3$) δ 6.38 (s, D_2O exch., 1H), 3.93 (s, 2H), 1.37 (s, 9H); ^{13}C NMR ($CDCl_3$) δ 164.8, 51.7, 42.9, 28.4. HRMS (EI) m/z; found 140.0608 $[M]^+$ (calcd.

149.0607 for $C_6H_{12}ClNO$); LRMS (EI) m/z (rel. abundance): 149 [M^+] (50), 134 (100), 84 (48). Spectral data were in agreement with those previously reported.

Preparation of *N*-*t*-butyl iodoacetamide (4.6): Sodium iodide (1.262 g, 8.42 mmol) was added to a solution of *N*-*t*-butyl chloroacetamide (**4.5**, 420 mg, 2.81 mmol) in acetone (18 ml). The mixture was stirred for 24 h at rt, was concentrated to ca. one third of its original volume, was diluted with EtOAc (30 ml) and was washed with 10% Na_2SO_3 solution (20 ml). An aqueous phase was then extracted with EtOAc (20 ml); combined organic extract was dried and was concentrated to dryness. The residue was crystallized from CH_2Cl_2/hexanes to give *N*-*t*-butyl iodoacetamide (**4.6**) as pale yellow crystals (464 mg, 68%). ^{1}H NMR ($CDCl_3$) δ 5.92 (s, D_2O exch., 1H), 3.62 (s, 2H), 1.35 (s, 9H); ^{13}C NMR ($CDCl_3$) δ 165.9, 51.9, 28.3, 1.2. HRMS (EI) m/z; found 240.9966 $[M]^+$ (calcd. 240.9964 for $C_6H_{12}INO$); LRMS (EI) m/z (rel. abundance): 240 [M^+] (95), 226 (100), 186 (40), 84 (52). Spectral data were in agreement with those previously reported.[1]

Preparation of 1,4,7,10-tetraazacyclododecane-1,4,7,10-tetra(*N*-*t*-butyl)acetamide (**4.8**): DIPEA (280 μl, 1.6 mmol) was added to a solution of cyclen (**4.7**, 69 mg, 0.4 mmol) in MeCN (4 ml). The mixture was stirred at 45 °C for 10 min followed by the addition of *N*-*t*-butyl iodoacetamide (**4.6**, 386 mg, 1.6 mmol). The mixture was stirred for 24 h at 45 ^{o}C. It was the cooled to rt, was diluted with H_2O (20 ml) and was extracted with EtOAc (3 × 20 ml). The combined organic extract was dried and was concentrated to dryness. The residue was crystallized from MeCN to give DOTAM *t*-butyl (**4.8**) as a colorless solid (135 mg, 49%). ^{1}H NMR ($CDCl_3$) δ 6.57 (m, D_2O exch., 4H), 3.10-1.90

(broad m, 24H) 1.36 (s, 36H); ^{13}C NMR ($CDCl_3$) δ 170.4, 58.4, 51.7, 28.9, 28.6. ^{1}H NMR (CD_3OD) δ 3.05 (m, 8H), 2.79 (m, 16H), 1.36 (s, 36H); ^{13}C NMR (CD_3OD) δ 173.0, 60.6.4, 54.5, 52.1, 29.3. HRMS (ESI) m/z; found 625.5115 $[M + H]^+$ (calcd. 625.5129 for $C_{32}H_{65}N_8O_4$). Spectral data in CD_3OD were in agreement with those previously reported.

Preparation of Tm^{3+}-1,4,7,10-tetraazacyclododecane-1,4,7,10-tetra(*N*-*t*-butyl)acetamide chloride (4.1): $TmCl_3 \cdot H_2O$ (54 mg, 0.134 mmol) was dissolved in H_2O (500 μl), the resulting solution was added to a solution of DOTAM *t*-butyl (**4.8**, 80 mg, 0.116 mmol) in dioxane (2 ml). The mixture was stirred at 70 °C for 24 h. The mixture was concentrated to dryness, followed by FCC on 15 g Al_2O_3, eluted with $CH_2Cl_2/MeOH/NH_4OH$ (60:39:1). The fractions containing the desired compound (I_2 vapour visualization) were concentrated to dryness, the residue was dissolved in H_2O; pH was adjusted to 7 with (1 M HCl). The solution was transferred into a dialysis bag and was dialysed (against H_2O) for 120 h. The concentration of the aqueous solution afforded the Tm^{3+} DOTAM *t*-butyl (**7**) as a colorless solid (53.8 mg, 54%). HRMS (ESI) m/z; found 791.4205 $[M - 2H]^+$ (calcd. 791.4236 for $C_{32}H_{62}N_8O_4Tm$).

S4.3. CEST Discussion

Although 90% D_2O sample solutions were used, the CEST results may be extrapolated to 100% H_2O systems since the concentration ratio of protons to agent available for proton binding, upon which CEST contrast is highly dependent, is unchanged in the present system (i.e. the signal of approximately 11 M of bulk protons is being modulated by one–

tenth of the agent with the balance 90% being engaged with deuterium exchange at any given moment).

4.5 References

1. J. Zhou and P. C. M. van Zijl, *Prog. Nucl. Magn. Reson. Spectrosc.*, 2006, **48**, 109-136.

2. J. Pacheco-Torres, D. Calle, B. Lizarbe, V. Negri, C. Ubide, R. Fayos, P. L. Larrubia, P. Ballesteros and S. Cerdan, *Curr. Top. Med. Chem.*, 2011, **11**, 115-130.

3. A. X. Li, R. H. E. Hudson, J. W. Barrett, C. K. Jones, S. H. Pasternak and R. Bartha, *Magn. Reson. Med.*, 2008, **60**, 1197-1206.

4. S. Aime, A. Barge, J. I. Bruce, M. Botta, J. A. K. Howard, J. M. Moloney, D. Parker, A. S. de Sousa and M. Woods, *J. Am. Chem. Soc.*, 1999, **121**, 5762-5771.

5. S. Aime, A. Barge, M. Botta, A. S. De Sousa and D. Parker, *Angew. Chem. Int. Ed.*, 1998, **37**, 2673-2675.

6. K. J. Miller, A. A. Saherwala, B. C. Webber, Y. Wu, A. D. Sherry and M. Woods, *Inorg. Chem.*, 2010, **49**, 8662-8664.

7. S. R. Zhang, M. Merritt, D. E. Woessner, R. E. Lenkinski and A. D. Sherry, *Acc. Chem. Res.*, 2003, **36**, 783-790.

8. B. Yoo and M. D. Pagel, *Bioconjugate Chem.*, 2007, **18**, 903-911.

9. B. Yoo and M. D. Pagel, *J. Am. Chem. Soc.*, 2006, **128**, 14032-14033.

10. Y. Li, V. R. Sheth, G. Liu and M. D. Pagel, *Contrast Media Mol. Imaging*, 2011, **6**, 219-228.

11. M. Suchy, A. X. Li, R. Bartha and R. H. E. Hudson, *Bioorg. Med. Chem.*, 2008, **16**, 6156-6166.

12. M. Milne, K. Chicas, A. Li, R. Bartha and R. H. E. Hudson, *Org. Biomol. Chem.*, 2012.

13. M. Woods, P. Caravan, C. F. G. C. Geraldes, M. T. Greenfield, G. E. Kiefer, M. Lin, K. McMillan, M. I. M. Prata, A. C. Santos, X. Sun, J. Wang, S. Zhang, P. Zhao and A. D. Sherry, *Invest. Radiol.*, 2008, **43**, 861-870.

14. J. A. Pikkemaat, R. T. Wegh, R. Lamerichs, R. A. van de Molengraaf, S. Langereis, D. Burdinski, A. Y. F. Raymond, H. M. Janssen, B. F. M. de Waal, N. P. Willard, E. W. Meijer and H. Grull, *Contrast Media Mol. Imaging*, 2007, **2**, 229-239.

15. T. Chauvin, P. Durand, M. Bernier, H. Meudal, B. T. Doan, F. Noury, B. Badet, J. C. Beloeil and E. Toth, *Angew. Chem. Int. Ed.*, 2008, **47**, 4370-4372.

16. M. Milne, K. Chicas, A. Li, R. Bartha and R. H. E. Hudson, *Org. Biomol. Chem.*, 2012, **10**, 287-292.

17. S. Viswanathan, Z. Kovacs, K. N. Green, S. J. Ratnakar and A. D. Sherry, *Chem. Rev.*, 2010, **110**, 2960-3018.

18. A. A. H. Elmehriki, M. Milne, M. Suchý, R. Bartha and R. H. E. Hudson, *Can. J. Chem.*, 2012, **91**, 211-219.

19. T. Mani, G. Tircso, O. Togao, P. Zhao, T. C. Soesbe, M. Takahashi and A. D. Sherry, *Contrast Media Mol. Imaging*, 2009, **4**, 183-191.

20. T. Mani, G. Tircsó, P. Zhao, A. D. Sherry and M. Woods, *Inorg. Chem.*, 2009, **48**, 10338-10345.

21. D. Delli Castelli, E. Terreno and S. Aime, *Angew. Chem. Int. Ed.*, 2011, **50**, 1798-1800.

22. F. Wojciechowski, M. Suchy, A. X. Li, H. A. Azab, R. Bartha and R. H. E. Hudson, *Bioconjugate Chem.*, 2007, **18**, 1625-1636.

23. H. M. McConnell, *J. Chem. Phys.*, 1958, **28**, 430-431.

24. S. J. Dorazio, P. B. Tsitovich, K. E. Siters, J. A. Spernyak and J. R. Morrow, *J. Am. Chem. Soc.*, 2011, **133**, 14154-14156.

Chapter 5: Synthesis and Characterization of Aniline Containing ParaCEST Agents

"MRI ParaCEST agents that improve amide based pH measurements by eliminating inner sphere water T_2 exchange" Mark Milne, Melissa Lewis, Nevin McVicar, Mojmir Suchý, Robert Bartha, Robert H. E. Hudson. Submitted to *RSC Advances*, **2013**. Manuscript # RA-ART-07-2013-043537.

5.1 Introduction

Lanthanide based contrast agents (CAs) have been exploited for a number of years in magnetic resonance imaging (MRI) with coordinated gadolinium (Gd^{3+}) agents being used primarily in clinical environments.[1-5] Of these agents cyclen-based macrocyclic agents have been predominantly utilized as chelators because of the high stability of the resulting metal complexes under *in vivo* conditions.

It has been shown that cyclen-based agents can adopt two main geometries in solution. The first geometry is a square antiprismatic (SAP) while the second is a twisted square antiprismatic (TSAP).[6, 7] In solution, these geometries can be identified by the chemical shifts of the cyclen backbone with their interconversion measured by EXSY NMR experiments. In solid state, the two geometries can be distinguished by the angle between planes of N-Ln-N and O-Ln-O. When the angle between the aforementioned planes is

~40°, the structure is assigned to the SAP form, while angles closer to 30° are assigned the TSAP form. Of these two forms, it has been shown that the TSAP geometry possesses a faster exchange of bound water compared to the SAP form, which is thought to occur because of the more open structure TSAP displays.[8]

A promising technique for the *in vivo* measurement of tissue environmental conditions is the use of chemical exchange saturation transfer (CEST) or paraCEST, when a paramagnetic species is used as a hyperfine shift agent.[9-12] The CEST and paraCEST techniques require exchangeable protons to transfer saturation to the bulk system, creating an overall decrease in the bulk water magnetization.[13-15] The exchangeable proton sources are usually bound water as seen in Eu^{3+}-containing paraCEST agents or amides, amines or alcohols in either diamagnetic CEST agents or in lanthanide paraCEST complexes.[16-19] Because these agents use saturation transfer of exchangeable protons, their exchange properties can be related to the environment around the agent. For example, temperature and pH both modulate the proton exchange rate, particularly when using the highly shifted paraCEST agents that utilize Eu^{3+}, Dy^{3+}, Tb^{3+} or Tm^{3+} ions.[20, 21] While there have been numerous agents that are capable of reporting pH and temperature,[12, 22-26] some of these agents either do not function at physiological temperatures, or their optimal pH response is above 7, which is outside the physiological range of interest. These drawbacks demonstrate the need to design agents that are responsive to the physiological parameters of interest, most notably when the tissue is slightly acidic (pH 6-7) and at temperatures between 35 °C - 45 °C. To address these issues, we have synthesized a series of Dy^{3+} and Tm^{3+} DOTAM anilides that are *para*-

substituted, which should allow for the modulation of the amide's pKa based on the electron donating/withdrawing nature of the substituent. (Figure 5.1)

Although paraCEST agents are generally inefficient at inducing T_1 relaxation, such agents are capable of producing significant signal loss during *in vivo* imaging,[27, 28] due to increased transverse relaxation mediated by water exchange (T_2 exchange) from the inner sphere to the bulk water. The use of ultra-short echo-time (UTE) pulse sequences can reduce this effect, as observed with the SWIFT pulse sequence when used for paraCEST imaging.[29] However, such sequences are not standard on most clinical scanners limiting their applicability. Therefore, we hypothesized that a paraCEST agent designed to reduce T_2 signal losses would therefore be of benefit. To this end, we have developed agents that do not contain inner sphere water and therefore are inefficient modulators to the bulk water T_2 relaxation time constant. It must be noted that the amides that generate the CEST effect will still induce T_2 relaxation, but to a much less extent compared to bound water.

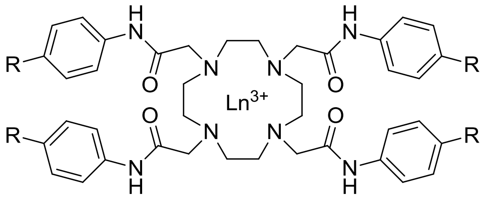

Ln = Tm	Ln = Dy
5.3a R = H	**5.4a** R = H
5.3b R = OMe	**5.4b** R = OMe
5.3c R = CH_3	**5.4c** R = CH_3
5.3d R = NO_2	**5.4d** R = NO_2
5.3e R = Cl	**5.4e** R = Cl

Figure 5.1. Lanthanide-based CAs synthesized.

Similar studies have been performed to monitor and adjust the water exchange rate on a series of Eu^{3+}-based ParaCEST agents.[30] While those results demonstrate the ability to modulate the bound water exchange rate based on the electron donating and withdrawing properties of the substituents, the effect of *para*-substitution on amide proton exchange of anilides was not studied. The use of Eu^{3+} as the lanthanide limits the ability to monitor how the amide is affected by the substitutions because the amides will exhibit a small shift compared to that induced by other lanthanides such as Dy^{3+}, Tm^{3+} or Tb^{3+}.

5.2 Results and Discussion

Synthesis of agents 5.3a-e , 5.4a-e

The electrophiles **5.1a-e** were synthesised by adding chloroacetyl chloride to the appropriate aniline in acetonitrile while cooled in an ice bath in the presence of potassium carbonate (Scheme 5.1). The reactions were stirred overnight at room temperature, then filtered and the crude products were recrystallized from methanol. The average yield of these reactions was good (~75%). Syntheses of the tetra-substituted cyclens were performed by mixing cyclen with 4.5 eq of the appropriate electrophiles in acetonitrile in the presence of potassium carbonate. It was necessary to heat the reaction at 55 °C - 80 °C over 1-3 days to ensure complete tetraalkylation. The progress of these reactions was monitored by UPLC MS. When the reaction was deemed complete, the mixtures were cooled and the product was allowed to precipitate along with the K_2CO_3. The mixture was then filtered and the precipitate was washed with cold water to remove the K_2CO_3.

At this point, attempts to recrystallize these compounds from methanol were unsuccessful due to their solubility properties. As such, the crude products were used without further purification. Crude yields ranged from of 94% to quantitative. The tetra-substituted cyclen products were then metallated using either $DyCl_3$ or $TmCl_3$ in a 1:1 water:dioxane mixture at 80 °C over 4 days. The metallated complexes were subjected to dialysis against water across a membrane with a 500 Dalton molecular weight cutoff to remove salts carried through from the previous step as well as unchleated lanthanide ion. The final products were isolated by lyophilization to give white powders, with exception of the *p*-nitro compound being a yellow powder. Identification of the metallated products was accomplished by high resolution mass spectrometry along with their UPLC trace which showed that all of the samples to be homogeneous tetra-substituted product.

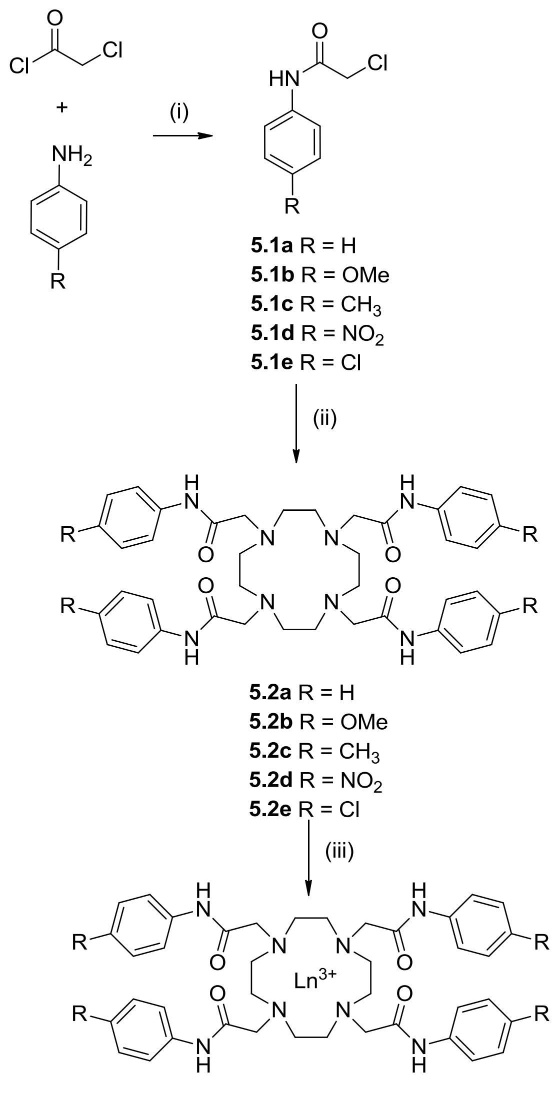

5.1a R = H
5.1b R = OMe
5.1c R = CH_3
5.1d R = NO_2
5.1e R = Cl

5.2a R = H
5.2b R = OMe
5.2c R = CH_3
5.2d R = NO_2
5.2e R = Cl

Ln = Tm^{3+}	Ln = Dy^{3+}
5.3a R = H	**5.4a** R = H
5.3b R = OMe	**5.4b** R = OMe
5.3c R = CH_3	**5.4c** R = CH_3
5.3d R = NO_2	**5.4d** R = NO_2
5.3e R = Cl	**5.4e** R = Cl

Scheme 5.1. Conditions for the synthesis of lanthanide-based CAs. i) Acetonitrile, K_2CO_3, Room temperature overnight. ii) Acetonitrile, K_2CO_3, 55 – 80 °C 2-3 days. iii) 1:1 H_2O:Dioxane, $DyCl_3$ or $TmCl_3$, 60 – 80 °C, 4 days.

CEST Evaluation

To study how the *para*-substitution affects the amide exchange rate of the Tm^{3+} and Dy^{3+} DOTAM anilides (**5.3a-e**, **5.4a-e**), we began with a pH study of the series at 20 mM. Quickly, we discovered many of the compounds were not sufficiently soluble to achieve this concentration, except for the unsubstituted anilides (**5.3a**, **5.4a**) and the *para*-OMe anilides (**5.3b**, **5.4b**). Unfortunately, the rest of the series (**5.3c-e**, **5.4c-e**) was not soluble enough to permit collection of reliable CEST spectra even at 5 mM. For the soluble **5.3a**,**b** and **5.4a**,**b** complexes, CEST experiments were performed using a 15 uT saturation pulse for 5 seconds at steps of 1 ppm from -100 ppm to 100 pm in the pH range of 6.5 to 9.0 for the unsubstituted anilides and the range of 5.1 to 8.0 for the *para*-OMe anilides. These ranges were chosen because of the observation that the maximum CEST effect was close to 8.0 for the unsubstituted anilides while the maximum CEST effect was between 7.0 - 7.5 for the *para*-OMe anilides. Of interest, we observed that the Tm^{3+} *para*-OMe (**5.3b**) compound displayed two CEST signals due to slow conformational equilibrium between the SAP and the TSAP geometries while the Dy^{3+} agent (**5.4b**) produced only one measurable signal. We have previously observed this feature during the study of a series of alkyl amides and designated the rarely seen higher shifted amide signal to a TSAP geometry while the signal less shifted is closer to the normally observed SAP geometry amide.[10, 31] This feature appears to be limited to Tm^{3+} agents and could be possibly due to the smaller lanthanide size compared to the Dy^{3+}, thus exacerbating steric interactions. The CEST spectra as a function of pH for **5.3a** and **5.3b** are shown in figure 5.2, with the CEST response for each of the 4 agents measured at pH 7.0 reported in table 5.1.

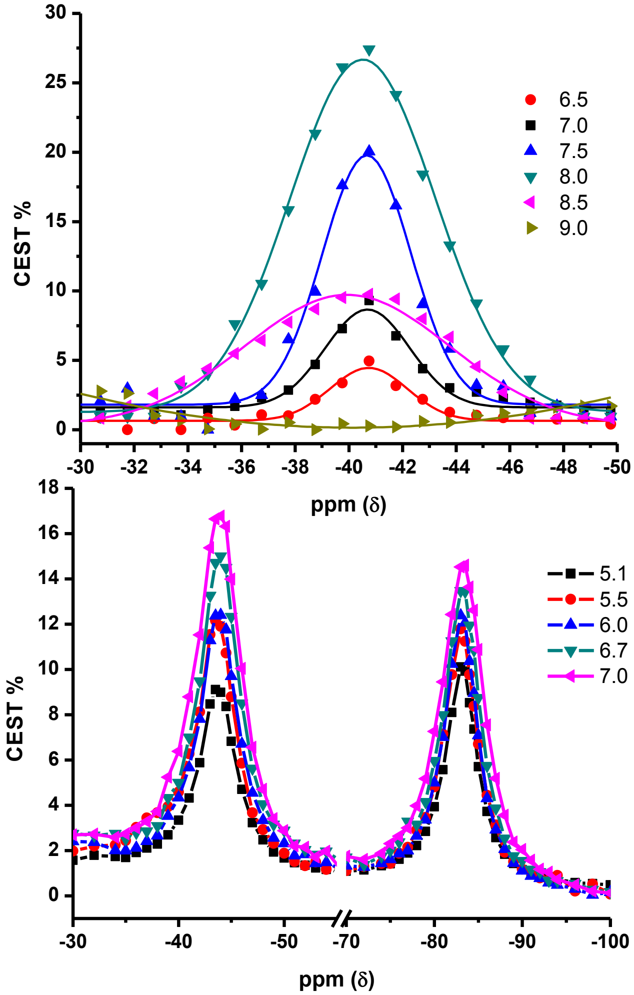

Figure 5.2. Top) CEST intensity of **5.3a** over the pH range of 6.5-9.0. Bottom) CEST intensity of **5.3b** over the pH range of 5.1-7.0. CEST spectra were acquired at 37 °C, 15 uT, 5 s.

Table 5.1. CEST % measured at pH 7, 37 °C, 20 mM with a saturation pulse of 15 uT for 5 s.

Agent	ppm (δ)	CEST %
5.3a	-41	20%
5.3b	-43	17%
	-83	15%
5.4a	70	6%
5.4b	74	3%

Figure 5.3 shows how the CEST effect of agents **5.3a** and **5.3b** changes over the pH ranges measured. The signal for the Tm^{3+}-*para*-OMe TSAP amide (-83 ppm) has a maximum signal at a slightly more acidic pH (7.0) compared to the SAP (-43 ppm) amide (pH 7.5). This effect has been observed previously for DOTAM agents where the signal possessing the greater chemical shift displays a maximum signal at lower pH compared to the signal with a smaller chemical shift.[32]

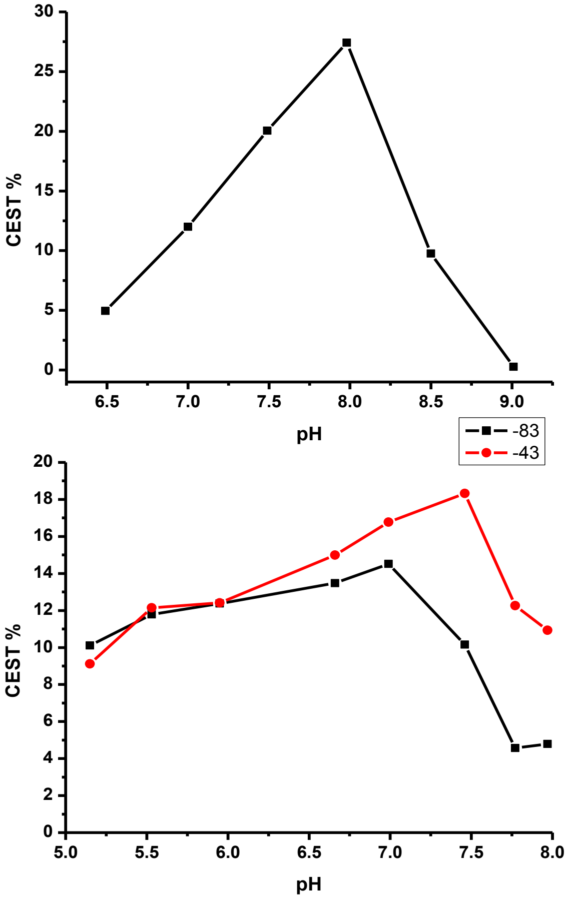

Figure 5.3. Maximum CEST response over a pH range. Top) **5.3a** shows a pH maximum at 8.0. Bottom) **5.3b** shows a pH maximum at 7.5 for the signal at -43 ppm and at 7.0 for the signal at -83 ppm.

An effective MRI CA for pH measurement must show a monotonic response to pH and must provide a concentration independent measurement. Both conditions are violated by these agents, although the first issue can be minimized by rationalizing that it would be rare to observe a pH above 8 *in vivo*. One method to overcome the concentration dependence is illustrated in Figure 4. Using a line width analysis, Tm^{3+} *p*-H (**5.3a**) can be used as a pH reporter with a monotonic response to pH over the range of 6.5 to 8.5 by following the procedure described in McVicar et. al.[12]

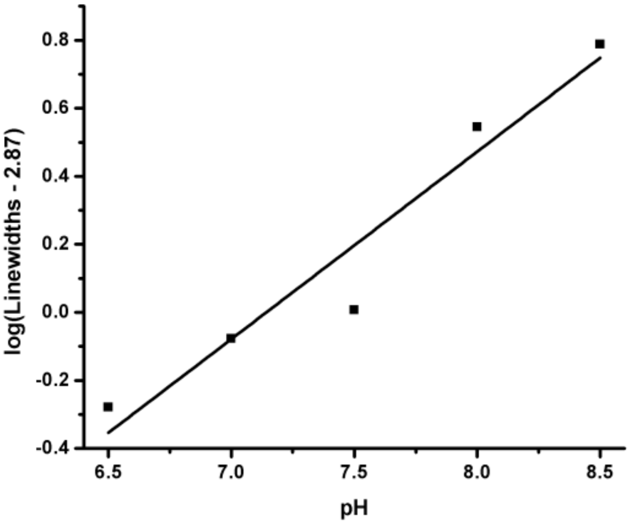

Figure 5.4. Line width analysis vs. pH of a 20 mM solution of Tm^{3+} p-H (**5.3a**) at 37°C, 15 µT, 5 s.

Another approach to overcome concentration dependence is to implemented a ratiometric approach as previously described, where two intramolecular signals are evaluated simultaneously.[22, 33] In particular, when two CEST responses arise from a single agent a ratio of the CEST effect eliminates the concentration dependence and enables the agent to be used as a physiological reporter. Since Tm^{3+}-*para*-OMe possesses two intramolecular amide signals that behave slightly different based on pH, we examined the possibility of using it as a ratiometric pH reporter. However, small pH responses and limited solubility of the Tm^{3+}-*para*-OMe agent frustrated attempts to demonstrate that this agent could be used as a concentration independent pH reporter (Data not shown). We are currently developing synthetic avenues to make this agent more pH responsive, as well as, increase its solubility to extend its functionality.

X-Ray Structures

Crystals suitable for X-ray diffraction were grown from slow evaporation of a concentrated solution of Tm^{3+}-*para*-OMe (**5.3b**) in water. Figure 5.5 illustrates a molecular representation of **5.3b** at 50% probability for the ellipsoids. It has been shown that macrocyclic CAs based on cyclen can exhibit a 9 coordination geometry around the lanthanide, where 8 of the coordination sites are filled with 4 nitrogens of the cyclen and 4 oxygens from the carbonyls pendant groups. The ninth coordination site is typically occupied by a water molecule that can be exchanged with the bulk water system and can be used to enhance relaxation or transfer saturation to the bulk system.

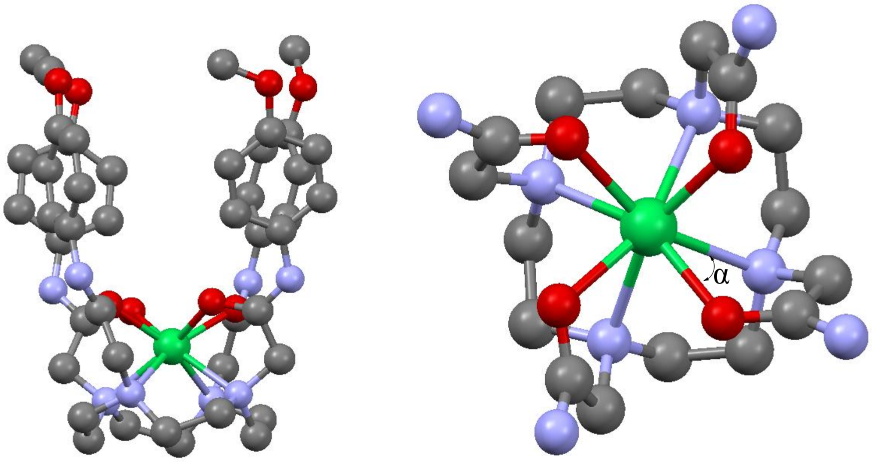

Figure 5.5. Molecular representation of the solid state structure of Tm^{3+}-*para*-OMe (**5.3b**) determined by single crystal X-ray studies. Hydrogens have been omitted for clarity. Left) Side on view of 3b showing eightfold coordination of the Tm^{3+} by the nitrogens of cyclen and the oxygens of the amide pendant groups. Right) Top down view of **5.3b**. The aniline rings are omitted for clarity. α indicates the angle created between the planes of N-Ln-N and O-Ln-O and is listed in Table 10 along with selected angles and bond lengths.

X-ray crystallography determined an 8 coordination system around the Tm^{3+} ion, with the 8 sites filled by either nitrogen atoms or oxygen atoms. The ninth potential coordination site was unoccupied - no bound water was found to directly coordinate the metal centre. This distinction has been observed before for lanthanide based CAs and has been denoted by ascribing a prime (') to the end of the geometry abbreviation.[7, 34-36] The α angle created between the planes of N-Ln-N and O-Ln-O is used in determining which geometry is present. Angles that near 40° are in a SAP geometry while angles that are closer to 30° are in the TSAP geometry.[37] In the case of the Tm^{3+} *para*-OMe, the geometry is a TSAP' system with an α angle of 27° and lacking inner sphere water, while the other geometry that is present is thought to be SAP' due to the bulkiness of the ligands. Selected angles and distances are listed in Table 5.2 and more detailed crystallographic parameters in Table 5.3.

Table 5.2. Summary of torsion angle α (°) and selected bond lengths (Å) for Tm^{3+} *para*-OMe (**5.3b**).

α angle	26.95
N_1-C-C-O_1	12.35
N_2-C-C-O_2	15.14
N_3-C-C-O_3	14.65
N_4-C-C-O_4	2.95
N_1-Ln	2.508
N_2-Ln	2.492
N_3-Ln	2.469
N_4-Ln	2.500
O_1-Ln	2.295
O_2-Ln	2.245
O_3-Ln	2.314
O_4-Ln	2.266

Table 5.3. Crystallographic Information for **5.3b**

Formula	$C_{44}H_{67}Cl_3N_8O_{13}Tm$
Formula Weight (*g/mol*)	1191.34
Crystal Dimensions (*mm*)	0.27 × 0.18 × 0.08
Crystal Colour and Habit	colourless prism
Crystal System	triclinic
Space Group	P -1
Temperature, K	110
a, Å	10.948(3)
b, Å	14.438(3)
c, Å	17.436(5)
a,°	77.345(10)
b,°	78.428(9)
g,°	85.152(10)
V, Å^3	2632.1(12)
Number of reflections to determine final unit cell	9059
Min and Max 2q for cell determination,	4.88, 64.1
°Z	2
F(000)	1222
r (*g/cm*)	1.503
l, Å, (MoKa)	0.71073
m, (*cm*$^{-1}$)	1.904

Relaxation Evaluation

With the ninth site of Tm^{3+} *para*-OMe (**5.3b**) vacant of inner sphere water, relaxation theory predicts that there should be sizable differences in the ability of this agent to induce bulk water relaxation compared to similar agents that contain bound water.[2, 38] While Tm^{3+} lanthanide agents are not thought to be efficient T_1 relaxation agents they have recently been shown to produce sizable T_2 relaxation effects (Table 5.4). Soesbe et al.[28] compared several Eu^{3+} based agents that contained inner sphere water with one that did not, and showed a darkening during *in vivo* paraCEST imaging of kidneys for those agents that had intermediate inner sphere water exchange rates. The darkening was linked to T_2 shortening. Another Eu^{3+} agent that lacked an inner sphere water (Eu^{3+} TETA) showed very little T_2 shortening and limited darkening. This shortening of the T_2 time constant lead to a reduction in the image signal intensity and reduced CEST contrast. Because Eu^{3+} based agents typically utilize the exchange of bound water from the inner sphere to generate the saturation used in paraCEST imaging such agents may also produce T_2 related signal loss when images are acquired with non-zero echo-time.

Development of agents that do not contain inner sphere water, such as Tm^{3+} *para*-OMe (**5.3b**) should have an advantage in -NH based paraCEST imaging as the major T_2 shortening mechanism from water exchange has been removed. It should be noted that the exchange of -NH protons of the anilides still contributes to the T_2 relaxation of bulk water, but to a lesser extent compared to highly shifted bound water.[28] Figure 6 shows the relaxation rate (R_2) as a function of concentration for Tm^{3+} based agents that are thought to either have bound water (Tm^{3+} DOTAM-Gly, Tm^{3+} DOTAM-Gly-Lys) and those that are thought to have no bound water (Tm^{3+} *para*-H (**5.3a**), Tm^{3+} *para*-OMe (**5.3b**)). The associated longitudinal and transverse relaxivity (r_1, r_2) is provided in Table 5.4.

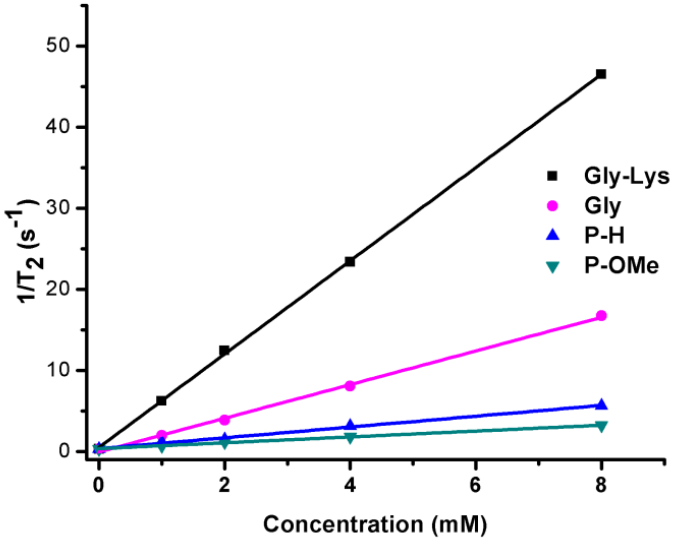

Figure 5.6. r_2 evaluation of agents Tm^{3+} *para*-H (**5.3a**), Tm^{3+} *para*-OMe (3b), and Tm^{3+} DOTAM-Gly and Tm^{3+} DOTAM-Gly-Lys. The slope of the linear fit is used as the r_2 value and reported in Table 5.4.

Table 5.4. r_1 and r_2 values of four Tm^{3+} at 37 °C, pH 7, 9.4 T.

Agent	q	r_1 (s^{-1} mM^{-1})	r_2 (s^{-1} mM^{-1})
Tm^{3+} *para*-H (**5.3a**)	0	0.06	0.67
Tm^{3+} *para*-OMe (**5.3b**)	0	0.05	0.36
Tm^{3+} DOTAM-Gly[39]	1	0.06	2.07
Tm^{3+} DOTAM-Gly-Lys[40]	1	0.09	5.75

The two anilide agents (**5.3a**, **5.3b**) produced a significantly lower relaxation rate (Figure 5.6) because they do not possess an inner sphere water. None of the agents tested produced strong T_1 relaxation of the bulk water, which is not surprising as Tm^{3+} is not known to act as a T_1 relaxation enhancer.[27] The benefit of having CEST agents with minimal effect on T_2 relaxation is demonstrated in Figure 5.7. Two phantoms are shown, one containing Tm^{3+} DOTAM-Gly-Lys as an example of a short T_2 agent (large r_2) and the second containing Tm^{3+} *para*-OMe (**5.3b**) as an example of a long T_2 agent (small r_2). T_1 and T_2 weighted images were acquired and demonstrate that Tm^{3+} DOTAM Gly-Lys (Figure 5.7c) produces signal loss due to the T_2 exchange effect, while Tm^{3+} *para*-OMe (Figure 5.7d) does not have a large T_2 exchange effect. The two phantoms were imaged at a concentration of 20 mM and compared to aqueous solutions containing no agents (outer circles in Figure 5.7). Both the signal to noise ratio (SNR) and CEST effect are important properties that can be used to characterize CEST images. In medical imaging practice however it is important to calculate the contrast to noise ratio (CNR) of CEST images to quantify the likelihood of distinguishing between diseased and surrounding normal tissue.[41] In Table 5.5, several CEST image properties including the SNR, CEST effect and CNR are provided for Tm^{3+}-*para*-OMe and Tm^{3+} DOTAM-Gly-Lys. The SNR is calculated using the signal intensity measured from the agent (inner circle) along with the water (outer cirle) after applying a saturation pulse CEST while the CNR takes into account the overall CEST response of each agent compared the SNR measured. While Tm^{3+} DOTAM-Gly-Lys produces the largest CEST effect, the agent with the longest T_2, Tm^{3+}-*para*-OMe, provides a significantly greater CNR. To visualize the significance of SNR and CNR, Figure 5.7 provides a direct comparison of T_1- and T_2-weighted images of 20 mM Tm^{3+}-*para*-OMe and Tm^{3+} DOTAM-Gly-Lys phantoms surrounded by an outer cylinder of distilled water. A 3.5% decrease in SNR was calculated for the long T_2 agent (Tm^{3+}-*para*-OMe) while a 85% decrease was measured for the short T_2 agent (Tm^{3+} DOTAM-Gly-Lys). It is apparent that even with a large CEST effect, the overall detectability of Tm^{3+} Gly-Lys is substantially lower than Tm^{3+}-*para*-OMe due to the short bulk water T_2 induced by Tm^{3+} DOTAM-Gly-Lys.

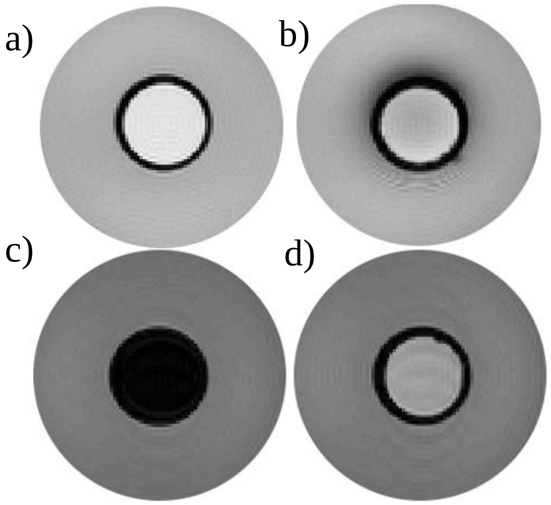

Figure 5.7. T_1 and T_2 weighted images collected at 37 °C and pH 7.0. Inner circle contains 20 mM CAs. Outer circle contains water with no agents. T_1 weighted images of a) Tm^{3+} DOTAM Gly-Lys b) Tm^{3+} *para*-OMe. T_2 weighted images of c) Tm^{3+} DOTAM Gly-Lys d) Tm^{3+} *para*-OMe (**5.3b**).

Table 5.5. *In vitro* MR image contrast parameters for Tm^{3+} *para*-OMe and Tm^{3+} DOTAM-Gly-Lys.

	CEST (%)	**CNR***
Bulk Water	--	--
Tm^{3+} *para*-OMe (-43 ppm)	16.9	59.0
Tm^{3+} *para*-OMe (-83 ppm)	12.2	42.6
Tm^{3+} DOTAM-Gly-Lys (-46 ppm)	43.3	23.9

*SNR and CNR were calculated as defined in ref. 41. [41]

Experimental

CEST fast spin-echo (FSE) images were acquired on a 9.4T MRI scanner (Agilent, Palo Alto, CA) with the following parameters, FOV (field of view): 25.6 x 25.6 mm^2, matrix: 64 x 64, TR: 5000 ms, TE: 10 ms, ETL = 32, 1 average, 2 prescans, 1 slice 3 mm thick. CEST spectra (Tm^{3+} and Dy^{3+}) were acquired using a 15 µT, 5s continuous wave presaturation pulse at offset frequencies ranging from -100 to 100 ppm in steps of 1 ppm. T_1 weighted images were acquired using a gradient echo pulse sequence. TR = 200 ms, TE = 2.62 ms, Flip angle = 20°, 10 averages, matrix = 128x128, FOV = 19.2 x 19.2 mm^2, 1 slick 4 mm thick. All samples were studied at 20 mM concentration, 37 °C. All solvents were HPLC grade and used as such, except for dioxane (dried by passing through columns of activated Al_2O_3) and water (18.2 MΩ·cm^{-1} deionized). Solvents were removed under reduced pressure in a rotary evaporator. NMR spectra were recorded on a 400 MHz spectrometer; for ^{1}H (400 MHz), chemical shift values (δ) are reported relative to TMS and were referenced to the residual proton in the deuterated solvents as follows: $CDCl_3$ (7.26 ppm); DMSO-d_6 (2.49 ppm); D_2O (4.75 ppm). Mass spectra (MS) were obtained using electrospray ionization (ESI). T_1 relaxation time constant measurements were made for 4 different concentrations (1, 2, 4, 8 mM) of CA using an inversion recovery sequence (10 inversion times in the range of 10 ms – 10 s) with a 20 second repetition time to ensure full recovery, pH 7 and 37 °C. T_2 rrelaxation time constant measurements were made for 4 different concentrations (1, 2, 4, 8 mM) of CA using a CPMG pulse sequence (10 train echo times in the range of 10 ms – 10 s) with a 20 second repetition time to ensure full recovery, pH 7 and 37 °C. Tm^{3+} DOTAM-Gly was prepared previously.[39] Tm^{3+} DOTAM-Gly-Lys was prepared previously.[40]

General Procedure for Electrophiles 5.1a-e

Chloroacetyl chloride (15.7 mmol) was added slowly on ice to a stirring solution of aniline (a-e) (7.84 mmol) and K_2CO_3 (15.7 mmol) in acetonitrile (50 mL). The solution was allowed to stir overnight at room temperature followed by filtration. The filtrate was concentrated and the product was crystallized from methanol.

5.1a. 2-chloro-N-phenylacetamide. White solid (1.06 g, 6.2 mmol) yield 80%. ^{1}H NMR (400 MHz, DMSO-d_6): δ 10.36 (1H, s); 7.60 (2H, d, *J* = 7.4 Hz); 7.33 (2H, t, *J* =7.4 Hz); 7.08 (1H, t, *J* = 7.4 Hz); 4.26 (2H, s). ^{13}C NMR (100 MHz, DMSO-d_6): δ 165.0, 138.9, 129.2, 124.2, 119.8, 44.0. ESI-TOF. m/z calcd for C_8H_9ClNO $(M+H)^+$, 170.0373, found 170.0366.

5.1b. 2-chloro-N-(4-methoxyphenyl)acetamide. Silver solid (1.29 g, 6.5 mmol), yield 82%. ^{1}H NMR (400 MHz, DMSO-d_6): δ 10.17 (1H, s); 7.51 (2H, d, *J* = 8.6 Hz); 6.90 (2H, d, *J* = 8.6 Hz); 4.22 (2H, s); 3.72 (3H, s). ^{13}C NMR (100 MHz, DMSO-d_6): δ 164.5, 156.0, 132.0, 121.4, 114.3, 55.6. 43.9. ESI-TOF. m/z calcd for $C_9H_{11}ClNO_2$ $(M+H)^+$, 200.0478, found 200.0477.

5.1c. 2-chloro-N-(p-tolyl)acetamide. White solid (1.08 g, 5.9 mmol), yield 75%. ^{1}H NMR (400 MHz, DMSO-d_6): δ 10.21 (1H, s); 7.50 (2H, d, *J* = 7.4 Hz); 7.13 (2H, d, *J* = 7.4 Hz); 4.24 (2H, s); 2.26 (3H, s). ^{13}C NMR (100 MHz, DMSO-d_6): δ 164.8, 136.4, 133.2, 129.6, 119.8, 44.0, 20.8. ESI-TOF. m/z calcd for $C_9H_{11}ClNO$ $(M+H)^+$, 184.0529, found 184.0524.

5.1d. 2-chloro-N-(4-nitrophenyl)acetamide. Yellow solid (1.80 g, 7.9 mmol), yield 79%. ^{1}H NMR (400 MHz, DMSO-d_6): δ 10.97 (1H, s); 8.22 (2H, d, *J* = 9.0 Hz); 7.84

(2H, d, *J* = 9.0 Hz); 4.35 (2H, s). ^{13}C NMR (100 MHz, DMSO-d$_6$): δ 166.0, 145.0, 143.0, 125.4, 119.5, 44.0. ESI-TOF. m/z calcd for $C_8H_8ClN_2O_3$ $(M+H)^+$, 215.0223, found 215.0220.

5.1e. 2-chloro-N-(4-chlorophenyl)acetamide. White solid (1.08 g, 5.3 mmol), yield 68%. ^{1}H NMR (400 MHz, DMSO-d$_6$): δ 10.43 (1H, s); 7.62 (2H, d, *J* = 8.6 Hz); 7.38 (2H, d, *J* = 8.6 Hz); 4.26 (2H, s). ^{13}C NMR (100 MHz, DMSO-d$_6$): δ 165.2, 137.8, 129.2, 127.9, 121.3, 43.9. ESI-TOF. m/z calcd for $C_8H_8Cl_2NO$ $(M+H)^+$, 203.9983, found 203.9983.

General Procedures for Tetra Substituted Cyclen 5.2a-e

Electrophiles 1a-e (2.25 mmol) in 3 mL acetonitrile were added to a stirring solution of cyclen (0.5 mmol) and K_2CO_3 (2.25 mmol) in acetonitrile (12 mL). The reaction was then stirred for 1-3 days at 55 °C - 80 °C and monitored by UPLC MS. Upon completion the reaction was filtered and the precipitate washed with water, then collected and used without further purification.

5.2a. 2,2',2'',2'''-(1,4,7,10-tetraazacyclododecane-1,4,7,10-tetrayl)tetrakis(N-phenylacetamide). The title compound was obtained as a white powder (0.348 g) yield quantitative (q). ^{1}H NMR (400 MHz, DMSO-d$_6$): δ 10.32 (4H, broad s); 7.61 (8H, d, *J* = 7.8 Hz); 7.22 (8H, t, *J* =7.8 Hz); 7.01 (4H, t, *J* = 7.8 Hz); 3.38 (16H, s); 2.81 (8H, broad s). ^{13}C NMR (100 MHz, DMSO-d$_6$): δ 169.3, 138.5, 128.3, 123.0, 119.3, 58.1, 51.9. ESI-TOF. m/z calcd for $C_{40}H_{49}N_8O_4$ $(M+H)^+$, 705.3877, found 705.399.

5.2b. 2,2',2'',2'''-(1,4,7,10-tetraazacyclododecane-1,4,7,10-tetrayl)tetrakis(N-(4-methoxyphenyl)acetamide). The title compound was obtained as a white powder (0.389 g) yield 94%. ^{1}H NMR (400 MHz, DMSO-d$_6$): δ 10.04 (4H, broad s); 7.51 (8H, s); 6.80 (8H, s); 3.68 (16H, s,); 3.25 (12H, s); 2.84 (8H, broad s). ^{13}C NMR (100 MHz, DMSO-d$_6$): δ 168.8, 155.1, 131.7, 120.8, 113.6, 58.1, 55.0, 52.0. ESI-TOF. m/z calcd for $C_{44}H_{57}N_8O_8$ (M+H)$^+$, 825.4299, found 825.4284.

5.2c. 2,2',2'',2'''-(1,4,7,10-tetraazacyclododecane-1,4,7,10-tetrayl)tetrakis(N-(p-tolyl)acetamide). The title compound was obtained as a white powder (0.375 g) yield (q). ^{1}H NMR (400 MHz, DMSO-d$_6$): δ 10.05 (4H, broad s); 7.47 (8H, d, *J* = 6.6 Hz); 7.03 (8H, d, *J* = 6.6 Hz); 3.26 (16H, s); 2.82 (8H, broad s); 2.22 (12H, s). ^{13}C NMR (100 MHz, DMSO-d$_6$): δ 169.0, 135.9, 131.9, 128.7, 119.3, 58.1, 52.3, 20.1 ESI-TOF. m/z calcd for $C_{44}H_{57}N_8O_4$ (M+H)$^+$, 761.4503, found 761.4529.

5.2d. 2,2',2'',2'''-(1,4,7,10-tetraazacyclododecane-1,4,7,10-tetrayl)tetrakis(N-(4-nitrophenyl)acetamide). The title compound was obtained as a yellow powder (0.437 g) yield (q). ^{1}H NMR (400 MHz, DMSO-d$_6$): δ 10.69 (4H, broad s); 8.10 (8H, s); 7.81 (8H, s); 3.39 (16H, s); 2.87 (8H, broad s). ^{13}C NMR (100 MHz, DMSO-d$_6$): δ 170.2, 144.5, 142.0 124.3, 118.7, 57.7, 52.0. ESI-TOF. m/z calcd for $C_{40}H_{45}N_{12}O_{12}$ (M+H)$^+$, 885.3280, found, 885.3254.

5.2e. 2,2',2'',2'''-(1,4,7,10-tetraazacyclododecane-1,4,7,10-tetrayl)tetrakis(N-(4-chlorophenyl)acetamide). The title compound was obtained as a white powder (0.394 g) yield 94%. ^{1}H NMR (400 MHz, DMSO-d$_6$): δ 10.6 (4H, broad s); 7.64 (8H, d, *J* = 8.8 Hz); 7.26 (8H, d, *J* = 8.8 Hz); 3.37 (16H, s); 2.78 (8H, broad s). ^{13}C NMR (100 MHz, DMSO-d$_6$): δ 169.5, 137.4, 128.1, 126.6, 120.8, 57.8, 51.7. ESI-TOF. m/z calcd for $C_{40}H_{45}Cl_4N_8O_4$ (M+H)$^+$, 841.2318, found, 841.2325.

General Procedure for Complexation of Tetra Substituted Cyclen Products 5.3a-e, 5.4a-e

To a stirring solution of appropriate tetra substituted cyclen (**5.2a-e**) (0.07 mmol) in 4 ml 1:1 H_2O: dioxane, $DyCl_3$ or $TmCl_3$ (0.07 mmol) was added and the reaction was stirred over a period of 1- 4 days at 60 °C - 80 °C. The complexation was monitored by UPLC MS and upon completion, the reaction mixture was concentrated and redissolved in 1 ml H_2O followed by dialysis (for 3 days) against water to remove any unchelated lanthanides.

5.3a. 2,2',2'',2'''-(1,4,7,10-tetraazacyclododecane-1,4,7,10-tetrayl)tetrakis(N-phenylacetamide), thulium(III) chloride. The title compound was obtained as a white powder (41 mg, 67%). ESI-TOF. m/z calcd for $C_{40}H_{46}N_8O_4Tm$ $(M-2H)^+$, 871.2984, found 871.2974.

5.3b. 2,2',2'',2'''-(1,4,7,10-tetraazacyclododecane-1,4,7,10-tetrayl)tetrakis(N-(4-methoxyphenyl)acetamide), thulium(III) chloride. The title compound was obtained as a white powder (58 mg, 83%). ESI-TOF. m/z calcd for $C_{44}H_{54}N_8O_8Tm$ $(M-2H)^+$, 991.3407, found 991.3387.

5.3c. 2,2',2'',2'''-(1,4,7,10-tetraazacyclododecane-1,4,7,10-tetrayl)tetrakis(N-(p-tolyl)acetamide), thulium(III) chloride. The title compound was obtained as a white powder (30 mg, 46%). ESI-TOF. m/z calcd for $C_{44}H_{54}N_8O_4Tm$ $(M-2H)^+$, 927.3610, found 927.3647.

5.3d. 2,2',2'',2'''-(1,4,7,10-tetraazacyclododecane-1,4,7,10-tetrayl)tetrakis(N-(4-nitrophenyl)acetamide), thulium(III) chloride. The title compound was obtained as a yellow powder (61mg, 82%). ESI-TOF. m/z calcd for $C_{40}H_{42}N_{12}O_{12}Tm$ $(M-2H)^+$, 1051.2387, found 1051.2408.

5.3e. 2,2',2'',2'''-(1,4,7,10-tetraazacyclododecane-1,4,7,10-tetrayl)tetrakis(N-(4-chlorophenyl)acetamide), thulium(III) chloride. The title compound was obtained as a white powder (40 mg, 56%). ESI-TOF. m/z calcd for $C_{40}H_{42}Cl_4N_8O_4Tm$ $(M-2H)^+$, 1007.1425, found 1007.1412.

5.4a. 2,2',2'',2'''-(1,4,7,10-tetraazacyclododecane-1,4,7,10-tetrayl)tetrakis(N-phenylacetamide), dysprosium(III) chloride. The title compound was obtained as a white powder (45 mg, 75%). ESI-TOF. m/z calcd for $C_{40}H_{46}N_8O_4Dy$ $(M-2H)^+$, 866.934, found 866.2903.

5.4b. 2,2',2'',2'''-(1,4,7,10-tetraazacyclododecane-1,4,7,10-tetrayl)tetrakis(N-(4-methoxyphenyl)acetamide), dysprosium(III) chloride. The title compound was obtained as a white powder (53 mg, 77%). ESI-TOF. m/z calcd for $C_{44}H_{54}N_8O_8Dy$ $(M-2H)^+$, 986.3356, found, 986.3383.

5.4c. 2,2',2'',2'''-(1,4,7,10-tetraazacyclododecane-1,4,7,10-tetrayl)tetrakis(N-(p-tolyl)acetamide), dysprosium(III) chloride. The title compound was obtained as a white powder (43 mg, 69%) ESI-TOF. m/z calcd for $C_{44}H_{54}N_8O_4Dy$ $(M-2H)^+$, 922.3560, found 922.3586.

5.4d. 2,2',2'',2'''-(1,4,7,10-tetraazacyclododecane-1,4,7,10-tetrayl)tetrakis(N-(4-nitrophenyl)acetamide), dysprosium(III) chloride. The title compound was obtained as a yellow powder (45 mg, 62%). ESI-TOF. m/z calcd for $C_{40}H_{42}N_{12}O_{12}Dy$ (M-2H)$^+$, 1046.2337, found 1046.2336.

5.4e. 2,2',2'',2'''-(1,4,7,10-tetraazacyclododecane-1,4,7,10-tetrayl)tetrakis(N-(4-chlorophenyl)acetamide), dysprosium(III) chloride. The title compound was obtained as a white powder (49 mg, 70%). ESI-TOF. m/z calcd for $C_{40}H_{42}Cl_4N_8O_4Dy$ (M-2H)$^+$, 1002.1375, found, 1002.1343.

5.3 Conclusion

A series of Dy^{3+} and Tm^{3+} *para*-substituted anilide CAs were synthesised and tested for their ability to respond to pH changes in a range of interest for *in vivo* reporting. Poor solubility of many of the compounds limited the possible measurements and prevented us from making a complete comparison of structure and effects. Even with the limited solubility, there were a number of interesting observations in the agents that were soluble. It was observed that the unsubsituted anilines had a maximum CEST effect at a pH near 8, while the maximum CEST effect for the *para*-OMe agents was between pH 7-7.5. A crystal structure indicated that a geometry of Tm^{3+} *para*-OMe is TSAP', which potentially leads to the highly shifted signal at -83 ppm. While we have observed a signal for a Tm^{3+} agent above 100 ppm previously, we were unable to grow a crystal to help determine if there was an inner sphere water. A pH and concentration study was attempted to determine if Tm^{3+} p*ara*-OMe could be used as a ratiometric agent to measure pH *in vivo*, independent of concentration, but due to solubility limitations, no suitable measurements could be performed. Modifications of this ligand are currently underway to increase solubility. With the lack of inner sphere water the Tm^{3+} aniline agents produce appreciable amide CEST contrast without decreasing image signal intensity due to lowering of the bulk water T_2 relaxation time constant.

5.4 Supplemental information

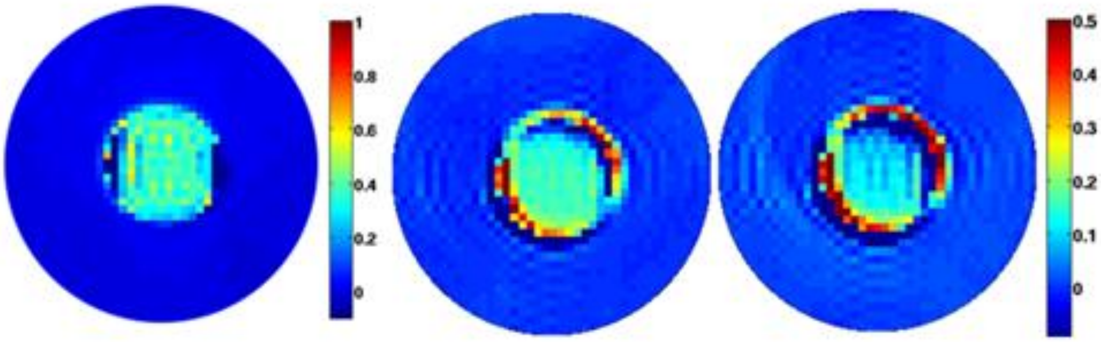

Figure S5.1. CEST images of agents a) Tm^{3+} DOTAM Gly-Lys b) Tm^{3+} *para*-OMe (-43 ppm) c) Tm^{3+} *para*-OMe (-83 ppm). Conditions: 20 mM, 5 s saturation, 15 µT, pH 7.0, 37 °C.

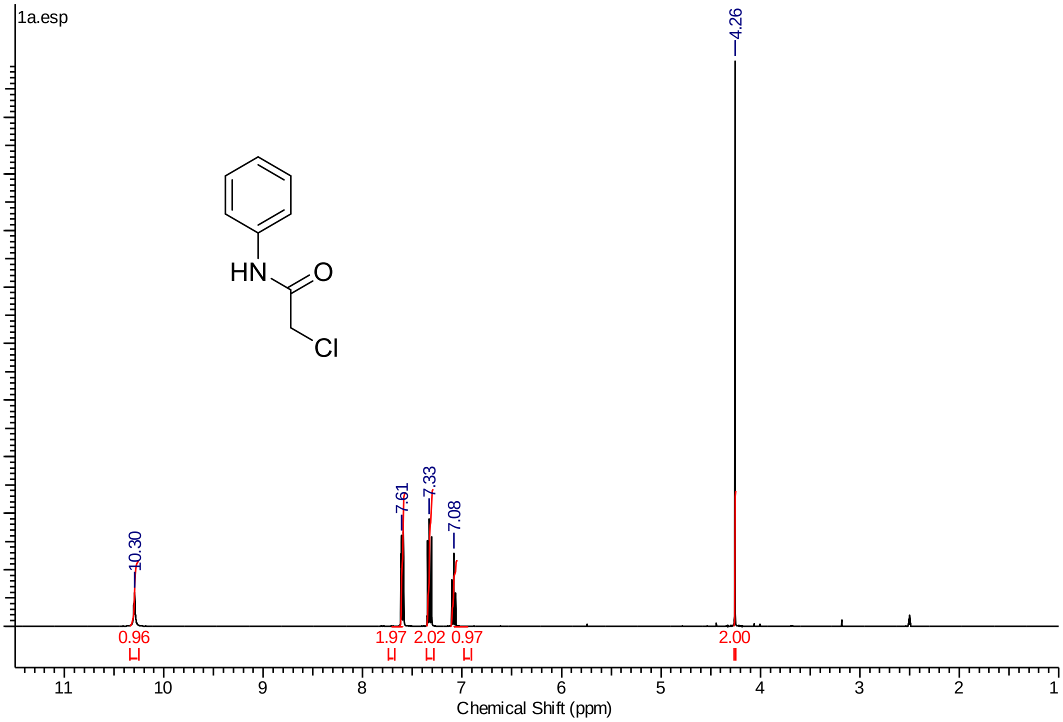

Figure S5.2. ^{1}H-NMR spectrum of **5.1a**.

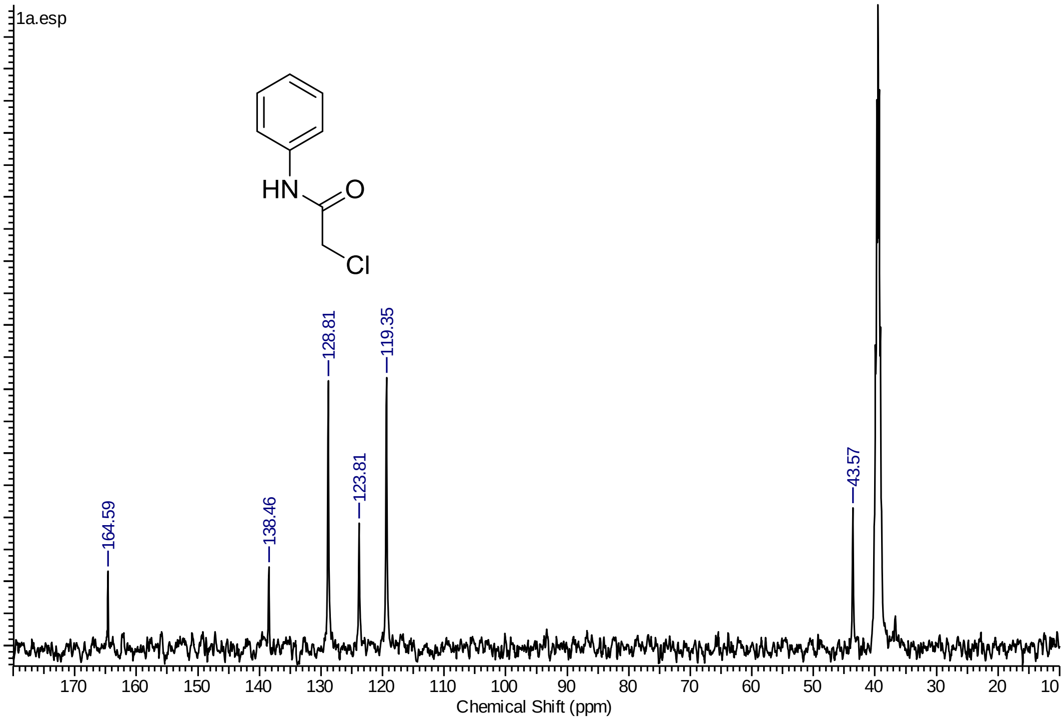

Figure S5.3. ^{13}C-NMR spectrum of **5.1a**.

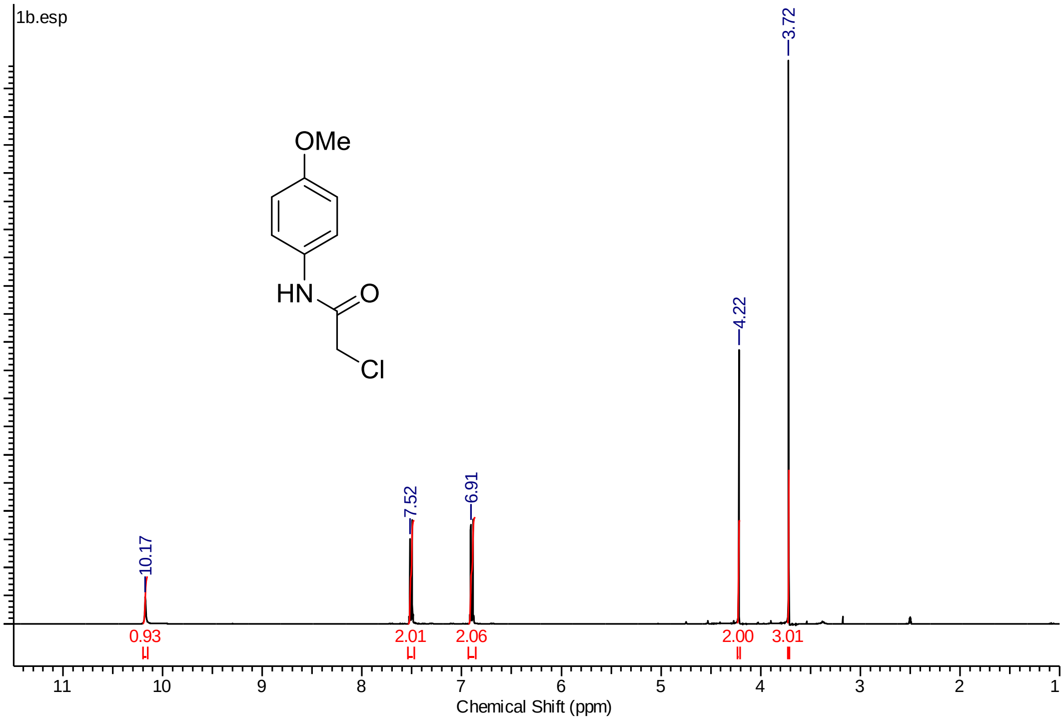

Figure S5.4. ^{1}H-NMR spectrum of **5.1b**.

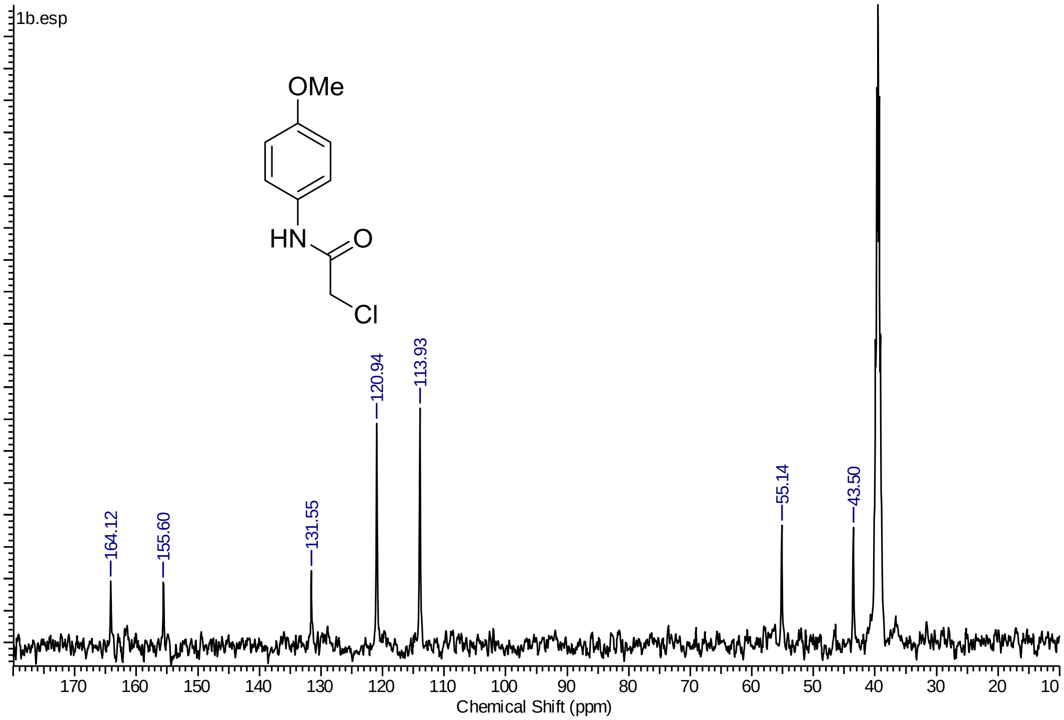

Figure S5.5. ^{13}C-NMR spectrum of **5.1b**.

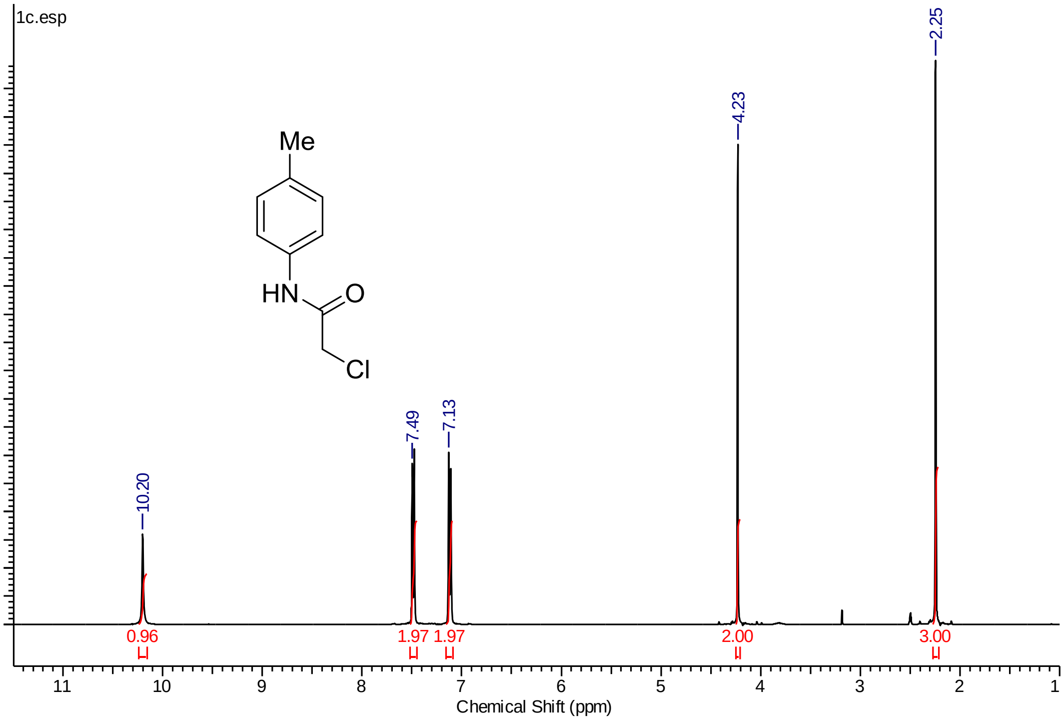

Figure S5.6. ^{1}H-NMR spectrum of **5.1c**.

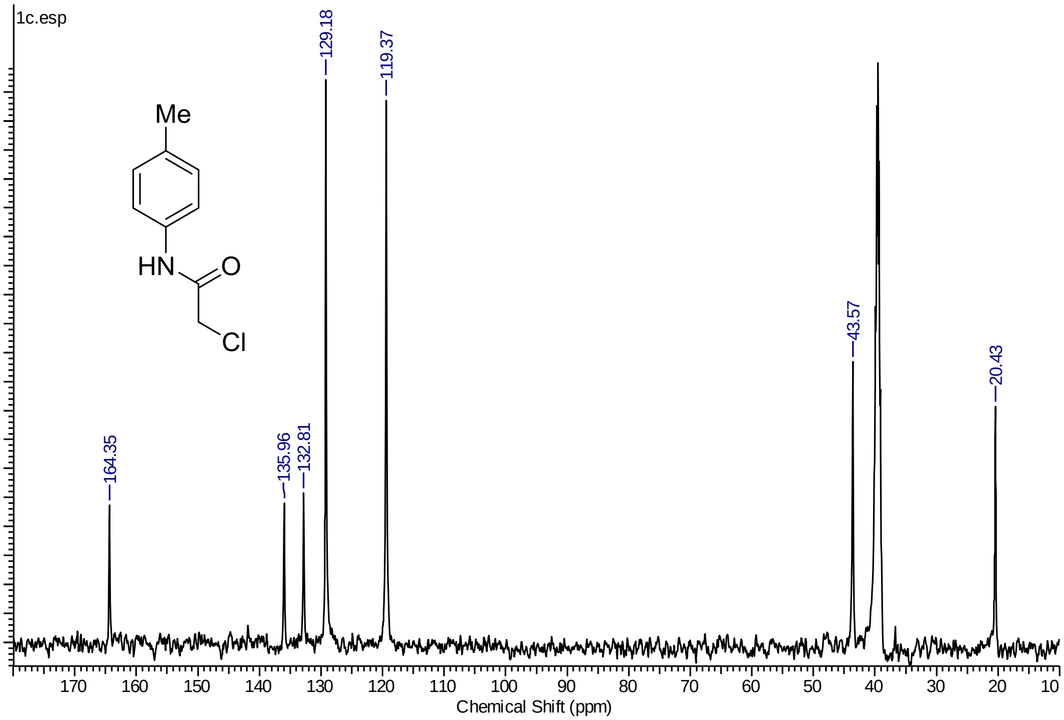

Figure S5.7. ^{13}C-NMR spectrum of **5.1c**.

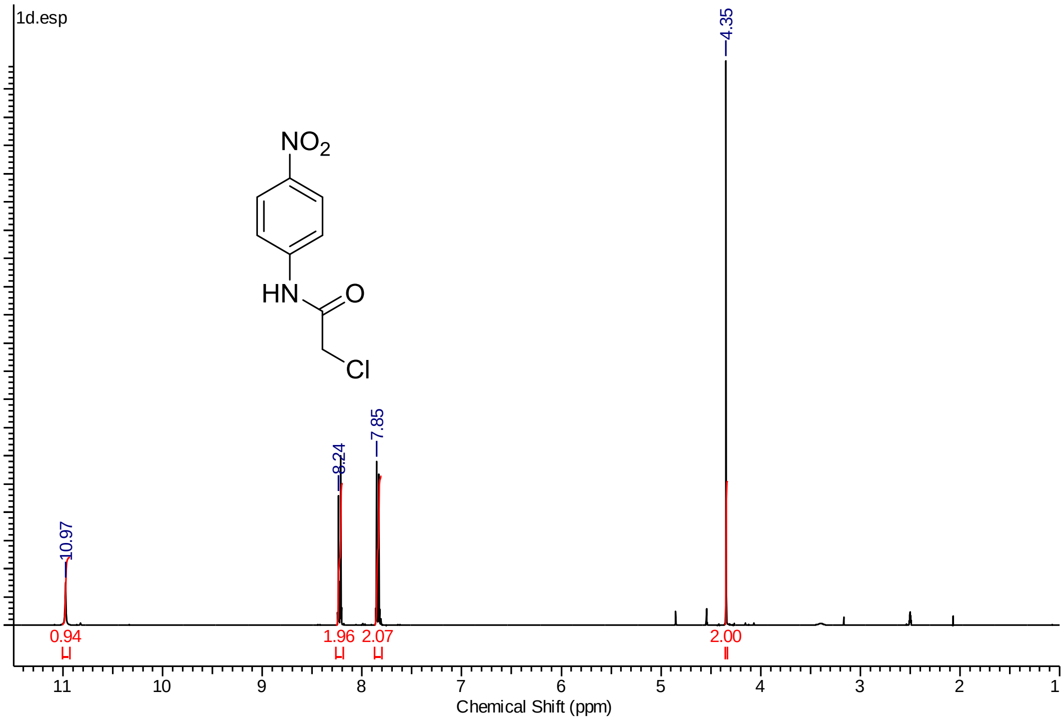

Figure S5.8. ^{1}H-NMR spectrum of **5.1d**.

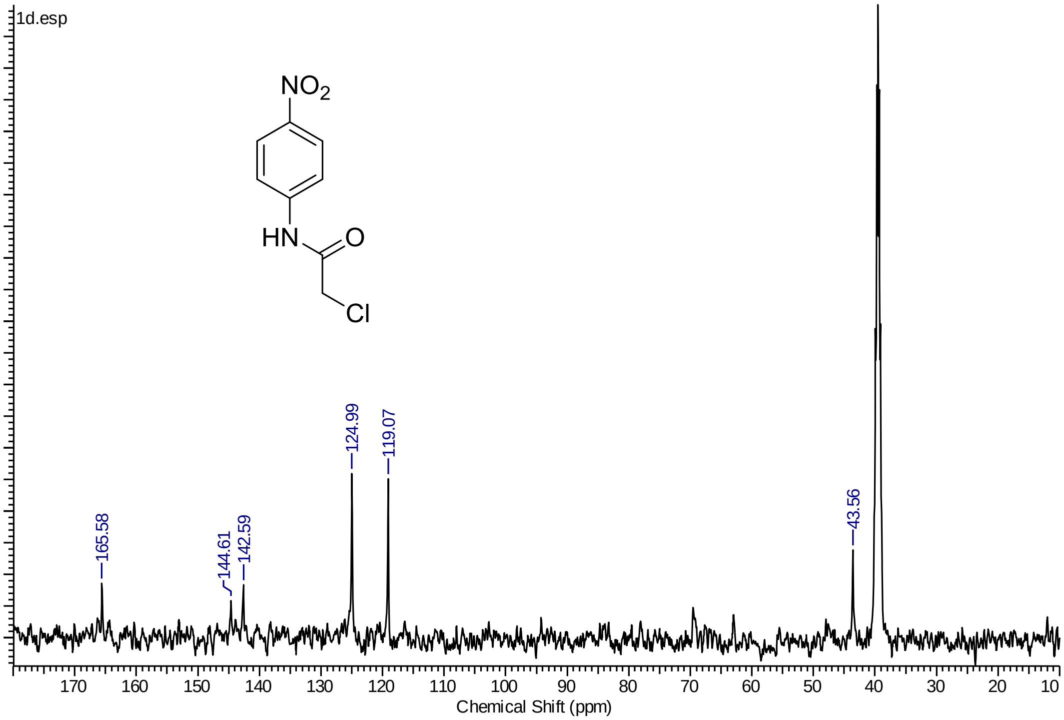

Figure S5.9. ^{13}C-NMR spectrum of **5.1d**.

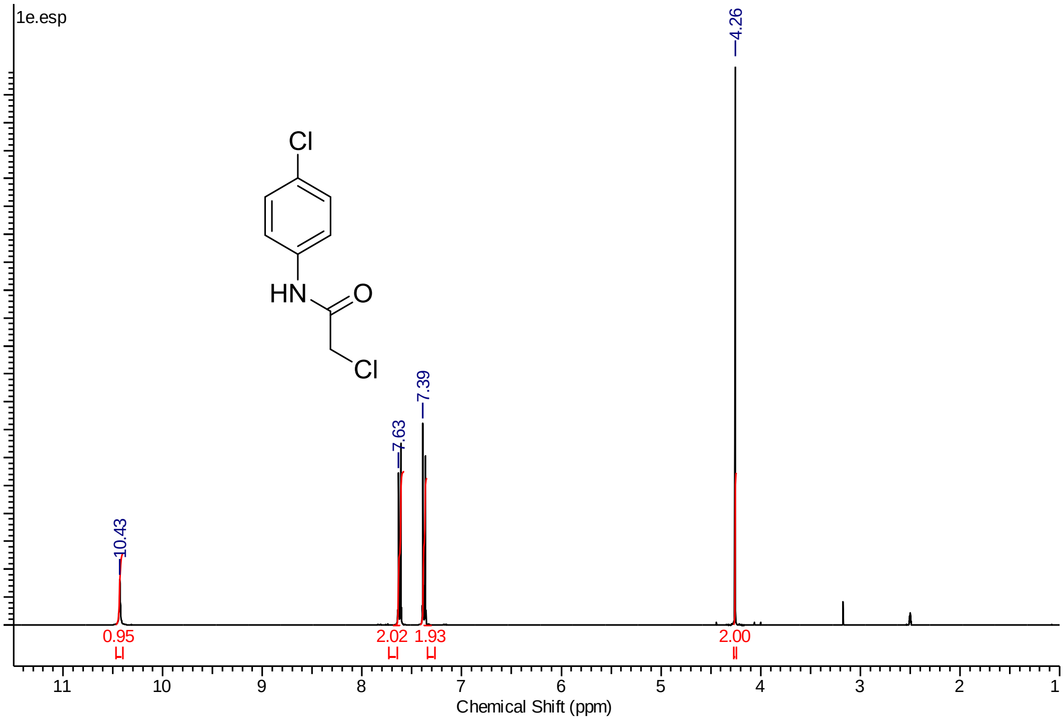

Figure S5.10. ^{1}H-NMR spectrum of **5.1e**.

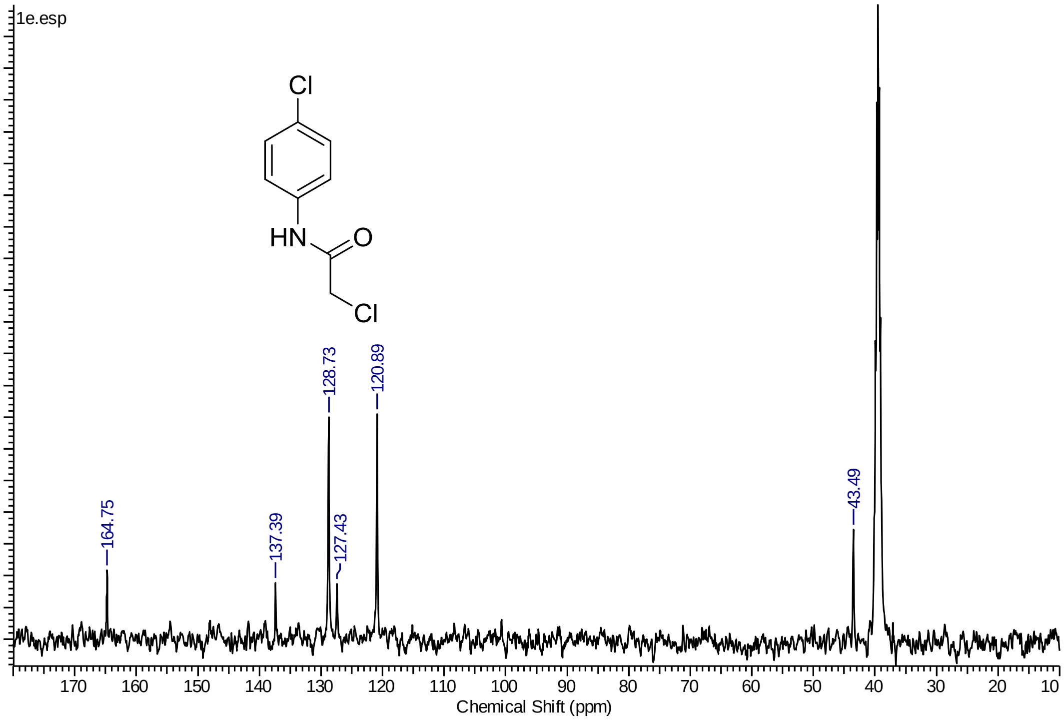

Figure S5.11. ^{13}C-NMR spectrum of **5.1e**.

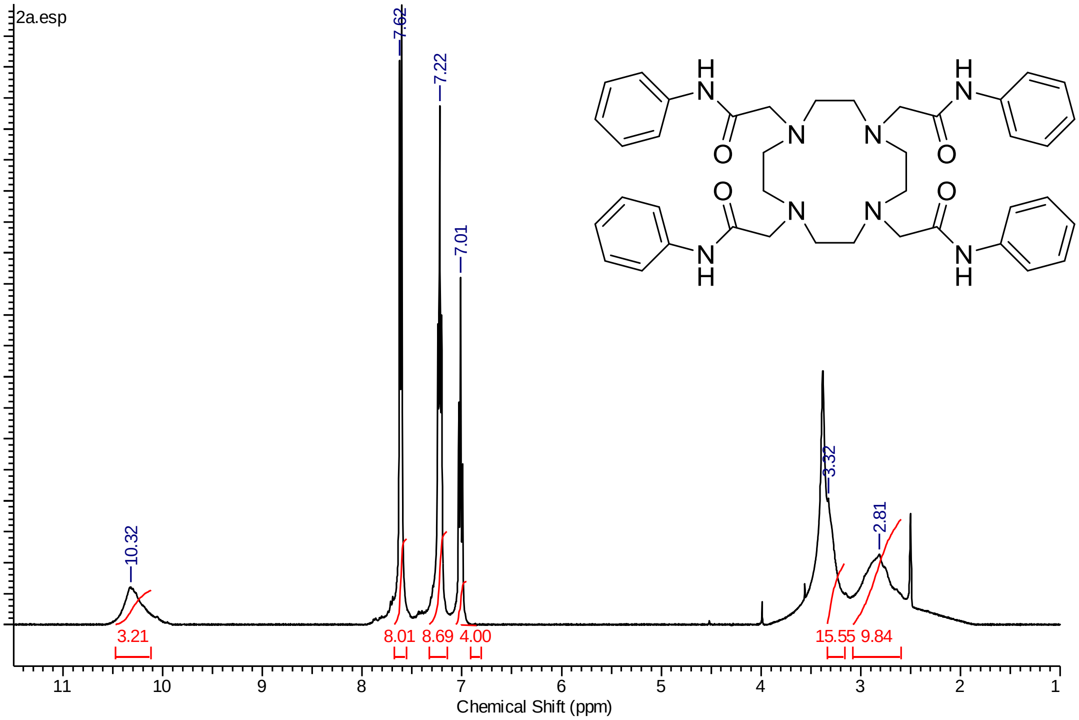

Figure S5.12. ^{1}H-NMR spectrum of **5.2a**.

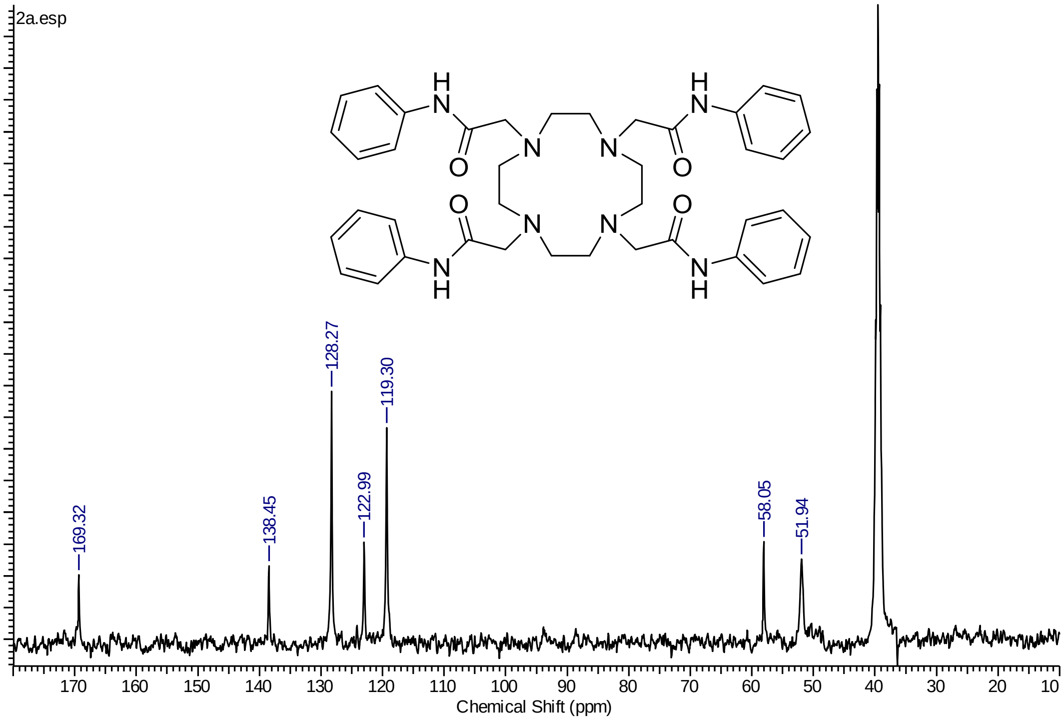

Figure S5.13. ^{13}C-NMR spectrum of **5.2a**.

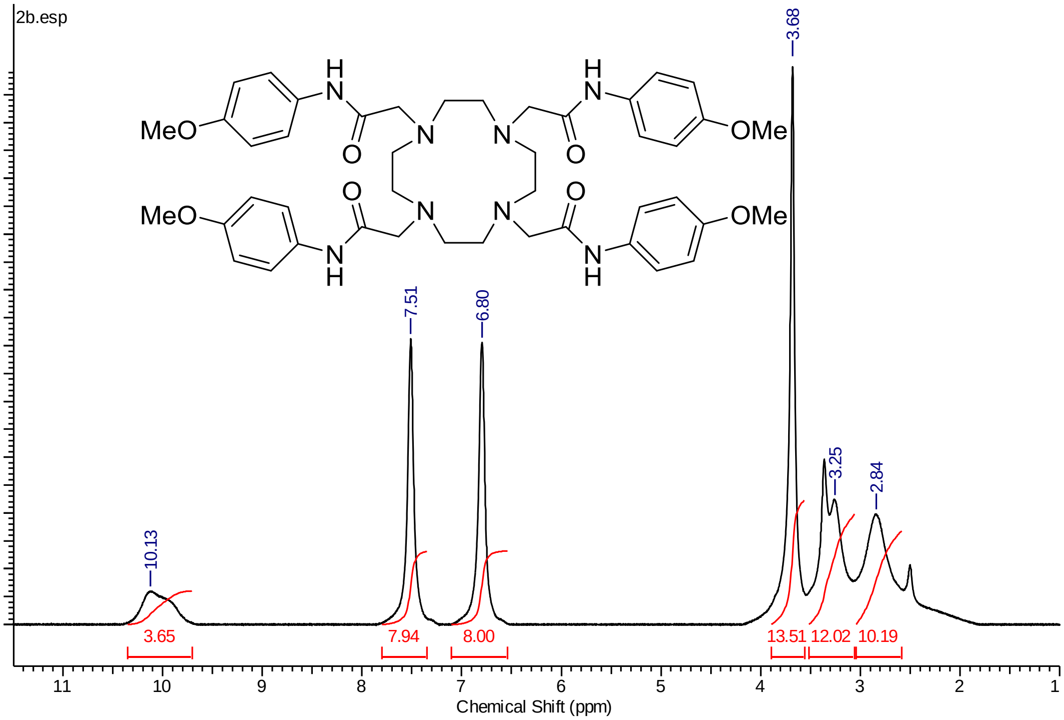

Figure S5.14. ^{1}H-NMR spectrum of **5.2b**.

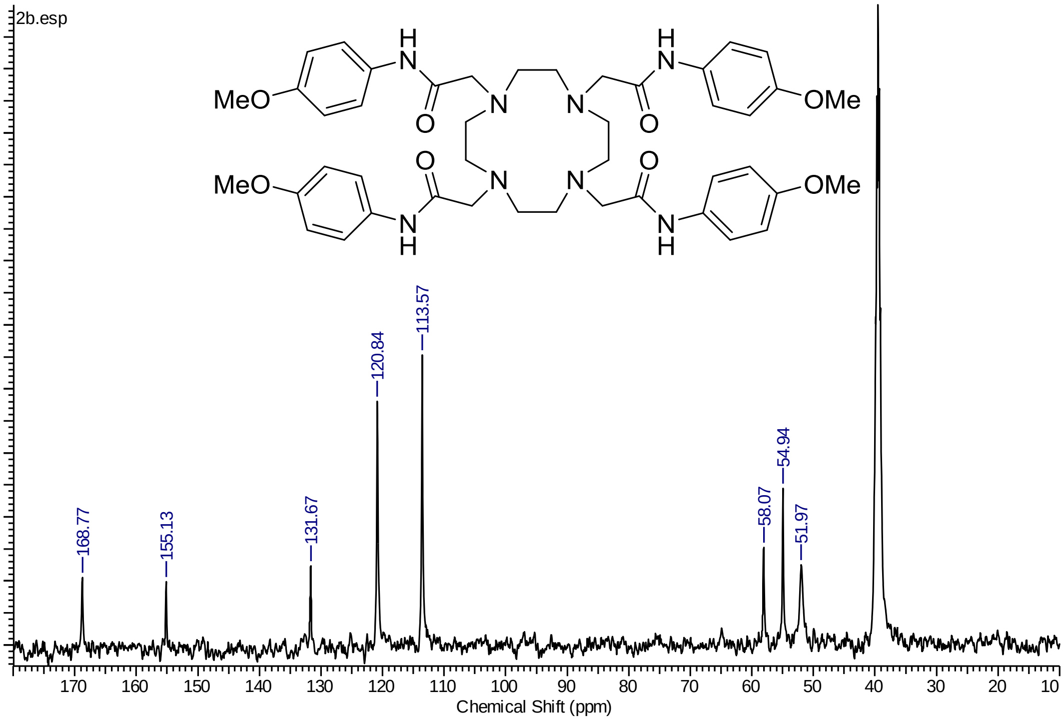

Figure S5.15. ^{13}C-NMR spectrum of **5.2b**.

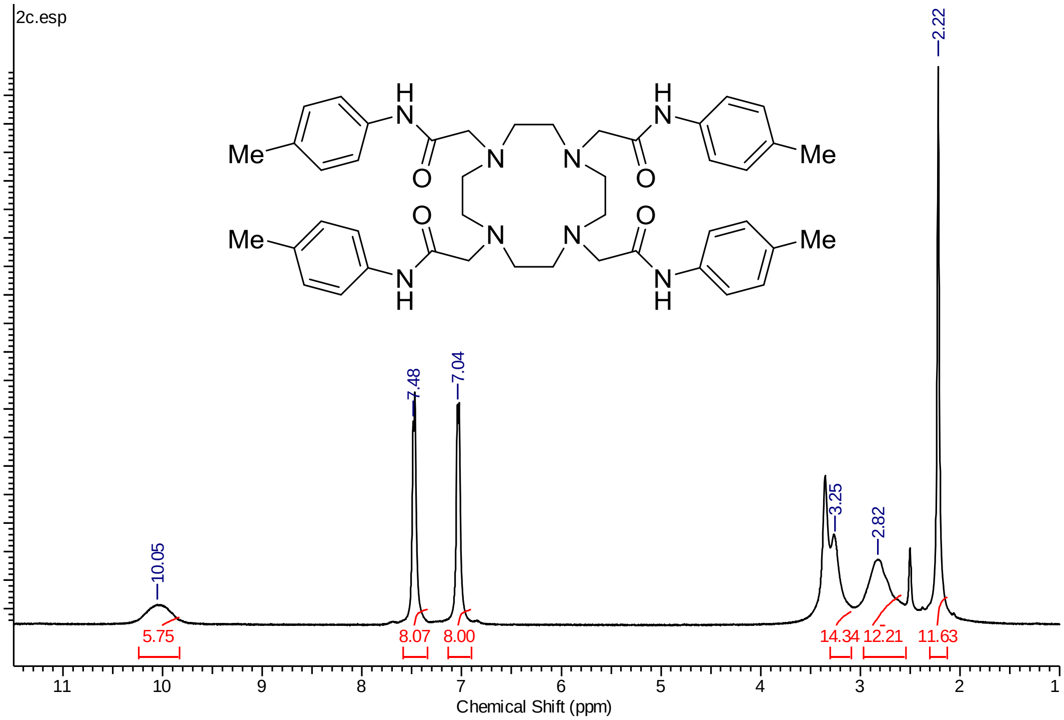

Figure S5.16. ^{1}H-NMR spectrum of **5.2c**.

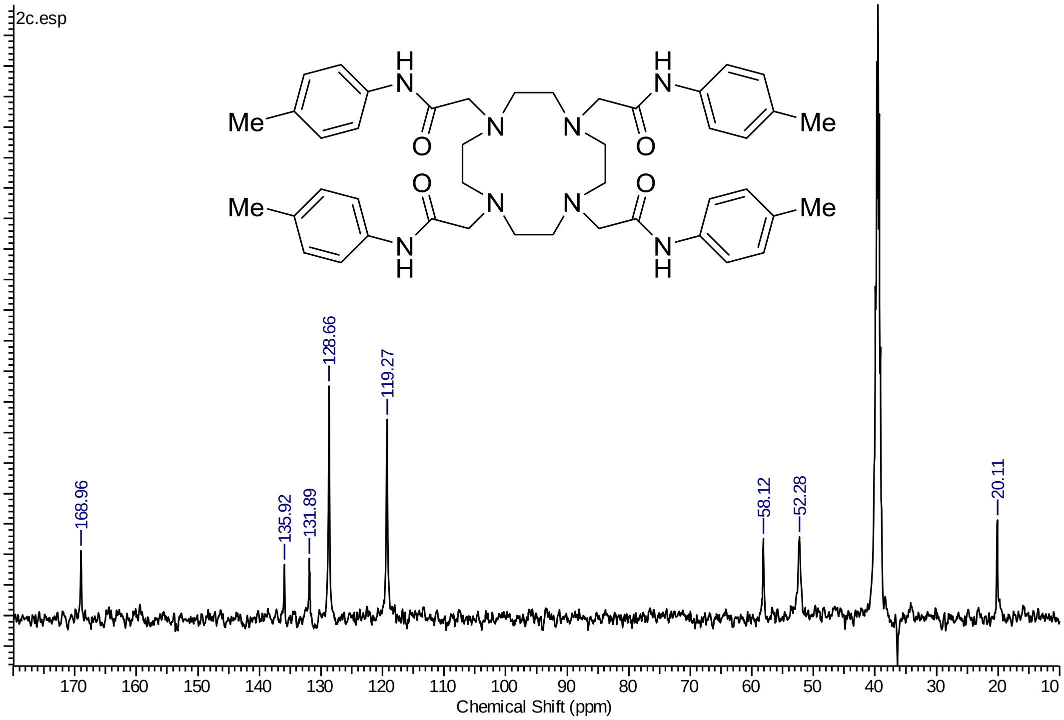

Figure S5.17. ^{13}C-NMR spectrum of **5.2c**.

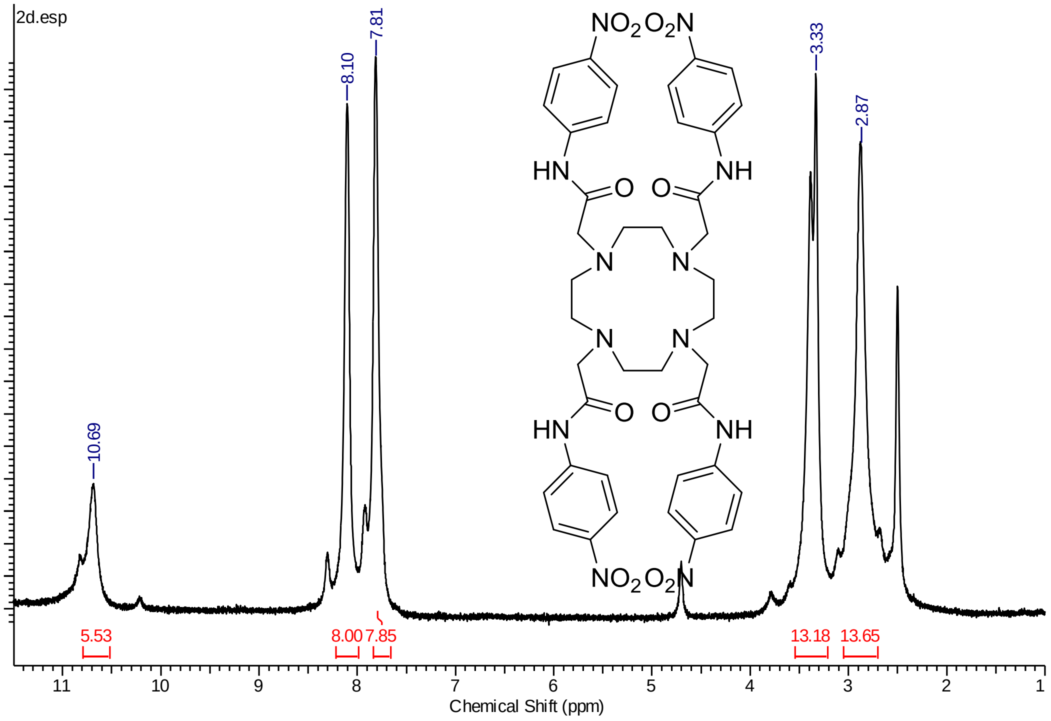

Figure S5.18. ^{1}H-NMR spectrum of **5.2d**.

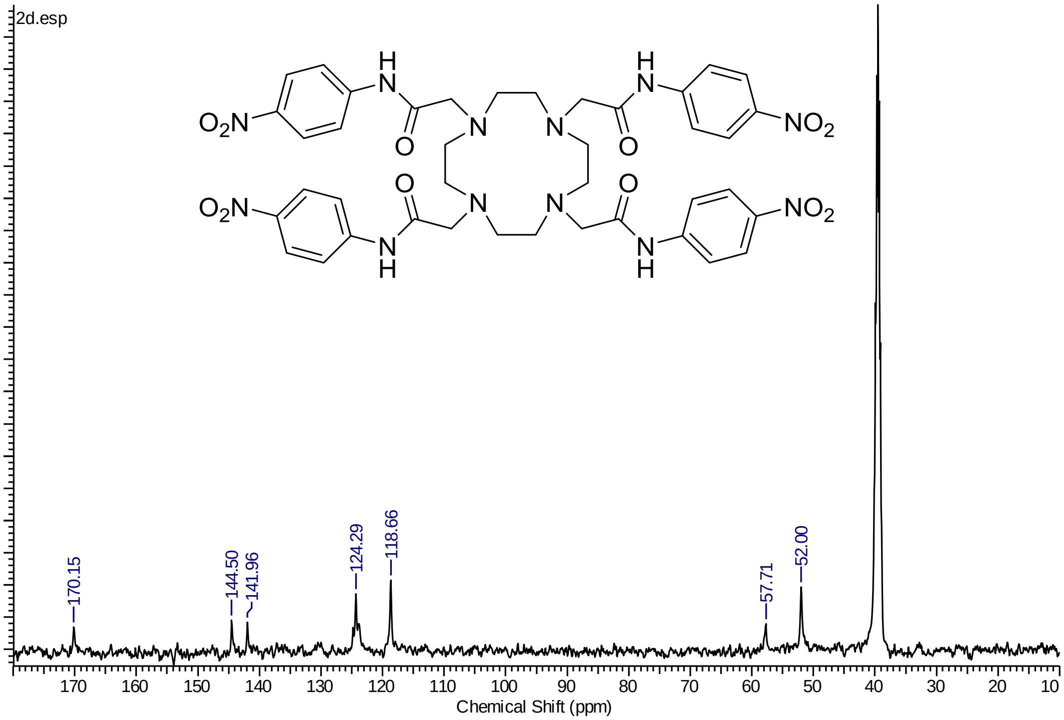

Figure S5.19. ^{13}C-NMR spectrum of **5.2d**.

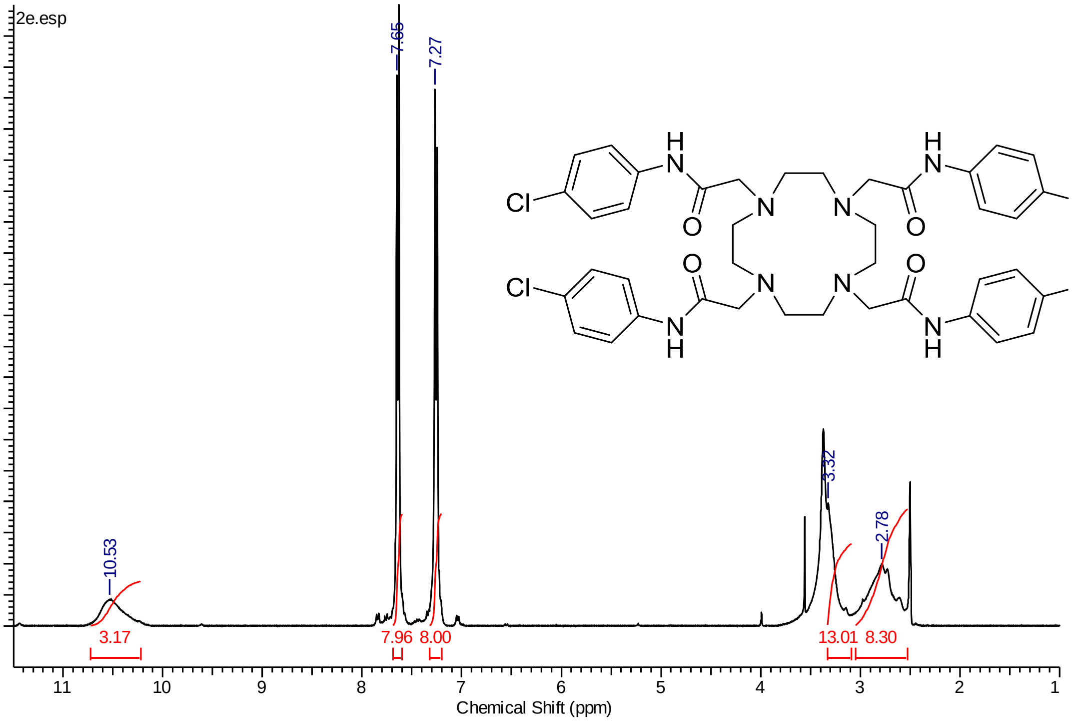

Figure S5.20. ^{1}H-NMR spectrum of **5.2e**.

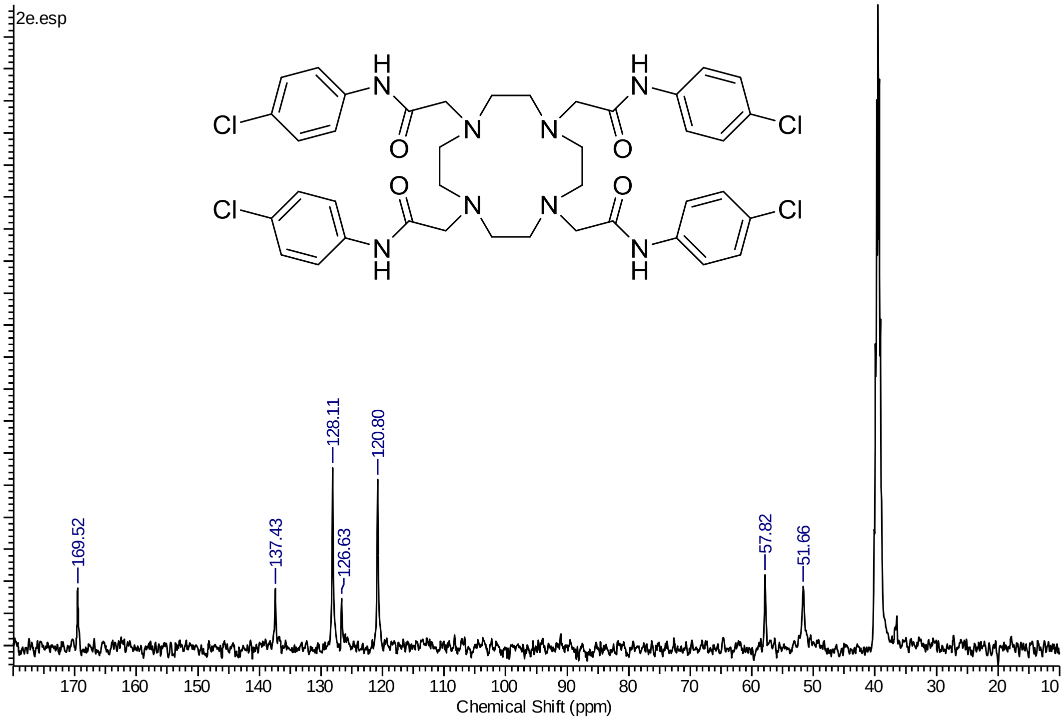

Figure S5.21. ^{13}C-NMR spectrum of **5.2e**.

5.5 References

1. P. Caravan, J. J. Ellison, T. J. McMurry and R. B. Lauffer, *Chem. Rev.*, 1999, **99**, 2293-2352.

2. S. Aime, M. Botta and E. Terreno, *Adv. Inorg. Chem.*, 2005, **57**, 173-237.

3. S. Aime, C. Cabella, S. Colombatto, S. G. Crich, E. Gianolio and F. Maggioni, *J. Magn. Reson. Imaging*, 2002, **16**, 394-406.

4. H. U. Rashid, K. Yu and J. Zhou, *J. Struct. Chem.*, 2013, **54**, 223-249.

5. E. Terreno, D. D. Castelli, A. Viale and S. Aime, *Chem. Rev.*, 2010, **110**, 3019-3042.

6. M. P. M. Marques, C. Geraldes, A. D. Sherry, A. E. Merbach, H. Powell, D. Pubanz, S. Aime and M. Botta, *J. Alloy. Compd.*, 1995, **225**, 303-307.

7. S. Aime, M. Botta, M. Fasano, M. P. M. Marques, C. Geraldes, D. Pubanz and A. E. Merbach, *Inorg. Chem.*, 1997, **36**, 2059-2068.

8. P. Lebduskova, P. Hermann, L. Helm, E. Toth, J. Kotek, K. Binnemans, J. Rudovsky, I. Lukes and A. E. Merbach, *Dalton Trans.*, 2007, **0**, 493-501.

9. K. M. Ward and R. S. Balaban, *Magn. Reson. Med.*, 2000, **44**, 799-802.

10. T. K. Stevens, M. Milne, A. A. H. Elmehriki, M. Suchý, R. Bartha and R. H. E. Hudson, *Contrast Media Mol. Imaging*, 2013, **8**, 289-292.

11. S. Aime, A. Barge, D. Delli Castelli, F. Fedeli, A. Mortillaro, F. U. Nielsen and E. Terreno, *Magn. Reson. Med.*, 2002, **47**, 639-648.

12. N. McVicar, A. X. Li, M. Suchý, R. H. E. Hudson, R. S. Menon and R. Bartha, *Magn. Reson. Med.*, 2012, DOI: 10.1002/mrm.24539.

13. S. R. Zhang, M. Merritt, D. E. Woessner, R. E. Lenkinski and A. D. Sherry, *Acc. Chem. Res.*, 2003, **36**, 783-790.

14. S. Zhang, X. Jiang and A. D. Sherry, *Helv. Chim. Acta*, 2005, **88**, 923-935.

15. M. Woods, E. W. C. Donald and A. D. Sherry, *Chem. Soc. Rev.*, 2006, **35**, 500-511.

16. K. Snoussi, J. W. M. Bulte, M. Gueron and P. C. M. van Zijl, *Magn. Reson. Med.*, 2003, **49**, 998-1005.

17. J. Zhou and P. C. M. van Zijl, *Prog. Nucl. Magn. Reson. Spectrosc.*, 2006, **48**, 109-136.

18. B. Yoo and M. D. Pagel, *J. Am. Chem. Soc.*, 2006, **128**, 14032-14033.

19. M. Woods, D. E. Woessner, P. Zhao, A. Pasha, M.-Y. Yang, C.-H. Huang, O. Vasalitiy, J. R. Morrow and A. D. Sherry, *J. Am. Chem. Soc.*, 2006, **128**, 10155-10162.

20. S. R. Zhang, K. C. Wu and A. D. Sherry, *Angew. Chem. Int. Ed.*, 1999, **38**, 3192-3194.

21. S. Aime, D. Delli Castelli and E. Terreno, *Angew. Chem. Int. Ed.*, 2002, **41**, 4334-4336.

22. D. Delli Castelli, E. Terreno and S. Aime, *Angew. Chem. Int. Ed.*, 2011, **50**, 1798-1800.

23. J. Pacheco-Torres, D. Calle, B. Lizarbe, V. Negri, C. Ubide, R. Fayos, P. L. Larrubia, P. Ballesteros and S. Cerdan, *Curr. Top. Med. Chem.*, 2011, **11**, 115-130.

24. A. X. Li, F. Wojciechowski, M. Suchy, C. K. Jones, R. H. E. Hudson, R. S. Merton and R. Bartha, *Magn. Reson. Med.*, 2008, **59**, 374-381.

25. M. Suchy, A. X. Li, R. Bartha and R. H. E. Hudson, *Org. Biomol. Chem.*, 2008, **6**, 3588-3596.

26. F. K. Kalman, M. Woods, P. Caravan, P. Jurek, M. Spiller, G. Tircso, R. Kiraly, E. Brucher and A. D. Sherry, *Inorg. Chem.*, 2007, **46**, 5260-5270.

27. C. K. Jones, A. X. Li, M. Suchý, R. H. E. Hudson, R. S. Menon and R. Bartha, *Magn. Reson. Med.*, 2010, **63**, 1184-1192.

28. T. C. Soesbe, M. E. Merritt, K. N. Green, F. A. Rojas-Quijano and A. D. Sherry, *Magn. Reson. Med.*, 2011, **66**, 1697-1703.

29. T. C. Soesbe, O. Togao, M. Takahashi and A. D. Sherry, *Magn. Reson. Med.*, 2012, **68**, 816-821.

30. S. J. Ratnakar, M. Woods, A. J. M. Lubag, Z. Kovács and A. D. Sherry, *J. Am. Chem. Soc.*, 2007, **130**, 6-7.

31. A. A. H. Elmehriki, M. Milne, M. Suchý, R. Bartha and R. H. E. Hudson, *Can. J. Chem.*, 2012, **91**, 211-219.

32. A. D. Z. Sherry, S.; Wu, K. , *WO 02/43775A2, 2002.*

33. Y. Li, V. R. Sheth, G. Liu and M. D. Pagel, *Contrast Media Mol. Imaging*, 2011, **6**, 219-228.

34. F. Benetollo, G. Bombieri, L. Calabi, S. Aime and M. Botta, *Inorg. Chem.*, 2003, **42**, 148-157.

35. A. Rodríguez-Rodríguez, D. Esteban-Gómez, A. de Blas, T. Rodríguez-Blas, M. Fekete, M. Botta, R. Tripier and C. Platas-Iglesias, *Inorg. Chem.*, 2012, **51**, 2509-2521.

36. P. Vojtíšek, P. Cígler, J. Kotek, J. Rudovský, P. Hermann and I. Lukeš, *Inorg. Chem.*, 2005, **44**, 5591-5599.

37. D. Parker, R. S. Dickins, H. Puschmann, C. Crossland and J. A. K. Howard, *Chem. Rev.*, 2002, **102**, 1977-2010.

38. S. Aime, M. Fasano and E. Terreno, *Chem. Soc. Rev.*, 1998, **27**, 19-29.

39. S. Aime, A. Barge, D. D. Castelli, F. Fedeli, A. Mortillaro, F. U. Nielsen and E. Terreno, *Magn. Reson. Med.*, 2002, **47**, 639-648.

40. F. Wojciechowski, M. Suchy, A. X. Li, H. A. Azab, R. Bartha and R. H. E. Hudson, *Bioconjugate Chem.*, 2007, **18**, 1625-1636.

41. E. M. Haacke, R. W. Brown, M. R. Thompson and R. Venkatesan, *Magnetic Resonance Imaging: Physical Principles and Sequence Design*, Wiley, 1999.

Chapter 6: Gold Nanoparticles Functionalized with Gadolinium as T_1 Based Contrast Agents

“Water-soluble gold nanoparticles (AuNP) functionalized with gadolinium (III) via Michael addition for use as a MRI contrast” Submitted to *Journal of Materials Chemistry B*, **2013**. Manuscript #TB-ART-05-2013-020699.

6.1 Introduction

Gadolinium (Gd^{3+}) based contrast agents (CA) for use in magnetic resonance imaging (MRI) have been employed because of their ability to enhance the T_1 relaxation of agent bound water protons *in vivo*.[1-7] This enhancement may highlight tissue involved in pathological processes that allow leakage of the agent from the vasculature into the tissue. The enhancement gained by Gd^{3+} based CAs is concentration dependent, such that a hyperintense region is observed as local CA concentrations increase. Ultimately, the enhancement of tissue contrast gained depends on the biodistribution of an agent, as a set molar amount is delivered per patient to limit the possible side effects associate with lanthanide-based CAs. To ensure that a site specific, effective concentration is achieved, there have been efforts to develop nano-sized carriers to aid in the delivery of clinically approved small molecule-based CAs. Covalent linkage of a small Gd^{3+} CA to a nano-carrier may increase its local concentration such that a single nanoparticle may provide sufficient signal enhancement without relying the need of accumulation of a high concentration of individual CAs. Strategies in this field include the development of dendrimers,[8-12] liposomes,[3, 13-15] micelles,[16-18] polymers[19-22] as well as silicon and gold-based nanoparticles.[22-27] While each of these systems have their benefits and drawbacks it is their size that will have the highest impact on their overall difference in MRI properties compared to the single Gd^{3+} CA. It has been shown that the size of the nano carrier is the limiting factor for a number of parameters such as loading of the chelator, *in vivo* distribution, as well as the enhancement of relaxation gained by slower tumbling molecules.[2, 28] The size distribution of known carriers usually range from a few nanometers (nm), to a few micrometers (µm). While loading of these nano carriers with 1000's of chelators generates agents with excellent sensitivity their synthesis relies on conventional nanoparticle synthesis methods.[24] The drawback of using conventional (one-pot) nanoparticle synthesis is the difficulty in reproducibility, lack of stability of the CA on the nanoparticle and the need to control a large number of reaction conditions where a change in one, may result in an undesired product that would not be suitable for the development of clinically acceptable CAs where the control and characterization of the structure is strict. A better approach is to utilize a previously prepared AuNP, where the size and solubility can be controlled and that contains a reactive functionality capable of undergoing a controlled interfacial reaction to introduce the CA covalently onto the nanoparticle. To this end we describe the synthesis of Gd^{3+} modified water-soluble gold nanoparticles (GdAuNP) that will have a reproducible and measureable number of chelators (Scheme 6.1). To efficiently attach the Gd^{3+} chelator and enhance the prospect for *in vivo* studies, we utilize a small water-soluble gold nanoparticle with a core size of 3 nm ± 1 nm that is functionalized with approximately 80 maleimide moieties at the interface. Maleimide-modified AuNPs were chosen as they undergo efficient interfacial

Michael addition when mixed with an appropriate nucleophile; [29, 30] in the present case we utilize a Gd^{3+} CA, Gd^{3+}DO3A-amine chelator (Scheme 6.1). [20,31]

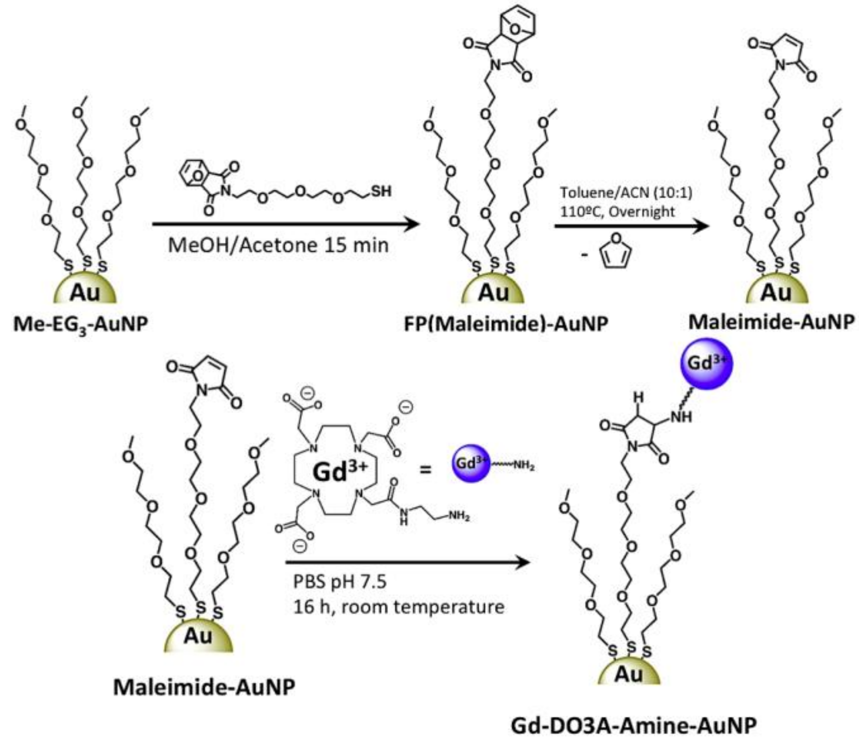

Scheme 6.1. Synthetic strategy used in the preparation of Maleimide-AuNP and the subsequent interfacial Michael addition between Gd^{3+}-DO3A-amine and Maleimide AuNP.

All chemicals and solvents were used as received unless specified. All solvents were HPLC grade, except water (18.2 MΩ cm^{-1}). Organic extracts were dried with Na_2SO_4, and solvents were removed under reduced pressure by rotary evaporation. Flash column chromatography (FCC) was carried out using silica gel, mesh size 230-400 Å. Cellulose ester dialysis membranes with MWCO of 6-8 KDa were used. *In vivo* contrast-enhanced T_1-weighted MR images were acquired using a 400 MHz horizontal bore small animal MRI scanner equipped with a 30 mm millipede radio frequency coil (Agilent, Palo Alto, CA). Images were acquired before and immediately following intravenous (IV) injection in the tail vein. NMR measurements were made on a spectrometer operating at 400 MHz. Relaxation measurements were made for 4 different concentrations of CA using an inversion recovery pulse sequence with 16 inversion times with a 2 second delay to ensure full relaxation.

Preparation of Maleimide AuNP

Maleimide–AuNP was synthesized accordingly to our recently established procedure.[29-31] Briefly, triethylene glycol monomethyl ether AuNP (Me-EG$_3$-AuNP) was synthesized mixing 3 equivalents of triethylene glycol monomethyl ether thiol with 1 equivalent of $AuHCl_4$ $3H_2O$ in a dry methanol/acetic acid solution (10:1), followed by slow addition of 10 equivalents of $NaBH_4$ in water. The purified Me-EG$_3$-AuNP underwent a place-exchange reaction with furan-protected-maleimide tetraethylene glycol–thiols ligands (FP(maleimide)-EG$_4$-SH). The resulting (FP(maleimide)–AuNPs were deprotected by dissolving them in a toluene–acetonitrile (10:1) mixture and heating the system at 110 ºC overnight under vigorous stirring. This method leads to small water-soluble maleimide–AuNP with a gold core diameter of 3 ± 1 nm. The maleimide-AuNP contains ca. 0.50 $\mu mol \cdot mg^{-1}$ of maleimide moieties as determined by thermogravimetric analysis and ^1H NMR spectroscopy. These AuNP were dissolved in acetonitrile to obtain a concentration of 10 $mg \cdot ml^{-1}$ and stored at -20 °C. Maleimide-AuNPs stored in this way were found to be stable for months.

Synthesis of DO3A-Amine

DO3A-amine was synthesized as previously reported.[32] In short, cyclen was alkylated with 3 eq. of ethyl bromoacetate in acetonitrile with potassium carbonate. After purification, the fourth alkylation was done with the previously reported boc-protected amino ethyl chloroacetamide. Complete deprotection was done with standard deprotection conditions. TFA/DCM 1:1 for 30 min to remove the Boc group, followed by drying and hydrolysis under basic conditions using 3.3 eq. of NaOH at 60 °C overnight.

Synthesis of Gd-DO3A-Amine

The agent was prepared using to previously reported conditions.[20, 33] After deprotection DO3A-amine was metallated with 1 eq of $GdCl_3$ at pH 6. This reaction was monitored by ESI-MS until metallation was complete. Finally, the complex was dialyzed at a 500 Dalton cutoff to remove free Gd^{3+}.

Conjugation of CA onto Maleimide AuNP via Michael Addition

The nucleophile (Gd-DO3A-amine or DO3A-amine, 6 eq.) was stirred overnight with AuNP-maleimide in a phosphate buffer at pH 7.5. The following day the pH of the solution was lowered to 3-4 and the reaction mixture was dialyzed at a cutoff of 6-8 KDa against water. The solution was then reduced in volume to achieve a concentration of 10 mM for *in vivo* testing. Gd-DO3A-amine-AuNPs were stored at -20 °C and were found to be stable for weeks. If stored in solution and at room temperature aggregation occurs after a week.

FT-IR Measurements

Infrared spectra were collected using a Bruker Vector33 spectrometer. The blanks were collected first by purging the instrument with nitrogen gas for 5 minutes and averaging 128 scans from 600 cm^{-1} to 4000 cm^{-1}. Subsequently, the sample (~0.5 mg of AuNP) was dispersed in dry KBr and packed into a pellet using a press. The AuNP spectra were recorded in the same conditions of the blank, which was automatically subtracted.

Zeta potential measurements of DO3A-AuNP and Gd-AuNP

Zeta potential measurements were performed using a Zetasizer Nano-ZS (Malvern Instrument). A solution of AuNP in PBS pH 7.5 was prepared with a concentration of 0.5 mg ml^{-1}. 1 ml of this solution was inserted in a latex folded capillary cell equipped with electrodes and the zeta potential was calculated by employing the Huckel approximation.

Relaxation measurements

The r_1 for both the Gd^{3+}-DO3A-amine and the GdAuNP were measured at 4 concentrations (Gd^{3+}-DO3A-amine = 1 mM, 2 mM, 4 mM, 8 mM and GdAuNP = 1 mM, 2 mM, 4 mM, 8.26 mM [Gd^{3+}]) at pH 6.8 using an inverse recovery sequence with a 2 second delay to ensure full T_1 relaxation between measurements. The slope of the plotted T_1 vs. concentration is measured and reported as the r_1. r_1 of Gd^{3+}-DO3A-amine = 2.3 mM^{-1} s^{-1}. r_1 GdAuNP = 2.2 mM^{-1} s^{-1}.

Gold and gadolinium concentration determination by ICP-OES.

ICP-OES measurements were done on a series of concentrations to allow for an accurate measurement of both the concentration as well as the ratio of Au to Gd using 4 wavelengths for each element. It was found that the ratio of Au to Gd was 14:1. Using the value of Au to maleimides calculated it is shown that 70% of the maleimides reacted with the Gd-DO3A-amine to afford ca. 56 Gd^{3+} chelators present per NP.

MRI studies

Animals

To demonstrate MRI T_1 contrast *in vivo*, a C57BL/6 mouse (8 months of age, weighing ~20 g) was anesthetized (induced using 4% isoflurane in oxygen and maintained using 1.5%–2.5% isoflurane in oxygen). To reduce motion, the abdomen of the mouse was lightly taped to a MRI-compatible stage. The mouse was placed in a 30 mm Agilent millipede coil. Temperature was monitored with a rectal temperature probe, and respiration was monitored with a respiratory sensor pad, which was connected to a pressure transducer placed over the thoracic/abdominal region (SA Instruments Inc., Stony Brook, NY). The mouse's body temperature was maintained at 37 ^{o}C using a warm-air feedback system. A catheter was placed in the tail vein using a 27-guage needle. Three pre-injection T_1-weighted MR images were acquired. Then 200 µL of 10 mM GdAuNP dissolved in water was injected directly into the tail vein at a constant rate of 40 uL/min, with the mouse secured to the MRI compatible stage. Post-injection MR image acquisition began within 2 min of injection. The animal procedure was performed according to a protocol approved by the Western University Animal Use Subcommittee. Same-slice pre- and post-injection images were acquired using a T_1-weighted fast spin echo (FSE) pulse sequence (TR/echo time = 500/10 ms, echo-train length = 4, 128 x 128 linear readout, 30.0 mm^2 field of view, 5 slices, 2 mm slice thickness, 2 prescans, 4 averages) were acquired continuously for ~90 min through both kidneys.

6.2 Results and Discussion

Synthesis and Characterization of Maleimide-AuNP

Our synthetic approach for preparing small water-soluble Maleimide-AuNP is summarized in scheme 6.1. This approach is based on a retro-Diels-Alder strategy where the maleimide is first protected, followed by its deprotection only once the ligand is attached to the gold core. The need for this protection is due the reactivity that thiols have for Michael addition onto unprotected maleimides. The AuNP template (Me-EG_3-AuNP) that is employed as starting material is based on using the ω-mercapto triethylene glycol monomethyl ether as the base ligand.[29] This ligand confers both water-solubility and organic-solvent solubility to the nanoparticle. This amphiphilic property permits the use of reactions in organic solvents, which is important in this case for the deprotection, yet confers water-solubility to the final maleimide-AuNP. The latter is the target because it can undergo the interfacial Michael addition reaction with the CA. In addition, the ethylene glycol based ligands are expected to hinder protein adsorption *in vivo* which should ensure prolongation of the AuNP circulation half-life and reduction of its immunogenicity.[34, 35] The triethylene glycol monomethyl ether gold nanoparticle (Me-EG_3-AuNP) was then subjected to a place-exchange reaction in presence of the furan-protected maleimide-tetraethylene glycol-thiol (FP(malemide)-EG_4-SH). This reaction was carried out by mixing 100 mg of Me-EG_3-AuNP with 37.1 mg of FP(malemide)-EG_4-SH for 15 minutes in a 10:1 mixture of methanol and acetone. The (FP(malemide)-EG_4-AuNP was then purified by repeatedly washing a film of the nanoparticles with hexanes, which removes the soluble, free thiols and leaves behind the insoluble AuNP. The AuNP were then further purified by dialysis to completely remove any trace of free thiol before the deprotection of the maleimide. The deprotection of the maleimide was accomplished using a retro-Diels-Alder strategy; this involved dissolving the particles in a mixture toluene/acetonitrile (10:1) and heating at 110 ºC overnight. Once the reaction was completed the solvent and liberated furan were removed under vacuum and the film of maleimide-AuNP was repeatedly washed with hexanes.

Characterization of the functionalized AuNPs was then done by ^1H NMR spectroscopy in D_2O.[29] In particular, the appearance of the following the signals after the place-exchange reaction where diagnostic: 6.60 ppm (alkene protons of the furan moiety), 5.25 ppm (protons adjacent to the bridged oxygen), and at 3.07 ppm (protons adjacent to maleimide carbonyl). After the retro-Diels-Alder reaction the olefinic signals at 6.60 and 5.25 ppm and the protons adjacent to maleimide carbonyl at 3.07 in the FP(malemide)-EG_4-AuNP disappear concomitant with the appearance of the expected maleimide olefinic protons at 6.86 ppm, see supplemental information. The ^{1}H NMR spectrum showed no indication of the double hydrolysis products that would have appeared as a signal at 6.23 ppm,[29] or the mono hydrolysis product that would have shown two broad doublets at 6.24 and 5.84 ppm. The target maleimide-AuNP was also characterized by thermogravimetric analysis (TGA) and transmission electron microscopy (TEM). TEM showed a gold core size of 3 ± 1 nm, while TGA showed the presence of 0.5 µmol of maleimide ligands per milligram of AuNP.

From the combination of the ^{1}H NMR, TGA and TEM data, and assuming that the AuNP are spherical and that their size is monodisperse (3 nm) it is possible to calculate an approximate molecular formula for the maleimide-AuNP. The number of gold atoms (N_{Au}) can be calculated using the following formula:

$$N = \frac{\pi \cdot \rho \cdot d^3 \cdot N_A}{6 \cdot M_{Au}}$$

Where ρ is the density of the face centered cubic (fcc) gold lattice (19.3 g cm^{-3}), *d* is the average diameter of the nanoparticles in centimeters found from the TEM images, M_{Au} is the mole atomic weight of gold (196.9665 g mol^{-1}), and N_A is Avogadro constant.

The number of thiol ligands surrounding the gold core (N_L) can be calculated using the following formula:

$$N_L = \frac{N \cdot M_{Au} \cdot W_{\%}}{(1 - W_{\%}) \cdot [MW_{Maleimide-S} \cdot M_{\%} + MW_{Me-EG3-S} \cdot (1 - M_{\%})]}$$

Where $W_{\%}$ is the percentage of mass loss due to the organic ligands found through TGA measurements, $MW_{Me\text{-}EG3\text{-}S}$ is the molecular weight of the base thiolate ligand, $MW_{Maleimide\text{-}S}$ is the molecular weight of the maleimide thiolates ligand, and $M_{\%}$ is the mole percentage of maleimide ligand.

Using these equations and determining the molar percentage of ligands from the ^{1}H NMR spectra, we can calculate an approximate nanoparticle formula of $Au_{800}(Me\text{-}EG_3\text{-}S)_{370}(maleimide\text{-}EG_4\text{-}S)_{80}$.

Interfacial Michael addition onto Maleimide-AuNP

To optimize the synthetic conditions for preparing the Gd^{3+}-DO3A-amine-AuNP, a model reaction was performed using the un-metalated DO3A-amine to avoid NMR line broadening caused by Gd^{3+}, which would hinder characterization. Using the uncomplexed ligand, DO3A-amine we could easily follow the course of the reaction using ^{1}H NMR spectroscopy observing the disappearance of the maleimide olefin protons signal at 6.86 ppm. The interfacial Michael addition reaction was performed by mixing DO3A-amine (181 mg) with maleimide-AuNP (60 mg) in a buffered solution at pH 7.5. This mixture was left overnight at room temperature. The amounts utilized correspond to ca. 6 equivalents of DO3-amine to every one maleimide; the total number of maleimide moieties (80/AuNP) was estimated as outlined above. Although an alkaline pH is required in order to avoid protonation of the amine nucleophile, it cannot be higher than 7.5 due to the propensity of the maleimide to hydrolyze in water (time scale of hours).[29] Additionally, the solubility of Gd^{3+}-DO3A-amine decreases at basic pHs. The model reaction was monitored by ^{1}H NMR spectroscopy following the disappearance of the alkene protons signal at 6.86 ppm. Once it was evident that the maleimide had reacted, the pH of the solution was lowered to 3-4 to re-dissolve the functionalized AuNP and the unreacted nucleophile. This acidic solution was then dialyzed against water using a membrane with a MWCO of 6-8 KDa to remove the excess nucleophile. The same reaction conditions and purification method were then employed to synthesize Gd^{3+}-DO3A-amine modified AuNP. Importantly, the final Gd^{3+}-DO3A-Amine-AuNP was found to be well soluble in water at up to pH 7.4, while the Gd^{3+}-DO3A-amine was found to have a limited solubility at this pH.

The success of the interfacial Michael addition reaction and the covalent linking of the CA were demonstrated by ^{1}H NMR spectroscopy, FT-IR spectroscopy and Zeta potential measurements. The ^{1}H NMR spectrum of the purified Gd^{3+}-DO3A-amine-AuNP showed the typical line broadening due to the presence of Gd^{3+}. Figure 6.1 shows the FT-IR spectra of maleimide-AuNP, DO3A-amine-AuNP and Gd^{3+}-DO3A-amine-AuNP, and confirms the success of our synthetic approach. The maleimide-AuNP spectrum (figure 6.1 a) shows the typical band at 2869 cm^{-1} due to the C-H stretching mode mainly due to the ethylene glycol units of the ligands, and maleimide's C=O stretching band at 1735 cm^{-1} (asymmetric) and at 1704 cm^{-1} (symmetric). The presence of the DO3A chelator is supported by the appearance of a broad band at 3600-3000cm^{-1} that is due to the N-H stretching. In addition the increase in the intensity ratio of the C=O stretches due to the maleimide moiety at 1704 cm^{-1} to 1735 cm^{-1} indicates the change in the C=O of the maleimide due to the Michael addition. This along with the appearance of the stretch at 1612cm^{-1} due to the amide II band of the DO3A-amine (especially visible for the Gd^{3+}-DO3A-amine-AuNP, figure 6.1 c) further supports the formation of Gd^{3+}-DO3A-amine-AuNP.

Zeta potential measurements were carried out at pH 7.5 on the maleimide-AuNP, on DO3A-amine-AuNP and on Gd^{3+}-DO3A-amine-AuNP, and were used to investigate the stability of the nanoparticle in aqueous solution and to measure the change in the surface charge after each interfacial reaction outlined in Scheme 6.1. The Zeta potential was found to shift from -36 ± 3 mV to -53± 3 mV from the maleimide-AuNP to the DO3A-amine-AuNP because of the presence of three deprotonated carboxylic groups per every interfacial Michael addition adduct. The presence of the cationic metal centre in Gd^{3+}-DO3A-amine-AuNP causes then the zeta potential to shift back to -30 ± 3 mV because Gd^{3+} compensates the negative charges carried by the carboxylates. A potential of -30 ±

3 mV for the final product confirms the visual observation that the Gd^{3+}-DO3A-amine-AuNP form a stable solution even at a slightly basic pH.

Finally, the metal composition (Au and Gd) of the nanoparticle was investigated by ICP-OES. From these results, we determined the ratio of Au:Gd and this was used to calculate the number of Gd chelators that had successfully reacted with maleimide moieties. ICP analysis showed that a ratio of 14:1 Au:Gd atoms was present after the interfacial Michael addition which indicated that 56 of the possible 80 maleimide sites underwent Michael addition (70% yield of the interfacial reaction). The remaining 30% of the maleimides likely underwent the mono-hydrolysis as observed through ^{1}H NMR spectroscopy for the model reaction using DO3A-amine (Supplemental Figure 4). The incomplete reaction may also be related to the large size of the chelator compared and possible charge repulsion between the chelators limiting a higher loading. It should be noted that when an excessively large number of chelators are present there is the possibility that the exchange of bound water will not be efficient, resulting in a detrimental effects on the relaxation and performance as a CA.

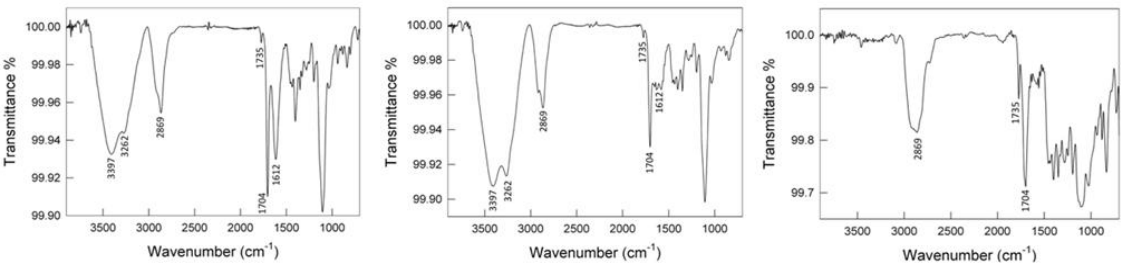

Figure 6.1. IR spectra of a) Gd^{3+}AuNP b) DO3A-AuNP c) maleimide-AuNP.

Relaxation measurements

Relaxation measurements were made on the individual Gd^{3+} chelator as well as the Gd^{3+}AuNP at four concentrations (Gd^{3+}DO3A-amine = 1 mM, 2 mM, 4 mM, 8 mM. Gd^{3+}AuNP = 1 mM, 2 mM, 4 mM, 8.26 mM) at pH 6.8 at 37 °C. The relaxation of Gd^{3+}-DO3A-amine as well as Gd^{3+}AuNP was the same within error. (r_1 Gd^{3+}-DO3A-amine = 2.3 mM^{-1} s^{-1}, r_1 Gd^{3+}AuNP = 2.2 mM^{-1} s^{-1}) (Figure 6.2).

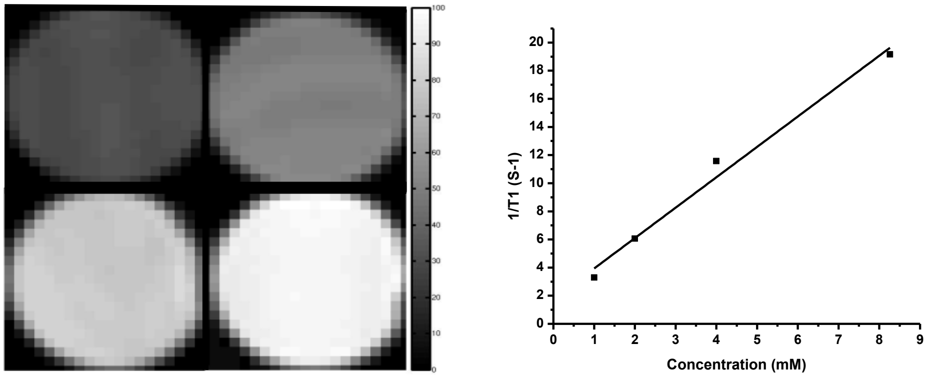

Figure 6.2. a) Images of phantoms of Gd-AuNP at concentrations 1 mM, 2 mM, 4mM and 8.26 mM at pH 6.8 and 37 °C. b) Calibration curve of (a). The slope of the graph is the r_1 GdAuNP = 2.2 mM^{-1}s^{-1}.

These values are comparable to other small molecule CAs at 9.4 T.[36] While it has been shown that a large, slower tumbling CA will have a more efficient relaxation compared to small fast tumbling molecules this is not observed for our Gd^{3+}AuNP. The free rotation of the chelator with respect to the AuNP is thought to limit the enhancement of slow tumbling and therefore the relaxation of the AuNP is the same as the free chelator.[5, 28] While these results indicate that there is no enhancement to the single Gd^{3+} chelator it is equally important to note that no decrease in relaxivity per chelator is noticed. This is important in the formation of AuNPs due to the likelihood that Gd^{3+} chelators are located in close proximity to each other, which has the potential to limit the access to the exchangeable proton source of the free pool resulting in a decrease in efficiency of relaxation. Because there is no decrease in relaxivity per Gd^{3+} the overall r_1 of the NP is 56 times the single r_1 of the Gd^{3+} CA and is therefore 123 mM^{-1} s^{-1} which is sufficient to ensure a local concentration high enough for *in vivo* imaging.

***In vivo* evaluation**

With the Gd^{3+}AuNP in hand, as a proof of concept we investigated its ability to act as a contrast agent in mice. Figure 6.3 shows the *in vivo* MR T_1 images of the kidneys of a mouse pre injection (a), 5 min post injection of a 0.1 mmol/kg [Gd] dose (b) and subtracted image (c). All *in vivo* images are from identical oblique slices and both kidneys are contained in the slice. Regions of interest containing the renal vasculature (solid line) and the medulla (dashed line) were identified using the 5 min post injection MR image as shown in Figure 6.3. Signal intensities collected from the regions of interest throughout the entire experiment are displayed in Figure 6.4.

An increase in signal intensity of roughly 200% was observed in the vascular region of both kidneys along with an enhancement of ~100% within in the medulla for each kidney. The signal enhancement was observed throughout the entire monitoring period of 90 min as shown in the wash in and out profiles, Figure 6.4. This elongated period of filtration is significant as it indicates that the agent is circulating in the blood for an extended period of time, which in turn should allow a generous period for imaging. The small size and prolonged circulation of Gd^{3+}AuNP contrast agent may allow for sufficient agent accumulation in pathological tissue, such as cancerous tumours where the vasculature membranes are permeable to circulating agents.[37] It should be noted that because of the small size of these nanoparticles, filtration would be primarily through renal excretion and as such is consistent with the observed enhancement in the kidneys and for this reason we began our *in viv*o testing of the renal system. Although the contrast enhancement is an important property, equally so is the toxicity of the contrast agent. The Gd^{3+}AuNP contrast agent displayed negligible toxicity during imaging and the mouse showed no ill effects 24 h post scan.

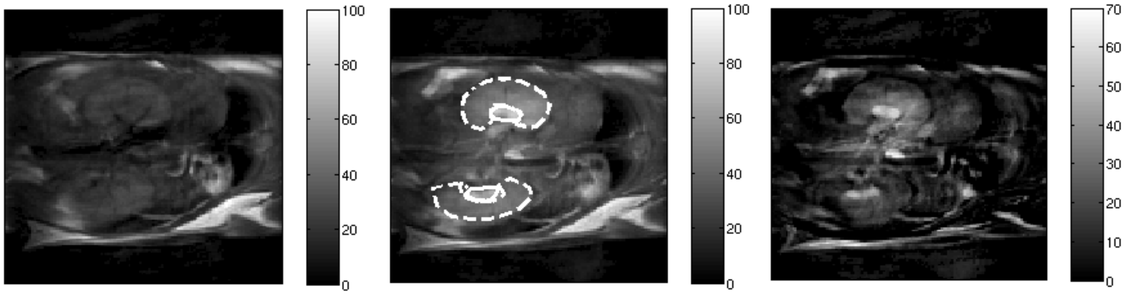

Figure 6.3. T_1 weighted images of kidneys of 0.1 mmol/kg of Gd^{3+}AuNP based on Gd concentration via tail injection. Left) Pre-injection Middle) 5 min post injection Right) Subtracted image of pre and post.

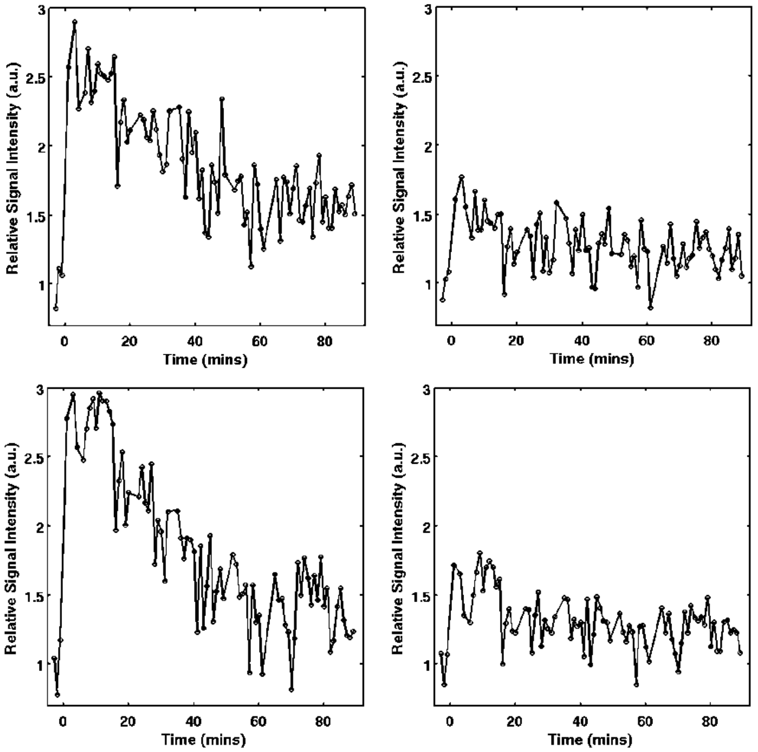

Figure 6.4. (Left) Signal enhancement of the vascular region of kidney 1 (Top) and kidney 2 (Bottom) showing a 200% signal enhancement immediately after injection with the enhancement falling to 50-100% at 90min. (Right) Signal enhancement of the medulla region of the kidney 1 (Top) and kidney 2 (Bottom) showing an enhancement of ~50% consistently throughout the 90 min of imaging.

6.3 Conclusion

We have demonstrated the ability to functionalize Au nanoparticles to nearly 70% under aqueous conditions to afford contrast agents that are suitable for MRI with over 50 Gd^{3+} chelators per AuNP. The GdAuNP are soluble at physiological pH and permit a higher concentration of CA to be delivered compared to the unbound CA that has a limited solubility at the same pH. We have developed a method to produce AuNP's of discrete size that function as their original clinically approved CA that are non toxic *in vivo*. Moving forward we are beginning to prepare agents that will benefit from the slow tumbling of the nano-sized agents as well as expanding on our imaging modalities. By employing AuNPs as our scaffold for our Gd^{3+} MRI CA we also have a strong X-Ray absorber that is suitable as a multimodal agent for MRI/computed tomography.[22-25]

6.4 Supplemental information

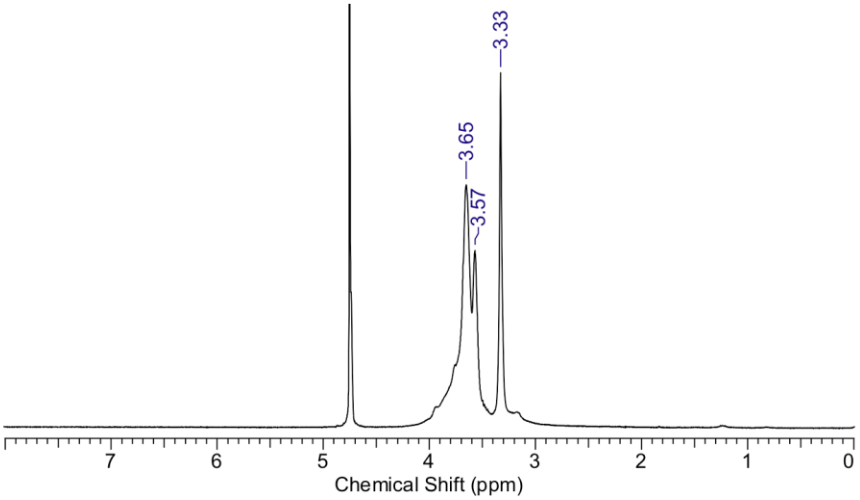

S6.1. ^{1}H NMR spectrum of Me-EG$_3$-AuNP referenced to residual H_2O (*).

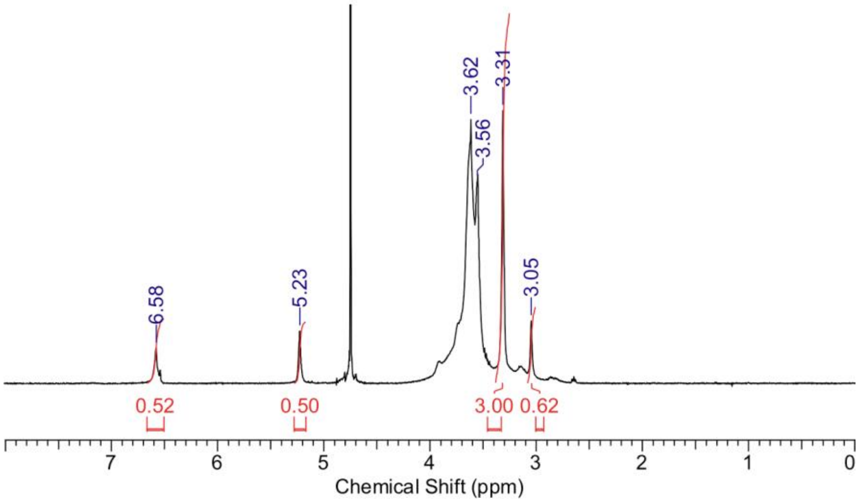

S6.2. ^{1}H NMR spectrum of FPMaleimide-AuNP referenced to residual H_2O (*).

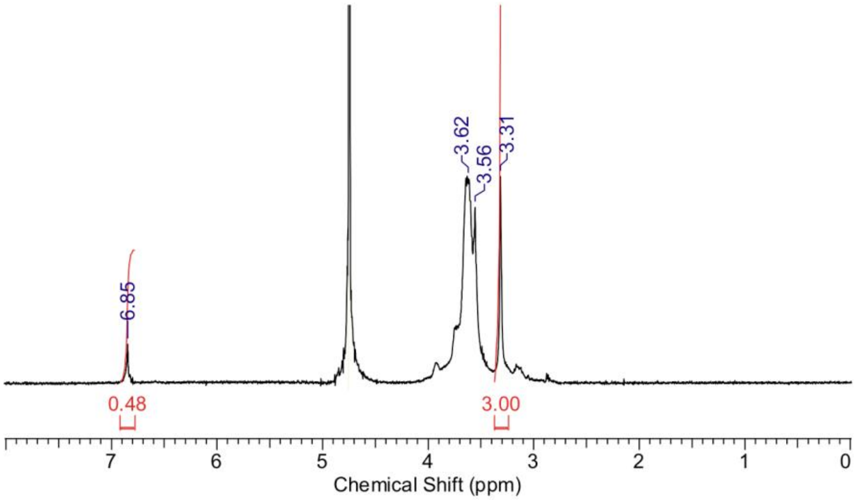

S6.3. 1H NMR spectrum of Maleimide-AuNP referenced to residual H_2O (*).

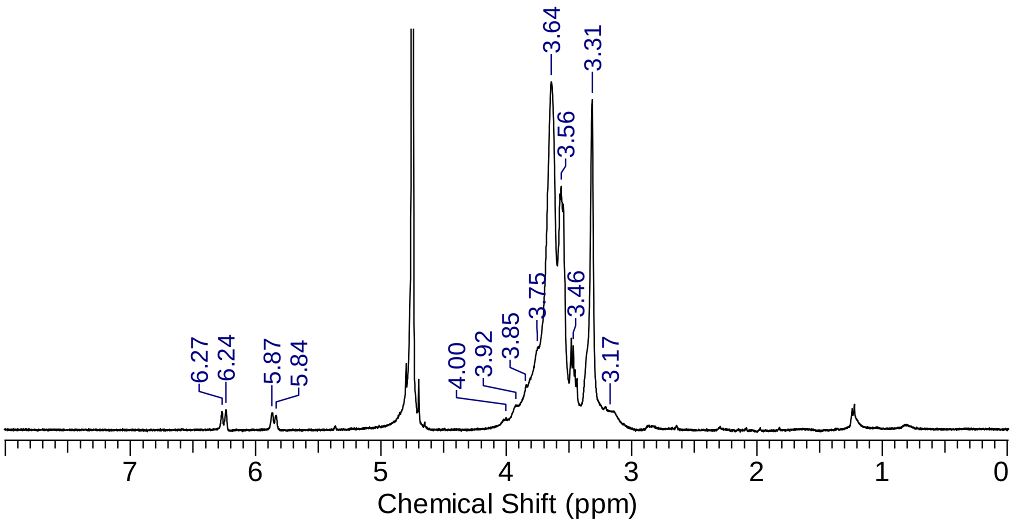

S6.4. 1H NMR spectrum of DO3A-Amine-AuNP referenced to residual H_2O (*). The peaks at 5.84 ppm and 6.24 ppm are related to the hydrolysis of the maleimide to the corresponding maleamic acid.

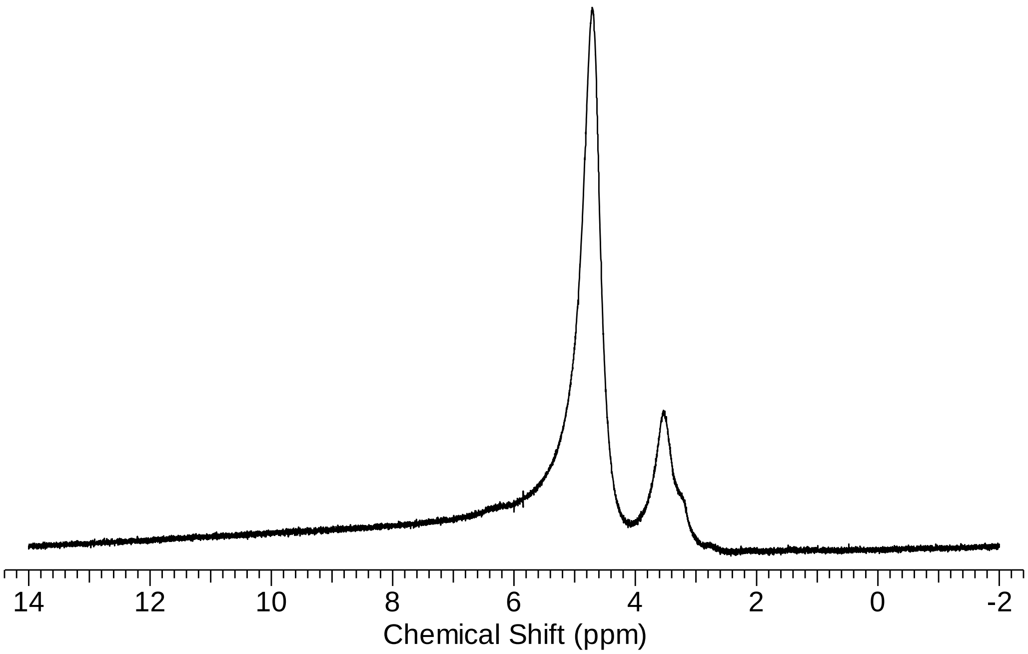

S6.5. ^{1}H NMR spectrum of Gd-DO3A-Amine-AuNP.

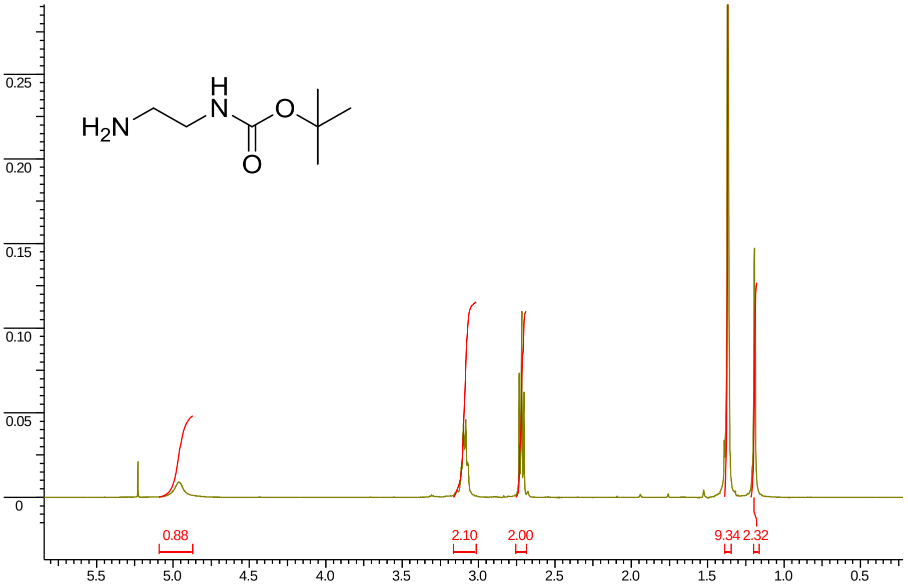

S6.6. ^{1}H NMR Spectrum of mono(Boc)Ethylene Diamine

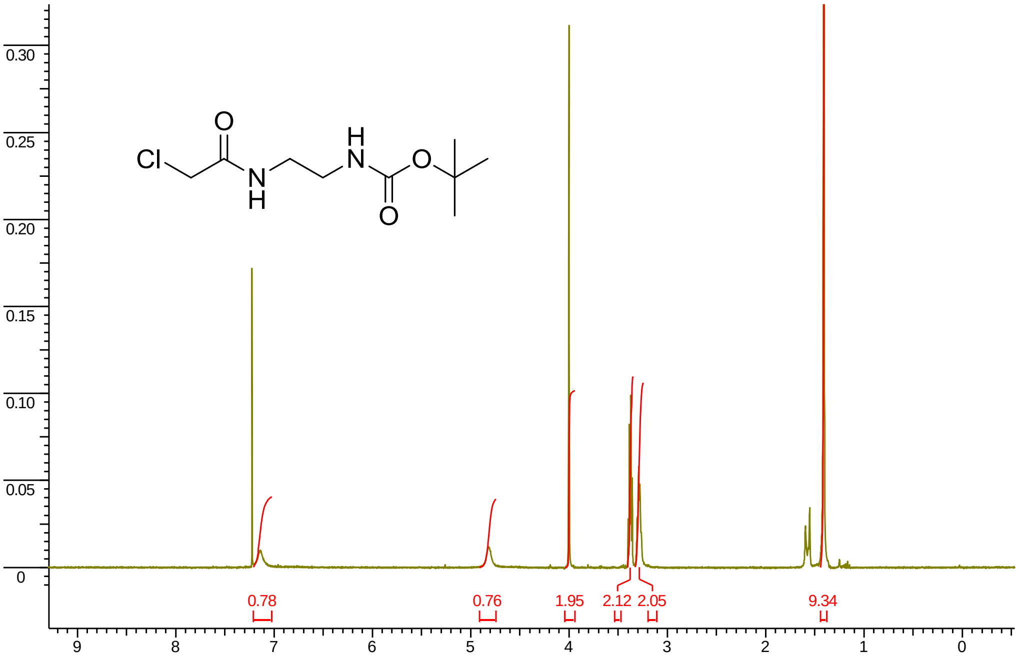

S6.7. ^{1}H NMR Spectrum of 2-*N*-Chloroacetyl-1-*N*-(Boc)ethylene Diamine

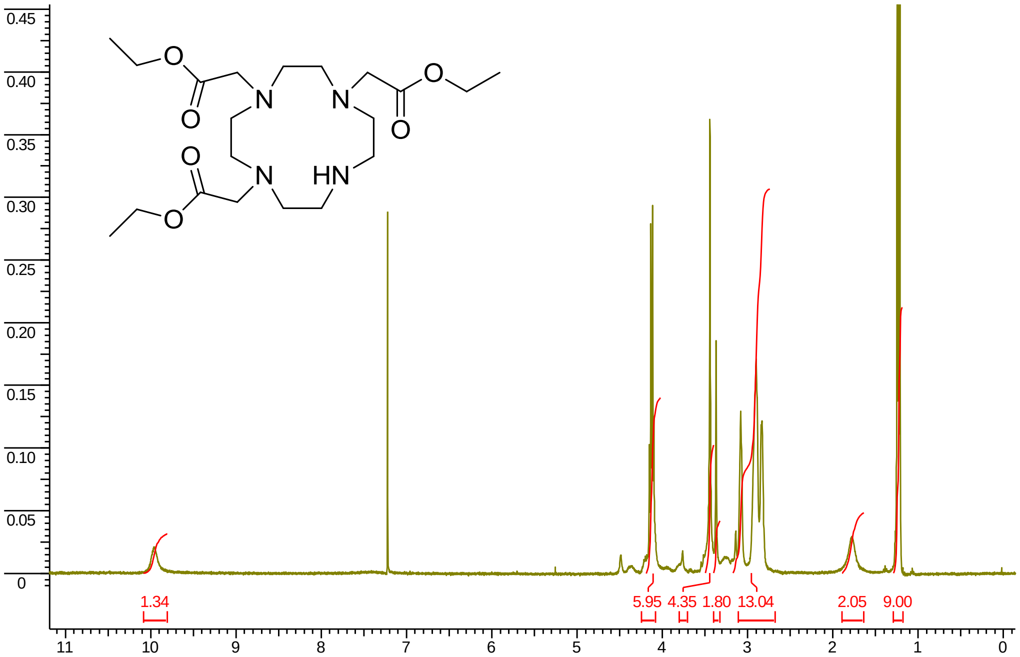

S6.8. ^{1}H NMR Spectrum of Tri(ethyl ester) Cyclen

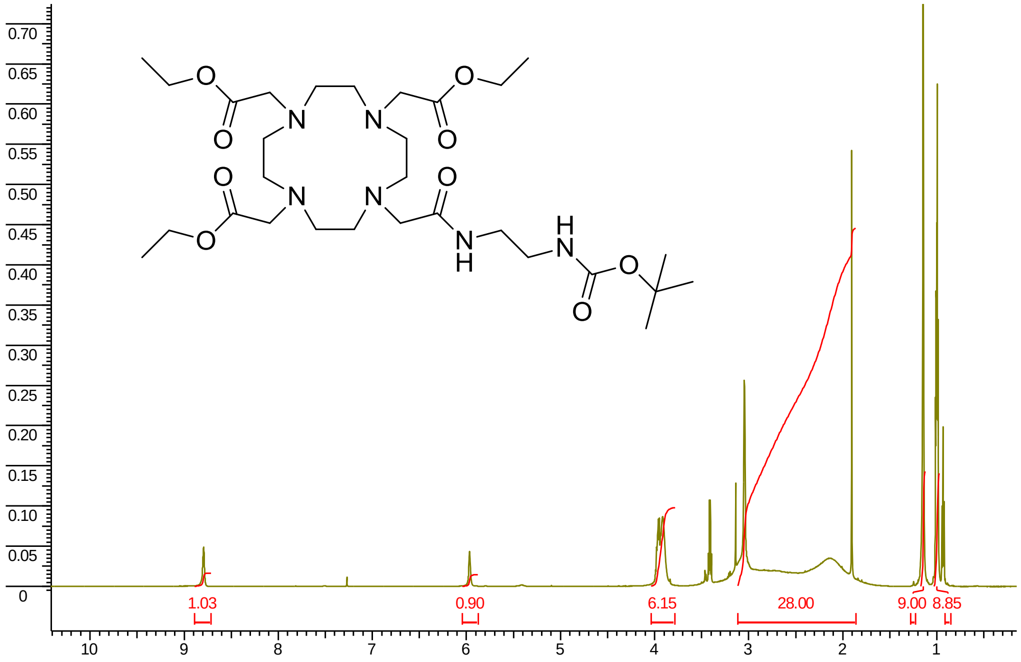

S6.9. ^{1}H NMR Spectrum of Tri(ethyl ester) Mono(Boc)Ethylene Diamine Cyclen

6.5 References

1. S. Aime, C. Cabella, S. Colombatto, S. G. Crich, E. Gianolio and F. Maggioni, *J. Magn. Reson. Imaging*, 2002, **16**, 394-406.

2. S. Aime, M. Botta and E. Terreno, *Adv. Inorg. Chem.*, 2005, **57**, 173-237.

3. D. D. Castelli, E. Gianolio, S. G. Crich, E. Terreno and S. Aime, *Coord. Chem. Rev.*, 2008, **252**, 2424-2443.

4. A. D. Sherry, P. Caravan and R. E. Lenkinski, *J. Magn. Reson. Imaging*, 2009, **30**, 1240-1248.

5. P. Caravan, *Chem. Soc. Rev.*, 2006, **35**, 512-523.

6. P. Caravan, J. J. Ellison, T. J. McMurry and R. B. Lauffer, *Chem. Rev.*, 1999, **99**, 2293-2352.

7. S. Laus, R. Ruloff, E. Toth and A. E. Merbach, *Chem. Eur. J.*, 2003, **9**, 3555-3566.

8. J. A. Pikkemaat, R. T. Wegh, R. Lamerichs, R. A. van de Molengraaf, S. Langereis, D. Burdinski, A. Y. F. Raymond, H. M. Janssen, B. F. M. de Waal, N. P. Willard, E. W. Meijer and H. Grull, *Contrast Media Mol. Imaging*, 2007, **2**, 229-239.

9. M. Longmire, P. L. Choyke and H. Kobayashi, *Curr. Top. Med. Chem.*, 2008, **8**, 1180-1186.

10. M. A. Mintzer and M. W. Grinstaff, *Chem. Soc. Rev.*, 2011, **40**, 173-190.

11. E. Toth, D. Pubanz, S. Vauthey, L. Helm and A. E. Merbach, *Chem. Eur. J.*, 1996, **2**, 1607-1615.

12. G. M. Nicolle, E. Toth, H. Schmitt-Willich, B. Raduchel and A. E. Merbach, *Chem. Eur. J.*, 2002, **8**, 1040-1048.

13. V. Weissig, J. Babich and V. Torchilin, *Colloid Surf. B-Biointerfaces*, 2000, **18**, 293-299.

14. E. Terreno, A. Sanino, C. Carrera, C. D. Delli, G. B. Giovenzana, A. Lombardi, R. Mazzon, L. Milone, M. Visigalli and S. Aime, *J. Inorg. Biochem.*, 2008, **102**, 1112-1119.

15. E. Terreno, W. Dastru, D. D. Castelli, E. Gianolio, S. G. Crich, D. Longo and S. Aime, *Curr. Med. Chem.*, 2010, **17**, 3684-3700.

16. G. M. Nicolle, E. Toth, K. P. Eisenwiener, H. R. Macke and A. E. Merbach, *J. Biol. Inorg. Chem.*, 2002, **7**, 757-769.

17. J. P. Andre, E. Toth, H. Fischer, A. Seelig, H. R. Macke and A. E. Merbach, *Chem. Eur. J.*, 1999, **5**, 2977-2983.

18. M. Grogna, R. Cloots, A. Luxen, C. Jerome, C. Passirani, N. Lautram, J. F. Desreux and C. Detrembleur, *Polym. Chem.*, 2010, **1**, 1485-1490.

19. A. Soleimani, F. Martinez, V. Economopoulos, P. J. Foster, T. J. Scholl and E. R. Gillies, *J. Mater. Chem. B*, 2013, **1**, 1027-1034.

20. M. Grogna, R. Cloots, A. Luxen, C. Jerome, J.-F. Desreux and C. Detrembleur, *J. Mater. Chem.*, 2011, **21**, 12917-12926.

21. K. M. Atkins, F. M. Martinez, A. Nazemi, T. J. Scholl and E. R. Gillies, *Can. J. Chem.*, 2011, **89**, 47-56.

22. M. Beija, Y. Li, H. T. Duong, S. Laurent, L. Vander Elst, R. N. Muller, A. B. Lowe, T. P. Davis and C. Boyer, *J. Mater. Chem.*, 2012, **22**, 21382-21386.

23. C. Alric, J. Taleb, G. L. Duc, C. Mandon, C. Billotey, A. L. Meur-Herland, T. Brochard, F. Vocanson, M. Janier, P. Perriat, S. Roux and O. Tillement, *J. Am. Chem. Soc.*, 2008, **130**, 5908-5915.

24. J.-A. Park, H.-K. Kim, J.-H. Kim, S.-W. Jeong, J.-C. Jung, G.-H. Lee, J. Lee, Y. Chang and T.-J. Kim, *Bioorg. Med. Chem. Lett.*, 2010, **20**, 2287-2291.

25. Y. Song, X. Xu, K. W. MacRenaris, X.-Q. Zhang, C. A. Mirkin and T. J. Meade, *Angew. Chem. Int. Ed.*, 2009, **48**, 9143-9147.

26. J.-L. Bridot, A.-C. Faure, S. Laurent, C. Riviere, C. Billotey, B. Hiba, M. Janier, V. Josserand, J.-L. Coll, L. Vander Elst, R. Muller, S. Roux, P. Perriat and O. Tillement, *J. Am. Chem. Soc.*, 2007, **129**, 5076-5084.

27. P.-J. Debouttiere, S. Roux, F. Vocanson, C. Billotey, O. Beuf, A. Favre-Reguillon, Y. Lin, S. Pellet-Rostaing, R. Lamartine, P. Perriat and O. Tillement, *Adv. Funct. Mater.*, 2006, **16**, 2330-2339.

28. P. Caravan, *Acc. Chem. Res.*, 2009, **42**, 851-862.

29. P. Gobbo and M. S. Workentin, *Langmuir*, 2012, **28**, 12357-12363.

30. K. D. Hartlen, H. Ismaili, J. Zhu and M. S. Workentin, *Langmuir*, 2012, **28**, 864-871.

31. P. Gobbo, M. C. Biesinger and M. S. Workentin, *Chem. Commun.*, 2013, **49**, 2831-2833.

32. L. S. Natrajan, A. J. L. Villaraza, A. M. Kenwright and S. Faulkner, *Chem. Commun.*, 2009, 6020-6022.

33. L. Tei, G. Gugliotta, Z. Baranyai and M. Botta, *Dalton Trans.*, 2009, **0**, 9712-9714.

34. J. Lu, M. Shi and M. S. Shoichet, *Bioconjugate Chem.*, 2008, **20**, 87-94.

35. A. Taylor, K. M. Wilson, P. Murray, D. G. Fernig and R. Levy, *Chem. Soc. Rev.*, 2012, **41**, 2707-2717.

36. M. Milne, K. Chicas, A. Li, R. Bartha and R. H. E. Hudson, *Org. Biomol. Chem.*, 2012, **10**, 287-292.

37. H. F. Dvorak, J. A. Nagy, J. T. Dvorak and A. M. Dvorak, *Am. J. Pathol.*, 1988, **133**, 95-109.

Chapter 7: Conclusion

The main theme of this thesis, was the synthesis of novel MRI contrast agents. While it is possible to synthesize a large array of agents with properties that are suitable for MR imaging, it is a more difficult task to rationally design agents with predictable properties. My investigations over the past four years have contributed to a greater understanding of the structure-properties relationships of cyclen-based ParaCEST contrast agents and will impact future rational CA design.

The studies described in this thesis began by designing a central moiety that would enable us to perform "click" reactions using targeting agents such as carbohydrates. While investigating the potential of this agent, it was discovered that parent alkyne-derivatized DOTAM had exceptional temperature sensitivity as described in chapter 2. Since the appearance of the publication (chapter 2), we were contacted by the NIST with the goal of using this agent as a temperature probe during NMR studies. These studies are still ongoing.

Using the "click" scaffold molecule (chapter 2), sugar-modified contrast agents were prepared and their potential as T_1 and paraCEST agents was evaluated, as described in chapter 3. Attempts to understand the structural-property relationship of these agents proved to be rather difficult due to multiple, simultaneous contributing factors, such as;

size, water exchange rates and hydrogen bonding ability of the pendant groups. However, this study highlighted the potential of the exchangeable amide protons to be used as paraCEST agents and this led us to develop a series of high shifting amide agents.

During the evaluation of a series of high shifting amide based paraCEST agents it was observed that an agent with an exchangeable proton past 100 ppm could be developed (chapter 4). Evaluating this agent showed that signals outside of 100 ppm will allow for *in vivo* detection while minimizing interference from magnetization transfer effects. This is a significant observation and research direction since the observation of bona fide ParaCEST contrast *in vivo* is severely affected from endogenous MT to such an extent that makes this imaging modality completely impractical. Thus, overcoming this limitation is critical in moving the field of ParaCEST MRI toward clinical application.

Next, we chose to tackle a second MR property that hinders *in vivo* imaging, namely T_2 shortening of lanthanide based agents due to T_2 exchange. By designing and synthesizing agents that do not possess an inner sphere water, we were able to demonstrate how the signal to noise increases substantially, which in turn increases the sensitivity of paraCEST imaging. Clearly, the next step is to combine properties of a highly shifted amide signal with agents that have long T_2 values to develop agents that are suitable for *in vivo* paraCEST imaging.

Finally, our final work focused on developing highly loaded T_1 nanoparticles using an interfacial Michael addition. Collaborating with a research group that had previously developed a water soluble gold nanoparticle we were able to synthesis an agent containing over 50 Gd^{3+} chelators to grant a high T_1 relaxation value at 9.4 T suitable for *in vivo* imaging which was demonstrated in chapter 6.

The culmination of the research described in this thesis provides the groundwork for further development of ParaCEST contrast agents that have high shifted amides, with no inner sphere water that are suitable for *in vivo* imaging.

Copyright Permission

- **Mark Milne**, Robert H.E. Hudson[†]. *"Contrast agents possessing high temperature sensitivity."* Chemical Communications, **2011**, 47, 32, 9194-9196. Reproduced by permission of The Royal Society of Chemistry.

- **Mark Milne**, Kirby Chicas, Alex Li, Robert Bartha and Robert H.E. Hudson[†]. *"ParaCEST MRI contrast agents capable of derivatization via 'click' chemistry."* Organic and Biomolecular Chemistry, **2012**, 10, 287-292. Reproduced by permission of The Royal Society of Chemistry.

- Todd K. Stevens*, **Mark Milne***, Adam A. H. Elmehriki, Mojmir Suchý, Robert Bartha, Robert H. E. Hudson[†]. *"DOTAM-based ParaCEST agent favoring TSAP geometry for enhanced amide proton chemical shift dispersion and temperature sensitivity."* Contrast Media and Molecular Imaging, **2012**, 3, 289–292. *Contributed equally. Copyright © 2013 John Wiley & Sons, Ltd.

CURRICULUM VITAE

MARK MILNE

EDUCATION

2009-2013	University of Western Ontario	London, ON
	Ph.D Candidate in Organic Chemistry	
	Supervisor: Dr. R. Hudson	
2006 – 2009	University of Saskatchewan/UWO	Saskatoon, SK
	M.S.c in Biological Chemistry	
	Supervisor: Dr. H-B Kraatz	
1999-2005	University of Saskatchewan	Saskatoon, SK
	B.S.c Chemistry	

Professional Development: A comprehensive introduction to the NMR relaxometry, field cycling technique and the interdisciplinary application. Mede, Italy, May 2009.

European molecular imaging laboratories- imaging probe preparation. Turin, Italy, April 2009.

SCHOLARLY WORKS

Peer-reviewed Publications:

1. **Mark Milne** , Pierangelo Gobbo, Nevin McVicar, Mark S. Workentin , Robert Bartha and Robert H. E. Hudson†, *"Water soluble gold nanoparticles functionalized with gadolinium through Michael addition for use as a MRI contrast agent"*. Submitted to J. Mater Chem. B. **2013.** Manuscript #TB-ART-05-2013-020699.

2. **Mark Milne**, Melissa Lewis, Nevin McVicar, Robert Bartha and Robert H. E. Hudson†, *"MRI ParaCEST agents that improve amide based pH measurements by eliminating inner sphere water* T_2 *exchange*. Submitted to RSC Advances, **2013**. Manuscript # RA-ART-07-2013-043537.

3. Adam A. H. Elmehriki, **Mark Milne,** Mojmir Suchý, , Robert H. E. Hudso^{n†}, *"Complexes of selected late period lanthanide(III) cations with 1,4,7,10-tetraazacyclododecane-1,4,7,10-tetraacetic acid amide (DOTAM)-alkyl ligands — A new platform for the development of paramagnetic chemical exchange saturation transfer (PARACEST) magnetic resonance imaging (MRI) contrast agents*" Can. J. Chem., **2013**, 91(3): 211-219.

4. Todd K. Stevens*, **Mark Milne***, Adam A. H. Elmehriki, Mojmir Suchý, Robert Bartha, Robert H. E. Hudson†. *"DOTAM-based ParaCEST agent favoring TSAP geometry for enhanced amide proton chemical shift dispersion and temperature sensitivity."* Contrast Media Mol. Imaging, **2012**, 3, 289–292. *Contributed equally.

5. Mojmír Suchý, Alex X. Li, **Mark Milne**, Robert Bartha and Robert H. E. Hudson†. *"DOTAM-type ligands possessing arginine pendant groups for use in PARACEST MRI"* Contrast Media Mol. Imaging, **2012**, 7, 441-445.

6. **Mark Milne**, Kirby Chicas, Alex Li, Robert Bartha and Robert H.E. Hudson†. *"ParaCEST MRI contrast agents capable of derivatization via 'click' chemistry."* Org. Biomol. Chem., **2012**, 10, 287-292.

7. **Mark Milne**, Robert H.E. Hudson†. *"Contrast agents possessing high temperature sensitivity."* Chem Commun., **2011**, 47, 32, 9194-9196.

8. Mojmír Suchý, **Mark Milne**, David W. Dodd, Alex X. Li, Nevin McVicar, Robert Bartha and Robert H. E. Hudson†. *"Mono- and tetraalkyne modified ligands and their* Eu^{3+} *complexes: utilizing "click" chemistry to expand the scope of conjugation chemistry."* Eur. J.Org. Chem., **2011**, 6532-6543.

9. Cailin Drexler, **Mark Milne**, Erin Morgan, Michael Jennings, Heinz B. Kraatz†. *"Synthesis and characterization of new ferrocene peptide conjugates."* Dalton Trans., **2009**, 22, 4370-4378.

Theses: *"Synthesis and characterisation of new ferrocene peptide diphenol phenanthroline macrocycles"* Masters Thesis, University of Saskatchewan, **2009**.

Academic Meetings:

1. Poster presentation: **Mark Milne**, Todd K. Stevens, Adam A. H. Elmehriki, Mojmír Suchý, Robert Bartha, Robert H. E. Hudson, "Overcoming Biological MT Effects by use of ParaCEST MRI Contrast Agents Possessing Highly Shifted Amide Proton Signals" at WMIC in Dublin Ireland, Sept. **2012**.

2. Oral presentation: **Mark Milne**, Todd K. Stevens, Adam A. H. Elmehriki, Mojmír Suchý, Robert Bartha, Robert H. E. Hudson, “Development and Evaluation of ParaCEST MRI Contrast Agents Possessing highly Shifted Amide Proton Signals” at ISBOMC in Toronto, Ont. July **2012**.

3. Poster presentation: **Mark Milne**, Mojmír Suchý, , David W. Dodd, Alex X. Li, Robert Bartha, Robert H. E. Hudson, “Decoration of Cyclen-Based Ligands by “Click” Chemistry: Toward PARACEST MRI Contrast Agents” at CSC Toronto Ont. April **2010**.

4. Oral and poster presentation: **Mark Milne**, H-B Kraatz, “Physical study of bioorganometalic peptide macrocycles” at ISBOMC in Missoula, MT. July **2008**.

5. Poster presentation: **Mark Milne**, H-B Kraatz, “New bioinorganic macrocycles and their use in synthesizing of topologically linked catenanes and rotaxanes” at IDW in Toronto Ont. Nov. **2007**.

Awards:

Western Graduate Research Scholarship – 2009-2013

Canadian Society for Chemistry Travel Award – 2012

Western ASPIRE – 2012

World Molecular Imaging Poster Award – 2012

Robert and Ruth Lumsden Graduate Award – 2013